Optimal Design of Porous Materials

Andreassen, Erik

Publication date:
2015

Document Version
Publisher's PDF, also known as Version of record

Optimal Design of Porous Materials

PhD Thesis

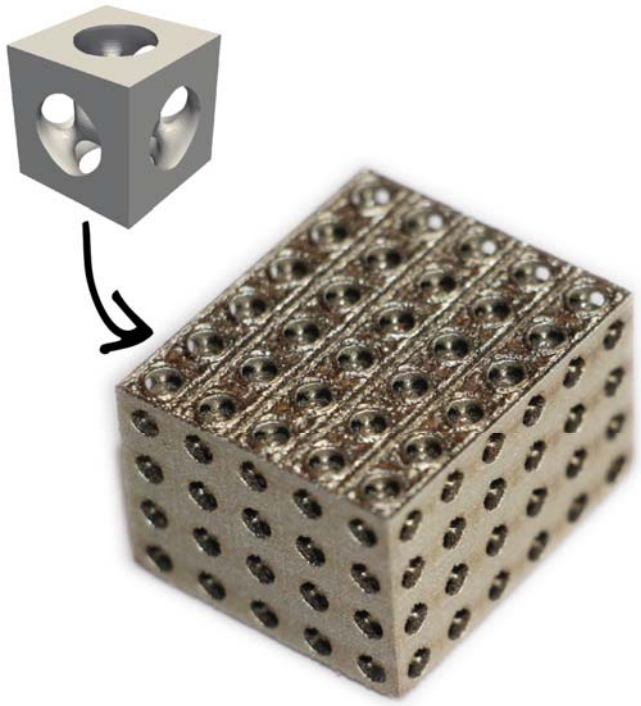

Erik Andreassen
DCAMM Special Report No. S172
January 2015

DTU Mechanical Engineering
Department of Mechanical Engineering

PhD thesis

Optimal Design of Porous Materials

January 16, 2015

PhD thesis by Erik Andreassen
Supervisor: Professor Jakob S. Jensen
Co-supervisors: Professor Ole Sigmund
Associate Professor Jon J. Thomsen

DTU Mechanical Engineering
Department of Mechanical Engineering

DTU

Title of the thesis:
Optimal design of porous materials

PhD student:
Erik Andreassen
E-mail: erand@mek.dtu.dk

Supervisors:
Jakob S. Jensen
E-mail: json@elektro.dtu.dk

Ole Sigmund
E-mail: sigmund@mek.dtu.dk

Jon J. Thomsen
E-mail: jjt@mek.dtu.dk

Address:
Department of Mechanical Engineering, Solid Mechanics
Technical University of Denmark
Nils Koppels Allé, Building 404, 2800 Kgs. Lyngby, Denmark

DCAMM Special Report no. S172
ISBN: 978-87-7475-394-0

Preface

This thesis is submitted in partial fulfillment of the requirements for obtaining the degree of PhD in mechanical engineering at the Technical University of Denmark (DTU). The PhD project was funded by the Danish Research Agency through the innovation consortium F•MAT, and it was carried out at the Solid Mechanics section in the Department of Mechanical Engineering at DTU in the period September 1st, 2011, to December 7th, 2014. Professor Jakob Søndergaard Jensen was the main supervisor on the project, while Professor Ole Sigmund and Associate Professor Jon Juel Thomsen acted as co-supervisors.

The first time I read a PhD thesis (or at least the first few pages) I was puzzled by the number of people the author thanked, but now I understand how much support means when you are working towards a PhD degree.

First, and foremost, I want to thank my supervisors, who have always been there to discuss problems and answer my questions. And a special thanks to Jakob, who bore with me and my always way too optimistic time schedules.

And to the other participants in the F•MAT consortium: I am grateful for your valuable input on manufacturing processes and feedback on optimization results.

Then, I would also like thank the rest of my colleagues at the Solid Mechanics section. The exceptional good working environment, which you all contribute to (especially our secretary Gerda H. Fogt), has been deeply appreciated. So has the expertise and training in parallel programming provided by Boyan S. Lazarov and Niels Aage. Of my fellow PhD students in room 127, who all deserve thanks for the contribution to the good mood in the office, a special thanks goes to Villads E. Johansen for his Python and Linux assistance, and Anders Clausen for giving early feedback on the thesis.

Part of the work presented in this thesis was carried out during a three months stay at Georgia Tech in Atlanta (US), under the guidance of Professor Massimo Ruzzene. I am grateful for getting a chance to visit his group, and I deeply appreciate all the time he spent educating me in the fundamentals of wave propagation. Massimo and his group made the stay a great experience, and I only regret it could not be longer.

Finally, I want to thank my family and friends for the comfort and support they provided during the last three years. Particularly my girlfriend Nina Løn and our daughter Linnea, who always motivate me to keep the coffee breaks modest and get home in time for dinner.

Kgs. Lyngby, January 16, 2015

Erik Andreassen

Resumé (in Danish)

Hovedfokus i afhandlingen er topologioptimering af materialemikrostrukturer. Målet er at designe nye materialer med attraktive egenskaber ved at kombinere traditionelle materialer i periodiske strukturer.

Først vises der, hvordan storskala-topologioptimering kan bruges til at designe komplicerede tredimensionelle materialestrukturer med eksotiske egenskaber, som for eksempel et negativt tværkontraktionstal eller en negativ termisk udvidelseskoefficient. Derudover præsenteres topologioptimeringsformuleringer, som kan bruges til at designe materialer med et godt kompromis mellem stivhed og dæmpning. Både en enkel kvasistatisk metode, som kan bruges for lavfrekvent bølgeudbredelse, og en generel metode (som baserer sig på Floquet-Bloch teori), for vilkårlige frekvensområder, præsenteres. Den kvasistatiske metode demonstreres på såvel to- og tredimensionelle mikrostrukturer. I tillæg vises der, hvordan den generelle metode kan anvendes til at designe frekvensafhængig dæmpning, som kan være højere end, hvad der kan opnås indenfor de kvasistatiske grænser.

Arbejdet, som præsenteres i afhandlingen, er inspireret af den øgende tilgængelighed af additiv fremstillingsmetoder (3D print), og den mulighed dette giver til at fremstille komplicerede strukturer. Derfor er det, at bruge topologioptimering til at opnå strukturer som er fremstillingsklare, et gennemgående tema i afhandlingen.

Dette er også tilfældet for den sidste del af afhandlingen, hvor en simpel multiskalametode til optimering af strukturel dæmpning præsenteres. Metoden kan anvendes til at opnå en optimeret komponent med detaljer, på samme niveau som 3D printere kan præstere. Dette er muligt uden, at metoden kræver uoverskuelige mængder regnekraft. Derudover sikrer metoden, at den stive materialefase er sammenhængende. Noget som gør det muligt at designe komponenter, som kan blive fremstillet ved at 3D printe den stive fase, for derefter at bruge dette som en støbeform for den bløde materialefase.

Abstract

The focus of this thesis is topology optimization of material microstructures. That is, creating new materials, with attractive properties, by combining classic materials in periodic patterns.

First, large-scale topology optimization is used to design complicated three-dimensional materials with exotic properties, such as isotropic negative Poisson's ratio and negative thermal expansion.

Furthermore, it is shown how topology optimization can be used to design materials with a good compromise between stiffness and damping. Both a simple quasi-static method suited for low frequency wave propagation, and a more general dynamic method (using Floquet-Bloch theory) applicable to arbitrary frequency ranges are presented. The quasi-static method is applied to the design of both two- and three-dimensional material microstructures. And it is shown, using two-dimensional examples, how the general method can be used to design materials with frequency dependent loss, which can be higher than depicted by the quasi-static bounds.

The work is inspired by the increased availability of additive manufacturing facilities, and, thus, the possibility of manufacturing complicated structures. Therefore, throughout the thesis extra attention is given to obtain structures that can be manufactured.

That is also the case in the final part, where a simple multiscale method for the optimization of structural damping is presented. The method can be used to obtain an optimized component with structural details on the same scale as the manufacturing precision, without being computationally exhaustive. Furthermore, the connectivity of the stiff phase is assured, making it possible to design components that can be manufactured, using additive manufacturing to print the stiff material phase, and, thereafter, infuse the component with the soft and lossy material phase.

Publications

The following publications are part of the thesis:

[P1] Andreassen, E. and Andreasen, C. S. (2014). "How to determine composite material properties using numerical homogenization". *Computational Materials Science* 83, pp. 488–495

[P2] Aage, N., Andreassen, E., and Lazarov, B. S. (2014). "Topology optimization using PETSc: An easy-to-use, fully parallel, open source topology optimization framework". *Structural and Multidisciplinary Optimization* [In press]

[P3] Andreassen, E., Lazarov, B. S., and Sigmund, O. (2014b). "Design of manufacturable 3D extremal elastic microstructure". *Mechanics of Materials* 69 (1), pp. 1–10

[P4] Andreasen, C. S., Andreassen, E., Jensen, J. S., and Sigmund, O. (2014). "On the realization of the bulk modulus bounds for two-phase viscoelastic composites". *Journal of the Mechanics and Physics of Solids* 63 (1), pp. 228–241

[P5] Andreassen, E. and Jensen, J. S. (2013). "Analysis of phononic bandgap structures with dissipation". *Journal of Vibration and Acoustics* 135 (4), pp. 041015–8

[P6] Andreassen, E. and Jensen, J. S. (2014b). "Topology optimization of periodic microstructures for enhanced dynamic properties of viscoelastic composite materials". *Structural and Multidisciplinary Optimization* 49 (5), pp. 695–705

[P7] Andreassen, E., Manktelow, K., and Ruzzene, M. (2015). "Directional bending wave propagation in periodically perforated plates". *Journal of Sound and Vibration* 335, pp. 187–203

[P8] Andreassen, E., Chang, H. R., Ruzzene, M., and Jensen, J. S. (2014a). "Optimization of directional elastic energy propagation". [In preparation]

[P9] Andreassen, E. and Jensen, J. S. (2014a). "A practical multiscale approach for optimization of structural damping". [To be submitted]

Contents

CHAPTER 1

INTRODUCTION

1.1 Project background

My PhD work is part of the F•MAT (Functional MATerials) project. One reason the F•MAT project came about was promising sound/damping characteristics of the phono cartridge shown in Fig. 1.1(a). The cartridge is produced using an additive manufacturing method called selective laser sintering (SLS). The manufacturer, Ortofon, noted that compared to conventionally milled cartridges, the damping ratio had increased enough to improve the performance. One reason could be the (unintentional) porosities, see Fig. 1.1(b), appearing when using SLS. The amount of porosity, which is reflected in the density of the manufactured part, can be controlled by adjusting the SLS parameters, and one initial idea was that this ability would allow for manufacturing of optimized designs with varying density. TEXTHEIGHT = 625.96062pt, TEXTWIDTH = 426.79134pt

Thus, the project included a study of how the mechanical properties of an SLS part vary with density. Measurements were performed on a range of steel beam specimens with varying porosity (measured as the density) manufactured by The Danish Technological Institute (DTI). When it came to stiffness the expected power law relation was observed, however, with respect to damping there was no clear trend, see measurement results in Fig. 1.2. The damping ratio was higher than for pure steel, but still lower than cheaper alternatives, such as cast iron.

Furthermore, it was observed that with this technique the lowest obtainable density is approximately 85% of the solid material, putting a limitation on the density range of the optimized designs.

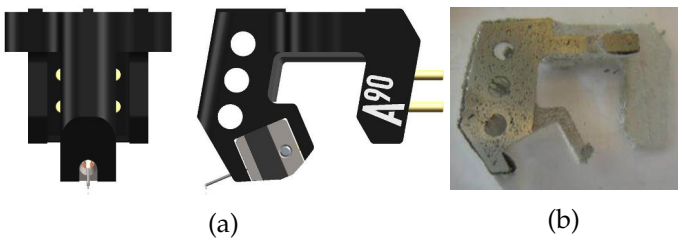

(a) (b)

Figure 1.1: Ortofon A90 phono cartridge manufactured using SLS. (a) Illustration from Ortofon's A90 user guide. (b) Picture of sliced cartridge indicating porosities.

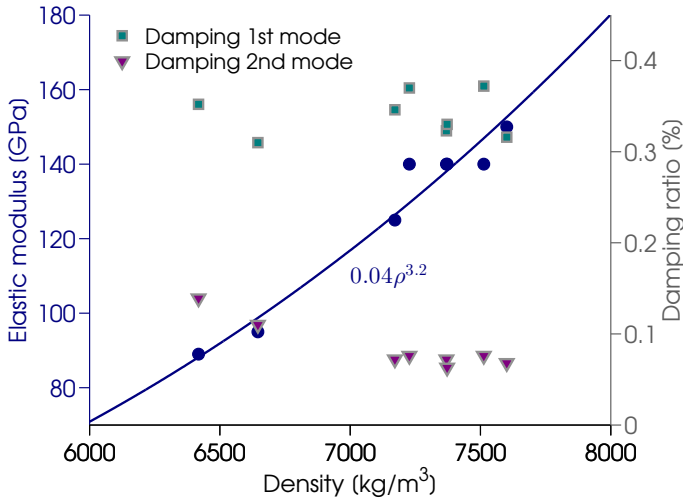

Figure 1.2: Measurements of stiffness (circles) and damping conducted on beam specimens with different density (ρ). The measurements were performed by Casper S. Andreasen at DTU Mechanical Engineering.

1.1.1 Project aim

Based on the obtained results, the focus in this part of F• MAT project turned towards the true advantage of additive manufacturing – the design freedom. When topology optimization is used to design three-dimensional (3D) structures, the resulting design can be difficult to manufacture by conventional manufacturing methods. Combining additive manufacturing with topology optimization, it should be possible to create structures with improved performance.

One common goal for all involved parties is to obtain materials with high damping, but without sacrificing too much on the stiffness. Since the damping did not seem to vary much with the porosities, we decided on a path where topology optimization could be used to design material microstructures with a good compromise between damping and stiffness. However, also developing materials with attractive static properties (e. g. high stiffness to weight ratio) were of interest. With that in mind, the final goal was to get to the point where topology optimization can be used to maximize the damping of a component at a range of eigenfrequencies with a simple multiscale approach. This thesis goes through the steps we have taken to get to that point.

1.2 Thesis structure

It has been my aim to make this thesis enjoyable to read, instead of writing as many pages as possible. Personally, I'm a big fan of the following (mis-)translation of a famous Voltaire quote:

> *The secret of being boring is to say everything.*[1]

[1] *Sixième discours: sur la nature de l'homme*, Sept Discours en Vers sur l'Homme, 1738. The original quote is "Le secret d'ennuyer est celui de tout dire.", which I have been told is more correctly translated to "The secret of being a bore is to tell everything."

This thesis is purposely kept short, and this because I believe the main points all too often are drowned in less important details.

The next chapter will give an introduction to the field of material microstructure design, including a short introduction to topology optimization. Thereafter, in Chapter 3, optimization of manufacturable microstructures for both static and quasi-static properties is discussed. Chapter 4 follows with an overview of the work I have been involved in on designing microstructures with frequency dependent properties. Chapter 5 presents a practical multiscale method that can be used when maximizing the damping of a component. Finally, the thesis ends with a few concluding remarks and thoughts on future work in Chapter 6.

CHAPTER 2

MATERIAL OPTIMIZATION

The title of this PhD is "Optimal design of porous materials", and this is to be understood as material design in a structural or architectural way. A material consists of more or less orderly arranged atoms or molecules, and in this work the focus has been on building new materials from existing materials.

Creating a new material in this way can be done by building orderly arranged (periodic) structures on a microscale. The periodic structure can for instance consist of one traditional material and air/void. In that case the microstructure would be a "porous" structure. However, the microstructure can also consist of several traditional materials. In the context of microstructure design I will use the term *material phase* for both a traditional material and for void. Put in another way, the microstructure can consist of several material phases, of which one could be void.

Finally, these material designs can be incorporated in a component to improve its performance. The relationship between the three different scales is illustrated in Fig. 2.1. This division is an oversimplification, but helps clarify what the term material design refers to in the current context.

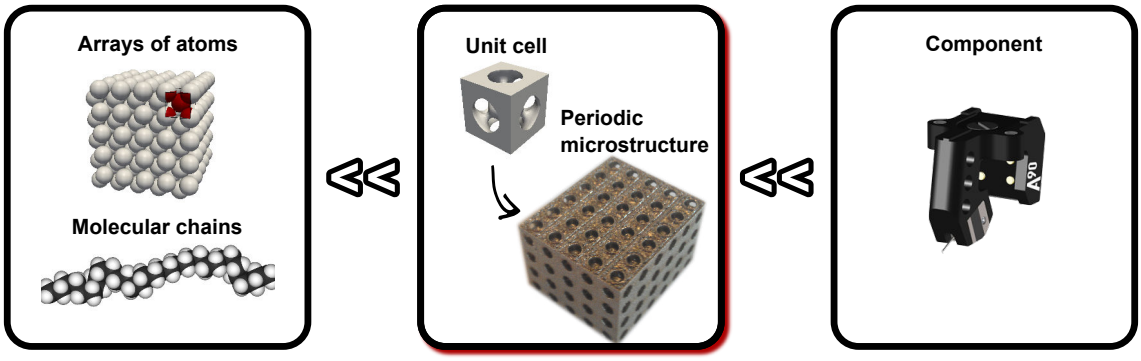

Figure 2.1: Length scale illustration. The microstructure is much larger than the atoms and molecules, but should also be clearly separated from the length scale of the component.

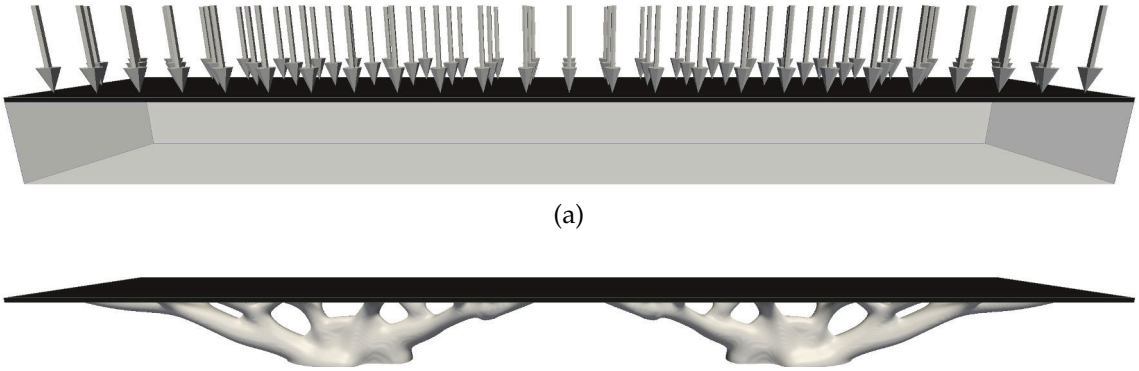

(a)

(b)

Figure 2.2: Topology optimization example. (a) Loaded surface and transparent box shows domain allocated for support. (b) Surface and supports as obtained with topology optimization.

2.1 Topology optimization

I have already mentioned the term *topology optimization* several times, and this section is dedicated to an explanation of it. Since Bendsøe and Kikuchi (1988) introduced a general computational material distribution method, topology optimization has grown into a research field of its own. Topology optimization is about optimizing the layout (topology) of a structure, and the aim is best illustrated by an example. Figure 2.2(a) shows a loaded surface (this could be a bridge, a platform, or a roof that needs support). The domain allocated for support material (e. g. steel or concrete) is indicated with a box. Since we live in a world with limited resource, filling up the entire box is not an option. If topology optimization is used to fill 12 percent of the box with support material in a way that minimize the deformation of the structure, the result will look like Figure 2.2(b).

Topology optimization separates itself from shape and sizing optimization by introducing a design field, which makes it possible to compute gradients in the *whole* domain. The gradients (also called sensitivities) give information on where in the domain it is most beneficial to add or remove material. The method bases itself on the fact that the physics of most problems can be modeled with partial differential equations (PDEs), which is often solved by numerical tools where the domain is divided (discretized) into many small pieces. By iteratively solving the PDEs, computing the gradients, and updating the distribution of material in the domain, it is possible to minimize a certain objective, e. g. compliance, given some constraints, such as the amount of material.

During the last decade several similar methods, with slightly different flavor, have developed in the field of topology optimization. It is my impression that the choice between them is more a personal taste, than one method actual being better than another. Therefore, in my work I have used what I consider the simplest one, where the gradients are computed for each element (piece) and element variables are iteratively updated with an optimization algorithm suited for a large number of design variables, such as a variant of the Method of Moving Asymptotes (MMA) (Svanberg, 1987, 2002; Bruyneel et al., 2002).

The process is discussed in detail in (Bendsøe and Sigmund, 2003), and I will refrain

from going into more details here. Instead, I will point out that (gradient-based) topology optimization can be used in all domains where the physics is modeled with PDEs as long as an interpolation between the different material phases, or material and void, can be introduced. Remark, that gradient-based optimization is a much better choice than genetic algorithms, assuming a good interpolation scheme can be devised, because it uses intelligent information (gradients) to decide where to put the material (Sigmund, 2011).

2.2 Microstructure design

The design of material microstructures has been an ongoing research field for several decades. In the current work the focus has been on designing the unit cell of a periodic structure to achieve certain macroscopic properties. One example is the unit cell and corresponding periodic structure shown in Fig. 2.1. Cadman et al. (2012) give a thorough review with more than 200 references to papers regarding microstructural design. A similar review is outside the scope of the present text. Instead, I will focus on those papers that have had the greatest influence on my work.

2.2.1 Inverse homogenization problem

The most used approach, and the approach adopted in the present work, is to combine numerical homogenization, which I will return to in the next chapter, and topology optimization. Here, Guedes and Kikuchi (1990) made the groundwork for what Sigmund (1994, 1995) coined the *inverse homogenization problem*. The term was natural at that time, because the problem formulation was to construct a microstructure with an a priori defined elasticity tensor. However, the term might be slightly misleading when consider some of the later work (e.g. Sigmund, 1997; Sigmund and Torquato, 1999; Neves et al., 2000), where the focus is minimizing/maximizing material properties given some constraints, which have later become the standard approach. The early work done on designing materials with extremal properties was done in continuation of development and improvement of theoretical bounds (Hashin and Shtrikman, 1963; Walpole, 1966; Berryman and Milton, 1988; Cherkaev and Gibiansky, 1993; Gibiansky and Lakes, 1993; Milton and Cherkaev, 1995; Gibiansky and Lakes, 1997, to mention some) - see (Torquato, 2002) for a detailed overview.

Intuitive or analytically obtained microstructural designs achieving extremal properties have also been proposed (e.g. Hashin, 1962; Almgren, 1985; Milton, 1986; Lakes, 1987; Vigdergauz, 1989; Milton, 1992; Milton and Cherkaev, 1995; Vigdergauz, 1999). Figure 2.3 shows four of these structures, where (a) presents an example of a one-length scale structure maximizing the bulk modulus, a so-called Vigdergauz structure. Earlier Hashin (1962) had proved that a material structure consisting of closely packed, two-phase, randomly distributed spheres, illustrated in 2D in Fig. 2.3(b), maximize the bulk modulus when the stiffest material phase is the outer. The negative Poisson's ratio structure in Fig. 2.3(c), based on illustration by Milton (1992), is more a mechanism than a material, because it assumes free rotation at the hinges. The same holds for the pentamode microstructure in Fig. 2.3(d), but recent experimental work (Kadic et al., 2012) shows that it

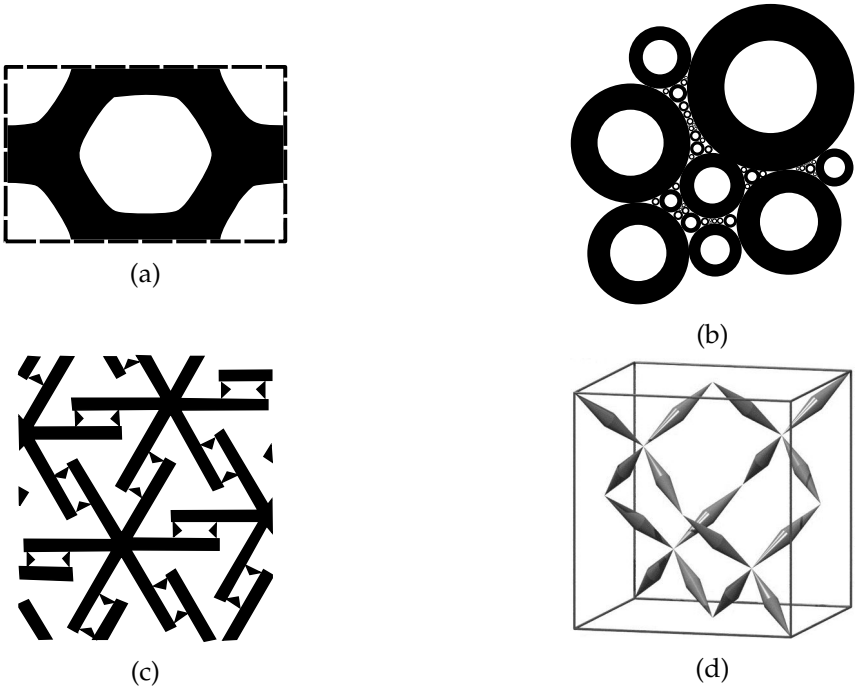

Figure 2.3: Analytically designed isotropic material microstructures found in the literature. Remark, here black indicates stiffest material phase and white the softest (or void). (a) Example of Vigdergauz microstructure unit cell (based on illustration by Sigmund (2000)) obtaining bulk modulus bound. (b) Schematical illustration of maximum bulk modulus microstructure suggested by Hashin (1962). (c) Hinged microstructure proposed by Milton (1992) for a minimum Poisson's ratio material. (d) Pentamode microstructure as proposed by Milton and Cherkaev (1995). Figure (d) is reprinted with permission from Kadic, M. et al (2012), Applied Physics Letters, 100 (19), copyright 2012, AIP Publishing LLC.

is possible to obtain similar properties by manufacturing the pentamode microstructure with slender contact points.

Isotropic microstructures with minimum/maximum thermal conductivity can also be found analytically (analogous to maximum/minimum bulk modulus), but when it comes to more complicated materials, such as a three-phase microstructure with a minimum (negative) thermal expansion, topology optimization is an obvious choice. Sigmund (1997) found two-dimensional structures achieving the thermal expansion bound, three-dimensional piezocomposites with extremal properties (Sigmund et al., 1998), and Larsen et al. (1997) showed experimentally that an optimized two-dimensional, continuum material structure actually exhibited a negative Poisson's ratio.

Topology optimization is also well suited to find microstructures with good compromise between competing properties, such as bulk modulus and fluid permeability. Here, Guest and Prévost (2006); Guest and Prevost (2007) made important contributions. Following this, several others used topology optimization to achieve microstructures with cross-property bounds (e.g. Challis et al., 2008; Kang et al., 2010; Andreasen and Sigmund, 2011).

A parallel development has been the focus on photonic (light) and phononic (elastic) materials. That is designing materials with interesting dynamic properties. Again,

intuitive designs have also been made, some of the first by Yablonovitch and Gmitter (1989); Sigalas and Economou (1992). While Cox and Dobson (1999) were the first to utilize gradient based optimization to design periodic structures with extremal dynamic properties. A thorough review of topology optimization for photonic structures can be found in (Jensen and Sigmund, 2011). I would like to point out that the projection method suggested by Guest et al. (2004) and extended by Xu et al. (2010) lay the ground for including multiple design realizations in the optimization and thus obtain manufacturable designs by so-called robust optimization (Sigmund, 2009; Wang et al., 2011). Wang et al. (2012) utilized this approach when designing manufacturable photonic waveguides.

The field of phononic materials has not received the same attention from the topology optimization community, but it should be mentioned that Sigmund and Jensen (2003) were the first to use topology optimization on the design of phononic materials, Diaz et al. (2005) used gradient based optimization to design phononic materials consisting of beams and point masses, and Halkjær et al. (2005, 2006) extended the method to plate structures.

2.2.2 Fiber reinforced composites

Finally, I would like to mention that a lot of industry relevant optimization research is related to the design of fiber composites, which quickly have become the industry standard for lightweight constructions. In the design of fiber composites, the goal is often to minimize the compliance for a range of load cases and constraints (e. g. buckling). The design variables are normally the fiber orientation, possible fiber volume fraction, and it can also be necessary to include the material thickness (Bruyneel and Duysinx, 2006). One of the main challenges here is that e. g. the aerospace industry works with a discrete set of fiber orientations, and this manufacturing restriction needs to be included.

These discrete sets of fiber orientations can be seen as periodic microstructures, and for fiber composites their corresponding unit cells are often referred to as representative volume elements (RVE), because in the manufactured fiber reinforce composite there will be an uncertainty related to exactly how the fibers are positioned. The material properties can be computed using different methods, including complicated statistical approaches (Torquato, 2002; Ostoja-Starzewski, 2008), but is most often done with computationally cheap, approximative analytically/semi-analytically expressions (Zenkert and Battley, 2006). Additive manufacturing allows another degree of control and freedom when it comes to the manufacturing, and that is why microstructures with a standard periodic unit cell is the focus.

Assuming the properties of each of the given fiber layouts are known, a popular gradient based optimization approach is the discrete material optimization (DMO) approach proposed by Stegmann and Lund (2005) This can be considered as a simplified multiscale problem, since the local fiber distribution is based on the loads experienced by the overall structure. This can be related to the work in Chapter 5, where a brief overview of other multiscale approaches in topology optimization is included.

2.3 When does material (microstructural) design make sense?

For a pure static problem – an optimization problem where the goal is to achieve the stiffest possible structure with a given amount of material (or alternatively minimize the amount of material for a given stiffness/stress constraint) - the upper Hashin-Shtrikman bound (Hashin and Shtrikman, 1963) with its sublinear form reveal that there is no point in creating a graded isotropic microstructure, unless the discretization is far from resolving the manufacturing precision. For an anisotropic structure Hill (1952) proved that the best that can be achieved is a linear relationship, because the arithmetic mean (often called the Reuss bound) is the upper bound for the effective moduli. Hence, there is no reason to aim for graded microstructure.

However, if stiffness/mass-ratio is not the only design consideration, then designing the microstructure can make sense. A classical example is fiber composites. Manufacturing stiff and strong fibers is relatively simple, but one cannot build the structure out of fibers alone; you need a matrix material to hold them in place and transfer loads between them (Zenkert and Battley, 2006). Furthermore, similar to additive manufacturing, there is an added advantage in the composite material being constructed at the same time as the product, allowing for product specific tailoring of material properties.

More recently, carbon nanotubes have been used as an additive in the composite matrix (Song et al., 2008). And if the tubes were not held in place by another material phase, they could potentially become airborne particles inducing inflammation and possibly cancer in the creatures exposed (Poland et al., 2008). An analogous additive manufacturing issue is a component containing unsintered, highly ignitable, titanium powder (which could be used to enhance the damping of a component).

Being able to hold one material phase in place, is also one of the microstructure applications in this work. In order to achieve a good combination of stiffness and damping, one should combine a stiff and a soft/lossy material. However, the manufacturing of such a component can be challenging - especially in the case of a complicated geometry. Therefore, designing a stiff microstructure that can be printed and later infused with a soft phase, such that the printed microstructure acts as a mold for the soft material, can be beneficial.

Another reason why designing and manufacturing parts, subject to dynamic loading, with a microstructure can be advantageous is that the excitation position might be unknown. A microstructure could assure that vibrations propagate in the same manner independent of the position.

Furthermore, microstructural design makes sense if the problem domain is far away from being discretized down to the manufacturing resolution. This would typically be the case for three-dimensional dynamic problems. Or if there are local constraints that are easier to impose with a microstructure. One such global constraint could be well-distributed, permeable, and connected pores in bone implants to encourage bone ingrowth (Kuboki et al., 1998; Takemoto et al., 2005). Imposing a microstructure could also be seen as an alternative to a maximum length scale constraint.

As a last note, I would like to mention that in this work the focus has been on linear elasticity, which from an engineering point of view makes the application of the material microstructures relatively easy. If one wanted to optimize for periodic structures with large deformation, it would be a good idea, if not a requirement, to know the final com-

ponent's design and load situation. Because the constitutive tensor will depend on the strains, such that it is necessary to cover an infinite number of strain configurations to obtain the constitutive tensor. This means that for most practical applications, it is necessary to compute the performance of the final part with all the details of the microstructure to know how it actually behaves.

CHAPTER 3

STATIC PROPERTIES

This chapter will start with an explanation of how to optimize for static material properties using numerical homogenization. Thereafter, some examples of optimized microstructures with attractive elastic, thermal, and low frequency (quasi-static) loss properties will be presented and discussed.

3.1 Homogenization in the context of topology optimization

Finding the static properties of a material using homogenization traces back to the seventies (see e. g. (Bensoussan et al., 1978)). Homogenization relies on a separation of length scales. This separation is analogous to the separation of time scales used in the method of multiple scales, which is often applied when analyzing nonlinear vibrations (Thomsen, 2003). Basically, one assumes that the microscopic length scale should be much smaller than the macroscopic length scale. This allows a deduction of macroscopic properties for a periodic material from an analysis of one unit cell.

To tailor materials with topology optimization we use numerical homogenization, as first described in detail by (Guedes and Kikuchi, 1990), to find the macroscopic properties. An in-depth description of homogenization of material properties can be found in (Torquato, 2002), while a series of papers by (Hassani and Hinton, 1998a,b,c) give a good introduction to the field of homogenization in the context of numerical homogenization and topology optimization.

3.2 Homogenization equations

With the paper [P1] we try to make numerical homogenization more accessible to researchers by providing a simple introduction together with a Matlab implementation. The code can be used to obtain macroscopic elastic, electric, thermal, and fluid properties. In [P1] the homogenization equations for these problems are presented in both their continuous and discretized form. Here, I will only present discretized equations. For a general introduction to the finite element method see (Zienkiewicz and Taylor, 2000).

Two homogenization problems will be presented. The first consider linear elastic properties, and the second is thermal expansion properties. The case of homogenized

(a) (b)

Figure 3.1: Illustration of deformation fields corresponding to the unit strains for a soft material with a stiff cube inclusion. Remark, for such a simple unit cell the deformation field for the three normal strains will look the same (only different axis orientation), and the same goes for the three shear strains. (a) Normal strain. (b) Shear strain.

conductivity (thermal or electric) is analogous to the elastic case, except that it is enough to consider a scalar field, and that is not treated separately. Each material phase is assumed to be homogeneous and linearly elastic, and the bonding between the material phases is assumed to be geometrically perfect. Derivations of the corresponding discrete sensitivities (gradients) can be found in Appendix A.

3.2.1 Elastic properties

In order to obtain the homogenized elastic constitutive matrix, $\mathbf{C}^*$, six macroscopic unit strain fields are applied. For a non-homogeneous unit cell, this will give rise to a varying strain field in the unit cell (see illustrations in Fig. 3.1), which can be used to compute $\mathbf{C}^*$. A discretized expression for $\mathbf{C}^*$, expressed as a sum of contributions from the N elements, is

$$\mathbf{C}^* = \frac{1}{|V|} \sum_{e=1}^{N} \int_{V_e} (\mathbf{I} - \mathbf{B}_e \mathbf{U})^T \, \mathbf{C}_e \, (\mathbf{I} - \mathbf{B}_e \mathbf{U}) \, \mathrm{dV}_e, \tag{3.1}$$

where $\mathbf{I}$ is a six-by-six identity matrix representing the unit strains, $\mathbf{B}_e$ is the element strain-displacement matrix (size is six-by-number of degrees of freedom, with zeros in all positions except those related to the local element's degrees of freedom). V_e is the element volume, while $|V|$ is the volume of the unit cell, $\mathbf{C}_e$ is the element constitutive matrix, and the six displacement fields $\mathbf{U}$ can be found by solving (for a unit cell)

$$\mathbf{K}\mathbf{U} = \mathbf{F}, \tag{3.2}$$

with periodic boundary conditions,

$$\mathbf{K} = \sum_{e=1}^{N} \int_{V_e} \mathbf{B}_e^T \mathbf{C}_e \mathbf{B}_e \, \mathrm{dV}_e, \tag{3.3}$$

and

$$\mathbf{F} = \sum_{e=1}^{N} \int_{V_e} \mathbf{B}_e^T \mathbf{C}_e \mathbf{I} \, \mathrm{dV}_e, \tag{3.4}$$

where the six-by-six identity matrix $\mathbf{I}$ is included to indicate that the six load cases correspond to six unit strains.

A simple derivation of the sensitivities for the homogenized constitutive matrix can be found in Appendix A.1.

3.2.2 Thermal expansion properties

The homogenized thermal stress properties of the material in vector form can be expressed as

$$\boldsymbol{\beta}^* = \frac{1}{|V|} \sum_{e=1}^{N} \int_{V_e} \left(\boldsymbol{\alpha}_e - \mathbf{B}_e \mathbf{U}_T\right)^T \mathbf{C}_e \left(\mathbf{I} - \mathbf{B}_e \mathbf{U}\right) \mathrm{dV}_e, \tag{3.5}$$

where $\boldsymbol{\alpha}_e = (\alpha_e, \alpha_e, \alpha_e, 0, 0, 0)^T$ is the thermal strain properties for element e (assumed to be isotropic in the element), and $\mathbf{U}_T$ are the nodal displacements found by solving the additional equation

$$\mathbf{K}\mathbf{U}_T = \sum_{e=1}^{N} \int_{V_e} \mathbf{B}^T \mathbf{C}_e \boldsymbol{\alpha}_e \, \mathrm{dV}_e, \tag{3.6}$$

corresponding to the displacements a unit increase in temperature would give.

The thermal strain properties can now be found as the solution to

$$\mathbf{C}^* \boldsymbol{\alpha}^* = \boldsymbol{\beta}^*. \tag{3.7}$$

The corresponding sensitivities can be found in Appendix A.2.

3.3 Optimization of elastic properties

For pure maximum stiffness to weight ratio (or minimization of stress for a given weight), creating a microstructure does not make sense unless the macroscopic domain discretization is coarse. Furthermore, when using topology optimization to design the stiffest possible microstructure for a given volume fraction, it is relatively easy to obtain manufacturable designs with a clear length scale. Therefore, when showing that it is possible design directly manufacturable microstructures with topology optimization [P3], we used an isotropic, negative Poisson's ratio microstructure as the main example, which is a challenging optimization problem.

The method applied is the so-called robust design method proposed by Wang et al. (2011). Instead of optimizing the performance of a single design, we optimize the performance for three versions of the design. In addition to the blueprint design (threshold value of 0.5), we optimize one eroded (corresponding to a threshold value > 0.5), and one dilated (corresponding to a threshold value < 0.5) design. This is discussed in detail in the paper [P3], where also measurements confirming the material behavior with a Poisson's ratio of $\nu = -0.5$ are presented.

The microstructures in [P3] are rather dense, and, therefore, I have decided to include a few more examples here, with lower volume fraction. The optimization problem is the

same as in [P3], simply formulated as:

$$
\begin{array}{lllll}
\min\limits_{\boldsymbol{\rho}}: & \max\left(\nu^*, \nu^*_{\text{dilated}}, \nu^*_{\text{eroded}}\right) & & & \text{Poisson's ratios} \\
\text{s. t.:} & \mathbf{KU} = \mathbf{F}, & & & \text{Homogenization equations} \\
& K^*_{\text{eroded}} \geq aK, & & & \text{Bulk constraint} \\
& \frac{\sum_{i,j}\left(C^{\text{iso}}_{ij} - C^*_{ij}\right)^2}{\left(C^{\text{iso}}_{11}\right)^2} \leq \varepsilon, & i,j = 1,...,6 & & \text{Isotropy constraint} \\
& \frac{1}{|V|}\sum\limits_e \left(V_e \rho_e\right) \leq V_{\max}, & e = 1,...,N & & \text{Volume constraint} \\
& 0 \leq \rho_e \leq 1, & e = 1,...,N & & \text{Element densities}
\end{array}
\tag{3.8}
$$

where $\boldsymbol{\rho}$ is a vector of element densities, and ν^* is the effective Poisson's ratio extracted from the homogenized elasticity tensor. ν^*_{dilated} and ν^*_{eroded} are the Poisson's ratios corresponding to a dilated and eroded version, respectively, of the blueprint design. K^* is the homogenized bulk modulus, K is the bulk modulus of the solid phase, a is the required minimum ratio between bulk modulus of solid material and microstructure. C^*_{ij} and C^{iso}_{ij} are entries in the homogenized tensor and a corresponding isotropic constitutive matrix (computed as in [P3]), respectively. ε is a small number (e.g. 10^{-5}), but it can be beneficial to start with a looser constraint (e.g. $\varepsilon = 10^{-3}$) to give the optimization algorithm more freedom to create a negative Poisson's ratio structure. ρ_e is the element density, and $V_{\max}$ is the ratio between the maximum solid material volume and the total unit cell volume. The isotropy constraint is applied to all three design realizations, while the volume constraint is only applied on the dilated design.

By using the framework presented in [P2], it is feasible to run optimization problems with a much higher resolution than the $100 \times 100 \times 100$ elements used in [P3]. The two microstructures shown in Fig. 3.2 have been obtained by optimization of a unit cell consisting of $200 \times 200 \times 200$ elements. The resemblance with the two-dimensional negative Poisson's ratio materials presented in [P3] and (Larsen et al., 1997) is quite clear for the microstructure in Fig. 3.2(a), where a central part of the domain is prescribed to be void. The microstructure in Fig. 3.2(b) is quite different, because it has been started from a structured initial guess (as opposed to the microstructure in Fig. 3.2(a), where the initial density distribution was random). This illustrates that there is not a unique negative Poisson's structure. How close to -1 the Poisson's ratio can become is mainly limited by the bulk modulus constraint (here $a = 1/1000$ is used - active on the eroded version). But the initial guess also has an influence, as the Poisson's ratio is -0.5 for the microstructure in Fig. 3.2(a) and -0.3 for the microstructure in 3.2(b), which also has a higher bulk modulus (even though the constraint on the eroded design is the same). The volume constraint is set to 25%.

Decreasing the volume fraction further to 20%, and keeping the prescribed void central part of the unit cell, it is possible to obtain a design that has an even clearer resemblance with the 2D negative Poisson's ratio material. Such a design is shown in Fig. 3.3, where the two unit cell sides resembling the 2D design the most are shown together with a 3D representation of the microstructure.

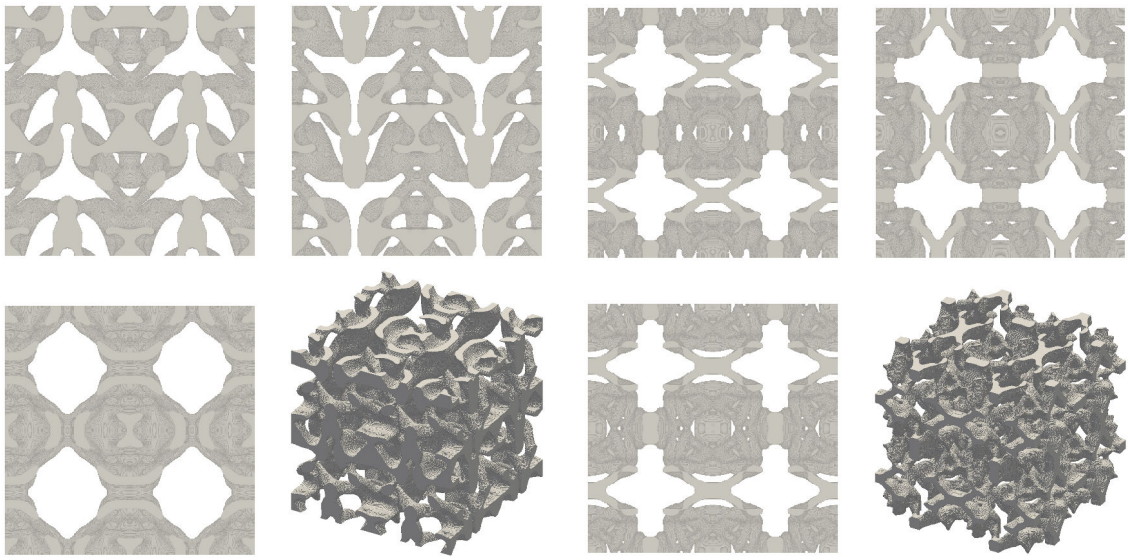

(a) (b)

Figure 3.2: Two examples of microstructures with a negative Poisson's ratio.The microstructures are illustrated by showing $2 \times 2 \times 2$ unit cells together; from three perpendicular directions and a 3D representation. (a) have been obtained with a prescribed central void region and random initial guess, while (b) have been found by using a soft sphere surrounded by stiffer material as an initial guess.

Figure 3.3: Another example of a microstructure with a negative Poisson's ratio (obtained with a volume constraint of 20%).The microstructure is illustrated by showing $2\times2\times2$ unit cells together; from two perpendicular directions and one angled viewpoint.

Table 3.1: Material properties for ABS and glass beads.

Material	Bulk modulus (K) [GPa]	Shear modulus (G) [GPa]	Thermal expansion (α) [-]
ABS	2	0.5	$80 \cdot 10^{-6}$
Glass	40	30	$4 \cdot 10^{-6}$

3.4 Negative thermal expansion

Here, I will present a three-dimensional negative thermal expansion material, obtained with topology optimization, which could be manufactured using additive manufacturing. To obtain a negative thermal expansion material, we need three distinct material phases (Sigmund, 1997). As with the negative Poisson's ratio microstructure, one of the phases can be void, but that still leaves us with two phases to print. To create a structure that in theory could be manufactured on cheap hobby printers printing in ABS, I consider a situation in which the second phase is created by adding particles, e.g. tiny glass beads, to the ABS (before printing) and the third phase is pure ABS.

Cribb (1968) showed that for two-phase composites the thermal expansion coefficient can be determined from the effective bulk modulus of the same composite. That means, for a two-phase composite that obtain the bound on the bulk modulus, such as the sphere structure in Fig. 2.3(b), we can compute the thermal expansion by combining the formula presented in (Hashin and Shtrikman, 1963) and (Rosen and Hashin, 1970). For a two-phase composite where ABS form the outer layer in the sphere structure and randomly distributed stiff glass beads are the inner spheres (white in Fig. 2.3(b)), the lower bound on the bulk modulus is obtained. Assuming material properties as given in Tab. 3.1, the thermal expansion of a ABS with 60 percent glass beads will be approximately $\alpha_{\text{composite}} = 1/3\alpha_{\text{ABS}}$, and the bulk modulus is approximately $K_{\text{composite}} = 3K_{\text{ABS}}$.[1] These are estimated properties, because the true structure will deviate some from the optimal sphere structure and the actual ABS and glass properties might differ slightly, but according to the bounds any deviations from the structure in 2.3(b) will increase the difference in properties between the composite and the ABS. Note, this means that the glass bead volume fraction probably can be reduced.

This optimization problem is easier to work with than the negative Poisson's ratio problem, because contrasting phases are beneficial for the objective. I have adopted the material interpolation scheme presented by Sigmund (1997) but using a modified SIMP scheme (Sigmund, 2007). And the optimization problem formulation is identical to the negative Poisson's ratio problem in Eq. (3.8), except for the additional element design variable (as opposed to only the element density), ν is exchanged with α in the objective, and the eroded and dilated designs are with respect to material versus void. More realization could have been included in the objective to obtain robustness with respect to the phases as well, but this was deemed unnecessary for the present example.

Again, the framework presented in [P2] is used, and the optimization is run with $200 \times 200 \times 200$ elements. The resulting design, with a thermal expansion coefficient of $\alpha^* = -83 \cdot 10^{-6}$ and a bulk modulus of $K^* = 1.1$ MPa, is shown in Fig. 3.4(a) where

[1] It is assumed that the Poisson's ratio of the composite material is the same as for the ABS

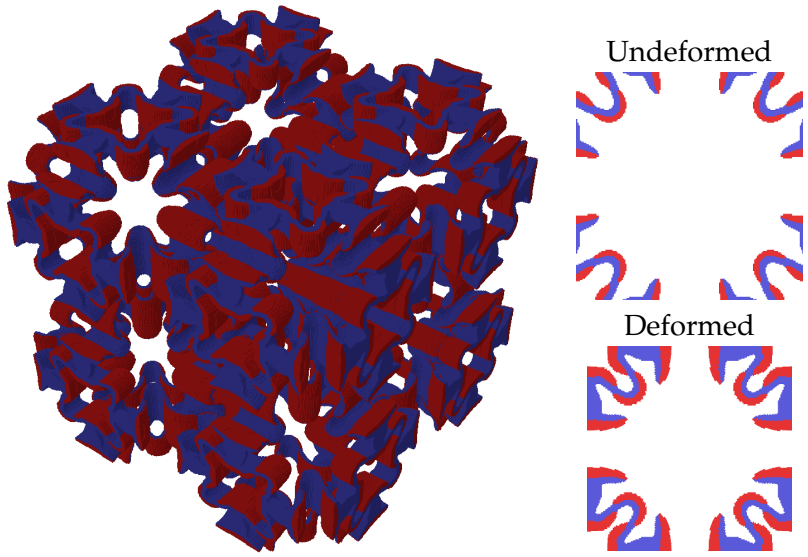

Figure 3.4: Negative thermal expansion microstructure consisting of ABS (red) and an ABS/glass sphere composite (blue). (a) The microstructure is illustrated by showing $2 \times 2 \times 2$ unit cells together. (b) A slice of the negative thermal expansion unit cell illustrating the deformation pattern of the microstructure when heated.

$2 \times 2 \times 2$ unit cells are put together. An illustration of the deformation is shown in Fig. 3.4(b), where an undeformed and a deformed cross section are plotted.

3.5 Quasi-static damping properties

All materials exhibit a degree of damping. This means that when the material deforms, some energy is lost; if one drops a ball on the ground, it bounces up to a level *below* the level it was dropped from. The difference is the lost energy. The simplest way to include the loss in the modeling is by adding an imaginary term to the elastic tensor (often called the structural damping model), which is the method used here. The bouncing ball is used to illustrate the split between the real and imaginary term of the elastic tensor in Fig. 3.5.

The problem is that when a material has a high degree of damping, it is normally too soft to be used in structural applications or it is very expensive (as the alloys used by

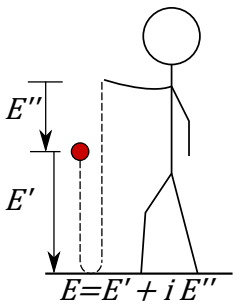

Figure 3.5: Illustration of how the elastic tensor is split by using a complex elastic modulus, where one prime denotes the storage part of the modulus, and two primes denote the loss part of the modulus. Drawing inspired by Sperling (1990).

Brodt and Lakes, 1995; Lakes, 2002). Therefore, we want to design a microstructure that both exhibit a high degree of damping and has a decent stiffness by combining a soft and lossy material phase with a stiff material phase.

The aim is to achieve a microstructure that can be manufactured with SLS, and thus we pursue a path where SLS can be used to manufacture a frame of metal into which a lossy material can be infused. The formulation used to optimize for such a microstructure is described in great detail in [P4], but simply put it involves homogenization with complex material properties (using the correspondence principle (Hashin, 1965)) and maximizing the imaginary part of the bulk modulus. A robust version of the optimization problem can be stated as:

$$
\begin{aligned}
\min_{\boldsymbol{\rho}}: \quad & \max\left(\mathrm{Im}(K^*), \mathrm{Im}(K^*_{\text{dilated}}), \mathrm{Im}(K^*_{\text{eroded}})\right) && \text{Imaginary part of bulk modulus} \\
\text{s. t.:} \quad & \mathbf{K}\mathbf{U} = \mathbf{F}, && \text{Homogenization equations} \\
& \mathrm{Re}(K^*) \geq a\,\mathrm{Re}(K_{\text{stiff}}), && \text{Storage modulus constraint} \\
& \frac{\sum_{i,j}\left(\mathrm{Re}(C^{\text{iso}}_{ij} - C^*_{ij})\right)^2}{\left(\mathrm{Re}(C^{\text{iso}}_{11})\right)^2} \leq \varepsilon, \qquad i,j = 1,...,6 && \text{Isotropy constraint} \\
& \mathbf{K}_\sigma \mathbf{U}_\sigma = \mathbf{F}_\sigma, && \text{Conductivity homogenization equations} \\
& \sigma^* \geq b\sigma_{\text{stiff}}, && \text{Conductivity constraint on stiff phase} \\
& 0 \leq \rho_e \leq 1, \qquad e = 1,...,N && \text{Element densities}
\end{aligned}
\tag{3.9}
$$

where b is the required fraction of the stiff materials conductivity. In this formulation, the material properties are assumed to be constant for the low frequency range (where inertia effects can be ignored). As described in [P4], the conductivity constraint on the stiff phase is present to achieve a connected stiff phase, and there is a conductivity constraint instead of a stiffness constraint because solving for the conductivity is computationally cheaper. Since the soft material phase is supposed to be infused in the structure, one could also have a conductivity constraint on the soft phase. But, it turns out that it is not beneficial for the loss properties to create isolated soft regions in the microstructure, such that the constraint would be superfluous.

In [P4] it was shown how topology optimization could be used to obtain microstructures reaching the theoretical bounds (Gibiansky and Lakes, 1993) for the bulk modulus. Here, a slightly different example is presented, where the two materials have different Poisson's ratio, and the stiffness of the two materials differs by two orders of magnitude. The material parameters used in the modeling for the two material phases are shown in Tab. 3.2. In Fig. 3.6 two sets of bounds are plotted, the solid line shows the bounds for the material phase properties in Tab. 3.2, while the dashed line shows the bound if the soft material phase also had a Poisson's ratio of 0.3. Since the bounds more or less coincide, it is expected that qualitatively the optimal microstructures will be the same as those obtained in [P4].

To verify this, the optimization formulation in Eq. (3.9) is first applied to maximize the loss for two microstructures without including the dilated and eroded design. The resulting microstructure for $b = 0$ is shown in Fig. 3.7(a). As expected, the result is qualitatively the same as in [P4], even though the Poisson's ratio of the two materials are different. The microstructure consist of stiff inclusions in a soft matrix. The corresponding result for the robust formulation is shown in Fig. 3.7(b), while Fig. 3.7(c) shows the result of an optimization where the robust formulation is used together with a small

Table 3.2: Material parameters used for the optimizations of quasi-static loss.

Material	E' [GPa]	$\eta = E''/E'$ [-]	ν [-]
Stiff	100	0.001	0.3
Soft	1	0.1	0.4

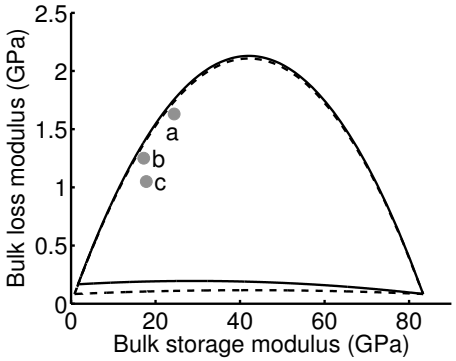

Figure 3.6: Theoretical bounds (Gibiansky and Lakes, 1993) for the homogenized complex bulk modulus. The solid line is the bound computed with the material parameters in Tab. 3.2 (that is, different Poisson's ratios), while the dashed line shows the bound if both materials had the same Poisson's ratio of 0.3.

conductivity constraint ($b = 0.05$).

The bulk moduli corresponding to the three microstructures are plotted in Fig. 3.6. Here, it is interesting to remark that even though the first microstructure only has a very thin layer of the soft material phase (microstructure consists of 92% stiff material), and is close to the bound, it is far from obtaining the maximum. Implying that a vanishingly thin soft layer is needed to obtain the maximum bulk loss modulus bound, when, as in this case, there is a large difference in the bulk storage moduli of the two material phases. Furthermore, even thin connecting rods, as the microstructure in 3.7(c) has, have a detrimental effect on the loss modulus. Finally, it is worth mentioning that in all three cases both the shear moduli and the shear loss factor are smaller than the bulk.

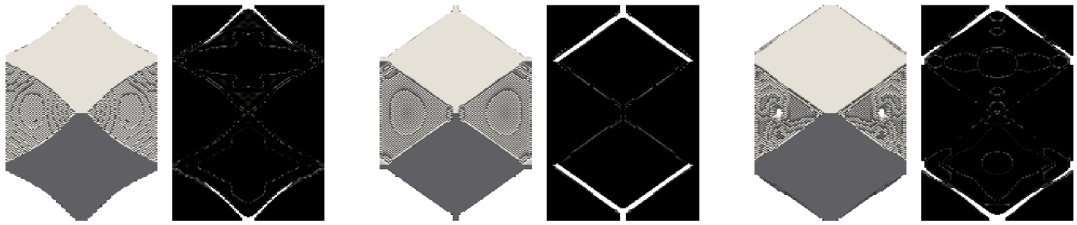

(a) (b) (c)

Figure 3.7: Three examples of microstructures optimized for quasi-static loss (all obtained with a mesh of $96 \times 96 \times 96$ elements). Left (light color) shows the soft material phase, and right (dark color) shows the stiff material phase. The microstructures in (a) and (b) have been found by setting $b = 0$ in Eq. 3.9, while (c) have been found by using $b = 0.05$. (a) has been obtained with the robust formulation, and, thus, has a very thin layer of soft material. The storage modulus constraint parameter a is set to 0 in all three optimizations.

CHAPTER 4

DYNAMIC PROPERTIES

This chapter will start with a short introduction to the modeling/computations of the dynamic properties of periodic structures. Then there will be a section on the optimization for high loss using a full dynamic model. And the chapter will be rounded off with a section on a method that can be used to optimize for directional wave propagation.

4.1 Floquet-Bloch theory

The focus is on waves in a periodic elastic medium induced by time-harmonic excitation, because this allows us to use the Bloch wave expansion (Bloch, 1929), which for the displacements $\mathbf{u}$ can be expressed as:

$$\mathbf{u}(\mathbf{x}, t) = \tilde{\mathbf{u}}(\mathbf{x}) e^{i\mathbf{k}^T\mathbf{x}} e^{i\omega t}, \tag{4.1}$$

in which ω is the temporal frequency, t is time, $\mathbf{k} = (k_x, k_y, k_z)^T$ is the wave vector and $\tilde{\mathbf{u}}$ is a periodic mode on the unit cell of the periodic material. In Fig. 4.1 this split of the spatial part into a local and global part is illustrated.

Normally, the Bloch expansion is represented in the numerical model by complex boundary conditions (corresponding to a phase shift). However, in our work we have

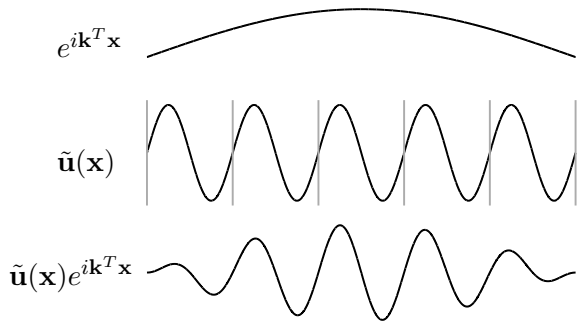

Figure 4.1: Top: Global part of the spatial variation, where period is determined by wave number. Center: Local part of spatial variation, where the period is determined by the unit cell size (unit cell edges shown as gray vertical lines). Bottom: Total spatial variation.

inserted the Bloch expansion in the governing PDE before discretizing the problem, because this makes it easier to solve for the spatial frequency (the wave number). The modeling is described in detail in [P5], and even though it is presented for the two-dimensional case, it is directly generalizable to other geometries, such as plates (as done in [P7]) or general three-dimensional solids.

4.1.1 Brillouin zone and band diagram

The Bloch theorem allows solving the eigenvalue problem for only one unit cell of the periodic structure. However, it is not enough to solve one eigenvalue problem - a range of eigenvalue problems must be solved. The wave vector **k** must be varied within a domain called the Brillouin zone (Brillouin, 1953), which is illustrated in Fig. 4.2 for a two-dimensional periodic structure with rectangular unit cells.

At A in Fig. 4.2, $k_x = \pi/l_x$ and $k_y = 0$, where l_x is the width of the periodic cell (the unit cell). While at C, $k_x = 0$ and $k_y = \pi/l_y$, where l_y is the height of the unit cell. As illustrated the wave vector could also be given by its length and corresponding angle θ between k_x and k_y.

If a unit cell possesses symmetry, the solutions of the eigenvalue problem will possess the same symmetry with respect to k_x and k_y. This means that the dynamic properties of the structure are fully described by covering a smaller part of the Brillouin zone (referred to as the irreducible Brillouin zone).The irreducible Brillouin zone for a unit cell with a 45° symmetry is the domain bounded by the line O-A-B-O in Fig. 4.2.

Furthermore, it is common practice for two-dimensional periodic structures to illustrate the dispersion properties in a so-called band diagram, where the temporal frequencies are plotted versus the wave vectors covering the boundary of the irreducible Brillouin zone. An example could be a square inclusion in a matrix, for which the corresponding band diagram is illustrated in Fig. 4.3.

The band diagram can be found by specifying **k** and solving for the temporal fre-

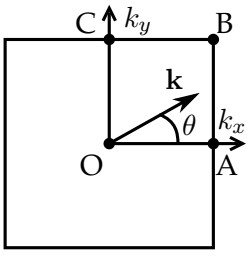

Figure 4.2: Illustration of the Brillouin zone and wave vector direction specified by the angle θ.

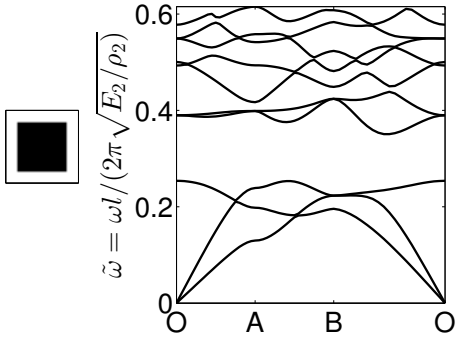

Figure 4.3: Band diagram with the ten first modes for a unit cell consisting of a stiff inclusion in a soft material. The elastic modulus of the stiff material E_2 is a factor ten larger than for the soft material. And the density ρ_2 is a factor 2 larger.

Table 4.1: Material parameters for the stiff and the soft material.

Material	ρ $\left[\mathrm{kg/m}^{3^3}\right]$	E' [GPa]	E'' [GPa]	ν [-]
Soft (1)	1000	1	0.1	0.3
Stiff (2)	4500	100	0.1	0.3

quency ω, but one can also specify ω and θ and solve for k. This approach is used, because it makes it easier to solve for the dynamic properties of a dissipative periodic structure at a given frequency. That is, it is possible to specify a fixed real frequency and solve for a complex wave vector ($\mathbf{k}(\omega)$-formulation (see e.g. Moiseyenko and Laude, 2011)).

4.2 High loss

Following the same line of thought as in Section 3.5, we want to create a microstructure with a high loss by combining a stiff and soft material, but now using a full dynamic model ([P6]). The material phase properties given in Tab. 4.1 are used to demonstrate the method.

When solving for k for a unit cell with complex material parameters, the result will be a complex value. The corresponding loss factor can be computed as (Cremer et al., 2005):

$$\eta = 2\frac{k''}{k'}. \tag{4.2}$$

As discussed in [P5], solving for k at a frequency ω in a bandgap (a frequency where you can draw a horizontal line in Fig. 4.3 from O to O without crossing a mode), will yield eigenvalues with a relatively large imaginary part compared to the real part. Thus, for these frequencies the loss ratio will be high. Remark, though, that the energy is not necessarily lost immediately even though it does not propagate far. It is more likely that most of it is reflected, but for a real structure (which will exhibit a certain degree of loss) the energy will at some point dissipate. Personally, I think of this as a ball bouncing between two walls (Fig. 4.4) - eventually it will lie still.

This is the reason why η is referred to as the attenuation factor in the paper [P6] covering the method proposed for optimization of microstructures for loss at arbitrary frequencies. I have summarized the most important results from the paper in a stiffness loss map in Fig. 4.5, where also the quasi-static bounds derived by Gibiansky and Lakes (1997) are plotted. The quasi-static bounds are bounds on what structural damping can be

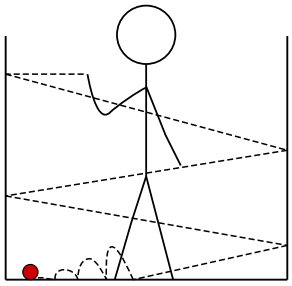

Figure 4.4: Illustration of how a wave trapped in a bandgap can be thought of a ball bouncing between two walls - in a material with some loss (a real material) it gradually looses its energy.

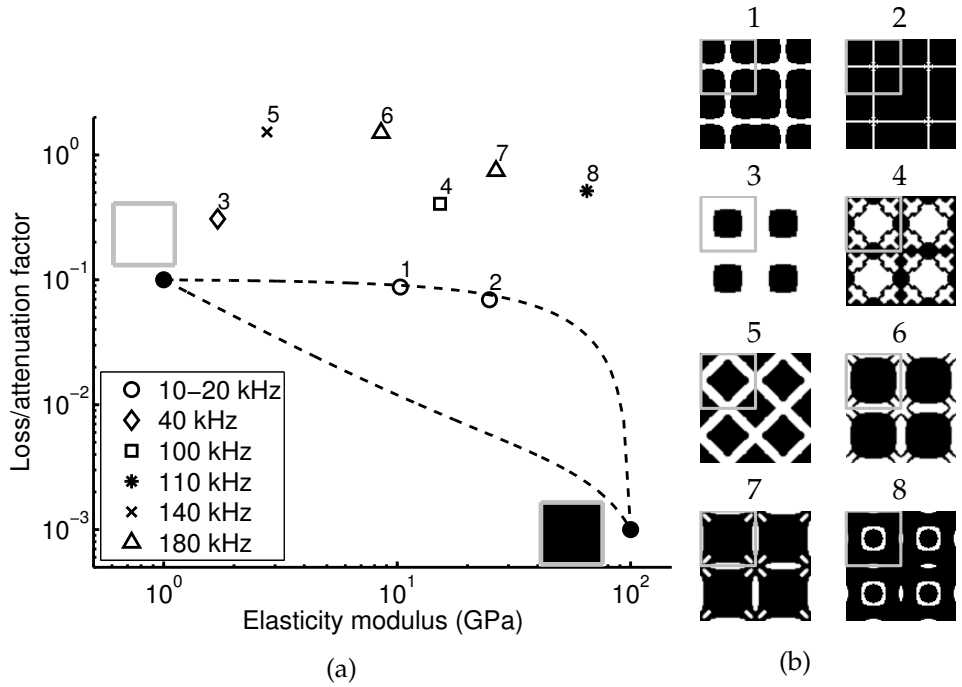

Figure 4.5: (a) Stiffness loss map for composites consisting of the two materials in Tab. 4.1 with the quasi-static bounds from (Gibiansky and Lakes, 1997) shown as a dotted line. (b) Corresponding material structures (unit cell marked by a gray line). The unit cell is $1\ \mathrm{cm}^2$.

achieved when inertia effects are not taken into account. That is for frequencies where the wavelength is longer than the unit cell size, and for the considered material combination and unit cell size of $1\ \mathrm{cm}^2$, which is rather large for a microstructure, inertia effects first come into play in the ultrasonic region.

For low frequencies (where the wave length is longer than the unit cell) the same microstructures as in [P4] are obtained (microstructure 1 and 2 in Fig. 4.5(b)), while at higher frequencies more complex structures, such as microstructures with internal resonators inside a stiff frame can be observed (microstructure 8 in Fig. 4.5(b)).

Finally, it is shown that it is possible to obtain microstructures with a connected stiff phase (microstructure 4, 6-8 in Fig. 4.5(b)), and thus a good stiffness, exhibiting a very high loss for certain frequency ranges. Actually, it turns out that when microstructure 6 in Fig. 4.5(b) is modeled with a stiff material without loss and void instead of the soft material, the bandgap size equals, if not exceeds, the largest bandgap obtained in (Bilal and Hussein, 2011), even though a maximization of the bandgap was not the objective. This illustrates that the method also can be used for maximizing the width of bandgaps.

The below list is an attempt to summarize the findings of [P4] and [P6]:

- A high attenuation factor for a wide range of frequencies is easiest achieved by a stiff inclusion in a soft material.
- A larger stiff inclusion means a stiffer material, but to obtain a stiffness comparable to the stiffest material phase, the stiff inclusion must constitute almost 100 percent of the unit cell making it very difficult to manufacture.

- For higher frequencies, it is possible to obtain a broadband high attenuation factor by connecting the stiff inclusions with thin rods. However, the static stiffness is still not comparable to the stiffest base material.

- Finally, it is shown that structures having a high static stiffness exhibit a narrow-band high attenuation factor if they contain an internal resonator. Topology or shape optimization could be used to tune the microstructure's attenuation factor at certain frequencies.

4.3 Directional wave propagation

In this section, I will present a method to optimize for a microstructure with tailored directional wave propagation. The presented method is applicable to three-dimensional solids, but is here illustrated on a periodically perforated plate.

Figure 4.6 shows part of a periodically perforated plate, and how a directional wave propagation could look when the plate is excited at the center. The group velocity component in the x-direction, c_{gx}, for waves propagating in the x-direction, is larger than the group velocity component in the y-direction, c_{gy}, for waves propagating the the y-direction.

4.3.1 Group velocity of elastic waves

The derivation of the equations necessary to compute the group velocity profile (for flexural waves in a plate with a periodic pattern) is described in detail in [P7]. Numerically, the group velocity profile at a given frequency ω can be computed by first finding the wave vectors by solving the discretized eigenvalue problem

$$(\mathbf{K}_k(\theta,\omega) - k\mathbf{M}_k(\theta))\,\mathbf{u}_k = \mathbf{0}, \tag{4.3}$$

where θ is the angle between the wave vector components k_x and k_y, ω is the temporal frequency, k is the wave vector length, and the finite element matrices $\mathbf{K}_k$ and $\mathbf{M}_k$ for a Mindlin plate problem can be found in both [P7] and [P8]. For a given combination of θ

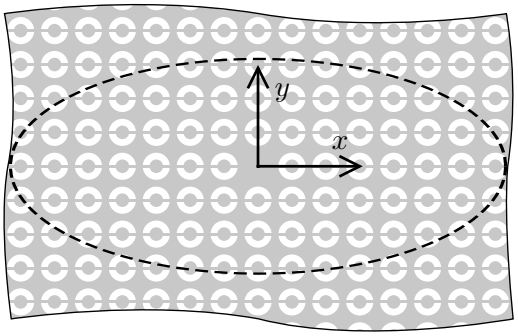

Figure 4.6: Part of a periodically perforated plate (seen from above). The dashed line shows a group velocity profile, caused by an excitation at the plate center, with a directional preference (propagation is faster in the x-direction).

and k the group velocity $\mathbf{c}_g = (c_{gx}, c_{gy})^T$ is given as

$$c_{gx} = \frac{1}{2\omega} \frac{\mathbf{v}^T \left(-i\mathbf{K}_1 + 2k\cos(\theta)\,\mathbf{K}_3 + k\sin(\theta)\,\mathbf{K}_4\right)\mathbf{u}}{\mathbf{v}^T\,\mathbf{M}\mathbf{u}}, \tag{4.4}$$

$$c_{gy} = \frac{1}{2\omega} \frac{\mathbf{v}^T \left(-i\mathbf{K}_2 + 2k\sin(\theta)\,\mathbf{K}_5 + k\cos(\theta)\,\mathbf{K}_4\right)\mathbf{u}}{\mathbf{v}^T\,\mathbf{M}\mathbf{u}}, \tag{4.5}$$

where the computations of the matrices $\mathbf{K}_i$ and $\mathbf{M}$ are detailed in [P8]. $\mathbf{u}$ can be found from $\mathbf{u}_k$, which is defined as

$$\mathbf{u}_k = \begin{bmatrix} k\mathbf{u} \\ \mathbf{u} \end{bmatrix}, \tag{4.6}$$

while $\mathbf{v}$ is the conjugated counterpart of $\mathbf{u}$. If dissipation were to be included, obtaining $\mathbf{v}$ would require the solution of an additional eigenvalue problem.

4.3.2 Optimizing for directional wave propagation

It is important to remark that $\mathbf{c}_g$ does not necessarily point in the same direction as $\mathbf{k}$. However, when $\theta = 0\,^\circ$ and $\theta = 90\,^\circ$ the two vectors point in the same direction. Utilizing this makes it simpler to define the objective for the optimization. In order to get a clear directional dependency, we can maximize the ratio between the group speed in those two perpendicular directions. The objective is therefore defined as

$$f_0 = \operatorname{sign}\left(\frac{c_{gx}|_{\theta=0}}{c_{gy}|_{\theta=\pi/2}}\right) \cdot \frac{c_{gx}|_{\theta=0}}{c_{gy}|_{\theta=\pi/2}}. \tag{4.7}$$

This ratio will vary with the considered frequency, but for a range of low frequencies (wave lengths larger than the periodic features) this ratio is well-defined and will vary slowly. We will return to the problem of higher frequencies shortly. How to compute the sensitivities are detailed in [P8].

The considered unit cell is $15\ \mathrm{mm} \times 15\ \mathrm{mm}$, and the plate is $2\ \mathrm{mm}$ thick and made of aluminum. In order to avoid islands of unconnected material we apply a conductivity constraint. Furthermore, filtering of the design variables is used to get rid of fast oscillations in the design (to avoid small features), but with a projection on top in order to allow the design to become black and white.

4.3.3 Results for low frequencies

The unit cell in Fig. 4.7(a) has been achieved by maximizing f_0 at $3.0\ \mathrm{kHz}$. The corresponding performance is shown in Fig. 4.8. It can be seen that the performance curve is almost constant for a range of low frequencies.

If we choose a lower or higher frequency, not much happens - we end up with more or less same design - until $5\ \mathrm{kHz}$. As can be seen in Fig. 4.7(b), where the optimized design for $\omega = 5.0$ kHz is shown, the design now contains clear bends. The performance, shown in Fig. 4.9, is slightly better at $5.0\ \mathrm{kHz}$ versus the design in Fig. 4.7(a).

Now, if the frequency is increased further, a circular inclusion clearly forms. Already at 5.5 kHz the resulting topology is quite different (see Fig. 4.7 (c)). It looks like the

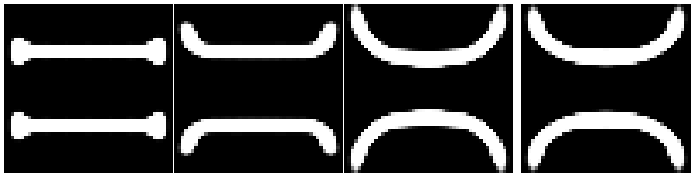

Figure 4.7: Unit cells from optimization of f_0 at (a) 3.0 kHz, (b) 5.0 kHz, (c) 5.5 kHz, and (d) 5.5 kHz with additional conductivity constraint in x-direction

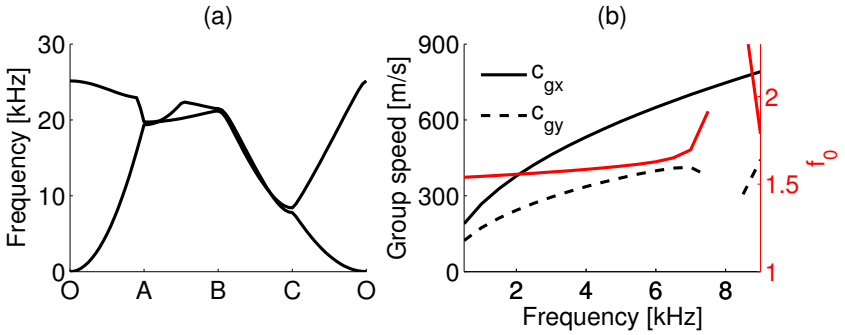

Figure 4.8: (a) The two lowest modes in the band diagram for the unit cell design in Fig.4.7(a) optimized at 3.0 kHz, and (b) the corresponding performance (f_0) and group speeds.

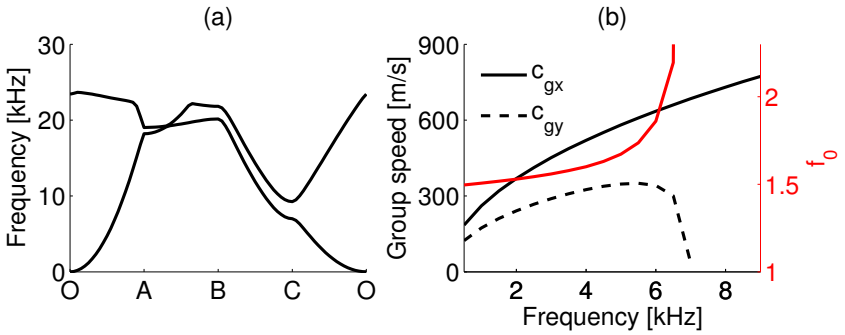

Figure 4.9: (a) The two lowest modes in the band diagram for the unit cell design in Fig. 4.7(b) optimized at 5.0 kHz, and (b) the corresponding performance (f_0) and group speeds.

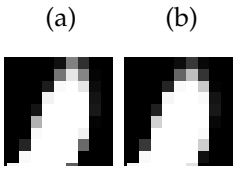

Figure 4.10: Close-up of one corner of unit cells (c) and (d) in Fig. 4.7. That is, (a) shows zoom in of 5.5 kHz unit cell, while (b) shows zoom in of the unit cell for $f_0 = 5.5$ kHz with additional conductivity constraint in x-direction.

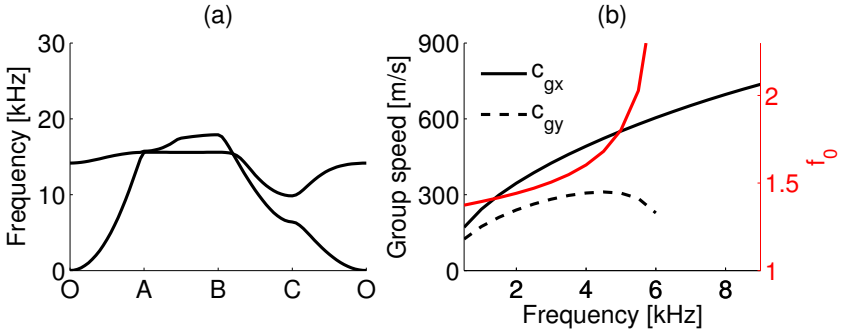

Figure 4.11: (a) The two lowest modes in the band diagram for the unit cell design in Fig. 4.7(d) optimized at 5.5 kHz with additional conductivity constraint, and (b) the corresponding performance (f_0) and group speeds.

optimization tries to form a resonant inclusion very similar to the one used in [P7]. Actually, the rods connecting the inclusion in the x-direction are low density elements (soft material), and disappear after thresholding (making the structure unphysical). In order to amend this, the optimization at 5.5 kHz is rerun with an additional conductivity constraint in the x-direction (same as in the y-direction). And, even though this is not a guaranteed solution it prevents the closing of the circle in this special case, because the isolated island of material would be so large that the design would not fulfill the conductivity constraint. The optimized design is shown in Fig. 4.7(d), and the performance is plotted in Fig. 4.11. Figure 4.10 shows a close-up of the critical region in the two 5.5 kHz designs.

The performance of the design in Fig. 4.7(d) at the lowest frequencies is not as good as the lower frequency designs. However, it has a very good performance at the higher frequencies.

4.3.4 Results for higher frequencies

For higher frequencies, problems with intermediate densities affecting the performance of the design are very pronounced, and there are issues with small features forming. This we amend by using the robust formulation discussed in Section 3.3.

Running such an optimization for the frequency range $27.5 - 32.5$ kHz, where the f_0 at 27.5 kHz, 30.0 kHz, and 32.5 kHz are included in the objective, the blueprint design in Fig. 4.12(a)[1] is obtained. One can take a look in [P8] to confirm that there is only a small amount of intermediate densities in the design. Due to the robustness to dilation and erosion, the performance of the thresholded design (shown in Fig. 4.13) increases slightly with the frequency, but with $f_0 > 1.8$ in the whole frequency range. Furthermore,

[1]Shown as a 3D contour plot in order to illustrate the thickness of the plate.

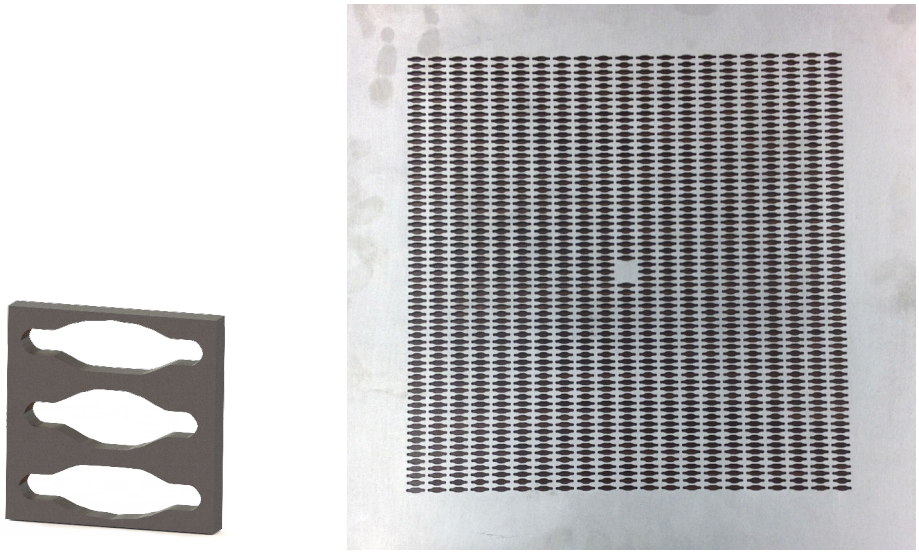

(a) (b)

Figure 4.12: (a) Unit cell of blueprint design resulting from a robust optimization for the frequencies 27.5, 30.0, and 32.5 kHz. (b) Aluminum plate with 25×25 unit cells, manufactured using a water-jet cutter.

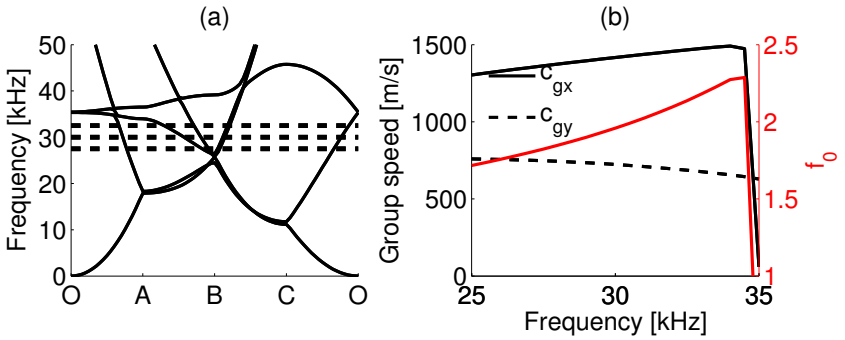

Figure 4.13: (a) The band diagram up to 50 kHz for the unit cell in Fig. 4.12 (as always the thresholded version) optimized at $27.5 - 32.5$ kHz (dashed lines indicate frequencies included in the optimization), and (b) the corresponding performance (f_0) and group speeds.

the design is now manufacturable, and the manufactured plate structure is shown in Fig. 4.12(b). Scanning laser vibrometer measurements on the manufactured structure will be performed in the near future, and included in [P8] before journal submission.

CHAPTER 5

MULTISCALE - APPLICATION IN LOSS MAXIMIZATION

This chapter will start with a brief discussion of recent developments of multiscale methods in topology optimization. Thereafter, the practical multiscale approach presented in [P9] is used to maximize the structural damping of a component. The goal is to achieve a component that has a good compromise between damping and stiffness, and is manufacturable, by combining a stiff and a soft material phase.

5.1 Multiscale optimization

The basic idea of much of the multiscale work in the field of topology optimization, is that it is possible to map intermediate densities to microstructures with properties found by solving a set of local microstructure optimization problems. Rodrigues et al. (2002) were among the first to suggest such an iterative approach, based on earlier works by among others Bendsøe et al. (1994), and Theocaris and Stavroulakis (1999). Coelho et al. (2008) extended the approach to 3D, and even applied it to bone replacement designs (see e.g. Coelho et al., 2011). The approach should be relatively straightforward to implement for minimization of compliance, and it has been shown to work well for such problems. I should also mention that Barbarosie and Toader (2012) have worked on extending the approach to include shape optimization on the unit cell level.

One drawback with the method is that it is not guaranteed to converge towards a manufacturable design. The fact that the microstructures are not necessarily connected can, at least for minimum compliance problems, be amended by post-processing (shifting the base unit cells until they match). However, this would be rather time-consuming. Furthermore, it is uncertain whether the approach would work equally well for more complex problems.

An alternative approach is to predefine regions which should have the same material, and then optimize the material structure in each of these regions for a macroscopic response (as done by Andreasen and Sigmund (2012), and with a full solution of the macroscopic problem by Alexandersen and Lazarov (2014)). Thus, simplifying the matter and making it easier to generalize to problems involving multiphysics, but also restricting the design space.

A third approach, suggested by Theocaris and Stavroulakis (1999), is to base the material interpolation on an a priori defined material library. A manufacturable 2D bone replacement prototype was achieved by Khanoki and Pasini (2012) using a precomputed interpolation for a simple orthotropic microstructure in the optimization.

In the following we will show how a version of this third approach can be applied in a multiscale optimization of the structural damping of a component. First, the homogenized loss factor is maximized by using an approach similar to the one described in Section 3.5 and [P4]. This is done in order to obtain several connected and isotropic microstructures, which can be used as material phases in a multi-material optimization problem. In order to achieve convergence towards a discrete set of material phases in the macroscopic problem, a material interpolation that favors values close to the predefined material densities is introduced.

5.2 Macroscopic problem

5.2.1 Formulation

The basic formulation of the macroscopic problem is similar to the one presented by Kim et al. (2013), who use topology optimization to find the best layout of damping treatments on a cylindrical shell structure. Other similar formulations have been suggested by Ling et al. (2011); El-Sabbagh and Baz (2014) for damping treatments of plane plate structures, but the presented results in these are less convincing than those of Kim et al. (2013).

The problem considered here is that of maximizing a component's structural damping for a range of eigenfrequencies by optimizing the distribution of the material. The macroscopic optimization problem is:

$$\begin{array}{lll} \min\limits_{\boldsymbol{\rho}}: & \max\left(-\log\zeta_i\right), & i=1,...,n \\ \text{s. t.:} & (\mathbf{K}-\omega^2\mathbf{M})\mathbf{U}=\mathbf{0}, & \text{Eigenvalue problem} \\ & \mathrm{Re}(\omega_1)\geq\omega_0, & \text{Constraint on first eigenvalue} \\ & 0\leq\varphi_e\leq 1, \quad e=1,...,m & \text{Macroscopic design variables} \end{array} \tag{5.1}$$

where the objective is to maximize the smallest of the structural damping ratios ζ_i for the n first eigenfrequencies. ζ_i can be computed from the complex eigenvalue ω_i as

$$\zeta_i=\sqrt{\frac{1}{1+(\mathrm{Re}(\omega_i)/\,\mathrm{Im}(\omega_i))^2}}. \tag{5.2}$$

The constraint on the lowest eigenvalue is present to assure a minimum stiffness of the component, which would be required in most applications. Without this constraint, the optimal design would be to use only the softest material. No filtering of the design variables is used in the macroscopic problem.

The key point of the multiscale approach is to base the material interpolation in the macroscopic problem on the homogenized material properties of corresponding microstructures. There are two main reasons to use a multiscale approach. First, and most important to us, to assure the stiff phase can be manufactured in one piece using additive manufacturing and infused with the soft material. Second, because resolving the macroscopic problem down to the manufacturing precision can be extremely computationally expensive, especially since it involves solving an eigenvalue problem.

5.3 Microscopic problem

5.3.1 Formulation

As mentioned, a practical approach to multiscale optimization is to optimize the properties of the microstructure first, and then use these optimized microstructures as material phases to interpolate between with a multi-material interpolation scheme. With this approach the connectivity of the graded microstructure can be assured a priori, which is an important consideration and not trivial to achieve. Furthermore, the computational burden is very low compared to a coupled multiscale optimization problem. The drawback is that the solution space is more limited. For the problem presented here, where the focus is on isotropic microstructures, this is not a big issue. If arbitrarily anisotropic microstructures should be allowed, the approach might not be suitable. However, this would most likely lead to a structure which would be difficult to manufacture.

In Section 3.5, a formulation to obtain microstructures with a maximized bulk loss modulus was presented. This results in microstructures that can have very different loss factors in bulk and shear. Therefore, a slightly modified approach is used here, where the goal is to maximize the smallest of the bulk and shear loss factor. Furthermore, the stiffness constraint is on the shear modulus instead of the bulk modulus. The mathematical formulation is detailed in [P9].

5.4 Results

The properties of the selected stiff and the soft material phase are listed in Tab. 5.1. The stiff phase is titanium, because it is a popular additive manufacturing material, and the soft phase, denoted S1, which is supposed to be molded/infused in the printed titanium, is a generic stiff plastic with properties similar to ABS.

In order to illustrate the multiscale approach a simple 2D problem is considered. The macroscopic design problem considered is that of a 2D simply supported beam with dimensions $200\ \mathrm{mm} \times 50\ \mathrm{mm}$. The dimensions are chosen based on the fact that few additive manufacturing machines have a build chamber where the largest dimension is larger than $200\ \mathrm{mm}$. Furthermore, assume the minimum feature size (wall thickness) is $1/4\ \mathrm{mm}$. To resolve the manufacturing precision of this simple 2D problem, 800×200 elements would be necessary. However, if each element was mapped to a microstructure with a unit cell size of $5 \times 5\ \mathrm{mm}$, a mere 40×10 design elements are necessary.

Table 5.1: Material properties for the stiff and soft material phases. The material phases are isotropic, and, thus, the material properties are uniquely given by Young's modulus $E = E'(1+i\eta)$ and Poisson's ratio ν, but for the sake of clarity K' and G' are also stated.

Material	ρ [$\mathrm{kg/m^3}$]	E' [GPa]	ν [-]	G' [GPa]	K' [GPa]	η [-]
Titanium	4500	100	0.3	38.46	83.33	0.001
S1	1000	2	0.4	0.71	3.33	0.05

However, before we can solve the macroscopic problem a suitable material interpolation must be obtained by solving the microscopic problem for a range of stiffness constraints.

5.4.1 2D microstructure

First, the microscopic optimization problem is used to maximize the loss factor of three connected microstructures consisting of titanium and S1.

The loss factor is maximized with three different values a for the stiffness constraint. The conductivity constraint value is set to $b = 0.05$, and the robust formulation with $\eta_{\text{eroded}} = 0.4$ and $\eta_{\text{eroded}} = 0.6$ and a filter radius of 0.07 times the unit cell width, have been used for all designs. A higher conductivity constraint would typically give larger stiff material phase feature sizes, and a larger filter radius (or wider η-values) will increase the minimum feature size. A 45 degree symmetry has been enforced in all designs - this makes it easier to fulfill the isotropy constraints and do not, based on numerical experiments, affect the performance.

The resulting microstructures are shown in Fig. 5.1(a). The corresponding homogenized material properties (evaluated from the thresholded designs) are plotted in Fig. 5.1(b-c). The stiffness of the microstructures follow a power law with a low exponent and the loss factors seem to follow a similar power law, just with the opposite sign. Furthermore, note that the bulk storage modulus is always larger than the shear, even though the constraint is on the shear storage modulus.

5.4.2 Material interpolation for macroscopic problem

In order to obtain a macroscopic structure consisting of only the discrete set of a priori obtained microstructures, we present a material interpolation for "guiding" multiscale optimizations to this discrete set.

First, power law interpolations between the material properties of the microstructures are created. These are plotted in Fig. 5.2, where the x-axis shows the normalized density φ.

The storage moduli follow power law functions, while the loss factors are described by similar power law functions (with opposite signs). This opposite relation between storage and loss moduli, where the two intermediate density microstructures have proportionally higher loss, but lower stiffness, is what makes it possible to introduce an interpolation on the loss factors that guides the macroscopic problem to a discrete set of densities and corresponding microstructures.

First, the macroscopic optimization problem is solved using the power law interpolations stated in Fig. 5.2. The resulting design is used as the initial design for a new optimization where the power law interpolation on the loss factors are exchanged with multi-step Heaviside functions (continuous step functions), which are also illustrated in Fig. 5.2(b-c). These functions are constructed to favor the densities corresponding to the microstructures Fig. 5.2(a-b), because the densities in-between microstructures become sufficiently uneconomical when the goal is to maximize the structural damping with a constraint on the stiffness (the first eigenvalue constraint).

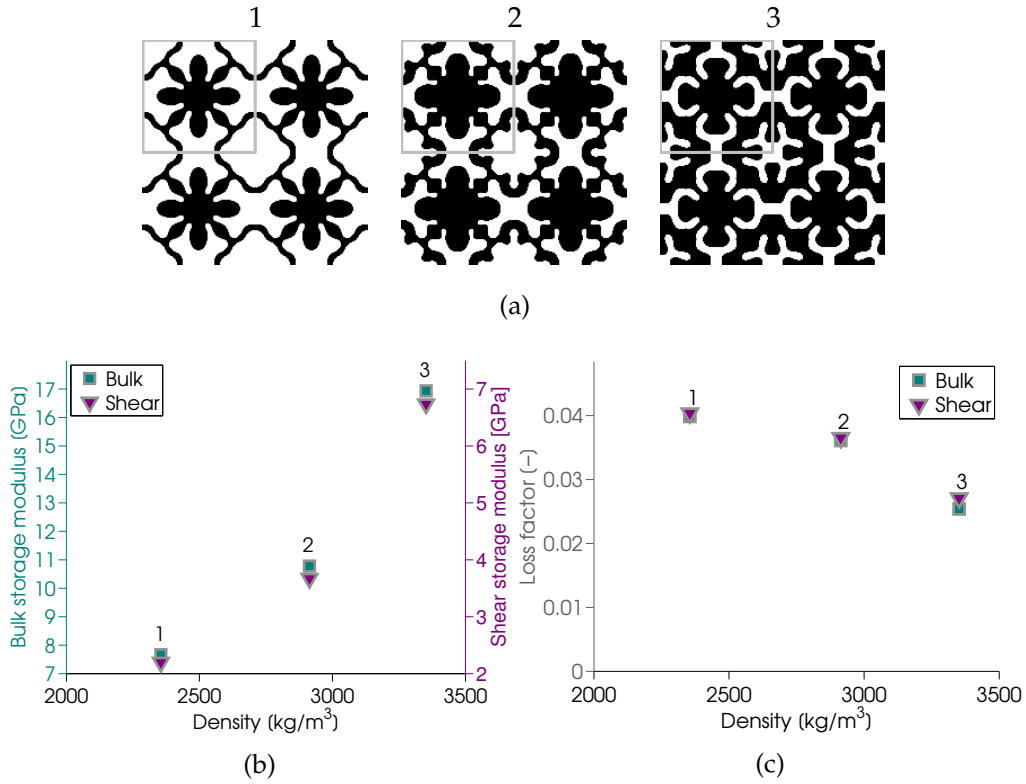

Figure 5.1: Results obtained by solving the microscopic optimization problem with S1 as the soft phase and titanium as the stiff phase. (a) The three microstructures, and (b-c) their corresponding properties.

The interpolation builds on ideas first presented by (Guest et al., 2004) and extended by (Xu et al., 2010) (projection of filtered densities), but the multistep version introduced here is only meant as a material interpolation for the loss factors and not in conjunction with any filtering. As mentioned, no filtering is used in the macroscopic problem. The details of the multistep function can be found in [P9].

5.4.3 2D simply supported beam

Consider the earlier described simply supported beam. If there is no constraint on the lowest eigenvalue, the optimized structure would be one purely consisting of microstructure 1. With S1 as the soft phase, the stiffest microstructure has $\zeta_1 = 0.013$ and $\mathrm{Re}(\omega_1) = 1219$ Hz. Thus, for the optimized beam we allow a slightly lower first eigenfrequency of $0.8 \cdot 1219$ Hz $= 975$ Hz with the aim of achieving a higher structural damping.

The result of the first part of the optimization, using only the power law interpolations for the S1 microstructures from Fig. 5.2(a), is shown in Fig. 5.3. The optimized beam has $\zeta_1 = 0.019$. Continuing with the step function interpolation, the design in Fig. 5.2(b) is obtained. A design with three discrete density values is nearly obtained. This beam also has a damping ratio that is only one percent lower than the beam in Fig. 5.2(a).

Figure 5.4 shows have the beam from Fig. 5.3(b) looks when each design variable is mapped to the corresponding microstructure.

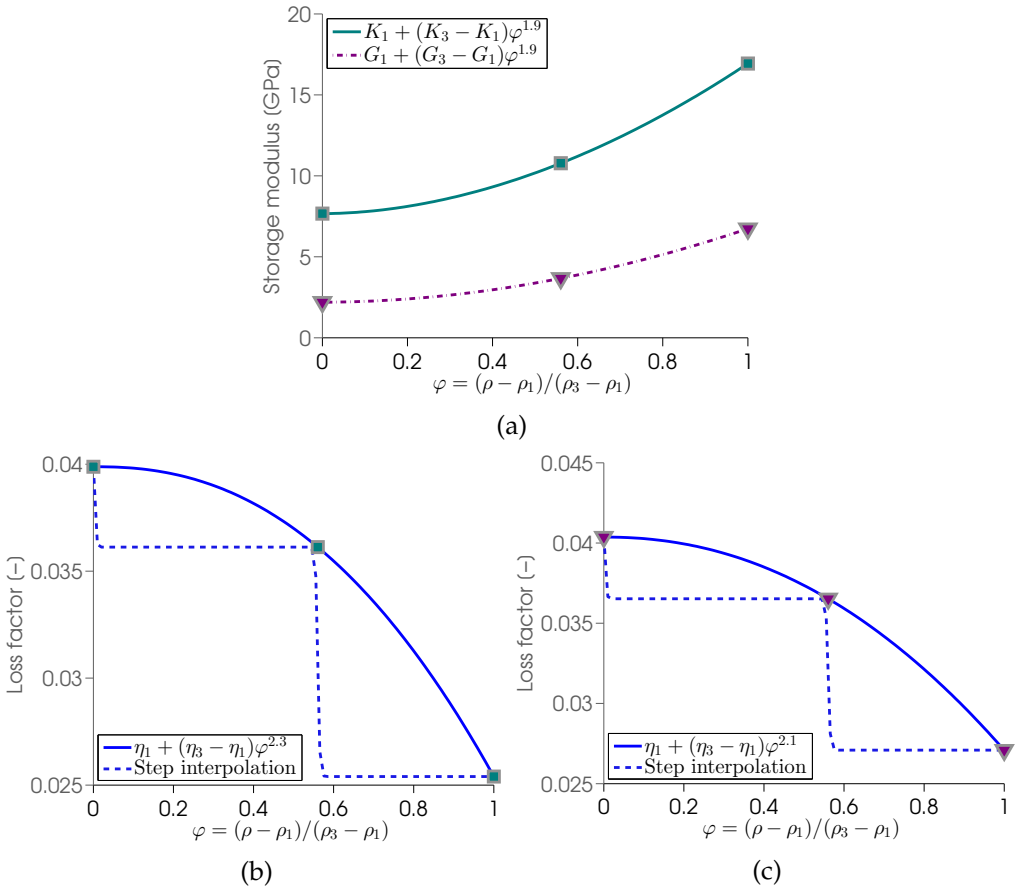

Figure 5.2: Material interpolations between microstructures 1-3 in Fig. 5.1(a).(a) shows the storage moduli interpolations, and (b-c) show the loss factor interpolation.

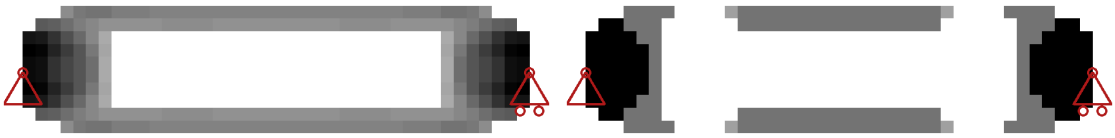

Figure 5.3: Optimized beams, where white indicates microstructure 1 and black indicates microstructure 3. Gray corresponds to intermediate microstructures. (a) shows the design obtained using the power law interpolation, and (b) shows the final design after continuing optimization with the Heaviside interpolation.

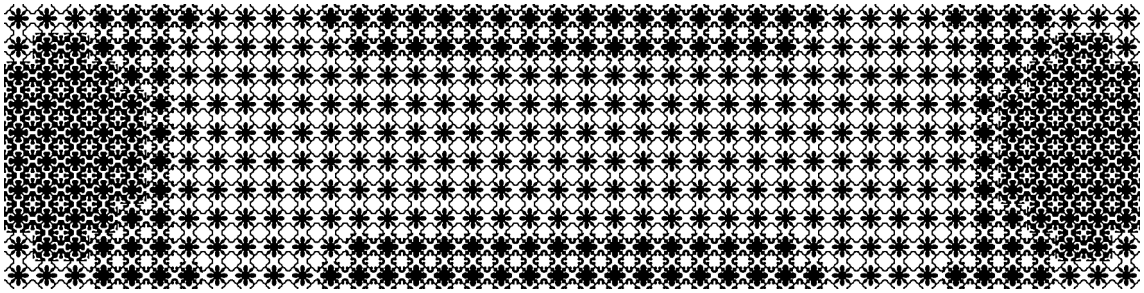

Figure 5.4: Optimized beam from Fig. 5.3(b) with microstructure. Black indicates stiff material phase and white indicates soft material phase.

Finally, it should be remarked that only the first eigenfrequency has been included in the optimizations here, even though the min-max formulation in Eq. (5.1) allows for a range of eigenfrequency. And the approach does work equally well with a range of eigenfrequencies, but in most cases the structural damping of the first one or two eigenfrequencies will drive the optimization.

CHAPTER 6

CONCLUDING REMARKS

I will conclude with a few remarks on how this work can be applied in the industry and what, in my opinion, should be the focus of future research in the field of material design.

In my opinion, much of the ongoing work within design of microstructures is either ahead of its time with respect to manufacturing possibilities or it is taking relatively simple problems and complicating them by adding microstructure. This also goes for part of the results presented in this thesis.

That said, I think the extensive use of fiber composites in the industry shows that developing materials with advanced or enhanced properties, enables engineers to develop better products (and the products do not need to be optimal as long as they are better).

Furthermore, in cases where a microstructure is beneficial (e.g. because of evenly distributed properties, such as conductivity, permeability, or support material in additive manufacturing, in a domain), optimization on a unit cell level will save considerable computational resources, and I believe future work within microstructure material optimization should focus on finding real world applications where there is an actual benefit of introducing a microstructure.

With respect to dynamic properties, I would like to see work exploiting the possibility of taking frequency dependent material parameters into account, which is possible with the material optimization formulations presented in this thesis. It is also with regards to dynamic properties I see the most interesting industrial applications. Applying the suggested multiscale method to a structural component where a high minimum stiffness needs to be combined with high structural damping could lead to innovative new designs. This entitles work with respect to identifying and characterizing lossy materials suitable for infiltration in the metal matrix. However, the extension of the proposed multiscale method to arbitrary 3D geometries should be straightforward.

Finally, it would be interesting to see how much additional damping can be achieved by introducing an active material phase, such as a piezoelectric material phase, and whether such designs could be manufactured. This, however, would probably be a PhD project in itself.

References

Alexandersen, J. and Lazarov, B. S. (2014). "Robust topology optimisation of microstructural details without length scale separation - using a spectral coarse basis preconditioner". *In review. Preprint available, arXiv:1411.3923*.

Almgren, R. F. (1985). "An isotropic three-dimensional structure with Poisson's ratio=-1". *Journal of Elasticity* 15 (4), pp. 427–430.

Andreasen, C. S. and Sigmund, O. (2011). "Saturated poroelastic actuators generated by topology optimization". *Structural and Multidisciplinary Optimization* 43 (5), pp. 693–706.

Andreasen, C. S. and Sigmund, O. (2012). "Multiscale modeling and topology optimization of poroelastic actuators". *Smart Materials and Structures* 21 (6).

Barbarosie, C. and Toader, A.-M. (2012). "Optimization of Bodies with Locally Periodic Microstructure". *Mechanics of Advanced Materials and Structures* 19 (4), pp. 290–301.

Bendsøe, M. P. and Sigmund, O. (2003). *Topology Optimization. Theory, Methods and Applications*. Springer.

Bendsøe, M. P. and Kikuchi, N. (1988). "Generating optimal topologies in structural design using a homogenization method". *Computer Methods in Applied Mechanics and Engineering* 71 (2), pp. 197–224.

Bendsøe, M., Guedes, J., Haber, R., Pedersen, P., and Taylor, J. (1994). "An analytical model to predict optimal material properties in the context of optimal structural design". *Journal of Applied Mechanics - Transactions of the ASME* 61 (4), pp. 930–937.

Bensoussan, A., Lions, J. L., and Papanicolaou, G. (1978). *Asymptotic analysis for periodic structures*. North-Holland Publishing Company.

Berryman, J. G. and Milton, G. W. (1988). "Microgeometry of random composites and porous media". *Journal of Physics D (Applied Physics)* 21 (1), pp. 87–94.

Bilal, O. R. and Hussein, M. I. (2011). "Ultrawide phononic band gap for combined in-plane and out-of-plane waves." *Phys Rev E* 84 (6-2), pp. 065701–4.

Bloch, F. (1929). "Über die Quantenmechanik der Elektronen in Kristallgittern". *Zeitschrift für Physik* 52 (7-8), pp. 555–600.

Brillouin, L. (1953). *Wave propagation in periodic structures*. Second. Dover Publications.

Brodt, M. and Lakes, R. (1995). "Composite-materials which exhibit high stiffness and high viscoelastic damping". *Journal of Composite Materials* 29 (14), pp. 1823–1833.

Bruyneel, M. and Duysinx, P. (2006). "Note on singular optima in laminate design problems". *Structural and Multidisciplinary Optimization* 31 (2), pp. 156–159.

Bruyneel, M., Duysinx, P., and Fleury, C. (2002). "A family of MMA approximations for structural optimization". *Structural and Multidisciplinary Optimization* 24 (4), pp. 263–276.

Cadman, J., Zhou, S., Chen, Y., and Li, Q. (2012). "On design of multi-functional microstructural materials". *Journal of Materials Science* 48 (1), pp. 1–16.

Challis, V. J., Roberts, A. P., and Wilkins, A. H. (2008). "Design of three dimensional isotropic microstructures for maximized stiffness and conductivity". *International Journal of Solids and Structures* 45 (14-15), pp. 4130–4146.

Cherkaev, A. and Gibiansky, L. (1993). "Coupled estimates for the bulk and shear moduli of a two-dimensional isotropic elastic composite". *Journal of the Mechanics and Physics of Solids* 41 (5), pp. 937–980.

Coelho, P. G., Fernandes, P. R., Guedes, J. M., and Rodrigues, H. C. (2008). "A hierarchical model for concurrent material and topology optimisation of three-dimensional structures". *Structural and Multidisciplinary Optimization* 35 (2), pp. 107–115.

Coelho, P. G., Cardoso, J. B., Fernandes, P. R., and Rodrigues, H. C. (2011). "Parallel computing techniques applied to the simultaneous design of structure and material". *Advances in Engineering Software* 42 (5), pp. 219–227.

Cox, S. and Dobson, D. (1999). "Maximizing band gaps in two-dimensional photonic crystals". *SIAM Journal on Applied Mathematics* 59 (6), pp. 2108–2120.

Cremer, L., Heckl, M., and Petersson, B. A. T. (2005). *Structure-borne sound : structural vibrations and sound radiation at audio frequencies*. Springer.

Cribb, J. L. (1968). "Shrinkage and thermal expansion of a two phase material". *Nature* 220 (5167), pp. 576–577.

Diaz, A., Haddow, A., and Ma, L. (2005). "Design of band-gap grid structures". *Structural and Multidisciplinary Optimization* 29 (6), pp. 418–431.

El-Sabbagh, A. and Baz, A. (2014). "Topology optimization of unconstrained damping treatments for plates". *Engineering Optimization* 46 (9), pp. 1153–1168.

Gibiansky, L. V. and Lakes, R. (1993). "Bounds on the complex bulk Modulus of a 2-phase viscoelastic composite with arbitrary volume fractions of the components". *Mechanics of Materials* 16 (3), pp. 317–331.

Gibiansky, L. and Lakes, R. (1997). "Bounds on the complex bulk and shear moduli of a two-dimensional two-phase viscoelastic composite". *Mechanics of Materials* 25 (2), pp. 79–95.

Guedes, J. M. and Kikuchi, N. (1990). "Preprocessing and postprocessing for materials based on the homogenization method with adaptive finite element methods". *Computer Methods in Applied Mechanics and Engineering* 83 (2), pp. 143–198.

Guest, J. K. and Prévost, J. H. (2006). "Optimizing multifunctional materials: Design of microstructures for maximized stiffness and fluid permeability". *International Journal of Solids and Structures* 43 (22-23), pp. 7028–7047.

Guest, J. K. and Prevost, J. H. (2007). "Design of maximum permeability material structures". *Computer Methods in Applied Mechanics and Engineering* 196 (4-6), pp. 1006–1017.

Guest, J., Prevost, J., and Belytschko, T. (2004). "Achieving minimum length scale in topology optimization using nodal design variables and projection functions". *International Journal for Numerical Methods in Engineering* 61 (2), pp. 238–254.

Halkjær, S., Sigmund, O., and Jensen, J. S. (2005). "Inverse design of phononic crystals by topology optimization". *Zeitschrift für Kristallographie - Crystalline Materials* 220 (9-10), pp. 895–905.

Halkjær, S., Sigmund, O., and Jensen, J. S. (2006). "Maximizing band gaps in plate structures". *Structural and Multidisciplinary Optimization* 32 (4), pp. 263–275.

Hashin and Shtrikman (1963). "A variational approach to the theory of the elastic behaviour of multiphase materials". *Journal of Mechanics and Physics of Solids* 11, pp. 127–140.

Hashin, Z. (1965). "Viscoelastic behavior of heterogeneous media". *Journal of Applied Mechanics - Transactions of the ASME* 32 (3), pp. 630–636.

Hashin, Z. (1962). "The elastic moduli of heterogeneous materials". *Journal of Applied Mechanics* 29 (1), pp. 143–150.

Hassani, B. and Hinton, E. (1998a). "A review of homogenization and topology optimization I - homogenization theory for media with periodic structure". *Computers & Structures* 69 (6), pp. 707–717.

Hassani, B. and Hinton, E. (1998b). "A review of homogenization and topology optimization II - analytical and numerical solution of homogenization equations". *Computers & Structures* 69 (6), pp. 719–738.

Hassani, B. and Hinton, E. (1998c). "A review of homogenization and topology optimization III - topology optimization using optimality criteria". *Computers & Structures* 69 (6), pp. 739–756.

Hill, R. (1952). "The Elastic Behaviour of a Crystalline Aggregate". *Proceedings of the Physical Society. Section A* 65 (5), pp. 349–354.

Jensen, J. S. and Sigmund, O. (2011). "Topology optimization for nano-photonics". *Laser and Photonics Reviews* 5 (2), pp. 308–321.

Kadic, M., Bückmann, T., Stenger, N., Thiel, M., and Wegener, M. (2012). "On the practicability of pentamode mechanical metamaterials". *Applied Physics Letters* 100 (19), pp. 191901–191904.

Kang, H., Lin, C.-Y., and Hollister, S. J. (2010). "Topology optimization of three dimensional tissue engineering scaffold architectures for prescribed bulk modulus and diffusivity". *Structural and Multidisciplinary Optimization* 42 (4), pp. 633–644.

Khanoki, S. A. and Pasini, D. (2012). "Multiscale Design and Multiobjective Optimization of Orthopedic Hip Implants with Functionally Graded Cellular Material". *Journal of Biomechanical Engineering - Transactions of the ASME* 134 (3), pp. –.

Kim, S. Y., Mechefske, C. K., and Kim, I. Y. (2013). "Optimal damping layout in a shell structure using topology optimization". *Journal of Sound and Vibration* 332 (12), pp. 2873–2883.

Kuboki, Y., Takita, H., Kobayashi, D., Tsuruga, E., Inoue, M., Murata, M., Nagai, N., Dohi, Y., and Ohgushi, H. (1998). "BMP-induced osteogenesis on the surface of hydroxyapatite with geometrically feasible and nonfeasible structures: Topology of osteogenesis". *Journal of Biomedical Materials Research* 39 (2), pp. 190–199.

Lakes, R. (1987). "Foam Structures with a Negative Poisson's Ratio." *Science* 235 (4792), pp. 1038–1040.

Lakes, R. (2002). "High damping composite materials: Effect of structural hierarchy". *Journal of Composite Materials* 36 (3), pp. 287–297.

Larsen, U., Sigmund, O., and Bouwstra, S. (1997). "Design and fabrication of compliant mechanisms and material structures with negative Poissons ratio". *Journal of Microelectromechanical Systems* 6 (2), pp. 99–106.

Ling, Z., Ronglu, X., Yi, W., and El-Sabbagh, A. (2011). "Topology optimization of constrained layer damping on plates using Method of Moving Asymptote (MMA) approach". *Shock and Vibration* 18 (1-2), pp. 221–244.

Milton and Cherkaev (1995). "Which elasticity tensors are realizable?" *Transasctions of ASME, Journal of Engineering Materials and Technology* 117 (4), pp. 483–493.

Milton, G. W. (1992). "Composite materials with poisson's ratios close to -1". *Journal of the Mechanics and Physics of Solids* 40 (5), pp. 1105–1137.

Milton, G. (1986). "Modelling the Properties of Composites by Laminates". *Homogenization and Effective Moduli of Materials and Media*. Ed. by Ericksen, J., Kinderlehrer, D., Kohn, R., and Lions, J.-L. Vol. 1. The IMA Volumes in Mathematics and its Applications. Springer, pp. 150–174.

Moiseyenko, R. P. and Laude, V. (2011). "Dynamics, dynamical systems, lattice effects - Material loss influence on the complex band structure and group velocity in phononic crystals (6 pages) 064301". *Physical review. B, Condensed matter and materials physics* 83 (6), pp. 064301–6.

Neves, M. M., Rodrigues, H., and Guedes, J. M. (2000). "Optimal design of periodic linear elastic microstructures". eng. *Computers and Structures* 76 (1), pp. 421–429.

Ostoja-Starzewski, M. (2008). *Microstructural randomness and scaling in mechanics of materials*. Chapman & Hall/CRC.

Poland, C. A., Duffin, R., Kinloch, I., Maynard, A., Wallace, W. A. H., Seaton, A., Stone, V., Brown, S., MacNee, W., and Donaldson, K. (2008). "Carbon nanotubes introduced into the abdominal cavity of mice show asbestos-like pathogenicity in a pilot study". *Nature Nano* 3 (7), pp. 423–428.

Rodrigues, H., Guedes, J. M., and Bendsoe, M. P. (2002). "Hierarchical optimization of material and structure". *Structural and Multidisciplinary Optimization* 24 (1), pp. 1–10.

Rosen, B. W. and Hashin, Z. (1970). "Effective thermal expansion coefficients and specific heats of composite materials". *International Journal of Engineering Science* 8 (2), pp. 157–174.

Sigalas, M. M. and Economou, E. N. (1992). "Elastic and acoustic wave band structure". *Journal of Sound and Vibration* 158 (2), pp. 377–382.

Sigmund and Jensen (2003). "Systematic design of phononic band-gap materials and structures by topology optimization". *Philosophical transactions - Royal Society. Mathematical, Physical and Engineering Sciences* 361 (1806), pp. 1001–1019.

Sigmund, O. (1994). "Materials with prescribed constitutive parameters: An inverse homogenization problem". *International Journal of Solids and Structures* 31 (17), pp. 2313–2329.

Sigmund, O. (1995). "Tailoring materials with prescribed elastic properties". *Mechanics of Materials* 20 (4), pp. 351–368.

Sigmund, O. (1997). "On the design of compliant mechanisms using topology optimization". *Mechanics of Structures and Machines* 25 (4), pp. 493–524.

Sigmund, O and Torquato, S (1999). "Design of smart composite materials using topology optimization". *Smart Materials & Structures* 8 (3), pp. 365–379.

Sigmund, O., Torquato, S., and Aksay, I. (1998). "On the design of 1-3 piezocomposites using topology optimization". *Journal of Materials Research* 13 (4), pp. 1038–1048.

Sigmund, O. (2000). "A new class of extremal composites". *Journal of the Mechanics and Physics of Solids* 48 (2), pp. 397–428.

Sigmund, O. (2007). "Morphology-based black and white filters for topology optimization". *Structural and Multidisciplinary Optimization* 33 (4-5), pp. 401–424.

Sigmund, O. (2009). "Manufacturing tolerant topology optimization". *Acta Mechanica Sinica* 25 (2), pp. 227–239.

Sigmund, O. (2011). "On the usefulness of non-gradient approaches in topology optimization". *Structural and Multidisciplinary Optimization* 43 (5), pp. 589–596.

Song, P., Zhang, Q., Liu, C., and Fan, S. (2008). "High thermal and electrical conductivity; alternating layers with polyacrylate material". Pat. US Patent App. 11/831,904.

Sperling, L. (1990). "Sound and Vibration Damping with Polymers - Basic Viscoelastic Definitions and Concepts". *ACS Symposium Series* 424, pp. 5–22.

Stegmann, J. and Lund, E. (2005). "Discrete material optimization of general composite shell structures". *International Journal for Numerical Methods in Engineering* 62 (14), pp. 2009–2027.

Svanberg, K. (1987). "Methods of moving asymptotes - a new method for structural optimization". *International Journal for Numerical Methods in Engineering* 24 (2), pp. 359–373.

Svanberg, K. (2002). "A Class of Globally Convergent Optimization Methods Based on Conservative Convex Separable Approximations". *SIAM Journal on Optimization* 12 (2), pp. 555–573.

Takemoto, M., Nakamura, T., Suzuki, J., Kokubo, T., Matsushita, T., and Fujibayashi, S. (2005). "Mechanical properties and osteoconductivity of porous bioactive titanium metal". *Key Engineering Materials* 284-286, pp. 263–266.

Theocaris, P. S. and Stavroulakis, G. E. (1999). "Optimal material design in composites: An iterative approach based on homogenized cells". *Computer Methods in Applied Mechanics and Engineering* 169 (1-2), pp. 31–42.

Thomsen, J. J. (2003). *Vibrations and Stability / Advanced Theory, Analysis, and Tools*. Second. Springer.

Torquato, S. (2002). *Random heterogeneous materials / Microstructure and macroscopic properties.* Springer.

Vigdergauz, S. (1999). "Energy-minimizing inclusions in a planar elastic structure with macroisotropy". *Structural Optimization* 17 (2), pp. 104–112.

Vigdergauz, S. B. (1989). "Regular structures with extremal elastic properties". *Mechanics of Solids* 24 (3), pp. 57–63.

Walpole (1966). "On bounds for the overall elastic moduli of inhomogeneous systems–II". *Journal of the Mechanics and Physics of Solids* 14 (5), pp. 289–301.

Wang, F., Lazarov, B. S., and Sigmund, O. (2011). "On projection methods, convergence and robust formulations in topology optimization". *Structural and Multidisciplinary Optimization* 43 (6), pp. 767–784.

Wang, F., Jensen, J. S., Sigmund, O., and Mørk, J. (2012). "Systematic design of loss-engineered slow-light waveguides". *Journal of the Optical Society of America A: Optics and Image Science, and Vision* 29 (12), pp. 2657–2666.

Xu, S., Cai, Y., and Cheng, G. (2010). "Volume preserving nonlinear density filter based on heaviside functions". *Structural and Multidisciplinary Optimization* 41 (4), pp. 495–505.

Yablonovitch, E and Gmitter, T. (1989). "Photonic band-structure - the-face-centered-cubic-case". *Physical Review Letters* 63 (18), pp. 1950–1953.

Zenkert, D. and Battley, M. (2006). *Composite Lightweight Structures*. Department of Mechanical Engineering, Technical University of Denmark.

Zienkiewicz, O. C. and Taylor, R. L. (2000). *The Finite Element Method. Fifth Edition. Volume 1: The Basis*. Butterworth-Heinemann.

APPENDIX A

SENSITIVITIES OF STATIC PROPERTIES

Below the sensitivities of the homogenized properties discussed in Chapter 3 are derived.

A.1 Sensitivities of elastic properties

Element i's constitutive matrix depends on the element design variable φ_i. In order to find the sensitivities, we differentiate $\mathbf{C}^*$ with respect to φ_i

$$\begin{aligned}\frac{d\mathbf{C}^*}{d\varphi_i} = \frac{1}{|V|}\sum_{e=1}^{N}\int_{V_e} &\frac{d\left(\mathbf{I}-\mathbf{B}_e\mathbf{U}\right)^T}{d\varphi_i}\mathbf{C}_e\left(\mathbf{I}-\mathbf{B}_e\mathbf{U}\right)\\ &+\left(\mathbf{I}-\mathbf{B}_e\mathbf{U}\right)^T\frac{d\mathbf{C}_e}{d\varphi_i}\left(\mathbf{I}-\mathbf{B}_e\mathbf{U}\right)+\left(\mathbf{I}-\mathbf{B}_e\mathbf{U}\right)^T\mathbf{C}_e\frac{d\left(\mathbf{I}-\mathbf{B}_e\mathbf{U}\right)}{d\varphi_i}\,\mathrm{dV}_e\,. \end{aligned} \tag{A.1}$$

The first term can be written out as

$$\begin{aligned}&\sum_{e=1}^{N}\int_{V_e}\frac{d\left(\mathbf{I}-\mathbf{B}_e\mathbf{U}\right)^T}{d\varphi_i}\mathbf{C}_e\left(\mathbf{I}-\mathbf{B}_e\mathbf{U}\right)\mathrm{dV}_e\\ &=\frac{d\mathbf{U}^T}{d\varphi_i}\sum_{e=1}^{N}\int_{V_e}-\mathbf{B}_e^T\mathbf{C}_e\left(\mathbf{I}-\mathbf{B}_e\mathbf{U}\right)\mathrm{dV}_e\\ &=\frac{d\mathbf{U}^T}{d\varphi_i}\sum_{e=1}^{N}\int_{V_e}\left(\mathbf{B}_e^T\mathbf{C}_e\mathbf{B}_e\mathbf{U}-\mathbf{B}_e^T\mathbf{C}_e\mathbf{I}\right)\mathrm{dV}_e=\frac{d\mathbf{U}^T}{d\varphi_i}\left(\mathbf{K}\mathbf{U}-\mathbf{F}\right)=\mathbf{0}, \end{aligned} \tag{A.2}$$

and the term vanishes, because the equilibrium equation must be satisfied. Since $\mathbf{C}_e$ is symmetric, the last term is identical to the first term (i.e. it is also zero). This leaves us with the following expression for the sensitivities

$$\frac{d\mathbf{C}^*}{d\varphi_i}=\frac{1}{|V|}\sum_{e=1}^{N}\int_{V_e}\left(\mathbf{I}-\mathbf{B}_e\mathbf{U}\right)^T\frac{d\mathbf{C}_e}{d\varphi_i}\left(\mathbf{I}-\mathbf{B}_e\mathbf{U}\right)\mathrm{dV}_e, \tag{A.3}$$

and since the element constitutive matrix $\mathbf{C}_e$ only depends on the element design variable (when $e=i$), the sum can be discarded

$$\frac{d\mathbf{C}^*}{d\varphi_i}=\frac{1}{|V|}\int_{V_i}\left(\mathbf{I}-\mathbf{B}_i\mathbf{U}\right)^T\frac{d\mathbf{C}_i}{d\varphi_i}\left(\mathbf{I}-\mathbf{B}_i\mathbf{U}\right)\mathrm{dV}_i\,. \tag{A.4}$$

A.2 Sensitivities of thermal expansion properties

Again, element i's material properties are functions of the element design variable φ_i. In order to find the sensitivities, we differentiate β^* with respect to φ_i

$$\frac{d\beta^*}{d\varphi_i} = \frac{1}{|V|}\sum_{e=1}^{N}\int_{V_e}\frac{d\left(\alpha_e - \mathbf{B}_e\mathbf{U}_T\right)^T}{d\varphi_i}\mathbf{C}_e\left(\mathbf{I}-\mathbf{B}_e\mathbf{U}\right) + \left(\alpha_e - \mathbf{B}_e\mathbf{U}_T\right)^T\frac{d\mathbf{C}_e}{d\varphi_i}\left(\mathbf{I}-\mathbf{B}_e\mathbf{U}\right) + \left(\alpha_e - \mathbf{B}_e\mathbf{U}_T\right)^T\mathbf{C}_e\frac{d\left(\mathbf{I}-\mathbf{B}_e\mathbf{U}\right)}{d\varphi_i}\,\mathrm{dV}_e, \tag{A.5}$$

where

$$\frac{d\left(\alpha_e - \mathbf{B}_e\mathbf{U}_T\right)^T}{d\varphi_i} = \frac{d\alpha_e}{d\varphi_i} - \frac{d\mathbf{U}_T^T}{d\varphi_i}\mathbf{B}_e^T, \tag{A.6}$$

and

$$\frac{d\left(\mathbf{I}-\mathbf{B}_e\mathbf{U}\right)}{d\varphi_i} = -\mathbf{B}_e\frac{d\mathbf{U}}{d\varphi_i}. \tag{A.7}$$

This means that we can write

$$\begin{aligned}\frac{d\beta^*}{d\varphi_i} = {}& \frac{1}{|V|}\sum_{e=1}^{N}\int_{V_e}\frac{d\alpha_e}{d\varphi_i}\mathbf{C}_e\left(\mathbf{I}-\mathbf{B}_e\mathbf{U}\right)\mathrm{dV}_e + \\ & \frac{d\mathbf{U}_T^T}{d\varphi_i}\frac{1}{|V|}\sum_{e=1}^{N}\int_{V_e}\left(\mathbf{B}_e^T\mathbf{C}_e\mathbf{B}_e\mathbf{U} - \mathbf{B}_e^T\mathbf{C}_e\right)\mathrm{dV}_e + \\ & \frac{1}{|V|}\sum_{e=1}^{N}\int_{V_e}\left(\alpha_e - \mathbf{B}_e\mathbf{U}_T\right)^T\frac{d\mathbf{C}_e}{d\varphi_i}\left(\mathbf{I}-\mathbf{B}_e\mathbf{U}\right)\mathrm{dV}_e + \\ & \frac{1}{|V|}\sum_{e=1}^{N}\int_{V_e}\left(\mathbf{U}_T^T\mathbf{B}_e^T\mathbf{C}_e\mathbf{B}_e - \alpha_e^T\mathbf{C}_e\mathbf{B}_e\right)\mathrm{dV}_e\frac{d\mathbf{U}}{d\varphi_i},\end{aligned} \tag{A.8}$$

where the two terms with implicit derivatives (the second and fourth integral term) are zero, because of Eq. 3.2 and 3.6, respectively. Furthermore, again we note that only element i's material properties depend on φ_i, such that we can drop the summation. Then the sensitivities of the thermal stress vector boils down to

$$\begin{aligned}\frac{d\beta^*}{d\varphi_i} = {}& \frac{1}{|V|}\int_{V_i}\left(\alpha_i - \mathbf{B}\mathbf{T}_i\right)^T\frac{d\mathbf{C}_i}{d\varphi_i}\left(\mathbf{I}-\mathbf{B}\mathbf{U}_i\right)\mathrm{dV}_i \\ & + \frac{1}{|V|}\sum_{i=1}^{N}\int_{V_i}\left(\frac{d\alpha_i}{d\varphi_i}\right)^T\mathbf{C}_i\left(\mathbf{I}-\mathbf{B}\mathbf{U}_i\right)\mathrm{dV}_i\,.\end{aligned} \tag{A.9}$$

We can see that for the thermal stress vector there is an extra term in the sensitivities, because the unit thermal strain vector also depends on the design variable

To find the sensitivities of the thermal strain vector we use the following expression

$$\begin{aligned}\frac{d\alpha^*}{d\varphi_i} &= \frac{d}{d\varphi_i}\left(\mathbf{C}^*\right)^{-1}\beta^* = \frac{d\left(\mathbf{C}^*\right)^{-1}}{d\varphi_i}\beta^* + \left(\mathbf{C}^*\right)^{-1}\frac{d\beta^*}{d\varphi_i} \\ &= -\left(\mathbf{C}^*\right)^{-1}\frac{d\mathbf{C}^*}{d\varphi_i}\left(\mathbf{C}^*\right)^{-1}\beta^* + \left(\mathbf{C}^*\right)^{-1}\frac{d\beta^*}{d\varphi_i} \\ &= -\left(\mathbf{C}^*\right)^{-1}\frac{d\mathbf{C}^*}{d\varphi_i}\alpha^* + \left(\mathbf{C}^*\right)^{-1}\frac{d\beta^*}{d\varphi_i},\end{aligned} \tag{A.10}$$

which means its sensitivity can be found as the solution to the equation

$$\mathbf{C}^*\frac{d\alpha^*}{d\varphi_i} = -\frac{d\mathbf{C}^*}{d\varphi_i}\alpha^* + \frac{d\beta^*}{d\varphi_i}. \tag{A.11}$$

Publication [P1]

How to determine composite material properties using numerical homogenization

Computational Materials Science 83 (2014) 488–495

Contents lists available at ScienceDirect

Computational Materials Science

journal homepage: www.elsevier.com/locate/commatsci

How to determine composite material properties using numerical homogenization

Erik Andreassen *, Casper Schousboe Andreasen

Department of Mechanical Engineering, Technical University of Denmark, Nils Koppels Allé, Building 404, Denmark

ARTICLE INFO

Article history:
Received 25 May 2013
Received in revised form 22 August 2013
Accepted 3 September 2013
Available online 18 November 2013

Keywords:
Numerical homogenization
Microstructure
MicroFE
Matlab

ABSTRACT

Numerical homogenization is an efficient way to determine effective macroscopic properties, such as the elasticity tensor, of a periodic composite material. In this paper an educational description of the method is provided based on a short, self-contained Matlab implementation. It is shown how the basic code, which computes the effective elasticity tensor of a two material composite, where one material could be void, is easily extended to include more materials. Furthermore, extensions to homogenization of conductivity, thermal expansion, and fluid permeability are described in detail. The unit cell of the periodic material can take the shape of a square, rectangle, or parallelogram, allowing for all kinds of 2D periodicities.

1. Introduction

The microstructure of composite materials, where two or more materials are combined to achieve a material with attractive properties, can often be described by a unit cell, which is periodically repeated in one or more directions, as illustrated in Fig. 1.

Such periodic, or almost periodic, microstructures can be found in materials such as fiber composites and bone. Information about the microstructure can be obtained by e.g. a CT-scan. The technique described in the following can thereafter be applied to find the effective properties of the material. For human bone this has been done by e.g. Hollister [1], who has also been among the first to apply the technique for the design of metal and polymer implants [2,3].

Assuming length scales where the theory of elasticity can be applied and perfect bonding between the different materials in the unit cell, homogenization can be used to compute the macroscopic composite material properties. Homogenization relies on an asymptotic expansion of the governing equations, which allows for a separation of scales. This is valid when there is a clear separation between the macro- and microscopic length scales. The theory behind homogenization is covered in detail in several works, some of the first being [4,5]. Another good theoretical introduction to the subject can be found in [6].

According to the theory of homogenization, the macroscopic elasticity tensor E^H_{ijkl} of a periodic composite material can be computed as:

$$E^H_{ijkl} = \frac{1}{|V|}\int_V E_{pqrs}\left(\varepsilon^{0(ij)}_{pq} - \varepsilon^{(ij)}_{pq}\right)\left(\varepsilon^{0(kl)}_{rs} - \varepsilon^{(kl)}_{rs}\right)\mathrm{d}V \tag{1}$$

where $|V|$ denotes the volume of the unit cell, E_{pqrs} is the locally varying stiffness tensor, $\varepsilon^{0(ij)}_{pq}$ are prescribed macroscopic strain fields (in 2D there are three; e.g. unit strain in the horizontal direction (11), unit strain in the vertical direction (22), and unit shear strain (12 or 21)), while the locally varying strain fields $\varepsilon^{(ij)}_{pq}$ are defined as:

$$\varepsilon^{(ij)}_{pq} = \varepsilon_{pq}(\chi^{ij}) = \frac{1}{2}\left(\chi^{ij}_{p,q} + \chi^{ij}_{q,p}\right) \tag{2}$$

based on the displacement fields χ^{kl} found by solving the elasticity equations with a prescribed macroscopic strain

$$\int_V E_{ijpq}\varepsilon_{ij}(v)\varepsilon_{pq}(\chi^{kl})\mathrm{d}V = \int_V E_{ijpq}\varepsilon_{ij}(v)\varepsilon^{0(kl)}_{pq}\mathrm{d}V \quad \forall v \in V \tag{3}$$

where v is a virtual displacement field. For most practical problems the homogenization is performed numerically by discretizing and solving Eq. (3) using e.g. the finite element method. This is often referred to as numerical homogenization. The numerical homogenization procedure is also well described in the literature. One of the first detailed descriptions of the procedure can be found in [7], while [8–10] provide a three paper review of both numerical homogenization and how it is used in conjunction with topology optimization to design periodic materials.

However, the implementation can still seem daunting, and with the small and self-contained Matlab example provided in Appendix A, we try to lower the barrier for using numerical homogenization. The code computes the homogenized elasticity tensor for a two

* Corresponding author.
E-mail address: erand@mek.dtu.dk (E. Andreassen).

0927-0256/$ - see front matter © 2013 Elsevier B.V. All rights reserved.
http://dx.doi.org/10.1016/j.commatsci.2013.09.006

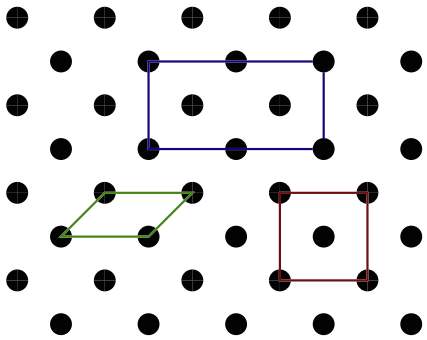

Fig. 1. A section of a 2D periodic microstructure consisting of two materials (white and black). The red line encloses a square unit cell, the blue a rectangular unit cell, and the green a parallelogram unit cell. (For interpretation of the references to colour in this figure legend, the reader is referred to the web version of this article.)

material composite. A detailed description of the implementation is provided in Section 2, while examples of extensions to three material composites, homogenized thermal expansion, and thermal conductivity are given in Section 3. Section 4 is devoted to a slightly more involved extension of homogenized permeability.

2. Matlab implementation

In the basic Matlab implementation we treat the case of a composite consisting of two materials. The unit cell is discretized using bilinear finite elements (plane strain elements are used, but plane stress can be specified by providing modified material data), and an indicator matrix `x` specifies whether a finite element contains material 1 ($x_e = 1$) or material 2 ($x_e = 2$).

In Fig. 2 the structure of the mesh used to discretize the unit cell and the indicator matrix `x` are illustrated. Fig. 2b also shows how the geometry of the unit cell is specified in the Matlab code. The homogenization function needs six user specified inputs. The two first arguments (`lx` and `ly`) are the width, l_x and height, l_y, of the unit cell. The third argument (`lambda`) is a vector containing Lame's first parameter for material 1 and for material 2. Similarly, the fourth argument (`mu`) is a vector with Lame's second parameter for the two materials. The fifth argument (`phi`) is the angle, ϕ, between the horizontal axis and the left wall in the unit cell. Finally, the sixth argument is the indicator matrix `x`. The discretization is determined from the size of `x`; number of rows equals number of elements in the vertical direction, and number of columns equals number of elements in the horizontal direction.

Remark the angle ϕ should be given in degrees and to avoid overly distorted elements it should not be smaller than 45° nor larger than 135°. As discussed in [11] a parallelogram unit cell allows for the analysis of general periodic materials, including polygonal cells.

Calling the function in Appendix A as:

```
x = randi([1 2],200)
homogenize(1,1,[.01 2],[0.02 4],90,x)
```

will compute the effective properties of a random microstructure consisting of two materials, where the stiff material has an elasticity modulus of about 100 times the soft material. The homogenization is done by discretizing the unit cell with 200 times 200 bilinear elements, since that is the size of `x`. The different parts of the homogenization procedure implementation are explained in detail in the following.

If only a single material is used the stiffness will be constant throughout the unit cell resulting in zero displacements i.e. $\varepsilon_{ij} = 0$ and the original stiffness is obtained when applying Eq. (1).

2.1. The element stiffness matrix and load vectors (lines 17 and 86–125)

The elasticity equation from (3) can be discretized using the finite element method. The left hand side, i.e. the stiffness matrix, yields:

$$\mathbf{K} = \sum_{e=1}^{N} \int_{V_e} \mathbf{B}_e^T \mathbf{C}_e \mathbf{B}_e \mathrm{d}V_e \tag{4}$$

where the summation denotes the assembly of N finite elements. The matrix $\mathbf{B}_e$ is the element strain–displacement matrix, V_e is the volume of element e, and $\mathbf{C}_e$ is the constitutive matrix for the element, which for an isotropic material (we assume the materials used to build the composite are isotropic) is:

$$\mathbf{C}_e = \lambda_e \cdot \begin{bmatrix} 1 & 1 & 0 \\ 1 & 1 & 0 \\ 0 & 0 & 0 \end{bmatrix} + \mu_e \cdot \begin{bmatrix} 2 & 0 & 0 \\ 0 & 2 & 0 \\ 0 & 0 & 1 \end{bmatrix} \tag{5}$$

where λ_e and μ_e are Lamé's first and second parameter for the material in element e, respectively. Lamé's parameters can be computed from Young's modulus E and the Poisson's ratio ν using the relations:

$$\lambda = \frac{\nu E}{(1+\nu)(1-2\nu)}, \quad \mu = \frac{E}{2(1+\nu)} \tag{6}$$

And to get plane stress properties Lamé's first parameter must further be modified as follows:

$$\hat{\lambda} = \frac{2\mu\lambda}{\lambda + 2\mu} \tag{7}$$

In the initialization the element stiffness matrix is split into two corresponding parts, such that the stiffness matrix is a function of the material properties in the elements:

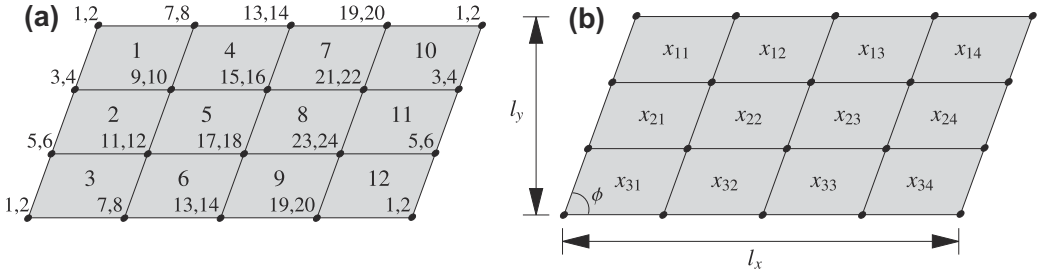

Fig. 2. (a) Illustration of finite element mesh used to discretize unit cell (element numbers are big, and degrees of freedom are small) and (b) corresponding structure of indicator matrix `x`.

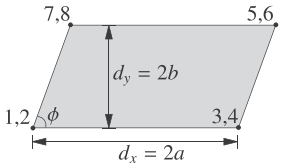

Fig. 3. Illustration of how local degrees of freedom in an element are numbered.

$$\mathbf{K} = \sum_{e=1}^{N} \mathbf{k_e} = \sum_{e=1}^{N} \left(\lambda_e \mathbf{k}_\lambda + \mu_e \mathbf{k}_\mu\right) \tag{8}$$

where the split simplifies the extension to more materials.

The discretization of the right hand side of (3) is the loads $\mathbf{f}^i$ which correspond to macroscopic volumetric straining

$$\mathbf{f}^i = \sum_e \int_{V_e} \mathbf{B}_e^T \mathbf{C}_e \boldsymbol{\varepsilon}^i \mathrm{d}V_e \tag{9}$$

where the strains are chosen to be:

$$\boldsymbol{\varepsilon}^1 = (1,0,0)^T, \quad \boldsymbol{\varepsilon}^2 = (0,1,0)^T, \quad \boldsymbol{\varepsilon}^3 = (0,0,1)^T \tag{10}$$

However, any three independent strains can be used, but for simplicity unit strains in the coordinate directions have been choosen. The load vectors are assembled using a split as for the stiffness matrix:

$$\mathbf{f}^i = \sum_e \left(\lambda_e \mathbf{f}^i_\lambda + \mu_e \mathbf{f}^i_\mu\right) \tag{11}$$

Finally, the displacement fields are computed solving the finite element problem with three loadcases (six in 3D):

$$\mathbf{K}\boldsymbol{\chi}^i = \mathbf{f}^i, \quad i = 1, \ldots, 3 \tag{12}$$

where the displacement vectors $\boldsymbol{\chi}^i$ are assumed to be V-periodic.

The computations of $\mathbf{k}_\lambda$, $\mathbf{k}_\mu$, $\mathbf{f}^i_\lambda$, and $\mathbf{f}^i_\mu$ are all done in the call to `elementMatVec` in line 17. Here we utilize the identical shape of the elements (not necessary as such for the homogenization, but makes the implementation simpler) by only executing this function once.

The element integration is done by mapping to an isoparametric element and computing the integral numerically using four Gauss points as described in e.g. [12]. The local numbering of degrees of freedom in the element is illustrated in Fig. 3, wherefrom the coordinate matrix in the computation of the Jacobian in lines 104 and 105 can be deduced. The use of tan (ϕ) in line 104 does not cause an issue when $\phi = 90°$, because Matlab just returns a very large number, implying 1/tan (90°) = 0.

In lines 119–123 the element matrix and element loads are computed, and as mentioned earlier these are kept in two separate parts; one should be multiplied with λ_e and one with μ_e.

2.2. Degrees of freedom and periodic boundary conditions (lines 19–36)

In order to assemble the global stiffness matrix and load vectors, we utilize the concept of an index matrix denoted `edofMat`, as also done in [13]. Consider the 12 element mesh in Fig. 2a. If the degrees of freedom were not periodic `edofMat` would have the structure in Fig. 4a. Each row i (shown in bold), contains the global degrees of freedom associated with element i. The non-periodic `edofMat`, which is created in line 21, is used to index into a periodic version of the mesh to create a periodic `edofMat` in line 35. The structure of the periodic `edofMat` is shown in Fig. 4b.

The periodic boundary conditions are imposed using elimination. This corresponds to using the same nodes on two opposite faces. This is implemented by using the matrix `edofMat` for a full, regular grid to index into a periodic version of the grid.

2.3. Assembly of the stiffness matrix (lines 37–46)

The assembly of the sparse stiffness matrix is based on triplets. First vectors with the row and column indices of the non-zero entries are created from `edofMat` in lines 39 and 40. Then matrices with the element material properties λ_e and μ_e are assigned in lines 42 and 43 based on the indicator matrix `x`. If the user supplies an indicator matrix with values other than 1 or 2, the element material properties will be wrongly assigned.

In line 45 the element matrices `keLambda` and `keMu` are multiplied with the corresponding element properties and added together. The resulting vector `sK` contains 64 (8 · 8) entries for each element. Finally, in line 46 the global stiffness matrix is assembled using the triplets.

2.4. Load vectors and solution (lines 47–54)

In lines 49–53 the load vectors are assembled in a similar fashion as the stiffness matrix. Thereafter the system in Eq. (12) is solved for $\boldsymbol{\chi}^i$. Due to small numerical differences Matlab might not recognize K as a symmetric matrix and therefore use a more general, but slower, linear solver. If speed is an issue, this could be remedied by adding `K = 0.5*(K + K.');`.

2.5. Homogenization (lines 55–84)

Before the homogenized elasticity tensor is computed the displacements of an element corresponding to the unit strain cases are found. This is simply done by solving for the element's nodal displacement corresponding to the uniform strains in Eq. (10), while constraining enough degrees of freedom to make the element stiffness matrix non-singular. This is done in line 62 as:

```
chi0_e([3 5:end],:)=ke([3 5:end],[3 5:end])\fe([3 5:end],:);
```

where the first, second, and fourth degree of freedom are constrained. The resulting element displacements are the same for all elements, since all elements are equivalent in the mesh used.

When the displacements have been obtained, the entries in the homogenized constitutive matrix $\mathbf{C}^H$ can be found as:

$$C^H_{ij} = \frac{1}{|V|} \sum_{e=1}^{N} \int_{V_e} \left(\boldsymbol{\chi}_e^{0(i)} - \boldsymbol{\chi}_e^{(i)}\right)^T \mathbf{k}_e \left(\boldsymbol{\chi}_e^{0(j)} - \boldsymbol{\chi}_e^{(j)}\right) \mathrm{d}V_e \tag{13}$$

where $\boldsymbol{\chi}_e^0$ contains the three displacement fields corresponding to the unit strains in Eq. (10), and $\boldsymbol{\chi}_e$ contains three columns corresponding to the three displacement fields resulting from

(a)

1	3	4	11	12	9	10	1	2
2	5	6	13	14	11	12	3	4
3	7	8	15	16	13	14	5	6
4	11	12	19	20	17	18	9	10
⋮	⋮	⋮	⋮	⋮				
12	31	32	39	40	37	38	29	30

(b)

1	3	4	9	10	7	8	1	2
2	5	6	11	12	9	10	3	4
3	1	2	7	8	11	12	5	6
4	9	10	15	16	13	14	7	8
⋮	⋮	⋮	⋮	⋮				
12	19	20	1	2	5	6	23	24

Fig. 4. Structure of the `edofMat`-matrix for 12 element mesh in (a) a non-periodic version, and (b) periodic version. The bold numbers denote the row numbers and indicate which element the degrees of freedom in the row belong to.

globally enforcing the unit strains in Eq. (10). The indices in parentheses refer to the column number. $|V|$ is the unit cell volume.

The sum in Eq. (13) is computed in lines 71–82, and it can be seen that again the summation is split in a λ and μ part, which is added together after being multiplied with the corresponding element material properties. After the homogenization is done, the homogenized elasticity tensor is displayed.

For meshes where the elements differ in shape, and thus the numerical integration must be performed for each element, the homogenization can be written as:

$$\mathbf{C}^H = \frac{1}{|V|}\sum_{e=1}^{N}\int_{V_e}(\mathbf{I}-\mathbf{B}_e\boldsymbol{\chi}_e)^T\mathbf{C}_e(\mathbf{I}-\mathbf{B}_e\boldsymbol{\chi}_e)\mathrm{d}V_e \tag{14}$$

where $\mathbf{I}$ is a three times three identity matrix (six in 3D). The term $\mathbf{B}_e\boldsymbol{\chi}_e$ can be interpreted as the strains caused by the non-homogeneous material distribution.

3. Extensions

In the following some extensions to allow for more materials and the homogenization of other properties are presented. The mentioned lines will refer to line numbers of the original unextended version of the code attached in Appendix A.

3.1. One material phase and void

Single-phase architecture cellular materials can be simulated by assigning a very soft second material. I. e. $\lambda_2 = 10^{-9}\lambda_1$, and $\mu_2 = 10^{-9}\mu_1$. Alternatively, the void elements can be ignored when solving the system by substituting line 54 with the lines:

```
activedofs = edofMat(x==1,:);
activedofs = sort(unique(activedofs(:)));
chi = zeros(ndof,3);
chi(activedofs(3:end),:) = ...
  K(activedofs(3:end),activedofs(3:end))...
\F(activedofs(3:end),:);
```

The last approach will save some computational time, but it does of course require material 1 to be connected. Furthermore, to get the correct homogenized constitutive matrix the material properties of material 2 must be set to 0.

3.2. Three material phases

In this section the extension to three material phases is described. Since the element stiffness matrix and load vectors have been split in a λ and μ part, the extension to more materials is straight-forward. The element material properties are assigned in lines 42 and 43 as:

```
mu = mu(1)*(x==1) + mu(2)*(x==2);
lambda = lambda(1)*(x==1) + lambda(2)*(x==2);
```

The above assumes entries in the indicator matrix contain either a 1 or 2. For three materials line 42 should be substituted with:

```
mu = mu(1)*(x==1) + mu(2)*(x==2) + mu(3)*(x==3);
```

which means the entries in the indicator matrix `x` should take one of the values 1, 2, or 3. Line 43 should of course be modified in the same way as line 42. Furthermore, the input vectors `lambda` and `mu` should have three entries each.

Assuming we have a material structure as the one shown in Fig. 1 where every other row of circular inclusions, each with a radius of 1/8 of the spacing between their centers, is alternating between material 2 and 3 in a matrix of material 1. If we assign the material properties $\lambda_1 = 1$, $\lambda_2 = 50$, $\lambda_3 = 100$ and $\mu_1 = 2$, $\mu_2 = 40$, $\lambda_3 = 80$ to the three phases, the resulting homogenized constitutive matrix is:

$$\mathbf{C}^H = \begin{bmatrix} 5.8 & 1.2 & 0.0 \\ 1.2 & 5.8 & 0.0 \\ 0.0 & 0.0 & 2.3 \end{bmatrix} \tag{15}$$

In Fig. 5 the corresponding square unit cell is shown together with force distributions. The force distributions illustrates clearly how the force vectors in Eq. (12) only have non-zero entries at the interfaces between the materials. If there are no material interfaces, there would be no local deformations in the unit cell. That is the solutions to Eq. (12) would be vectors of zeros.

3.3. Thermal conductivity

The homogenization equations for the thermal conductivity are analogous to those of the elastic problem though it is enough to solve for a scalar field – the temperature. Remark also that the problem is identical for electrical conductivity. The equations can be written as:

$$\int_V v_{,i}\mu_{ij}T^k_{,j}\mathrm{d}V = \int_V v_{,i}\mu_{ij}T^{0(k)}_{,j}\mathrm{d}V \quad \forall v \in V \tag{16}$$

$$\mu^H_{ij} = \frac{1}{|V|}\int_V (T^{0(i)}_{,l} - T^{(i)}_{,l})\mu_{lm}(T^{0(j)}_{,m} - T^{(j)}_{,m})\mathrm{d}V \tag{17}$$

where v is a virtual temperature field, μ_{ij} is the conductivity tensor and T is the temperature field. The finite element problem and the homogenization is analogous to the elasticity tensor homogenization. However, only one material parameter, μ, is necessary to describe the conductivity of an isotropic material, which should be an input vector to the homogenization function. Therefore, the changes described below assume the user gives the conductivity

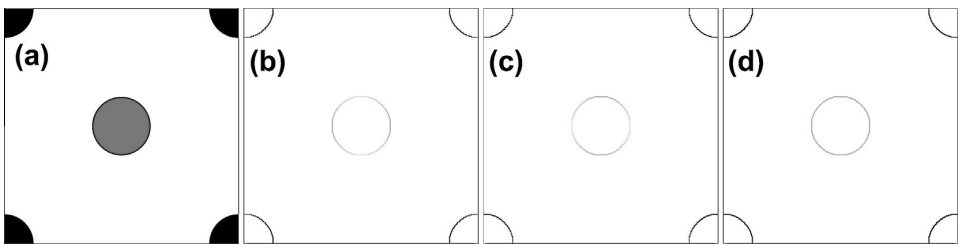

Fig. 5. (a) Square unit cell for a three material structure. Force magnitudes for $\mathbf{f}^1$, $\mathbf{f}^2$, and $\mathbf{f}^3$ are shown in (b), (c), and (d), respectively. Dark indicates large magnitude, while white indicates a zero magnitude.

of the materials in the input argument `mu` and that the input argument `lambda` is a vector of zeros. Then only minor changes to the code are necessary to compute the conductivity tensor of a composite.

In the computations of the element matrices only one line needs to be changed; line 88 should be updated to read:

```
CMu = diag([1 1 0]); CLambda = zeros(3);
```

This assures that the odd rows and columns in `keMu` contain the contributions associated with variations in potential in the x-direction (horizontal), and the even rows and columns contain the corresponding contributions for variations in the y-direction.

As mentioned, only a scalar field is necessary, this means that the element matrix is really a four times four matrix, found by summing the contributions from the odd and even rows/columns. To keep the changes in the code to a minimum, this four times four matrix is put into the odd rows and columns of `keMu` by adding the below line after the call to `elementMatVec` in line 17:

```
keMu(1:2:end,1:2:end) = keMu(1:2:end,1:2:end) + ...
    keMu(2:2:end, 2:2:end);
```

Now the remaining parts of the code should be modified to work with the odd rows and columns. The solution of the finite element problem in line 54 should be changed to:

```
chi = zeros(ndof,2);
chi(3:2:ndof,:) = K(3:2:end,3:2:end)\...
    [F(3:2:end,1) F(4:2:end,2)];
```

Similarly, the solution of the element strain cases in line 62 should be changed to:

```
chi0_e(3:2:end,1:2) = keMu(3:2:end,3:2:end)\...
    [feMu(3:2:end,1) feMu(4:2:end,2)];
```

Finally, the two loops in lines 71 and 72 should only run through indices 1 and 2.

The homogenized conductivity for the composite in Fig. 1, with high conducting circular disks/cylinders ($\mu_1 = 10$) with a radius $r = 0.125 l_x$ in a matrix with a lower conductivity ($\mu_2 = 1$), is $\mu^H = 1.175$. This fits perfectly with the analytical result derived in [14], which for a low disk volume fraction $f = 2\pi r^2$ can accurately be expressed by the low order approximation:

$$\mu^H = \mu_2 \frac{1 + 2\beta f}{1 - \beta f - 0.075422\beta^2 f^6} \tag{18}$$

with $\beta = (\mu_2 - \mu_1)/(\mu_2 + \mu_1)$.

3.4. Thermal expansion

In [15] numerical homogenization was used together with topology optimization to design a three material (two materials and void) isotropic composite with a negative thermal expansion. The composite's unit cell is pictured in Fig. 6.

The homogenized thermal stress tensor can be computed as:

$$\beta_{ij}^H = \frac{1}{|V|} \int_V E_{pqrs} \left(\alpha_{pq} - \varepsilon_{pq}^{\alpha} \right) \left(\varepsilon_{rs}^{0(ij)} - \varepsilon_{rs}^{(ij)} \right) \mathrm{d}V \tag{19}$$

where α_{pq} is the thermal expansion tensor, corresponding to a unit strain for a unit thermal load. The strain field $\varepsilon_{pq}^{\alpha}$ is computed according to Eq. (2) based on the displacement field Γ, which is found for a unit thermal load:

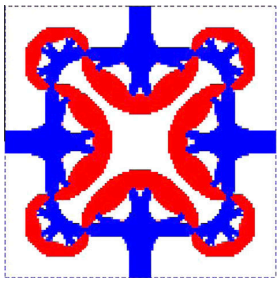

Fig. 6. A unit cell of a three material composite with macroscopic negative thermal expansion. The white part is void, modeled by setting the material stiffness to a millionth of the solid parts. The thermal expansion coefficient of the red and blue material are α_2 and α_3, respectively. The red and blue material have identical elastic properties, but $\alpha_2/\alpha_3 = 10$. Figure courtesy of Ole Sigmund, Technical University of Denmark. (For interpretation of the references to colour in this figure legend, the reader is referred to the web version of this article.)

$$\int_V \varepsilon_{ij}(v) E_{ijpq} \varepsilon_{pq}(\Gamma) \mathrm{d}V = \int_V \varepsilon_{ij}(v) E_{ijpq} \alpha_{pq} \mathrm{d}V \quad \forall v \in V \tag{20}$$

Continuing from the three material extension, the homogenization function needs to be extended with an input vector (`alpha`) specifying the thermal expansion coefficient of the three materials. Furthermore, after line 43 a line assigning the corresponding element thermal expansion coefficients must be added:

```
alpha = alpha(1)*(x==1) + alpha(2)*(x==2) + alpha(3)*
   (x==3);
```

In order to compute the macroscopic thermal expansion using homogenization it is necessary to find the displacement vector $\boldsymbol{\Gamma}$ corresponding to a unit thermal strain load case:

$$\mathbf{K}\boldsymbol{\Gamma} = \mathbf{f}_{\alpha} \tag{21}$$

with the unit thermal load defined as:

$$\mathbf{f}_{\alpha} = \sum_e \int_{V_e} \mathbf{B}_e^T \mathbf{C}_e \boldsymbol{\alpha}_e \mathrm{d}V_e \tag{22}$$

where $\boldsymbol{\alpha}_e$ is the unit thermal strain corresponding to a unit increase in the temperature field. Therefore, `elementMatVec` must be extended with the computation of this element load vector. This is done by initializing an additional load vector below line 94:

```
feAlpha = zeros(8,1);
```

and adding the computation of it below line 123:

```
feAlpha = feAlpha + weight*(B.'*CMu*[1;1;0]);
```

And remember to return the element load vector from the function. It is clear that the load vector's two parts, corresponding to μ_e and λ_e, are equal and that is why only the first part is computed.

The load assembly must also be modified. Lines 51–53 are substituted with:

```
sF = [sF;feAlpha(:)*(alpha(:).*(lambda(:)+mu(:))).'];
iF = repmat(edofMat',4,1);
jF = [ones(8,nel); 2*ones(8,nel);
    3*ones(8,nel); 4*ones(8,nel)];
F = sparse(iF(:), jF(:), sF(:), ndof, 4);
```

This means that when the system is solved, the fourth displacement vector is $\boldsymbol{\Gamma}$. For sake of clarity assign this vector to its own variable by adding after line 54:

```
gamma = chi(:,4);
```

The element displacements $\boldsymbol{\Gamma}_e^0$ corresponding to the unit thermal strains must also be computed. This is done by changing the number of columns in line 59 from three to four, and adding:

```
fe = [fe 2*feAlpha];
```

below line 61, where one should remember that `feAlpha` only contains one part of the thermal strain to understand the multiplication with two. Now, $\boldsymbol{\Gamma}_e^0$ can be computed by adding after line 62:

```
gamma0 = alpha(:)*chi0_e(:,4)';
```

The entries in the homogenized thermal stress vector $\boldsymbol{\beta}$ can be found as:

$$\beta_i^H = \frac{1}{|V|}\sum_e \int_{V_e} (\boldsymbol{\Gamma}_e^0 - \boldsymbol{\Gamma}_e)^T \mathbf{k}_e (\boldsymbol{\chi}_e^{0(i)} - \boldsymbol{\chi}_e^i) \mathrm{d}V_e \tag{23}$$

This is done in the code snippet below, which can be added in the outer for-loop starting on line 71.

```
sumLambda = ((gamma0(:,:)-gamma(edofMat))*...
    keLambda).*(chi0(:,:,i)-chi(edofMat+(i-1)*ndof));
sumMu = ((gamma0(:,:)-gamma(edofMat))*keMu).*...
    (chi0(:,:,i)-chi(edofMat+(i-1)*ndof));
sumLambda = reshape(sum(sumLambda,2), nely, nelx);
sumMu = reshape(sum(sumMu,2), nely, nelx);
beta(i) = 1/cellVolume*sum(sum(lambda.*sumLambda+...
   mu. *sumMu));
```

Finally, the homogenized thermal strain vector is given as the solution to:

$$\mathbf{C}^H \boldsymbol{\alpha}^H = \boldsymbol{\beta}^H \tag{24}$$

which is solved as C^H/β in the Matlab code.

With the above extensions the thermal expansion coefficient of the composite in Fig. 6 is computed to be $-4.3\alpha_2$, which fits well with the reported $-4.2\alpha_2$ in [15]. The small discrepancy can be explained by the fact that [15] used a continuous interpolation between the three materials, while we have thresholded to get an indicator matrix with discrete entries. Furthermore, the discretization used here is based on a compressed image, and not the mesh used in [15].

4. Fluid permeability

The base program can also be extended such that the fluid permeability of a porous structure, having one solid and one fluid phase, can be computed. The permeability can be used in macroscopic porous flow simulations of slowly moving incompressible fluids using Darcy's law. Examples of materials where the permeability influences the design are discussed in e.g. [16,17].

Stokes flow is modeled within the fluid domain while the solid, no flow domain, is enforced using Brinkman penalization. The penalization parameter, ζ, is zero in the fluid domain while it takes a large value e.g. $\zeta = 10^6$ in the solid domain. Elaborating on the existing implementation a pressure degree of freedom is added to every node. In order to avoid pressure oscillations due to the even ordered elements a pressure stabilization method is applied [18]. The permeability can be computed as the volume average of the fluid velocity for Stokes flow with a prescribed unit pressure gradient. The weak form including Brinkman penalization and stabilization reads:

$$\int_V v_{i,j} u_{i,j}^k dV + \int_V v_{i,i} p dV + \int_V \zeta v_i u_i^k dV = \int_V v_i \delta_{ik} dV \quad \forall v \in V_0 \tag{25}$$

$$\int_V q u_{i,i}^k dV - \int_V \tau q_{,i} p_{,i} dV = 0 \quad \forall q \in Q \tag{26}$$

where $\tau = \frac{h^2}{12}$ is the pressure stabilization coefficient with h being the longest diagonal of the element, u is the velocity field, p is the pressure and v and q are virtual velocity and pressure fields, respectively. From the velocity field the permeability can be computed as:

$$\kappa_{ik} = \frac{l^2}{|V|}\int_V u_i^k \mathrm{d}V \tag{27}$$

where l is the characteristic length of the unit cell as the permeability, opposed to the effective stiffness, is size dependent.

The equation system is slightly more complicated for flow problems and more element matrices are needed. Therefore line 17 needs to be changed to:

```
[ke, ke_brink,be,pe,le] = ...
    elementMatVec(dx/2, dy/2,phi);
```

in order to obtain the additional Brinkman (`ke_brink`), coupling (`be`), stabilization (`pe`), and load (`le`) terms. The extra element matrices also need to be implemented yielding the following changes in the `elementMatVec` function, where first the function header needs to be adjusted accordingly:

```
function [ke, ke_brink, be, pe, le] = elementMatVec (a,b,phi)
```

Extra element matrices must be initialized along with the stabilization parameter. Therefore, lines 93 and 94 should be substituted with:

```
ke = zeros(8); ke_brink = zeros(8);
be = zeros(8,4); pe = zeros(4);
le = zeros(4,1);
h2 = 4*(a^2+b^2+2*a*b*abs(cos(phi)/sin(phi)));
stab = h2/12;
```

As the pressure coupling utilize the shape functions, these are included by adding the shape function matrix `N` after line 99:

```
N = 1/4*[(1-y)*(1-x) 0 (1-y)*(1+x) 0 ...
    (1+y)*(1+x) 0 (1-x)*(1+y) 0;
    0 (1-y)*(1-x) 0 (1-y)*(1+x) ...
    0 (1+y)*(1+x) 0 (1-x)*(1+y)] ;
```

The pressure gradient matrix is computed by inserting:

```
Bp = invJ*[dNx;dNy;];
```

after line 107, while the additional element matrices and vectors can be obtained by substituting the lines 119–123 with:

```
ke = ke + weight*(B'*CMu*B);
ke_brink = ke_brink + weight*(N'*N);
be = be + weight*(B'*[1 1 0]'*N(1:4:end));
pe = pe + weight*(Bp'*Bp*stab);
le = le + weight*(N(1,1:2:end)');
```

In the main program an extra degree of freedom, assigned to the pressure, is added in every node by after line 21 to introduce the lines:

```
edofVecp = 2*(nelx+1)*(nely+1) + ...
    reshape(1*nodenrs(1:end-1,1:end-1)+1,nel,1);
edofMatp = repmat(edofVecp,1,4) + ...
    repmat([0 nely+[1 0] -1],nel,1);
```

In line 36 the total number of dofs needs to be updated (`ndof = 3*nnP;`). The dof-vector also needs an extension in order to accommodate the pressure by adding these two lines after line 35:

```
dofVector(2*nn+1:3*nn) = 2*nnP+nnPArray(:);
edofMatp= dofVector(edofMatp);
```

The design dependence and the assembly of the system matrix is altered. Due to the pressure coupling it is now a saddle-point system assembled as:

```
%% ASSEMBLE STIFFNESS MATRIX
zeta = zeta(1)*(x==1) + zeta(2)*(x==2);
K = repmat(ke(:),1,nel)+ke_brink(:)*zeta(:).';
B = repmat(be(:),nel,1);
P = repmat(pe(:),nel,1);
iK = kron(edofMat,ones(8,1))';
iB = iK(:,1:2:end);
iP = kron(edofMatp,ones(4,1))';
jK = kron(edofMat,ones(1,8))';
jB = kron(edofMatp,ones(1,8))';
jP = jB(1:2:end,:);
sA = [K(:); B; B; -P];
iA = [iK(:); iB(:); jB(:); iP(:)];
jA = [jK(:); jB(:); iB(:); jP(:)];
A = sparse(iA,jA,sA);
```

while the load vectors can be assembled by changing lines 49–52 to:

```
iF = [reshape(edofMat(:,1:2:end)',4*nel,1)' ...
   reshape(edofMat(:,2:2:end)',4*nel,1)']';
jF = [ones(4*nel,1); 2*ones(4*nel,1)];
sF = repmat(le(:),2*nel,1);
F = sparse(iF,jF,sF,3*nnP,2);
```

The system is solved constraining a single pressure degree of freedom:

```
chi = zeros(ndof,2);
solfor = 1:ndof-1; % all except last pressure dof
chi(solfor,:) = A(solfor,solfor)\F(solfor,:);
```

The homogenization is, compared to the elastic case, much simpler and reads:

```
CH = zeros(2);
CH(1,1) = sum(chi(dofVector(1:2:2*nn),1));
CH(1,2) = sum(chi(dofVector(2:2:2*nn),1));
CH(2,1) = sum(chi(dofVector(1:2:2*nn),2));
CH(2,2) = sum(chi(dofVector(2:2:2*nn),2));
CH = CH/nel;
```

Finally, substitute the two input arguments `lambda` and `mu` with `zeta`, in which the material permeabilities of the two materials are specified. Solving for the material in Fig. 1 assuming white is fluid ($\zeta = 0$) and black is impermeable material ($\zeta = 10^6$) yields the isotropic permeability $\kappa^H = 0.0207$. This compares well to $\kappa = r^2/(8c)\ (-\ln(c) - 1.476 + 2c - 1.774c^2) = 0.0209$, which is the analytical permeability prediction by [19], where r is inclusion radius and c is solid volume fraction.

5. Other extensions

Other, more involved extensions, could be multiphysics (see e.g. [20]) or optimization of the material distribution using e.g. topology optimization as first described in [21].

Extending the code's applicability to a three-dimensional unit cell is straight-forward, but imply that the computations can become very time-consuming on a personal computer. Therefore, numerical homogenization of a three-dimensional, continuum, unit cell should preferable be done in parallel using an iterative solver, such as a multigrid PCG, to solve the linear system of equations.

6. Conclusion

The Matlab implementation provided here is simple and efficient; it can quickly compute the macroscopic properties of a 2D composite material where the unit cell is finely discretized. However, if the considered unit cell is three-dimensional, a parallel implementation in e.g. Fortran or C++ is better suited. But the same principles still apply, especially the implementation of the periodic boundary conditions should be analogous, since a penalty approach or Lagrange multipliers will increase the solution time considerably. Finally, we want to mention that a 3D unit cell consisting of discrete elements, such as beam elements, can be computationally much cheaper than a continuum unit cell.

Acknowledgement

This work was funded by the Danish Research Agency through the innovation consortium F · MAT.

Appendix A. Matlab code

The code can be downloaded from http://dx.doi.org/10.1016/j.commatsci.2013.09.006.

```
1  function CH = homogenize(lx, ly, lambda, mu, phi, x)
2  %%%%%%%%%%%%%%%%%%%%%%%%%%%%%%%%%%%%%%%%%%%%%%%%%%%%%%%%%%%%%%%%%%%%%%%%%%%%%%%%
3  % lx = Unit cell length in x-direction.
4  % ly = Unit cell length in y-direction.
5  % lambda = Lame's first parameter for both materials. Two entries.
6  % mu = Lame's second parameter for both materials. Two entries.
7  % phi = Angle between horizontal and vertical cell wall. Degrees
8  % x = Material indicator matrix. Size used to determine nelx/nely
9  %%%%%%%%%%%%%%%%%%%%%%%%%%%%%%%%%%%%%%%%%%%%%%%%%%%%%%%%%%%%%%%%%%%%%%%%%%%%%%%%
10 %% INITIALIZE
11 % Deduce discretization
12 [nely, nelx] = size(x);
13 % Stiffness matrix consists of two parts, one belonging to lambda and
14 % one belonging to mu. Same goes for load vector
15 dx = lx/nelx; dy = ly/nely;
16 nel = nelx*nely;
17 [keLambda, keMu, feLambda, feMu] = elementMatVec(dx/2, dy/2, phi);
18 % Node numbers and element degrees of freedom for full (not periodic) mesh
19 nodenrs = reshape(1:(1+nelx)*(1+nely),1+nely,1+nelx);
20 edofVec = reshape(2*nodenrs(1:end-1,1:end-1)+1,nel,1);
21 edofMat = repmat(edofVec,1,8)+repmat([0 1 2*nely+[2 3 0 1] -2 -1],nel,1);
22 %% IMPOSE PERIODIC BOUNDARY CONDITIONS
23 % Use original edofMat to index into list with the periodic dofs
```

```
nn = (nelx+1)*(nely+1); % Total number of nodes
nnP = (nelx)*(nely); % Total number of unique nodes
nnPArray = reshape(1:nnP, nely, nelx);
% Extend with a mirror of the top border
nnPArray(end+1,:) = nnPArray(1,:);
% Extend with a mirror of the left border
nnPArray(:,end+1) = nnPArray(:,1);
% Make a vector into which we can index using edofMat:
dofVector = zeros(2*nn, 1);
dofVector(1:2:end) = 2*nnPArray(:)-1;
dofVector(2:2:end) = 2*nnPArray(:);
edofMat = dofVector(edofMat);
ndof = 2*nnP; % Number of dofs
%% ASSEMBLE STIFFNESS MATRIX
% Indexing vectors
iK = kron(edofMat,ones(8,1))';
jK = kron(edofMat,ones(1,8))';
% Material properties in the different elements
lambda = lambda(1)*(x==1) + lambda(2)*(x==2);
mu = mu(1)*(x==1) + mu(2)*(x==2);
% The corresponding stiffness matrix entries
sK = keLambda(:)*lambda(:).' + keMu(:)*mu(:).';
K = sparse(iK(:), jK(:), sK(:), ndof, ndof);
%% LOAD VECTORS AND SOLUTION
% Assembly three load cases corresponding to the three strain cases
sF = feLambda(:)*lambda(:).'+feMu(:)*mu(:).';
iF = repmat(edofMat',3,1);
jF = [ones(8,nel); 2*ones(8,nel); 3*ones(8,nel)];
F = sparse(iF(:), jF(:), sF(:), ndof, 3);
% Solve (remember to constrain one node)
chi(3:ndof,:) = K(3:ndof,3:ndof)\F(3:ndof,:);
%% HOMOGENIZATION
% The displacement vectors corresponding to the unit strain cases
chi0 = zeros(nel, 8, 3);
% The element displacements for the three unit strains
chi0_e = zeros(8, 3);
ke = keMu + keLambda; % Here the exact ratio does not matter, because
fe = feMu + feLambda; % it is reflected in the load vector
chi0_e([3 5:end],:) = ke([3 5:end],[3 5:end])\fe([3 5:end],:);
% epsilon0_11 = (1, 0, 0)
chi0(:,:,1) = kron(chi0_e(:,1)', ones(nel,1));
% epsilon0_22 = (0, 1, 0)
chi0(:,:,2) = kron(chi0_e(:,2)', ones(nel,1));
% epsilon0_12 = (0, 0, 1)
chi0(:,:,3) = kron(chi0_e(:,3)', ones(nel,1));
CH = zeros(3);
cellVolume = lx*ly;
for i = 1:3
  for j = 1:3
    sumLambda = ((chi0(:,:,i) - chi(edofMat+(i-1)*ndof))*keLambda).*...
      (chi0(:,:,j) - chi(edofMat+(j-1)*ndof));
    sumMu = ((chi0(:,:,i) - chi(edofMat+(i-1)*ndof))*keMu).*...
      (chi0(:,:,j) - chi(edofMat+(j-1)*ndof));
    sumLambda = reshape(sum(sumLambda,2), nely, nelx);
    sumMu = reshape(sum(sumMu,2), nely, nelx);
    % Homogenized elasticity tensor
    CH(i,j) = 1/cellVolume*sum(sum(lambda.*sumLambda + mu.*sumMu));
  end
end
disp('--- Homogenized elasticity tensor ---'); disp(CH)

%% COMPUTE ELEMENT STIFFNESS MATRIX AND FORCE VECTOR (NUMERICALLY)
function [keLambda, keMu, feLambda, feMu] = elementMatVec(a, b, phi)
% Constitutive matrix contributions
CMu = diag([2 2 1]); CLambda = zeros(3); CLambda(1:2,1:2) = 1;
% Two Gauss points in both directions
xx=[-1/sqrt(3), 1/sqrt(3)]; yy = xx;
ww=[1,1];
% Initialize
keLambda = zeros(8,8); keMu = zeros(8,8);
feLambda = zeros(8,3); feMu = zeros(8,3);
L = zeros(3,4); L(1,1) = 1; L(2,4) = 1; L(3,2:3) = 1;
for ii=1:length(xx)
  for jj=1:length(yy)
    % Integration point
    x = xx(ii); y = yy(jj);
    % Differentiated shape functions
    dNx = 1/4*[-(1-y) (1-y) (1+y) -(1+y)];
    dNy = 1/4*[-(1-x) -(1+x) (1+x) (1-x)];
    % Jacobian
    J = [dNx; dNy]*[-a a a+2*b/tan(phi*pi/180) 2*b/tan(phi*pi/180)-a; ...
        -b -b b b]';
    detJ = J(1,1)*J(2,2) - J(1,2)*J(2,1);
    invJ = 1/detJ*[J(2,2) -J(1,2); -J(2,1) J(1,1)];
    % Weight factor at this point
    weight = ww(ii)*ww(jj)*detJ;
    % Strain-displacement matrix
    G = [invJ zeros(2); zeros(2) invJ];
    dN = zeros(4,8);
    dN(1,1:2:8) = dNx;
    dN(2,1:2:8) = dNy;
    dN(3,2:2:8) = dNx;
    dN(4,2:2:8) = dNy;
    B = L*G*dN;
    % Element matrices
    keLambda = keLambda + weight*(B' * CLambda * B);
    keMu = keMu + weight*(B' * CMu * B);
    % Element loads
    feLambda = feLambda + weight*(B' * CLambda * diag([1 1 1]));
    feMu = feMu + weight*(B' * CMu * diag([1 1 1]));
  end
end
```

References

[1] S.J. Hollister, Nat. Mater. 4 (2005) 518–524.
[2] J.M. Kemppainen, S.J. Hollister, J. Biomed. Mater. Res. Part A 94 (2010) 9–18.
[3] M. Dias, P. Fernandes, J. Guedes, S. Hollister, J. Biomech. 45 (2012) 938–944.
[4] A. Bensoussan, J.L. Lions, G. Papanicolaou, Asymptotic Analysis for Periodic Structures, North-Holland, 1978.
[5] E. Sanchez-Palencia, Lecture Notes in Physics, vol. 127, Springer-Verlag, 1980.
[6] S. Torquato, Random Heterogeneous Materials/Microstructure and Macroscopic Properties, Springer, New York,NY, 2002.
[7] J. Guedes, N. Kikuchi, Comput. Methods Appl. Mech. Eng. 83 (1990) 143–198.
[8] B. Hassani, E. Hinton, Comput. Struct. 69 (1998) 707–717.
[9] B. Hassani, E. Hinton, Comput. Struct. 69 (1998) 719–738.
[10] B. Hassani, E. Hinton, Comput. Struct. 69 (1998) 739–756.
[11] A.R. Diaz, A. Bernard, Int. J. Numer. Methods Eng. 57 (2003) 301–314.
[12] R.D. Cook, D.S. Malkus, M.E. Plesha, R.J. Witt, Concepts and Applications of Finite Element Analysis, fourth ed., John Wiley and Sons, 2002.
[13] E. Andreassen, A. Clausen, M. Schevenels, B.S. Lazarov, O. Sigmund, Struct. Multidisc. Optim. 43 (2011) 1–16.
[14] W.T. Perrins, D.R. McKenzie, R.C. McPhedran, Proc. Roy. Soc. Lond. A: Math. Phys. Sci. 369 (1979) 207–225.
[15] O. Sigmund, S. Torquato, J. Mech. Phys. Solids 45 (1997) 1037–1067.
[16] J.K. Guest, J.H. Prévost, Int. J. Solids Struct. 43 (2006) 7028–7047.
[17] C.S. Andreasen, O. Sigmund, Struct. Multidisc. Optim. 43 (2011) 693–706.
[18] T.J.R. Hughes, L.P. Franca, Comput. Methods Appl. Mech. Eng. 65 (1987) 85–96.
[19] J. Drummond, M. Tahir, Int. J. Multiphase Flow 10 (1984) 515–540.
[20] Q. Yu, J. Fish, Int. J. Solids Struct. 39 (2002) 6429–6452.
[21] O. Sigmund, Int. J. Solids Struct. 31 (1994) 2313–2329.

Publication [P2]

Topology optimization using PETSc: An easy-to-use, fully parallel, open source topology optimization framework

myjournal manuscript No.
(will be inserted by the editor)

Topology optimization using PETSc:

An easy-to-use, fully parallel, open source topology optimization framework

Niels Aage · Erik Andreassen · Boyan Stefanov Lazarov

Received: date / Accepted: date

Abstract This paper presents a flexible framework for parallel and easy-to-implement topology optimization using the Portable and Extendable Toolkit for Scientific Computing (PETSc). The presented framework is based on a standardized, and freely available library and in the published form it solves the minimum compliance problem on structured grids, using standard FEM and filtering techniques. For completeness a parallel implementation of the Method of Moving Asymptotes is included as well. The capabilities are exemplified by minimum compliance and homogenization problems. In both cases the unprecedented fine discretization reveals new design features, providing novel insight. The code can be downloaded from `www.topopt.dtu.dk/PETSc`.

Keywords Topology optimization · parallel computing · PETSc · homogenization · large scale

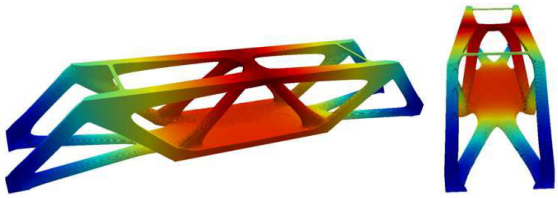

(a) (b)

Fig. 1 The classical MMB beam in 3D on a $6 \times 1 \times 1$ domain. The beam is loaded on the line at the center top of domain and have roller supports at the bottom left and right edges. The volume fraction is set to 12% and the filter radius for the PDE filter is 0.08. The problem is solved using symmetry on a mesh of $1008 \times 336 \times 336$ elements, i.e. a total of 113.8 million design elements and 343.8 million state dofs. The visualized design is thresholded at $\rho_{\text{Phys}} = 0.5$ and colored by the magnitude of the displacement field. The problem was terminated at a design change less than 0.01, which occured after 928 iterations. The problem was distributed on 1800 cores and took a total of 4 hours and 32 minutes to complete.

1 Introduction

The educational aim of this paper is to demonstrate how large scale topology optimization allows for optimization of three-dimensional problems with yet unseen fine discretizations, and to show how this leads to the discovery of new effects in otherwise well-studied design problems. Furthermore, the paper presents a flexible framework for parallel topology optimization, made freely available in order to facilitate the transit to large scale topology optimization for the interested reader. However, the paper is not intended to be a detailed introduction to parallel programming, instead we focus on showing some interesting examples and presenting the framework.

The utilization of parallel processing in scientific computing is constantly increasing, and has also made an impact on the topology optimization community. Within the past decade several works have been published on the subject, see e.g. (Borrvall and Petersson, 2001), (Kim et al, 2004), (Vemaganti and Lawrence, 2005), (Mahdavi et al, 2006), (Aage et al, 2008), (Evgrafov et al, 2008), (Wadbro and Berggren, 2009), (Schmidt and Schulz, 2011), (Challis et al, 2013) and (Aage and Lazarov, 2013). Though many of these works provide schematics on how the parallelization is realized and/or platform specific code, no one provides an easy to use and portable code. In this work we provide such a framework based on the freely available library for high

The authors acknowledge the support from the Villum foundation through the NextTop project and the Danish Research Agency through the innovation consortium F•MAT. Fruitful discussions with members of the DTU TopOpt-group are also gratefully acknowledged.

N. Aage · E. Andreassen · B.S. Lazarov
Department of Mechanical Engineering, Solid Mechanics,
Technical University of Denmark, Nils Koppels Alle, B.404,
DK-2800 Kgs. Lyngby, Denmark
E-mail: naage@mek.dtu.dk

performance and scientific computing PETSc (Balay et al, 2013). Using PETSc reduces the size of the actual implementation, and results in a compact code (compared to our existing in-house parallel optimization codes), which is easy to read, use and extend. Therefore, the presented framework is an ideal development platform for topology optimization problems.

PETSc is an acronym for the *Portable and Extendable Toolkit for Scientific Computing* and it forms the basis for the presented parallel topology optimization code. PETSc is a collection of parallelized (and sequential) libraries that contain most of the necessary building blocks needed for large scale topology optimization, i.e. sparse matrices, vectors, iterative linear solvers, non-linear solvers and time-stepping scheme. The package eliminates the need to write such low-level math libraries and thus speeds up development time by orders of magnitude. The main advantages of PETSc are as follows: a) The libraries are tested extensively and the code is well maintained by specialists. The implementation is parallel scalable to thousands of cores and portable to Linux, UNIX, Mac and Windows. b) The code is written in C in an object oriented manner, such that the base-code is easily extendable and hides the parallel complexity from the user. c) The library is extremely easy to install and use which, combined with the above highlights, makes PETSc well suited for both novices and experts within the field of parallel and scientific computing. The authors acknowledge that several other numerical libraries have similar functionality to PETSc, e.g. Trilinos (Heroux et al, 2005). However, PETSc is (one of) the simplest frameworks that provide the basic sparse linear algebra routines, while e.g. Trilinos is a larger and more complex framework, which makes it more difficult to customize. This, and fact that PETSc can interface most other relevant libraries, have made PETSc the obvious choice for the framework.

The framework presented in this work is made freely available and can be downloaded from `www.topopt.dtu.dk/PETSc`. The package contains the building blocks for conducting large scale, parallel topology optimization of the standard minimum compliance problem on structured grids (Bendsøe and Sigmund, 2004) based on the multigrid approach, similar to the one presented in Amir et al (2013). The code solves a minimum compliance cantilever problem for which an example can be seen in Fig. 1.

In the following sections we present the PETSc based topology optimziation framework along with guidelines for usage and extensions. Next we demonstrate the possibilities of the framework by solving two minimum compliance problems as well as two problems from homogenization (minimum Poisson ratio and maximum bulk modulus problems).

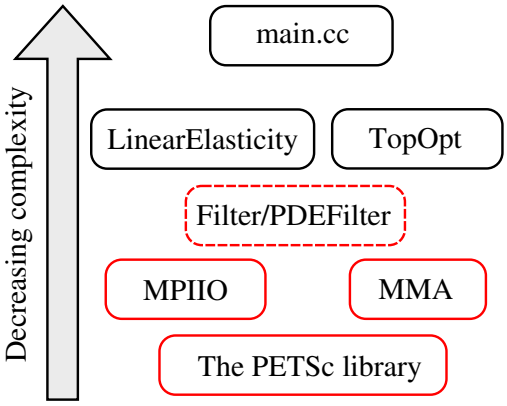

Fig. 2 Layout of the optimization framework. The names in the boxes refer to the main program and to the classes containing physics, optimization settings, filtering, output, MMA and the PETSc library. The box colors indicate whether or not a given class needs modification when changing the problem type, such that red indicates no need for modifications, dashed red that some minor modifications can be needed and black that modifications likely to be are needed. The arrow to the left indicates the complexity of the different components, i.e. the higher in the diagram the simpler the code.

2 Code layout, usage and extensions

The main motivation for the development of the proposed topology optimization framework is to have an easy-to-use and easy-to-extend basis for conducting large scale topology optimization of various physical problems. However, to ensure that the publicly available distribution is easily accessible to the topology optimization community, the default problem is a minimum compliance problem.

Basing the code on PETSc means that structured grid generation, partitioning, parallel assemblies, matrix-vector operations, linear and non-linear solvers are readily available. Thus, the focus can be put on the physics and the optimization, and not on the development of high performance linear algebra libraries. The PETSc library can be downloaded from `www.mcs.anl.gov/petsc` and compiled following the simple instructions on the website.

To provide an overview of the topology optimization framework, a diagram of the code components can be seen in Fig. 2. The foundation of the framework is the PETSc library, and from the diagram one can see that the code we provide consist of five C++ classes and a short main program. The diagram also indicates which classes that need to be modified in order to solve a different optimization problem, i.e.: black boxes mean that modifications are likely to be required and red boxes that no modifications should be applied. The dashed red box indicates that modifications might be necessary, depending on the application. Finally, the code complexity is indicated by the large arrow to the left which points in the direction of less complex code.

2.1 Class structure

Since the goal is to obtain a versatile framework, the classes are divided into clearly separated units. This means for example, that changing the physics only requires modifications of a single class, i.e. the physics class which in the default case solves a linear elasticity problem. A list of the classes with description is given below

- `TopOpt` Contains information on the optimization problem, gridsize, parameters and general settings.
- `LinearElasticity` The physics class which solves the linear elasticity problem on a structured 3D grid using 8-node linear brick elements, see e.g. Zienkiewicz and Taylor (2000). It also contains methods necessary for the minimum compliance problem, i.e. objective, constraint and sensitivity calculations (Bendsøe and Sigmund, 2004). The default linear solver is a Galerkin projection multigrid preconditioned flexible GMRES with GMRES/SOR smoothing, which follows the implementation presented in Amir et al (2013), except for the choice of Krylov method and smoother. An example on how to change the solver is given in the upcoming section.
- `Filter/PDEFilter` are filter classes which contains both sensitivity (Sigmund, 1997), density (Bruns and Tortorelli, 2001; Bourdin, 2001) and PDE (Lazarov and Sigmund, 2011) filters through a common interface.
- `MMA` Class containing a fully parallelized implementation of the Method of Moving Asymptotes (MMA) (Svanberg, 1987) following the description given in Aage and Lazarov (2013).
- `MPIIO` A versatile output class capable of dumping arbitrary field data into a single binary file.

The distribution also includes Python scripts that conveniently converts the binary outputdata to the VTU format (Schroeder et al, 2003) that can be visualized in e.g. ParaView version 4 or newer (Ahrens et al, 2005).

2.2 Compiling and running the code

Assuming that PETSc is already installed (see `www.mcs.anl.gov/petsc`) the user is only required to perform the following six steps to get started on a 64-bit Linux platform [1]. Note that visualization of the results requires Python for postprocessing and ParaView for the actual visualization.

1. Download and extract the code from `www.topopt.dtu.dk/PETSc`.
2. Modify the `makefile` such that `PETSC_DIR` and `PETSC_ARCH` points to the local PETSc installation on your system.
3. Type `make topopt` in a terminal to compile the code.
4. Type `mpiexec -np 2 ./topopt` to run the code on two processors using the default settings. The optimization and solver settings along with optimization history will be written to the terminal.
5. Prepare the outputdata for ParaView by typing `python bin2vtu #`, where # is the desired timestep. Note that the default settings saves data the first 10 iterations and then subsequently every 10th iteration in order to save space.
6. Visualize in ParaView by typing `paraview *.vtu`.

The default problem is the minimum compliance cantilever problem as described in Aage and Lazarov (2013) on a $2 \times 1 \times 1$ domain using sensitivity filter with radius 0.08 and a volume fraction of 0.12 percent. The contrast between solid and void is set to 10^9, the convergence criteria is $||x_k - x_{k-1}||_\infty < 0.01$ or a maximum of 400 design cycles. Results based on the default settings can be seen on the download page.

2.3 Run time options

The flexibility of the framework allows the user to change a number of settings and parameters at run time. The optimization specific options that can be changed at run time are written to screen before the optimization begins, whereas the PETSc specific options, e.g. linear solver, can be found in the PETSc manual. For example changing the filter to PDE filtering with a radius of 0.2, a volume fraction of 0.3 and a total of 200 iterations is done in the following command

```
mpiexec -np 2 ./topopt -filter 2 -rmin 0.2 \
       -volfrac 0.3 -maxItr 200
```

Due to the flexible construction of PETSc it is possible to change, monitor and test a vast variety of different solver combinations simply by changing the run command. For example, changing the linear solver from the default to a Jacobi preconditioned conjugate gradient method can be obtained as follows

```
mpiexec -np 2 ./topopt -ksp_type cg \
       -ksp_max_it 10000 -pc_type jacobi
```

However, using such a simple solver would result in increased CPU time, especially for large problems.

2.4 Extension

The list of possible extension that can be achieved, using the presented framework as a platform, covers everything from linear to non-linear mechanics, fluid mechanics, acoustics, electromagnetics and generalized multiphysics problems. Describing all aspects of such extensions is outside

[1] For other operating systems please follow the guidelines on `www.mcs.anl.gov/petsc`. After PETSc is installed, the compilation of the TopOpt application is done similar to that described in section 2.2.

the scope of this paper, and we will therefore limit this section to discuss how to change the boundary conditions for the minimum compliance problem and give a few general guidelines for switching to a new physical setting.

To solve the minimum compliance problem with different loading and support conditions, changes should only be made to a single method in the physics class, i.e. the `SetUpLoadandBC()` method in `LinearElasticity.h/cc`. This method simply sets the boundary conditions based on coordinates and modifications are therefore straightforward.

The modular composition of the optimization framework means that changing the physics to e.g. fluids, homogenization, etc, only requires that a single new class is written. The coding complexity is further minimized since much of the provided linear elasticity solver can be reused or at least provide inspiration for the new physical problem. To demonstrate the versatility of the framework we also show results from homogenization problems in the example section.

3 Examples

In the following sections the capabilities of the framework is presented by solving different minimum compliance problems as well as material design problems for maximum bulk modulus and minimum Poison's ratio. Unless otherwise stated, all examples are run on a cluster with a total of 21 nodes, each equipped with two Intel Xeon 5650 6-core CPUs and 48GB memory connected by Infiniband. All problems are solved using the afore mentioned Galerkin projection geometric multigrid preconditioned flexible-GMRES. If not otherwise stated we use four multigrid levels, four GMRES/SOR smoothing steps per level and a relative convergence tolerance of 10^{-5}. The coarse level problem is solved with GMRES/SOR to 10^{-8} or a maximum of 30 iterations. Due to the effectiveness of the multigrid preconditioning strategy, the F-GMRES is never restarted, i.e. for the presented examples all linear solves are obtained with much less than the allowed 200 F-GMRES iterations.

3.1 Minimum compliance

The first example is a re-run of the cantilever problem presented in (Aage and Lazarov, 2013). In this work we discretize the $2\times1\times1$ cantilever by $480\times240\times240$ elements, i.e. 27.6 million design elements and 83.8 million state dofs. The problem is then solved for various filter radii, i.e. from $r_{\min}=0.01$ to 0.1, with a solid/void contrast of 10^9. The design problems have been run for 1000 design iterations on 24 CPUs (144 cores) yielding an average iteration time varying from 60s to 30s for the smallest and largest filter radius, respectively. The relationship between lengthscale and solution time (i.e. number of iterations for GMRES) is expected for the chosen multigrid preconditioner, since smaller lengthscales are harder to represent on the coarse grids. The optimized designs can be seen in Fig. 3. It is especially interesting to note that the high design resolution and small filter radius, leads to a design where the beams contain internal holes.

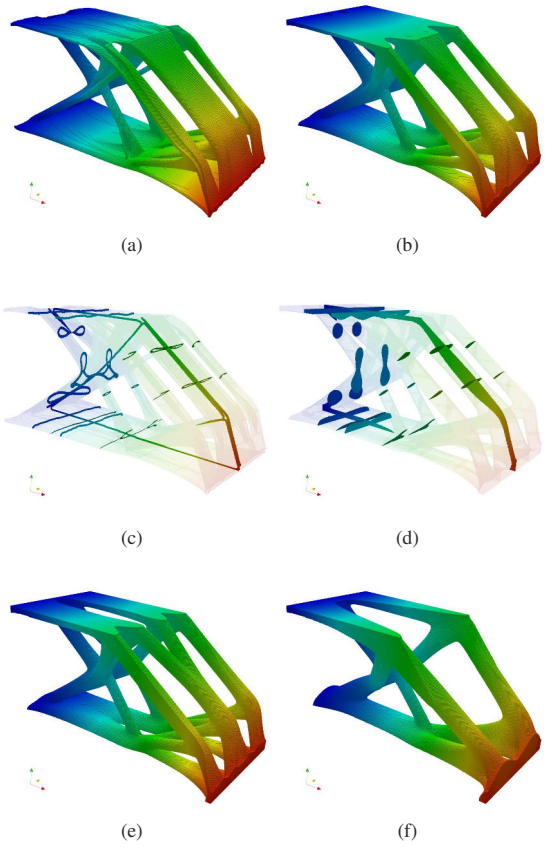

Fig. 3 Optimized cantilever beams on a $2\times1\times1$ domain allowing 12% material discretized by 27.6 million elements. The design problems differ through the filter radius such that $r_{\min}=0.01$ for (a,c), $r_{\min}=0.03$ for (b,d), $r_{\min}=0.04$ for (e) and $r_{\min}=0.10$ for (f). Plot (c) and (d) shows cross sections of the designs with $r_{\min}=0.01$ and 0.03, and illustrates the internal holes generated for the smaller filter radius. All the designs are thresholded at $\rho_{\text{Phys}}=0.5$ and colored by the magnitude of the displacement field.

The second minimum compliance example is the design of a roof support for the Qatar Convention center as described in (Sasaki, 2007). The design domain consists of a rectangular domain of size $125\times15\times20$ which, using symmetry conditions, corresponds to half of the design seen in Fig. 4(b). The domain is discretized using $512\times64\times86=$ 3.1 million elements and the problem is solved using 12 CPUs (72 cores). Finally, a volume fraction of 12% and a

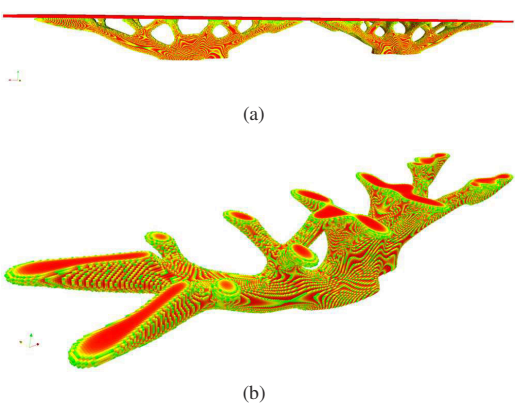

Fig. 4 Minimum compliance design of a roof support, c.f. the Qatar Convention center (Sasaki, 2007). The plot in (a) shows the full optimized roof structure, while plot (b) shows a single of the two support structures. The design domain is due to symmetry reduced to one quarter of the domain seen in (a) or half of (b). The computational mesh consists of 3.1 million elements. Both plots are thresholded at $\rho_{\text{Phys}} = 0.5$ and colored by the density field.

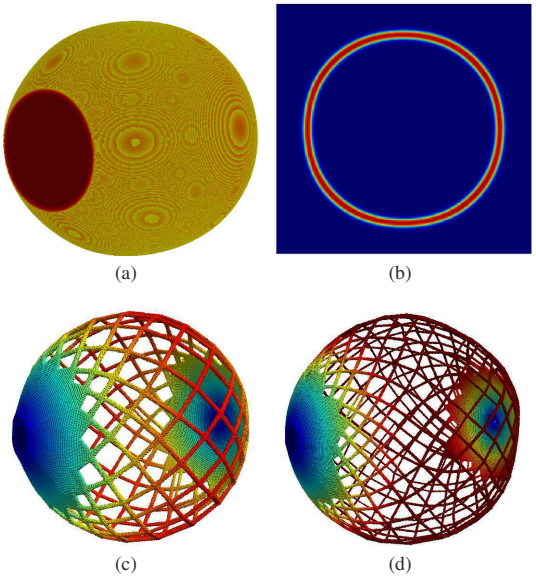

Fig. 5 Optimized designs for a $1 \times 1.2 \times 1.2$ box subjected to pure torsion. Figures (a) and (b) shows the design, and a slice thereof, for a volume fraction of 10% and a filter radius of 0.025 when using an uniform initial guess. For the designs in (c) and (d) the initial guess is a hollow sphere, optimized for a volume fraction of 1% and a filter radius of 0.003 and a volume fraction of 0.5% and a filter radius of 0.001, respectively. Designs (a-c) are obtained using a mesh of 26.1 million elements distributed on 1000 cores while the design in (d) was run on a mesh of 82.1 million elements on 2000 cores.

filter radius of $r_{\text{min}} = 3.0$ is used to obtain the design shown in Fig. 4. The design of the roof support requires two extensions to the default code: First a passive solid domain of size $125 \times 15 \times 1$, i.e. the roof, is introduced and secondly a Heaviside projection continuation method (Guest et al, 2004) is necessary due to the large filter radius used for the PDE filter.

The third and final minimum compliance example concerns pure torsion of a $1 \times 1.2 \times 1.2$ box. The design problem is inspired by the work of Lewinski (2004) and thus by classical Michell truss layout (Michell, 1904). The model is loaded by a moment, i.e. four point forces on one side and clamped on an equivalent area on the opposite surface. Optimized designs for varying filter radii and volume fractions can be seen in Fig. 5. Note that these examples are computed on a bigger cluster with 320 nodes, each with two ten Intel Xeon E5-2650 10-core CPUs. The design in Fig 5(d) was obtained using a mesh of 82.1 million elements distributed on 2000 cores, and the wall-clock time for 2000 design cycles was approximately 4.5 hours. The optimized designs show that for a sufficiently small volume fraction the optimal structure is no longer a closed sphere but a truss-like structure, similar to the result presented in (Lewinski, 2004).

These examples demonstrate how the presented framework can be used to gain new insight into ultra-lightweight structures - even for the otherwise thoroughly studied minimum compliance problem. An indepth examination of these possibilities are left for a subsequent paper.

3.2 Material design

To demonstrate the versatility of the presented framework, the physics is changed from static linear elasticity to elastic material design. With respect to code complexity, this implies that the `LinearElasticity` class is modified to handle periodic boundary conditions, while only minor modifications are needed for `TopOpt` and `Filter` classes. The implementation of the homogenization procedure follows the approach given in (Andreassen et al, 2014).

The first design problem is to optimize for isotropic minimum Poisson's ratio materials. The optimized design can be seen in Fig. 6. The Poisson's ratio of the optimized structure is -0.80 computed using a volume fraction of 0.08 and on a mesh of $200^3 = 8$ million elements. A lower bound on the bulk stiffness is assured by requiring the bulk modulus of material structure to be at least 1/4000 of the bulk modulus of the base material. This assures that no single node hinges appear in the design. For filtering the PDE version of the sensitivity filter has been used with an initial radius of 10%, decreased to a final radius of 2.5%. It is interesting to note that the high resolution leads to "line hinges", which is something that has not been clearly observed in other 3D topology optimization results because the resolu-

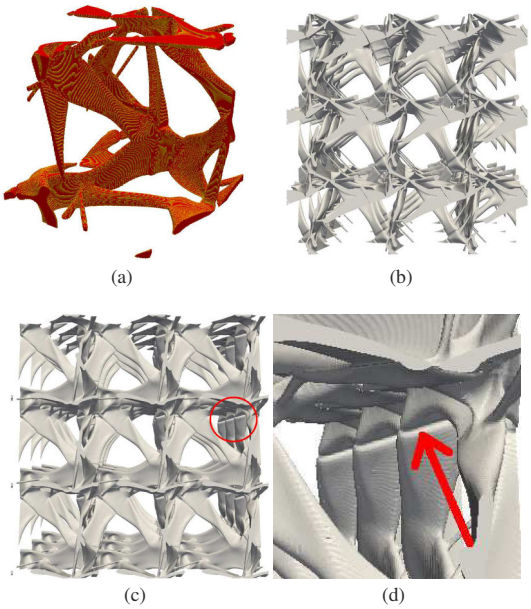

Fig. 6 Optimized 3D isotropic microstructure with a Poisson's ratio of -0.80. The unit cell is discretized by $200^3 = 8$ million elements and is shown in (a). The plots in (b-c) show $3 \times 3 \times 3$ unit cells from two different angles. The clearest occurence of a "line hinge" is marked by a red circle in (c) and a close up is shown in (d).

tion has been too coarse. A close up of a "line hinge" is shown in Fig. 6(d).

The second material design problem is the maximization of the bulk modulus. The optimized design can be seen in Fig. 7 run for a volume fraction of 30%. The resulting bulk modulus is within 99% of the optimal modulus for porous materials, i.e. the Hashin-Shtrikman bounds. The example is run with a discretization of $288^3 = 23.8$ million elements for which one iteration, i.e. solving six load cases, filtering and design update, takes approximately 60s on 40 CPUs (240 cores).

It should be emphasized that both design problems include an isotropy constraint (see e.g. Andreassen et al (2014)), and that the negative Poisson's ratio structure would be difficult to manufacture due to the small features.

4 Concluding remarks

A framework for large scale topology optimization on structured grids is presented and made publicly available at `www.topopt.dtu.dk/PETSc`. The framework is based on PETSc and forms an easy-to-use, fully parallelized and open source base for conducting large scale topology optimization. Included in the framework is a number of key building blocks

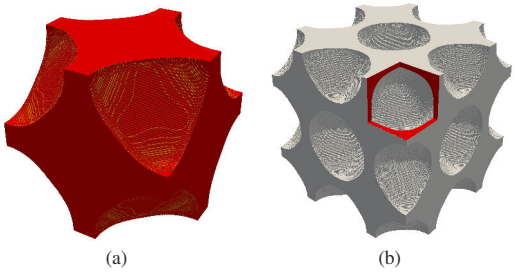

Fig. 7 Optimized maximum bulk modulus unit cell discretized with $288^3 = 23.8$ million elements (a) and $2 \times 2 \times 2$ unit cells (b). The isotropic and optimized unit cell has a bulk modulus within 99% of the Hashin-Shtrikman bounds for a volume fraction of 30%. The red surface in (b) indicate that a unit cell has been cut to illustrate that it is indeed hollow.

for structural optimization such as filters, a simple, parallelized MMA and input/output classes.

The validity and performance of the framework is demonstrated through a number of numerical examples covering both compliance and material design. It is shown that the framework can be used to solve optimization problems with more than 100 million design variables, and thus that the problem size is only bounded by the amount of computational resources available. The versatility of the framework is exemplified by extensions such as projection methods, passive domains and homogenization problems.

References

Aage N, Lazarov B (2013) Parallel framework for topology optimization using the method of moving asymptotes. Structural and Multidisciplinary Optimization 47(4):493–505, DOI 10.1007/s00158-012-0869-2

Aage N, Poulsen T, Gersborg-Hansen A, Sigmund O (2008) Topology optimization of large scale stokes flow problems. Structural and Multidisciplinary Optimization 35(2):175–180

Ahrens J, Geveci B, Law C (2005) ParaView: An End-User Tool for Large Data Visualization. Elsevier

Amir O, Aage N, Lazarov B (2013) On multigrid-cg for efficient topology optimization. Structural and Multidisciplinary Optimization pp 1–15, DOI 10.1007/s00158-013-1015-5

Andreassen E, Lazarov BS, Sigmund O (2014) Design of manufacturable 3d extremal elastic microstructure. Mechanics of Materials 69(1):1 – 10, DOI 10.1016/j.mechmat.2013.09.018

Balay S, Brown J, , Buschelman K, Eijkhout V, Gropp WD, Kaushik D, Knepley MG, McInnes LC, Smith BF, Zhang H (2013) PETSc users manual. Tech. Rep. ANL-95/11 - Revision 3.4, Argonne National Laboratory

Bendsøe M, Sigmund O (2004) Topology Optimization; Theory, Methods and Applications, 2nd edn. Springer Verlag Berlin Heidelberg New York

Borrvall T, Petersson J (2001) Large-scale topology optimization in 3d using parallel computing. Computer Methods in Applied Mechanics and Engineering 190(46-47):6201–6229

Bourdin B (2001) Filters in topology optimization. Int J Numer Meth Engng 50(9):2143–2158

Bruns TE, Tortorelli DA (2001) Topology optimization of non-linear elastic structures and compliant mechanisms. Computer Methods in Applied Mechanics and Engineering 190(26-27):3443–3459

Challis V, Roberts A, Grotowski J (2013) High resolution topology optimization using graphics processing units (GPUs). Structural and Multidisciplinary Optimization pp 1–11, DOI 10.1007/s00158-013-0980-z

Evgrafov A, Rupp CJ, Maute K, Dunn ML (2008) Large-scale parallel topology optimization using a dual-primal substructuring solver. Structural And Multidisciplinary Optimization 36(4):329–345

Guest JK, Prevost JH, Belytschko T (2004) Achieving minimum length scale in topology optimization using nodal design variables and projection functions. International Journal For Numerical Methods In Engineering 61(2):238–254

Heroux MA, Bartlett RA, Howle VE, Hoekstra RJ, Hu JJ, Kolda TG, Lehoucq RB, Long KR, Pawlowski RP, Phipps ET, Salinger AG, Thornquist HK, Tuminaro RS, Willenbring JM, Williams A, Stanley KS (2005) An overview of the trilinos project. ACM Trans Math Softw 31(3):397–423, DOI http://doi.acm.org/10.1145/1089014.1089021

Kim TS, Kim JE, Kim YY (2004) Parallelized structural topology optimization for eigenvalue problems. International Journal of Solids and Structures 41(9-10):2623–2641

Lazarov BS, Sigmund O (2011) Filters in topology optimization based on helmholtz-type differential equations. International Journal For Numerical Methods In Engineering

Lewinski T (2004) Michell structures formed on surfaces of revolution. Structural and Multidisciplinary Optimization 28(1):20–30, DOI 10.1007/s00158-004-0419-7

Mahdavi A, Balaji R, Frecker M, Mockensturm EM (2006) Topology optimization of 2D continua for minimum compliance using parallel computing. Structural And Multidisciplinary Optimization 32(2):121–132

Michell AGM (1904) The limits of economy of materials in frame structures. DOI 10.1080/14786440409463229

Sasaki M (2007) Morphogenesis of Flux Structure. Architectural Association Publications London

Schmidt S, Schulz V (2011) A 2589 line topology optimization code written for the graphics card. Computing and Visualization in Science 14(6):249–256, DOI 10.1007/s00791-012-0180-1

Schroeder W, Martin K, Lorensen B (2003) The Visualization Toolkit, Third Edition. Kitware Inc.

Sigmund O (1997) On the design of compliant mechanisms using topology optimization. Mechanics of Structures and Machines 25(4):493–525

Svanberg K (1987) The method of moving asymptotes - a new method for structural optimization. International Journal for Numerical Methods in Engineering 25

Vemaganti K, Lawrence WE (2005) Parallel methods for optimality criteria-based topology optimization. Computer Methods in Applied Mechanics and Engineering 194(34-35):3637–3667

Wadbro E, Berggren M (2009) Megapixel topology optimization on a graphics processing unit. SIAM Review 51(4):707–721

Zienkiewicz OC, Taylor RL (2000) Finite Element Method: Volume 1, 5th edn. Butterworth-Heinemann

Publication [P3]

Design of manufacturable 3D extremal elastic microstructure

Mechanics of Materials 69 (2014) 1–10

Contents lists available at ScienceDirect

Mechanics of Materials

journal homepage: www.elsevier.com/locate/mechmat

Design of manufacturable 3D extremal elastic microstructure

Erik Andreassen *, Boyan S. Lazarov, Ole Sigmund

Department of Mechanical Engineering, Technical University of Denmark, Nils Koppels Allé, Building 404, Denmark

ARTICLE INFO

Article history:
Received 22 October 2012
Received in revised form 12 June 2013
Available online 3 October 2013

Keywords:
Topology optimization
Auxetic material
Microstructure
Additive manufacturing
Inverse homogenization

ABSTRACT

We present a method to design manufacturable extremal elastic materials. Extremal materials can possess interesting properties such as a negative Poisson's ratio. The effective properties of the obtained microstructures are shown to be close to the theoretical limit given by mathematical bounds, and the deviations are due to the imposed manufacturing constraints. The designs are generated using topology optimization. Due to high resolution and the imposed robustness requirement they are manufacturable without any need for post-processing. This has been validated by the manufacturing of an isotropic material with a Poisson's ratio of $\nu = -0.5$ and a bulk modulus of 0.2% times the solid base material's bulk modulus.

1. Introduction

The focus of this paper is on the design of elastic three-dimensional materials with periodic microstructures manufacturable by additive manufacturing techniques like selective laser sintering (SLS) (see Kalpakjian et al., 2010, for a description of the technique). The microstructures are built from a single material with voids, and effective material properties are found by numerical homogenization (Guedes and Kikuchi, 1990). The designs are obtained using topology optimization without any post-processing by requiring their performance to be insensitive with respect to uniform variations of the geometry like erosion or dilation (over- or under-etching). The requirement for robustness leads to the definition of a minimum length scale in the topology (Wang et al., 2011), and therefore any imperfections with dimensions smaller than the defined length scale, which might appear due to uncertainties in the production process, do not significantly affect the effective material properties on macroscale.

The topology optimization method is an iterative design process, which optimizes a material distribution in a given design domain with respect to a specified objective function and a set of constraints. It is utilized in a broad range of problems varying from pure mechanical designs (e.g., aerospace structures (Krog et al., 2004)) to designs in electromagnetics and photonics (e.g., Jensen and Sigmund, 2011). A popular introduction to the method can be found in (Sigmund, 2000b), while a thorough description is given in (Bendsøe and Sigmund, 2003). Already in (Sigmund, 1994) it is shown that topology optimization can be used to design materials with a prescribed elasticity tensor by inverse homogenization. Several papers followed on the design of elastic materials (e.g., Swan and Kosaka, 1997; Theocaris and Stavroulakis, 1998) as well as (Sigmund, 2000a), where a new class of extremal composites were presented. Gibiansky and Sigmund (2000) demonstrate the method on the design of three-phase elastic materials, and Sigmund and Torquato (1999) extend this to obtain designs with prescribed thermal and electrothermal properties. Designs optimized for multiple properties, such as fluid permeability and stiffness are shown by Guest and Prévost (2006).

The application of topology optimization to design structural materials is an active field of research. Recent examples are given by Coelho et al. (2011), who demonstrate how a multi-scale formulation can be used to design a trabecular bone section, and Diaz and Sigmund (2010), who apply topology optimization to design a so-called

* Corresponding author. Tel.: +45 45254159.
E-mail address: erand@mek.dtu.dk (E. Andreassen).

0167-6636/$ - see front matter © 2013 Elsevier Ltd. All rights reserved.
http://dx.doi.org/10.1016/j.mechmat.2013.09.018

metamaterial with negative permeability (electromagnetic). A thorough review of microstructure design by topology optimization is given by Cadman et al. (2012).

Here, the procedure is exemplified by considering the design of manufacturable extremal elastic materials and negative Poisson's ratio materials (auxetic materials). Several examples of two-phase two-dimensional structures with negative Poisson's ratio exist in the literature. Milton (1992) is the first who found a family of two-dimensional materials with Poisson's ratio arbitrarily close to -1 within the framework of laminated elastic materials. Later, Sigmund (2000a) shows that topology optimization can be applied to the design of both two- and three-dimensional isotropic materials with negative Poisson's ratio. However, the obtained designs are not always manufacturable due to the thin hinge connections in the microstructure. Topology optimization can also be applied to decrease Poisson's ratio between two of the principal directions (Sigmund et al., 1998; Schwerdtfeger et al., 2011) for anisotropic materials.

Theoretically, all achievable effective elastic material tensors can be generated using so-called pentamode material microstructure (Milton and Cherkaev, 1995), which possess parts connected by infinitely thin hinges. These theoretical designs can hardly be produced, and their manufacturability for a modified version with a finite extent is explored in a recent paper by Kadic et al. (2012). The topology optimization procedure presented here ensures manufacturability of the resulting microstructure. Furthermore, we demonstrate that the optimized robust designs can reach the mathematical bounds for three-dimensional isotropic materials in certain cases.

In the next section the mathematical formulation of the optimization problem for the minimization of Poisson's ratio is stated. A slightly modified formulation that can be used to optimize for other extreme material properties is explained as well. In Section 3 the method used to achieve manufacturable designs is described and illustrated. The optimized structures are presented and discussed in Section 4 together with measurements on a manufactured version of the isotropic negative Poisson's ratio material.

2. Optimization problem formulation

The objective and the constraints in the design process are calculated by extracting material properties from the macroscale elasticity tensor. The material is constructed by repeating a unit cell in all spatial directions. The design is periodic and the effective elasticity tensor is obtained using numerical homogenization (e.g., Guedes and Kikuchi, 1990). A compact description of the process is included in A.

The unit cell is discretized using first-order finite elements. A design variable is associated with each element, which takes values between zero (void) and one (element filled with material). A modified SIMP scheme (Bendsøe and Sigmund, 2003), with a constant penalization factor of 3, is used to interpolate between void and solid in each finite element. The continuous design variables are updated by a standard topology optimization approach. A full description of the method is outside the scope of the current paper and here only the steps important to the design of material microstructures are discussed in details. A compact educational implementation of a typical topology optimization procedure can be found in (Andreassen et al., 2011).

2.1. Minimizing Poisson's ratio

The optimization problem for minimizing the effective Poisson's ratio ν^* can be stated as:

$$\begin{aligned}
&\min_{\boldsymbol{\rho}}: \ \nu^* && && \text{Poisson's ratio}\\
&\text{s.t.}: \ \mathbf{K}\boldsymbol{\chi}^i = \mathbf{f}^i, && i=1,\dots,6 && \text{Homogenization equations}\\
&\quad K^* \geqslant aK, && && \text{Bulk constraint}\\
&\quad \frac{\sum_{ij}\left(C^{iso}_{ij}-C^*_{ij}\right)^2}{\left(C^{iso}_{11}\right)^2} \leqslant \varepsilon, && i,j=1,\dots,6 && \text{Isotropy constraint}\\
&\quad \frac{1}{|\Upsilon|}\sum_e (v_e\rho_e) \leqslant V, && e=1,\dots,N && \text{Volume constraint}\\
&\quad 0 \leqslant \rho_e \leq 1, && e=1,\dots,N && \text{Element densities}
\end{aligned} \tag{1}$$

where $\boldsymbol{\rho}$ is a vector of element densities, and ν^* is the effective Poisson's ratio extracted from the homogenized elasticity tensor. $\mathbf{K}$ is the finite element stiffness matrix for the discretized unit cell and $\boldsymbol{\chi}^i$ are the displacement vectors corresponding to six (three in 2D) different unit load cases $\mathbf{f}^i$ (for more details see A). K^* is the homogenized bulk modulus, K is the bulk modulus of the solid phase, a is the required minimum ratio between bulk modulus of solid material and microstructure. C^*_{ij} and C^{iso}_{ij} are entries in the homogenized constitutive matrix and a corresponding isotropic constitutive matrix, respectively. ε is a small number (e.g., 10^{-5}), $|\Upsilon|$is the volume of the considered unit cell, v_e is the volume of each finite element in the unit cell, ρ_e is the corresponding density, and V is the ratio between the allowed solid material volume and the total unit cell volume.

The bulk modulus constraint ensures a minimum stiffness of the material. An alternative formulation would be to impose a limit on the effective Young's modulus. The isotropy constraint ensures that the material properties are isotropic in all spatial directions. $\mathbf{C}^{iso}$ is defined as:

$$C^{iso}_{ii} = \left(C^*_{11}+C^*_{22}+C^*_{33}\right)/3, \quad i=1,2,3 \tag{2}$$

$$C^{iso}_{ij} = \left(C^*_{12}+C^*_{13}+C^*_{23}\right)/3, \quad i,j=1,2,3, \quad i\neq j \tag{3}$$

$$C^{iso}_{ii} = \left(C^{iso}_{11}-C^{iso}_{12}\right)/2, \quad i=4,5,6 \tag{4}$$

$$C^{iso}_{ij} = 0 \quad \text{else}, \tag{5}$$

where $\mathbf{C}^*$ is the homogenized constitutive matrix. The isotropy constraint can be changed to a cubic symmetric constraint by substituting Eq. (4) with

$$C^{iso}_{ii} = \left(C^*_{44}+C^*_{55}+C^*_{66}\right)/3, \quad i=4,5,6 \tag{6}$$

The nonlinear optimization problem defined by Eq. (1) is solved using the gradient-based Method of Moving Asymptotes (MMA) (Svanberg, 1987) with analytical sensitivity computations. The topology optimization problem is regularized by a projection scheme combined with the so-called robust optimization formulation (Wang et al., 2011; Lazarov et al., 2011) which ensures black and white

(0/1) designs with a minimum length scale. When using a projection approach, it is advisable to gradually increase the projection parameter β (going from a linear function to a step function), and we use a continuation scheme similar to the one in Wang et al. (2011); however, the continuation scheme is only applied after the design has converged with an initial $\beta = 1$. Filters and projection methods are discussed in depth by Sigmund (2007) and more details on the robust optimization scheme are given in Section 3.

2.2. Analytic bounds for isotropic materials

By substituting the objective function in Eq. (1) with a maximization of the effective shear modulus G^* and varying a, or alternatively maximizing K^* and having a constraint on G^*, material structures close to the Hashin–Shtrikman bounds can be found. For an isotropic material with microstructure consisting of one material with voids the upper Hashin–Shtrikman bounds (Hashin and Shtrikman, 1963) on the effective bulk K^* and effective shear modulus G^* are given as:

$$K^* \leqslant \frac{4GKV}{4G + 3K(1-V)}, \tag{7}$$

$$G^* \leqslant G + \frac{1-V}{\frac{6}{5G}\frac{(K+2G)V}{(3K+4G)} - \frac{1}{G}}, \tag{8}$$

where V is the volume fraction of base material, K the bulk modulus, and G the shear modulus of the base material. The corresponding lower bounds are zero. It should be pointed out that the upper limit on K^* also holds for cubic symmetric materials. For two-dimensional materials the improved Cherkaev–Gibiansky bounds (Cherkaev and Gibiansky, 1993) can be used as well. Berryman and Milton (1988) have presented improved bounds correlating K^* and G^* for two-phase isotropic three-dimensional materials, however, for the case considered here, where one phase is void, those bounds coincide with the Hashin–Shtrikman bounds.

3. Manufacturable design

The designs obtained by standard topology optimization without projection and the requirement for robustness possess gray scale, i.e., design values between zero and one. Such solutions of the optimization problem require post-processing before manufacturing. For two-dimensional structures it is relatively easy to manually correct the design and verify it. However, for three-dimensional structures, with complex designs, the post-processing and the verification process can be prohibitive. Therefore, to be of real practical use when designing microstructures, the topology optimization process must result in designs ready for manufacturing. A standard smoothing or thresholding might be necessary to generate an STL-file for the SLS process, but preferably no manual decision-making, as this can easily violate the constraints imposed on the design and decrease performance.

3.1. Isotropic minimum Poisson's ratio design

The first examples where Poisson's ratios are minimized are two-dimensional, as it is relatively easy to illustrate the effect of lack of robustness here. A base material with $\nu = 0.3$ is considered in the optimization process. Designs with density and sensitivity filters obtained without any manufacturing constraints are shown in Fig. 1. The design in Fig. 1(a) is a result of an optimization with a random initial distribution of densities. To make the visual comparison of the microstructures straightforward, the optimizations for the other 2D designs presented in this initial example (Figs. 1 and 2(b)) have been run with the design from Fig. 1(a) as an initial guess. Starting with a random guess results in similar but shifted or flipped designs, obscuring the possibility of direct comparisons. All the three-dimensional designs presented in Section 4 are results of optimizations with random initial density distributions. The constitutive matrices for the microstructures in Fig. 1 are:

$$\mathbf{C}_a^* = 10^{-2}E \cdot \begin{pmatrix} 1.50 & -1.21 & 0.00 \\ -1.21 & 1.50 & 0.00 \\ 0.00 & 0.00 & 1.35 \end{pmatrix},$$

$$\mathbf{C}_b^* = 10^{-2}E \cdot \begin{pmatrix} 0.77 & -0.49 & 0.00 \\ -0.49 & 0.77 & 0.00 \\ 0.00 & 0.00 & 0.63 \end{pmatrix}, \tag{9}$$

which imply isotropic materials with Poisson's ratios of

$$\nu_a^* = -0.81, \quad \nu_b^* = -0.64. \tag{10}$$

However, the gray transition areas, imposed by the filters, correspond to porous regions. It is not possible to manufacture these designs without post-processing, and it is not possible to say a priori how the post-processing will change the constitutive matrix. Due to the nature of the filters these areas are more pronounced for the density filter despite that the same filter radius was used for both cases.

It shall be pointed out that the designs in Fig. 1 have been generated with a constant filter size, as opposed to the designs in e.g., Sigmund (1994), where the filter radius was gradually decreased during the optimization process. With a gradually decreasing filter radius both designs would become black and white, but at the risk of loosing the length scale and potentially getting one-node hinges (infinitely thin structures). The same holds for the case where a simple projection is used on top of the filter (Sigmund, 2007; Wang et al., 2011), as discussed in the next section.

3.2. Black and white design

In Fig. 2(a) the microstructure resulting from an optimization where a projection is used on top of the density filter is shown. The resulting design become black and white, and has the constitutive matrix

$$\mathbf{C}^* = 10^{-2}E \cdot \begin{pmatrix} 2.81 & -2.53 & 0.00 \\ -2.53 & 2.81 & 0.00 \\ 0.00 & 0.00 & 2.67 \end{pmatrix}, \tag{11}$$

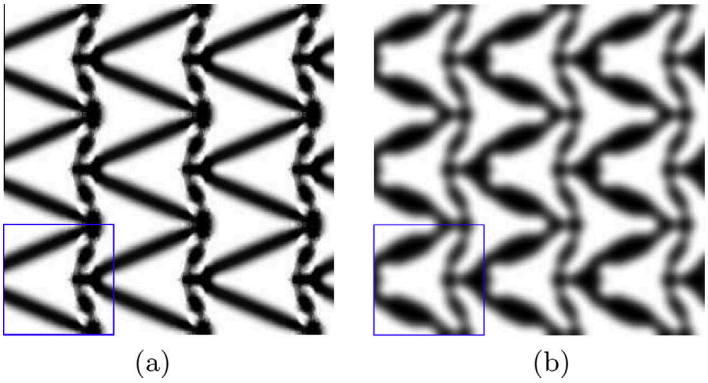

Fig. 1. Minimum Poisson's ratio design obtained with standard filtering. In both cases a linearly decaying filter with a radius of 1/10 of the unit cell side length was used. Other parameters are: $a = 0.2\%, \epsilon = 10^{-5}, N = 10000$, and $V = 35\%$. (a) Sensitivity filter started from a random distribution of densities. (b) Density filter started from the design in (a). The box in the corner encloses one unit cell.

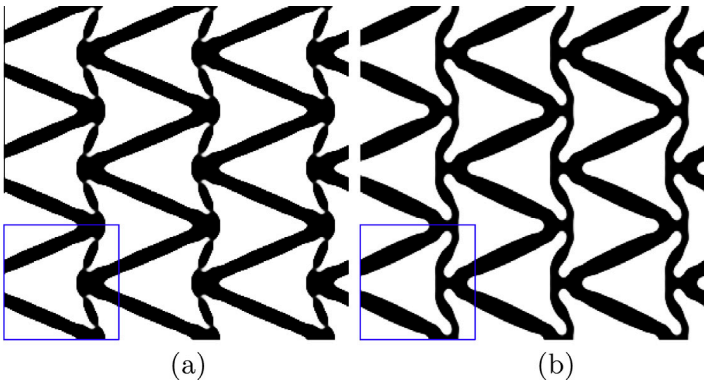

Fig. 2. Negative Poisson's ratio structures obtained with (a) a projection, and (b) robust formulation. Parameters are the same as for the designs in Fig. 1, except for the volume constraint in the robust formulation, which is applied on the dilated design and is set 15 percent higher. The design in Fig. 1(a) is used as the initial guess.

implying a Poisson's ratio of −0.90. The lower bound on the bulk modulus prevents one node hinges from forming, and, thus, removing a tiny strip of material from the structure uniformly (eroding it), would decrease the Poisson's ratio further. This is illustrated in Fig. 3(a), however, at some point the material would become disconnected, because the hinges are completely eroded away and connectivity lost. As one can deduce from Fig. 3(a), this happens around a volume fraction of 0.33. When the material becomes disconnected, it does not make sense to talk about a Poisson's ratio, but since we model void as an extremely soft material, it can still be computed. Increasing the material in the structure uniformly (dilating it) will make the hinges less pronounced and this is reflected in a higher Poisson's ratio in Fig. 3(a). Furthermore, the only point on the graph in Fig. 3(a) that satisfies the isotropy constraint

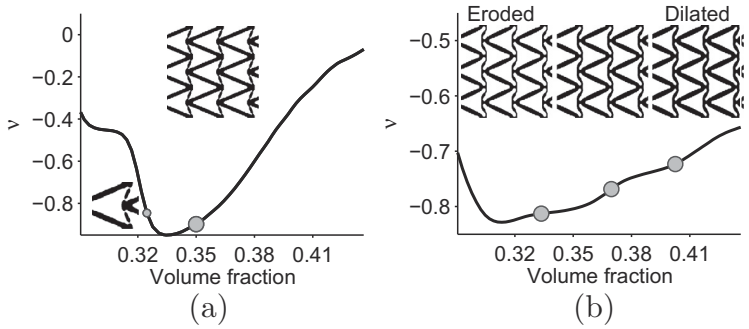

Fig. 3. Graphs illustrating variation of the effective Poisson's ratio with respect to erosion/dilation of the designs in (a) Fig. 2(a) – projected design, and (b) Fig. 2(b) – robust design.

is the one we optimized for ($V = 35\%$). How to achieve a microstructure that is robust (for both the objective and the constraints), w.r.t. to removing or adding material, is illustrated in the next section.

3.3. Robust design

Manufacturable designs can be obtained using the approach suggested in Sigmund (2009), Wang et al. (2011), which is referred to as deterministic robust formulation. The optimized designs in this formulation are required to perform equally well if they are eroded or dilated. The objective function is substituted with

$$\min_{\rho}: \quad \max\left(\nu^*, \nu_d^*, \nu_e^*\right), \tag{12}$$

where ν_d^* and ν_e^* are the effective Poisson's ratios of the dilated and eroded structures, and ν^* is the effective Poisson's ratio of the blueprint (intermediate) design supplied to the manufacturer. The three designs are required to be isotropic. The filter radius of 0.10 is the same as before, which combined with the applied projection thresholds ensures a minimum length scale of 0.09 (see Wang et al., 2011). The bulk modulus constraint is applied only on the eroded case, since it is the weakest of the three structures. The deterministic robust formulation results in a design shown in Fig. 2(b), with an effective constitutive tensor

$$\mathbf{C}^* = 10^{-2}E \cdot \begin{pmatrix} 2.40 & -1.85 & 0.00 \\ -1.85 & 2.40 & 0.00 \\ 0.00 & 0.00 & 2.12 \end{pmatrix}, \tag{13}$$

which corresponds to a Poisson's ratio of -0.77.

In Fig. 3(b) the dependence of the objective with respect to uniform dilation or erosion is illustrated. Eroding the design further than the selected erosion threshold improves the effective Poisson's ratio. This effect is due to the bulk modulus constraint. Without it, hinges appear in the eroded design and the performance deteriorates immediately.

For the design with the objective shown in Fig. 3(b) it seems that only the dilated structure is active in the min/max objective function, hence, one might be tempted to select only the dilated case in the optimization process. However, we have observed that such a reduced formulation can lead to poor performance since during the first few hundred iterations all three designs play a role in the design update. Furthermore, the isotropy constraint is active on all three designs. Since manufacturing tolerances are taken into account, Poisson's ratios very close to -1 are not achievable (pure hinges are prohibited, cf. (Kadic et al., 2012)), however the blueprint design is manufacturable without any amendments. Materials with Poisson's ratios of -1 can be created with mechanism-like structures built from trusses connected through hinges that do not resist bending; imperfect hinges will limit the achievable Poisson's ratio.

As discussed by Wang et al. (2011) a minimum length scale is assured as long as the topologies of the three designs are the same. Obtaining the same topologies can be a challenge and difference in the topologies can severely affect the performance. Including more projections in the optimization objective can give smoother transition between the designs. This case can be naturally handled by modeling the projection threshold as a random variable. Such a formulation is presented by Lazarov et al. (2011) and is the one we implemented and utilized for the three-dimensional designs discussed in the next section. However, comparing designs from runs with more than three design realizations and runs with only three design realizations, little difference was found. Thus, for all the three-dimensional designs presented in the next section, three designs (eroded, blueprint, and dilated) were included in the optimization.

4. Three-dimensional design

The two-dimensional designs presented above illustrate how manufacturable material designs can be achieved. The approach is directly applicable to three dimensions, with the main issue being the computational cost. Therefore, the optimization results presented below have been obtained using a parallel implementation of the optimization process (Aage and Lazarov, 2013).

Our main example is a three-dimensional isotropic negative Poisson's ratio material, which has been manufactured in polyamid using SLS. Several three-dimensional designs close to the theoretical limits mentioned in Section 2.2 are presented as well. Finally, we briefly discuss the computational cost.

4.1. Isotropic minimum Poisson's ratio

The structure is manufactured using polyamid with Poisson's ratio 0.4, which is the base material in the optimization process. The 3D material microstructure resulting from the optimization process is shown in Fig. 4. The effective constitutive tensor is:

$$\mathbf{C}^* = 10^{-2}E_{polyamid} \begin{pmatrix} 3.42 & -1.15 & -1.15 & 0.00 & 0.00 & 0.00 \\ -1.15 & 3.42 & -1.15 & 0.00 & 0.00 & 0.00 \\ -1.15 & -1.15 & 3.42 & 0.00 & 0.00 & 0.00 \\ 0.00 & 0.00 & 0.00 & 2.28 & 0.00 & 0.00 \\ 0.00 & 0.00 & 0.00 & 0.00 & 2.28 & 0.00 \\ 0.00 & 0.00 & 0.00 & 0.00 & 0.00 & 2.28 \end{pmatrix}, \tag{14}$$

which implies an isotropic material with a Poisson's ratio of

$$\nu = -0.51 \tag{15}$$

The only physically realized three-dimensional isotropic material presented in the literature with a comparable Poisson's ratio is Lakes' reentrant foam (see e.g., Lakes, 1987). However, compared to the presented 3D microstructure, the foam materials have a much lower bulk modulus. For the polyester foam in Lakes (1987) $K^*/K \approx 10^{-6}$ (where K is taken for pure polyester), while $K^*/K \approx 2 \cdot 10^{-3}$ for the structure in Fig. 4. It should be mentioned that Lakes' design was a conceptual development – proving that it is indeed possible to produce negative

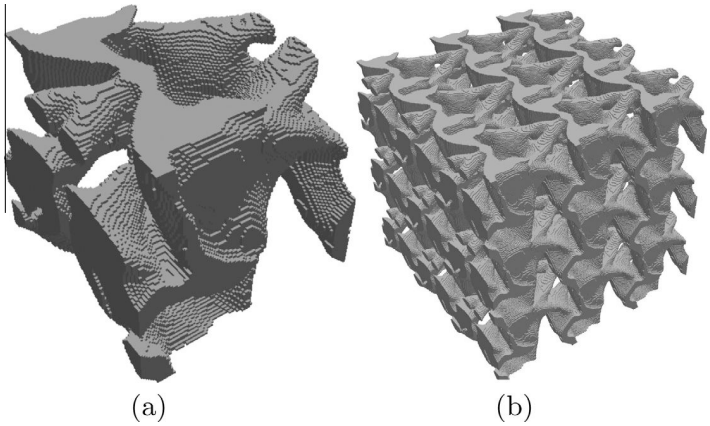

Fig. 4. 3D isotropic microstructure with Poisson's ratio -0.51. $a = 0.125\%$ is used for the stiffness constraint on the eroded design, while the isotropy constraint parameter ϵ is set to 10^{-5} for all three designs. The solid volume fraction of the dilated design is constrained to 40%. The initial guess is a random distribution of densities. (a) One unit cell. (b) $3 \times 3 \times 3$ unit cells.

Poisson's ratio material – based on insight, and not the result of an analytical approach.

4.2. Experimental test

To validate the manufacturability of the three-dimensional design the isotropic negative Poisson's ratio material is produced in polyamid using an SLS machine and Poisson's ratio is measured using a simple compressive test. A photo of the manufactured structure can be seen in Fig. 7. It consists of $8 \times 4 \times 4$ unit cells, with side lengths of 2 cm. The aspect ratio of 2 is chosen to reduce the effect of the friction from the end surfaces when the sample is compressed. Requiring an aspect ratio of 2, a specimen with $8 \times 4 \times 4$ cells was the biggest that could be manufactured in the SLS machine.

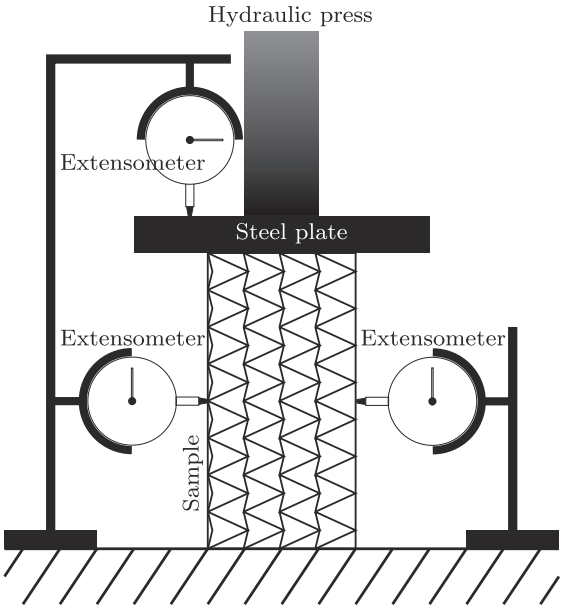

Fig. 5. Experimental setup for measurements of Poisson's ratio.

The experimental setup is shown in Fig. 5. The loading is provided by a hydraulic press while extensometers with a sensitivity of 0.01 mm are used to measure the deformation of the sample along the longest and perpendicular lines located at the center of the sample. In the setup the load on the sample could not be accurately controlled, so to assure full contact between all surfaces before starting the measurements, a small prestress force is applied. In order to avoid damage to the structure the load is increased six times with the aim of achieving maximal vertical strain below one percent. After each load increment the horizontal and vertical deflection values are recorded. The deflection curves are shown in Fig. 6. The two plots correspond to the two short directions of the sample (the second direction is obtained by rotating the sample 90 degrees around the long axis and is perpendicular to the first).

As mentioned earlier the extensometers sensitivity is $\delta = 0.01$ mm, hence this, being a quantifiable source of measurement error, has been used to generate the error curves in Fig. 6. The upper curve is found by subtracting 2δ from the horizontal displacements and adding 1δ to the vertical displacements, while the lower curve is found by adding 2δ to the horizontal displacements and subtracting 1δ from the vertical displacements. Considering the last measurement point, which has the smallest relative error, the measured Poisson's ratio of the material is -0.50 ± 0.03 for both sets of measurements. Furthermore, there is only one measurement point where the measured interval for Poisson's ratio does not contain -0.51. Possible reason for this behavior is the influence of the boundary conditions. The homogenization theory assumes an infinite extent of the material while the sample only contains a finite number of unit cell. Other possible sources of error are the local deformations at the measurement points for the two horizontally aligned extensometer. To compensate for this we positioned them on two opposite flat areas of the structure. It should be emphasized that little influence

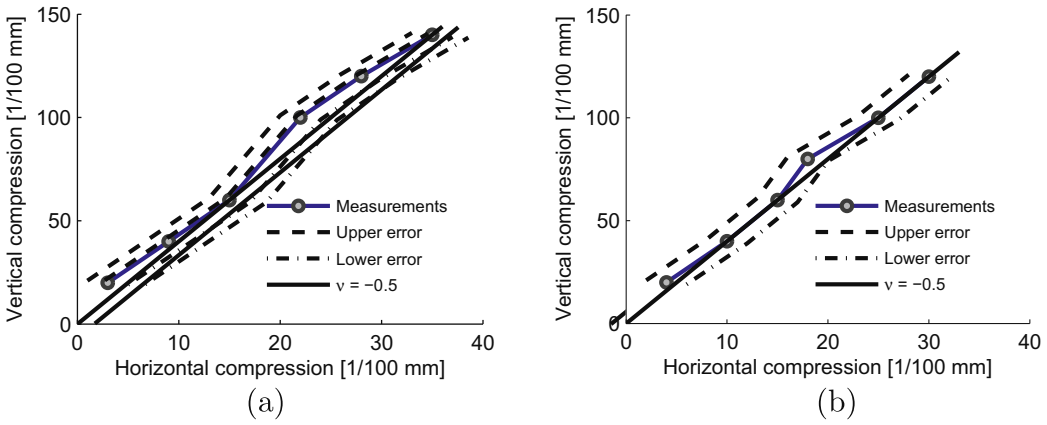

Fig. 6. Deflection curves from measurements of Poisson's ratio. In (a) the sample was rotated 90 degrees around its longest axis compared to (b).

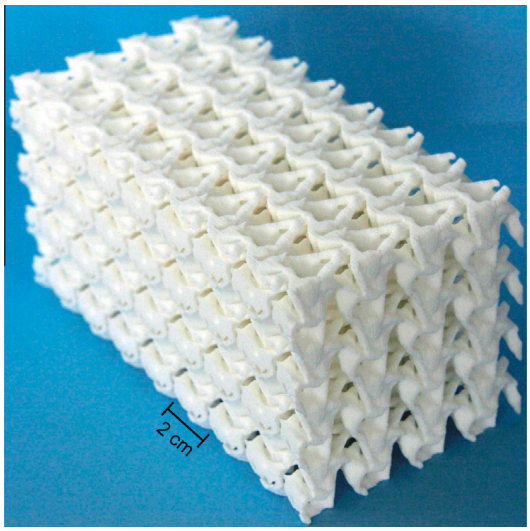

Fig. 7. Manufactured minimum Poisson's ratio structure.

on the measurements is observed if these extensometers were repositioned, e.g., moved one unit cell vertically or horizontally. The results presented here are from a single measurement and not an average of several measurements.

In Fig. 8 close-ups of the undeformed and deformed structure are compared. It is clearly visible how the structure contracts in the horizontal direction when compressed in the vertical direction. As already stated no post-processing is performed on the structure before sending it to manufacturing and an STL-file of the unit cell is available for download from our webpage www.topopt.dtu.dk/negativePoissonsRatio/unitCell.stl.

Ideally, the experimental test should consist of repeated measurements on multiple specimens, but due to the manufacturing cost this was not feasible. However, we encourage other researchers with manufacturing capabilities to download the STL-file and conduct more advanced experiments.

4.3. Theoretical limits

The negative Poisson's ratio problem is used as a case example, because it is difficult to obtain a manufacturable design. A negative Poisson's ratio material requires a large shear to bulk modulus ratio. The bulk and shear modulus of the material in Fig. 4 are plotted as a point (denoted Fig. 4) together with the theoretical bounds in Fig. 9. It can be seen that the design is in the lower left corner. Designs can be obtained in the upper left corner (cf. pentamode Milton and Cherkaev, 1995), however, it will be difficult to achieve manufacturability for them. Several optimization runs are performed to verify this conclusion. The resulting bulk and shear moduli of these extremal materials are also shown in Fig. 9. It should be pointed out that the plot shows the moduli for the middle design which is different than the mean moduli. For small erosion or dilation it will not change significantly due to the required robust performance. The hatched area in Fig. 9 indicates where isotropic materials with a negative Poisson's ratio can be found.

First, consider the designs obtained with an isotropy constraint ($\epsilon = 10^{-5}$). The unit cells for the material designs corresponding to the points in the graph are shown in Fig. 10. The design corresponding to point (a) is just a disconnected unit cell without any stiffness. Setting constraint on the bulk modulus and maximizing the shear modulus leads to the designs shown in (b), (c) and (d), where (b) and (c) have topologies similar to the negative Poisson's ratio cell. Maximizing the bulk modulus and constraining the shear modulus leads to the designs shown in (h), (g) and (f). Maximizing the bulk modulus without any constraints results in a Vigdergauz-like cell (Vigdergauz, 1989).

Also included in Figs. 9 and 10 are two designs, points (i) and (j), for which instead of an isotropy constraint a cubic symmetry constraint was applied in the optimization

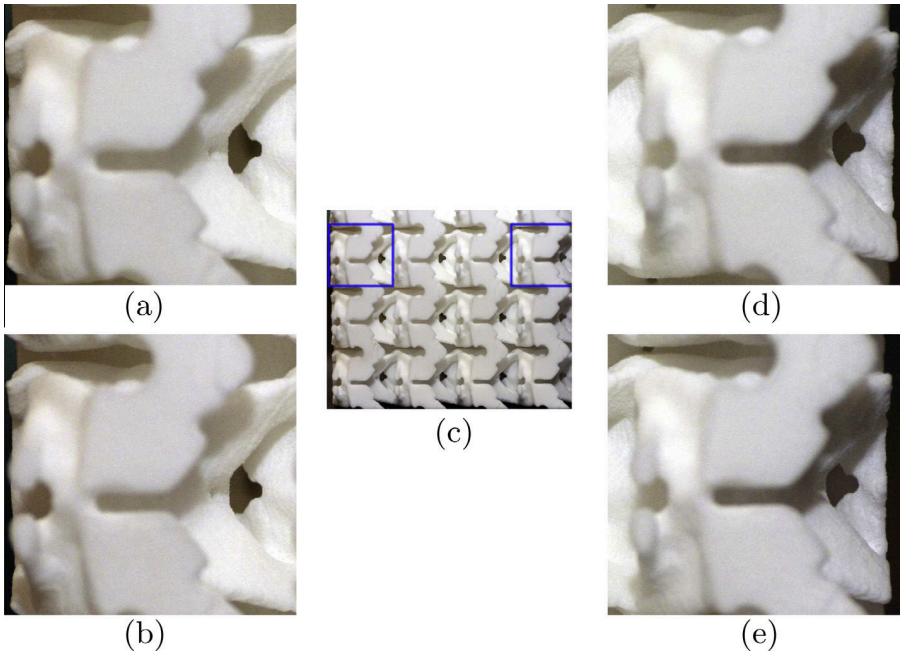

Fig. 8. Visualization of the structure deformations. (a) Undeformed unit cell on left side, (b) deformed version. (d) Undeformed unit cell on right side, (e) deformed version. (c) Three bottom rows of the sample. The blue selections indicate the positions of the close ups. The negative Poisson's ratio behavior is illustrated by how both sides contract (the black edge area becomes larger).

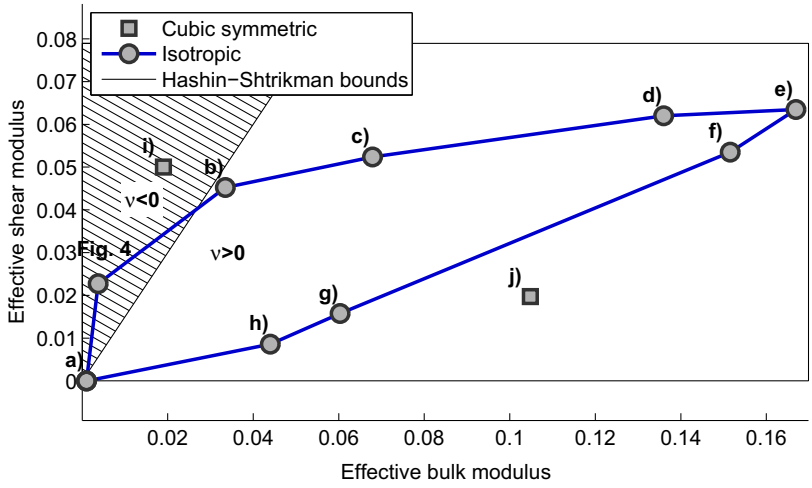

Fig. 9. Hashin–Shtrikman bounds and effective moduli for several topology optimized designs. The base material properties are the same as for the structure in Fig. 10, and the volume fraction of the blueprint design is constrained to 33.8% (corresponding to the design in Fig. 10). Unit cells corresponding to the points are shown in Fig. 10.

(still with $\epsilon = 10^{-5}$). This is done to illustrate that even for structures with cubic symmetry the upper left and lower right corner are unachievable when the requirement for robustness is imposed in the optimization.

Finally, it should be mentioned that a cubic unit cell is not necessarily the best choice for design of isotropic materials. In 2D more extremal designs can sometimes be obtained with a rectangular unit cell (Sigmund, 2000a). In 3D it is not clear what cell shape would be most beneficial. Due to the high computational cost we have only utilized a cubic unit cell in our numerical experiments.

4.4. Computational issues

Design of three-dimensional structures requires extensive computational power, since the number of degrees of freedom explodes (the curse of dimensionality). A two-dimensional problem with 100^2 elements will have

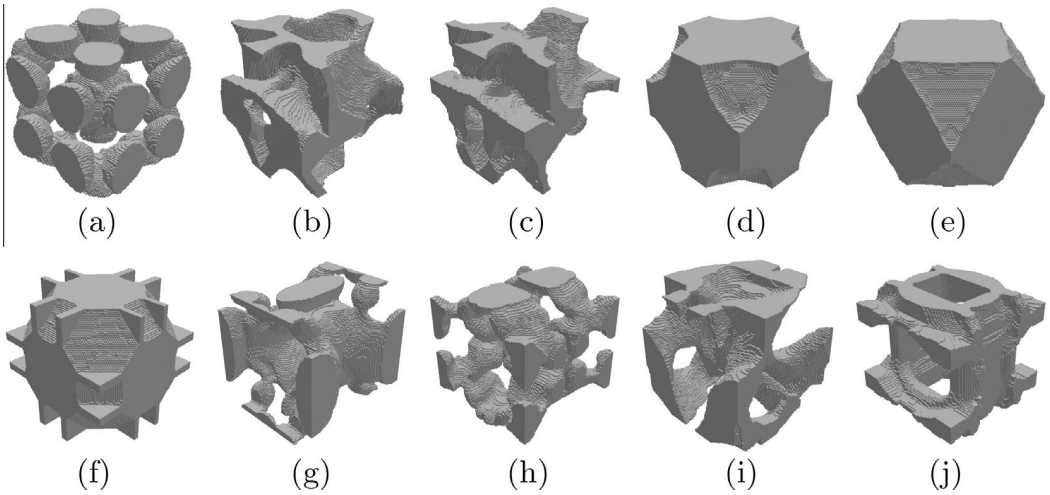

Fig. 10. Unit cells for the extremal microstructures in Fig. 9.

20,000 degrees of freedom (dofs). In 3D discretizing the unit cell with 100^3 elements equates to three million dofs.

The number of iterations in each optimization run varies, but all the optimization results in this paper took more than 1000 iterations. In each iteration three state problems are solved (eroded, blueprint, and dilated design), and an optimization run with 1000 iterations takes approximately 10 h on 120 CPU cores.

The time per iteration is not constant, because the solutions of the state problems are obtained iteratively using a preconditioned conjugate gradient method (PCG). Its convergence depends on the effectiveness of the supplied preconditioner. The classical preconditioning techniques like incomplete factorization, diagonal and block-diagonal scaling cannot ensure a constant number of iterations with increasing number of dofs. To save time in 3D we split the optimization into two parts. First, an optimization with a coarser mesh (50^3 elements) is performed. The result of this optimization is used as an initial guess for the fine mesh optimization. For the design presented in Fig. 4 the number of coarse mesh iterations was around 3000, while the fine mesh optimization, with the coarse mesh initial guess, needed less than 500 iterations.

5. Conclusion

Topology optimization is now mature enough for optimization of directly manufacturable three-dimensional materials. With the presented method the optimized designs can directly be manufactured without any need for post-processing. This is especially important when working with three-dimensional structures, since post-processing is hardly possible without decreasing performance or violating imposed constraints.

It is relatively easy to optimize for a stiff material, and with the presented method a one length-scale Vigdergauz like structure is obtained. The presented formulation can be used to optimize for other extremal elastic microstructures, such as negative Poisson's ratio, without any amendments. This is illustrated with the manufacturing of an isotropic material with a Poisson's ratio of -0.5. Finally, it should be pointed out that the extension to multiphase materials is straightforward, however the resulting structures would require more complex manufacturing processes.

Acknowledgements

The work was funded by the Danish Research Agency through the innovation consortium F•MAT and the Villum Foundation through the NextTop project. The authors are grateful to the Product Development center at the Danish Technological Institute for manufacturing of the negative Poisson's ratio structure.

Appendix A. Numerical homogenization

Assuming a perfectly periodic material with infinite extent in all dimensions, the effective elasticity tensor can be computed by homogenization (e.g., Guedes and Kikuchi, 1990). Here, a description of the numerical procedure is presented in a compact form together with the gradients of the effective tensor components with respect to a design variable.

The domain occupied by a single periodic unit cell is denoted with Υ. It is discretized using finite elements and the stiffness matrix of the discretized structure (Zienkiewicz et al., 2005) can be written as

$$\mathbf{K} = \sum_{e=1}^{N} \int_{V_e} \mathbf{B}^T \mathbf{C}_e \mathbf{B} dV_e, \tag{A.1}$$

where N denotes the finite elements number. The matrix $\mathbf{B}$ is the strain–displacement matrix, $\mathbf{C}_e$ is the constitutive matrix for the element, which in topology optimization will depends on the density of the element, and V_e is the domain of element e.

To find the effective properties of the material the following finite element problem is solved with six load cases (three in 2D):

$$\mathbf{K}\boldsymbol{\chi}^i = \mathbf{f}^i, \quad i = 1, \ldots, 6, \tag{A.2}$$

where the displacement vectors $\boldsymbol{\chi}^i$ are assumed to be Υ periodic, and the loads $\mathbf{f}^i$ correspond to unit strain fields computed as

$$\mathbf{f}^i = \sum_e \int_{V_e} \mathbf{B}^T \mathbf{C}_e \boldsymbol{\varepsilon}^i dV_e, \tag{A.3}$$

where the unit strains are

$$\begin{aligned} \boldsymbol{\varepsilon}^1 &= (1,0,0,0,0,0)^T, \\ \boldsymbol{\varepsilon}^2 &= (0,1,0,0,0,0)^T, \quad \text{and so on} \end{aligned} \tag{A.4}$$

With the computed displacements, the homogenized constitutive matrix $\mathbf{C}^*$ can be found as

$$\mathbf{C}^* = \frac{1}{|\Upsilon|} \sum_{e=1}^{N} \int_{V_e} (\mathbf{I} - \mathbf{B}\boldsymbol{\chi}_e)^T \mathbf{C}_e (\mathbf{I} - \mathbf{B}\boldsymbol{\chi}_e) dV_e, \tag{A.5}$$

where $\boldsymbol{\chi}_e$ contains six columns corresponding to the six displacement fields, and $\mathbf{I}$ is a six times six identity matrix. The term $\mathbf{B}\boldsymbol{\chi}_e$ can be interpreted as the strains caused by the non-homogeneous material distribution.

Using the adjoint method it can be shown that the sensitivity of $\mathbf{C}^*$ with respect to change in an element design variable is:

$$\frac{\partial \mathbf{C}^*}{\partial \rho_e} = \frac{1}{|\Upsilon|} \sum_{e=1}^{N} \int_{V_e} (\mathbf{I} - \mathbf{B}\boldsymbol{\chi}_e)^T \frac{\partial \mathbf{C}_e}{\partial \rho_e} (\mathbf{I} - \mathbf{B}\boldsymbol{\chi}_e) dV_e.$$

References

Aage, N., Lazarov, B.S., 2013. Parallel framework for topology optimization using the method of moving asymptotes. Structural and Multidisciplinary Optimization 47, 493–505.

Andreassen, E., Clausen, A., Schevenels, M., Lazarov, B.S., Sigmund, O., 2011. Efficient topology optimization in matlab using 88 lines of code. Structural and Multidisciplinary Optimization 43, 1–16.

Bendse, M., Sigmund, O., 2003. Topology Optimization. Theory, Methods and Applications. Springer.

Berryman, J.G., Milton, G.W., 1988. Microgeometry of random composites and porous media. Journal of Physics D: Applied Physics 21, 87–94.

Cadman, J., Zhou, S., Chen, Y., Li, Q., 2012. On design of multi-functional microstructural materials. Journal of Materials Science 48, 1–16.

Cherkaev, A., Gibiansky, L., 1993. Coupled estimates for the bulk and shear moduli of a two-dimensional isotropic elastic composite. Journal of the Mechanics and Physics of Solids 41, 937–980.

Coelho, P.G., Cardoso, J.B., Fernandes, P.R., Rodrigues, H.C., 2011. Parallel computing techniques applied to the simultaneous design of structure and material. Advances in Engineering Software 42, 219–227.

Diaz, A., Sigmund, O., 2010. A topology optimization method for design of negative permeability metamaterials. Structural and Multidisciplinary Optimization 41, 163–177.

Gibiansky, L.V., Sigmund, O., 2000. Multiphase composites with extremal bulk modulus. Journal of the Mechanics and Physics of Solids 48, 461–498.

Guedes, J., Kikuchi, N., 1990. Preprocessing and postprocessing for materials based on the homogenization method with adaptive finite element methods. Computer Methods in Applied Mechanics and Engineering 83, 143–198.

Guest, J.K., Prévost, J.H., 2006. Optimizing multifunctional materials: design of microstructures for maximized stiffness and fluid permeability. International Journal of Solids and Structures 43, 7028–7047.

Hashin, Z., Shtrikman, S., 1963. A variational approach to the theory of the elastic behaviour of multiphase materials. Journal of the Mechanics and Physics of Solids (UK) 11, 127–140.

Jensen, J., Sigmund, O., 2011. Topology optimization for nano-photonics. Laser & Photonics Reviews 5, 308–321.

Kadic, M., Bückmann, T., Stenger, N., Thiel, M., Wegener, M., 2012. On the practicability of pentamode mechanical metamaterials. Applied Physics Letters (USA) 100, 191901–191904.

Kalpakjian, S., Schmid, S.R., Musa, H., 2010. Manufacturing engineering and technology. Pearson, Jurong, Singapore.

Krog, L., Tucker, A., Kemp, M., Boyd, R. 2004. Topology optimization of aircraft wing box ribs. In: Proceedings of The Altair Technology Conference.

Lakes, R., 1987. Foam structures with a negative Poisson's ratio. Science 235, 1038–1040.

Lazarov, B.S., Schevenels, M., Sigmund, O., 2011. Robust design of large-displacement compliant mechanisms. Mechanical Sciences 2, 175–182.

Milton, G.W., 1992. Composite materials with poisson's ratios close to −1. Journal of the Mechanics and Physics of Solids 40, 1105–1137.

Milton, G.W., Cherkaev, A., 1995. Which elasticity tensors are realizable? Trans ASME, J. Eng. Mater. Technol. (USA). Journal of Engineering Materials and Technology 117, 483–493.

Schwerdtfeger, J., Wein, F., Leugering, G., Singer, R.F., Körner, C., Stingl, M., Schury, F., 2011. Design of auxetic structures via mathematical optimization. Advanced Materials 23, 2650–2654.

Sigmund, O., 1994. Materials with prescribed constitutive parameters: an inverse homogenization problem. International Journal of Solids and Structures 31, 2313–2329.

Sigmund, O., 2000a. A new class of extremal composites. Journal of the Mechanics and Physics of Solids 48, 397–428.

Sigmund, O., 2000b. Topology optimization: a tool for the tailoring of structures and materials. Philosophical Transactions of the Royal Society A: Mathematical, Physical and Engineering Sciences 358, 211–288.

Sigmund, O., 2007. Morphology-based black and white filters for topology optimization. Structural and Multidisciplinary Optimization 33, 401–424.

Sigmund, O., 2009. Manufacturing tolerant topology optimization. Acta Mechanica Sinica 25, 227–239.

Sigmund, O., Torquato, S., 1999. Design of smart composite materials using topology optimization. Smart Materials and Structures 8, 365–379.

Sigmund, O., Torquato, S., Aksay, I., 1998. On the design of 1–3 piezo-composites using topology optimization. Journal of Materials Research 13, 1038–1048.

Svanberg, K., 1987. Method of moving asymptotes – a new method for structural optimization. International Journal for Numerical Methods in Engineering 24, 359–373.

Swan, C.C., Kosaka, I., 1997. Homogenization-based analysis and design of composites. Computers & Structures 64, 603–621.

Theocaris, P.S., Stavroulakis, G.E., 1998. Multilevel optimal design of composite structures including materials with negative poisson's ratio. Structural Optimization 15, 8–15.

Vigdergauz, S.B., 1989. Regular structures with extremal elastic properties. Mechanics of Solids 24, 57–63.

Wang, F., Lazarov, B.S., Sigmund, O., 2011. On projection methods, convergence and robust formulations in topology optimization. Structural and Multidisciplinary Optimization 43, 767–784.

Zienkiewicz, O.C., Taylor, R.L., Zhu, J., 2005. The Finite Element Method. Elsevier.

Publication [P4]

On the realization of the bulk modulus bounds for two-phase viscoelastic composites

ARTICLE IN PRESS

Journal of the Mechanics and Physics of Solids ▮ (▮▮▮▮) ▮▮▮–▮▮▮

Contents lists available at ScienceDirect

Journal of the Mechanics and Physics of Solids

journal homepage: www.elsevier.com/locate/jmps

On the realization of the bulk modulus bounds for two-phase viscoelastic composites

Casper Schousboe Andreasen*, Erik Andreassen, Jakob Søndergaard Jensen, Ole Sigmund

Department of Mechanical Engineering, Section for Solid Mechanics, Technical University of Denmark, Nils Koppels Allé, Building 404, DK-2800 Kgs. Lyngby, Denmark

ARTICLE INFO

Article history:
Received 3 September 2012
Received in revised form
11 September 2013
Accepted 13 September 2013

Keywords:
Viscoelasticity
Topology optimization
Microstructure
Analytical bounds

ABSTRACT

Materials with good vibration damping properties and high stiffness are of great industrial interest. In this paper the bounds for viscoelastic composites are investigated and material microstructures that realize the upper bound are obtained by topology optimization. These viscoelastic composites can be realized by additive manufacturing technologies followed by an infiltration process. Viscoelastic composites consisting of a relatively stiff elastic phase, e.g. steel, and a relatively lossy viscoelastic phase, e.g. silicone rubber, have non-connected stiff regions when optimized for maximum damping. In order to ensure manufacturability of such composites the connectivity of the matrix is ensured by imposing a conductivity constraint and the influence on the bounds is discussed.

1. Introduction

Materials with enhanced vibration damping capabilities are of great interest in a variety of industrial and personal appliances ranging from pumps over satellite communication equipment to phono cartridges. Typical structural materials such as steel display low intrinsic damping and additional measures need to be taken to damp unwanted vibrations. A composite material such as gray cast iron shows significant damping in the order of 1–1.5% of the critical damping due to its graphite content (Millet et al., 1981), however, metallic materials in general exhibit damping less than 1%. Cast iron is just one composite material to consider for increased damping, other cast composites could potentially have larger damping ratios. The development of viscoelastic composites has attained quite some attention in order to develop materials with both high stiffness and high damping (Brodt and Lakes, 1995).

One production method for generating advanced composites with architectured microstructure is additive manufacturing (AM), e.g. selective laser sintering/melting where it is possible to manufacture composite materials with a geometrically advanced metallic matrix which afterwards can be infiltrated by a viscoelastic material. These advanced composites may exhibit very large damping, though obviously, limited by the theoretical bounds.

For low frequency harmonic vibrations where the inertia effects can be neglected the loss can be described by the elasticity equations using a complex modulus of elasticity (Hashin, 1970) according to the correspondence principle (Hashin, 1965). The theoretical bounds for the complex stiffness of viscoelastic composites have been developed with offset in the corresponding bounds for elastic composites by Hashin and Shtrikman (1963). The bounds for the complex material properties are derived

* Corresponding author. Tel.: +45 452 54262.
E-mail address: csan@mek.dtu.dk (C.S. Andreasen).

0022-5096/$ - see front matter © 2013 Elsevier Ltd. All rights reserved.
http://dx.doi.org/10.1016/j.jmps.2013.09.007

using the translation method developed by Cherkaev and Gibiansky (1994). In Gibiansky and Milton (1993) and Gibiansky and Lakes (1993) the bounds for the complex bulk modulus for two- and three-dimensional two-phase isotropic viscoelastic composites are derived for a fixed and an arbitrary volume fraction, respectively. Gibiansky and Lakes (1997) summarize the bounds, both for complex bulk and shear moduli of two-dimensional two-phase isotropic viscoelastic composites and present a method for computing the bounds. The bounds for the three-dimensional two-phase complex shear modulus are presented in Milton and Berryman (1997).

The structures that realize the viscoelastic bounds include multiscale structures such as the Hashin coated spheres assemblage (Hashin and Shtrikman, 1963) and rank-N laminates (Lurie and Cherkaev, 1986; Francfort and Murat, 1986). These structures are also optimal for elastic materials with respect to stiffness. For elastic materials the bounds have been realized using single scale structures in Vigdergauz (1994) and two scale structures in Sigmund (2000) which presumably also apply to the viscoelastic bounds as it does for the coated spheres assemblage.

The structure of viscoelastic composites has been studied by e.g. Yi et al. (1998) where the effective viscoelastic stiffness for a certain composite is computed by homogenization. The approach is extended in Yi et al. (2000) where viscoelastic composites are optimized using topology optimization for increased damping using an inverse homogenization approach similar to the one introduced in Sigmund (1994, 1995) for elastic materials. The inverse homogenization approach has also been used in e.g. Otomori et al. (2012) in order to obtain materials with prescribed electromagnetic permittivity for studying the bounds for this complex-valued material property.

The inverse homogenization concept is taken even further in this paper where the microstructures of the viscoelastic composites that realize the theoretical bounds, especially the upper bound, for the viscoelastic bulk modulus are assessed. An important contribution is the development of numerical bounds due to the influence of a connectivity constraint. This is an important bound as it applies to manufacturing processes, such as additive manufacturing, where the metallic phase needs to be connected.

The paper is organized as follows. The viscoelastic model is introduced in Section 2 along with the corresponding bounds. Section 3 presents the homogenization procedure and the topology optimization problem to be solved. The implementation is described in Section 4 and the results are presented in Section 5. Finally, the paper is concluded in Section 6.

2. Method and materials

In this paper a linear viscoelastic material is modeled which is governed by the conservation of momentum, here in time-harmonic form

$$\nabla_X \cdot \boldsymbol{\sigma} + \rho\omega^2 \mathbf{u} = 0 \tag{1}$$

where the capital X denotes the dimensional coordinates, $\boldsymbol{\sigma}$ is the stress tensor which for viscoelastic materials is frequency dependent, ρ is the mass density, ω the frequency, and $\mathbf{u}$ the displacement vector.

The stress–strain relation, Hooke's law, for an isotropic material may be written as a combination of the volumetric and deviatoric contributions as

$$\sigma_{ij}(\omega) = \frac{E(\omega)}{d(1+\nu(1-d))}\varepsilon_{kk}\delta_{ij} + \frac{E(\omega)}{1+\nu}\left(\varepsilon_{ij} - \frac{1}{d}\delta_{ij}\varepsilon_{kk}\right) \tag{2}$$

where $E(\omega)$ is the frequency-dependent stiffness at frequency ω and ν is Poisson's ratio. The parameter $d = \{2, 3\}$ is the spatial dimension and ε_{ij} is the infinitesimal strain defined as

$$\varepsilon_{ij}(\mathbf{u}) = \frac{1}{2}\left(\frac{\partial u_i}{\partial X_j} + \frac{\partial u_j}{\partial X_i}\right) \tag{3}$$

The stiffness of the viscoelastic material is modeled by the Standard Linear Solid (SLS) model (Zener, 1948) which is a relatively simple three parameter model for viscoelastic materials. A spring is assembled in series with a dashpot, a so-called Maxwell element, while another spring is parallel to this assembly. The SLS model is a further development of the Maxwell model, which suffers from vanishing stiffness at infinity. This is addressed by the introduction of the additional spring. The derivation is considered in Appendix A. For a harmonic excitation, the stiffness and the damping can be represented by a complex frequency-dependent stiffness

$$k^*(\omega) = k' + ik'' = k_0 + \frac{k_m\omega^2\tau^2}{1+\omega^2\tau^2} + i\frac{k_m\omega\tau}{1+\omega^2\tau^2} \tag{4}$$

where $\tau = \mu/k_m$ is a characteristic relaxation time i.e. the ratio of viscosity μ and stiffness of the spring k_m in series with the dashpot and k_0 is the stiffness of the spring assembled in parallel. The asterisk indicates a complex number and the single prime denotes the real part of the modulus, which is referred to as the storage modulus, while the double prime denotes the complex part, which is referred to as the loss modulus. This one-dimensional model is used to model the stiffness of the continuum, E, while assuming that the Poisson's ratio is constant, i.e. independent of frequency, and equal to $\nu = 0.3$. The physical consequence of this is the neglection of the possible phase lag between the longitudinal and transversal strains (common relaxation function for both bulk and shear modulus) which may have an impact on the damping properties of the composites (Meaud and Hulbert, 2012). Furthermore Poisson's ratio will be constant in time which is debatable if

Please cite this article as: Andreasen, C.S., et al., On the realization of the bulk modulus bounds for two-phase viscoelastic composites. J. Mech. Phys. Solids (2013), http://dx.doi.org/10.1016/j.jmps.2013.09.007

e.g. a polymer is used as a constituent cf. Lakes and Wineman (2006). The restriction to the choice of materials is only chosen to limit the amount of parameters that change with frequency. The presented procedure for obtaining bounds is general and works independently of these parameter choices.

In order to generalize the approach the governing equations (1)–(4) are non-dimensionalized. Since the effective viscoelastic properties of the two-material composites will be considered, the non-dimensionalization is based on the properties of a reference material, this could e.g. be the softest material. The following relations are introduced with $\widetilde{\square}$ denoting the non-dimensionalized quantities:

$$\widetilde{E}^* = \frac{E^*}{E_0^{ref}}, \quad \widetilde{x}_i = X_i/L_0, \quad \widetilde{u}_i = u_i/L_0, \quad \widetilde{\rho} = \rho/\rho_0^{ref}, \quad \widetilde{\omega} = \sqrt{\frac{\rho_0^{ref}}{E_0^{ref}}} L_0 \omega$$

where E_0^{ref} is the stiffness of the reference material at zero frequency, L_0 the characteristic length e.g. the unit cell size and ρ_0^{ref} the mass density of the reference material. This yields the following non-dimensional equations:

$$\nabla_{\widetilde{x}} \cdot \widetilde{\boldsymbol{\sigma}} + \widetilde{\rho}\widetilde{\omega}^2 \widetilde{\mathbf{u}} = 0 \tag{5}$$

$$\widetilde{\sigma}_{ij} = \frac{\widetilde{E}^*}{d(1+\nu(1-d))} \widetilde{\varepsilon}_{kk}\delta_{ij} + \frac{\widetilde{E}^*}{1+\nu}\left(\widetilde{\varepsilon}_{ij} - \frac{1}{d}\delta_{ij}\widetilde{\varepsilon}_{kk}\right) \tag{6}$$

$$\widetilde{\varepsilon}_{ij}(\widetilde{\mathbf{u}}) = \frac{1}{2}\left(\frac{\partial \widetilde{u}_i}{\partial \widetilde{x}_j} + \frac{\partial \widetilde{u}_j}{\partial \widetilde{x}_i}\right) \tag{7}$$

$$\widetilde{E}^* = \widetilde{E}_0 + \widetilde{E}_m \widetilde{\omega}^2 \frac{\widetilde{\tau}^2}{1+\widetilde{\omega}^2\widetilde{\tau}^2 + i\frac{\widetilde{E}_m \widetilde{\omega}\widetilde{\tau}}{1+\widetilde{\omega}^2\widetilde{\tau}^2}} \tag{8}$$

where

$$\widetilde{E}_0 = E_0/E_0^{ref}, \quad \widetilde{E}_m = E_m/E_0^{ref}, \quad \widetilde{\tau} = \sqrt{\frac{E_0^{ref}}{\rho_0^{ref} L_0}}\,\tau \tag{9}$$

This paper is focused on the damping of vibrations and thus it is appropriate to introduce the loss factor

$$\eta = 2\xi = \tan\,\delta = \frac{\widetilde{E}''}{\widetilde{E}'} \tag{10}$$

where ξ is the damping ratio, and δ the phase angle between cyclic stress and strain.

Furthermore, the vibrations considered are assumed to be in the low frequency range such that quasi-static conditions apply, i.e. the forces due to inertia are negligible and the inertial term in (5) can be neglected.

For the optimization results presented, two base materials with different time-dependent behavior are used. The material parameters used are given in terms of stiffnesses and relaxation times for each of the two materials and are presented in Table 1. One is acting almost as an elastic material i.e. having a large long-term storage modulus, while the other is more *rubbery* with a large instantaneous modulus and a lower long-term storage modulus.

Using the above mentioned material model the stiffness depends on the frequency $\widetilde{\omega}$ as seen from (8) and this is illustrated in Fig. 1 where the storage and loss moduli are plotted versus frequency. The frequency dependence of the viscoelastic material is most pronounced in the two decades from $\widetilde{\omega} = 0.01$ to $\widetilde{\omega} = 1$ in which the storage modulus increases and the damping peaks. The almost elastic material (number 1) has vanishing frequency-dependence. For low frequencies the viscoelastic material (number 2) is relatively soft while it hardens for higher frequencies. In the transition zone from soft to hard the loss modulus is increasing, which is also reflected in Fig. 2 where the loss tangent for both materials is plotted versus the frequency.

The material bounds for isotropic viscoelastic materials are usually not stated using the stiffness, E, and Poisson's ratio, ν, but generally in terms of bulk, $K = E/3(1+2\nu)$ and shear $G = E/2(1+\nu)$ modulus. Furthermore, in order to simplify the notation, the tilde will be omitted in the following sections and the quantities are thus the non-dimensionalized versions.

Table 1
Non-dimensional material parameters for viscoelastic base materials.

	$\widetilde{E}_0$	$\widetilde{E}_m$	$\widetilde{\tau}$	$\widetilde{E}'$ at $\widetilde{\omega} = 0.01$	$\widetilde{E}''$ at $\widetilde{\omega} = 0.01$
Material 1	$20\text{–}10^{-5}$	10^{-5}	10^{7}	20	10^{-10}
Material 2	3	17	5.882	3.059	0.997

Please cite this article as: Andreasen, C.S., et al., On the realization of the bulk modulus bounds for two-phase viscoelastic composites. J. Mech. Phys. Solids (2013), http://dx.doi.org/10.1016/j.jmps.2013.09.007

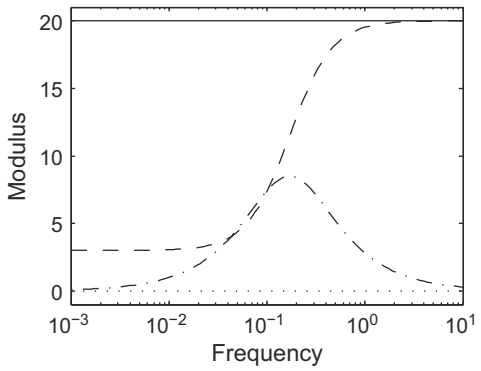

Fig. 1. Frequency dependence of the storage modulus $\widetilde{E}'$ and the loss modulus $\widetilde{E}''$. The solid and dotted lines denote the storage and loss modulus of material 1, respectively. The dashed and dash-dot lines denote the storage and the loss modulus of material 2, respectively.

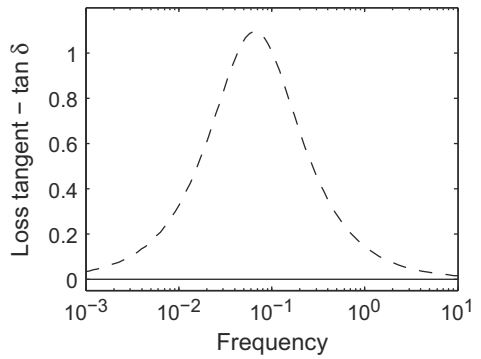

Fig. 2. Frequency dependence of the loss tangent, tan δ. The solid line denotes material 1 while the dashed line denotes material 2.

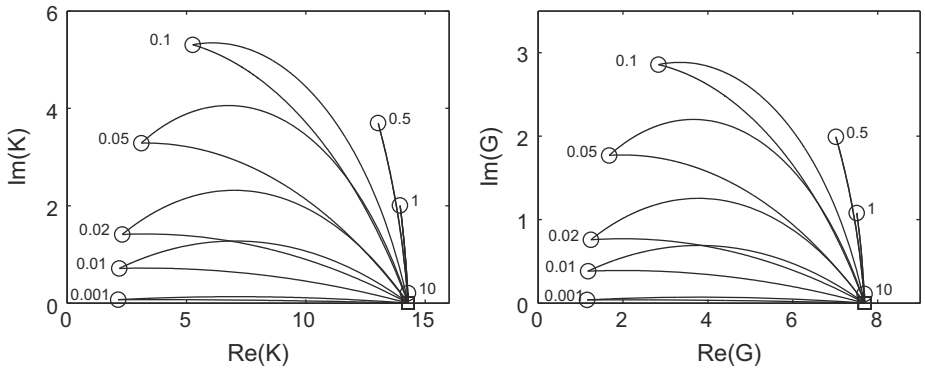

Fig. 3. Frequency dependence of the bounds for two-dimensional viscoelastic composites based on the materials described in Table 1. The small numbers indicate the frequency associated with each set of bounds (Gibiansky and Lakes, 1997).

2.1. Bounds for viscoelastic composites

The bounds for composites of viscoelastic materials have been investigated in the papers by Gibiansky and Milton (1993), Gibiansky and Lakes (1993, 1997), Milton and Berryman (1997) among others. In comparison to the bounds for elastic materials where the bounds for a given volume ratio of the constituents will be given by two numbers, the bounds for the viscoelastic moduli enclose an area in the complex plane. The frequency dependence of the bounds for the moduli of a composite consisting of the aforementioned constituents are illustrated in Fig. 3 for both the bulk and shear modulus.

The bounds are lens shaped with end points that correspond to the material properties of each phase. When the frequency is increased, the moduli change and as material 2 exhibits a clear frequency dependence this endpoint moves in accordance with the plots in Fig. 1. For low frequencies the lens region is very narrow. As the frequency is increased the lens

Please cite this article as: Andreasen, C.S., et al., On the realization of the bulk modulus bounds for two-phase viscoelastic composites. J. Mech. Phys. Solids (2013), http://dx.doi.org/10.1016/j.jmps.2013.09.007

region first expands with increasing frequency and then narrows again. In accordance with the previous plots the storage modulus of the composite will increase with frequency and the loss will peak during the transition frequencies.

3. Theory

The effective moduli for an elastic composite can be computed by homogenization assuming that a unit cell can represent the periodic material (Bensoussan et al., 1978; Sanchez-Palencia, 1980). For a two-phase periodic heterogeneous material (cf. Fig. 4) having the stiffness tensors C^1_{ijkl} and C^2_{ijkl} corresponding to the black (Ω_1) and white (Ω_2) domains, respectively, the effective stiffness can be computed, based on the displacements χ of some test problems, by evaluating the volume integral over the unit cell

$$C^H_{ijkl} = \frac{1}{|\Omega|}\int_\Omega C_{pqrs}\left(\varepsilon^{0(kl)}_{pq} - \varepsilon_{pq}\left(\chi^{kl}\right)\right)\left(\varepsilon^{0(ij)}_{rs} - \varepsilon_{rs}\left(\chi^{ij}\right)\right)\,\mathrm{d}\Omega \tag{11}$$

where $\varepsilon_{rs}(\chi^{ij}) = (\chi^{ij}_{r,s} + \chi^{ij}_{s,r})/2$ is the linear strain tensor and $\varepsilon^{0(ij)}$ is a second order tensor with a single non-zero entry at $\varepsilon^{0(ij)}_{ij}$. The local stiffness tensor, C_{ijkl}, depends on the distribution of material within the unit cell and is here denoted by the indicator function $\mathcal{I}$

$$C_{ijkl} = \begin{cases} C^1_{ijkl} & \text{if } \mathcal{I} \in \Omega_1 \\ C^2_{ijkl} & \text{if } \mathcal{I} \in \Omega_2 \end{cases} \tag{12}$$

where each of the stiffness tensors, $q = \{1, 2\}$, are defined as

$$C^q_{ijkl} = \frac{E^q}{d(1+\nu(1-d))}\delta_{ij}\delta_{kl} + \frac{E^q}{1+\nu}\left(\delta_{ik}\delta_{jl} + \delta_{il}\delta_{jk} - \frac{2}{d}\delta_{ij}\delta_{kl}\right) \tag{13}$$

The displacement fields χ^{kl} are obtained as the solutions to a set of cell problems with periodic boundary conditions obeying the elasticity equations (2). The state equations can in weak form be stated as

Find $\chi^{kl} \in V^3$ such that

$$\int_\Omega \varepsilon_{ij}(\mathbf{v}) C_{ijpq}\varepsilon_{pq}(\chi^{kl})\,\mathrm{d}\Omega = \int_\Omega \varepsilon_{ij}(\mathbf{v}) C_{ijpq}\varepsilon^{0(kl)}_{pq}\,\mathrm{d}\Omega \quad \forall \mathbf{v} \in V^3 \tag{14}$$

where χ^{kl} is V-periodic and corresponds to a straining of the unit cell in each normal and shear direction. Due to symmetry of the stiffness tensor only three and six cases need to be considered for 2D and 3D, respectively.

In a finite element formulation (14) yields a linear equation system

$$\mathbf{K}\mathbf{u}^k = \mathbf{b}^k \tag{15}$$

where the stiffness matrix and load vectors are given by

$$\mathbf{K} = \int_\Omega \mathbf{B}^T\mathbf{D}\mathbf{B}\,\mathrm{d}\Omega, \quad \mathbf{b}^k = \int_\Omega \mathbf{B}^T\mathbf{D}\mathbf{B}\mathbf{u}^k_0\,\mathrm{d}\Omega$$

and periodic boundary conditions are imposed, and where k is the number of load cases (three or six). The strain displacement matrix is denoted $\mathbf{B}$ and the constitutive matrix $\mathbf{D}$ while the pre-strain is given in terms of the prescribed displacements in $\mathbf{u}^k_0$.

3.1. Viscoelasticity—the correspondence principle

The correspondence principle states that it is possible to compute the solution to a viscoelastic problem by the corresponding elastic solution. The viscoelastic solution is obtained by substituting the static stiffness tensor $\mathbf{C}$ with its Laplace transformed counterpart multiplied by the transform variable, i.e. $s\tilde{\mathbf{C}}(s)$. For a harmonic excitation this can be simplified to substituting the static stiffness tensor by the Fourier transformed counterpart, the complex stiffness $\mathbf{C}^*(\omega)$ (cf. Lakes, 2009). By applying the

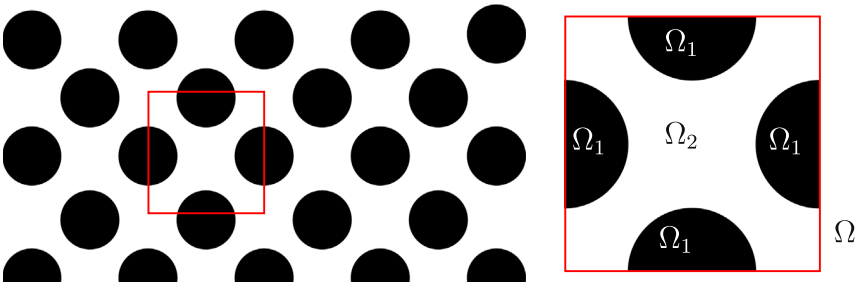

Fig. 4. An illustration of a periodic medium and a representative unit cell.

Please cite this article as: Andreasen, C.S., et al., On the realization of the bulk modulus bounds for two-phase viscoelastic composites. J. Mech. Phys. Solids (2013), http://dx.doi.org/10.1016/j.jmps.2013.09.007

correspondence principle to the homogenization procedure the effective complex stiffness can be computed in analog to the effective static stiffness using the same formulas and methods except that complex arithmetics are needed. In practice we solve (14) where the stiffness tensor **C** is complex.

3.2. Investigating the bounds

The bounds by Gibiansky and Lakes (1997) for the material parameters mentioned previously at frequency $\omega = 0.01$ are plotted in Fig. 5. The results of a simple parameter study of the effective moduli are also presented as markers in the figure. By homogenizing a 30×30 element (2D) square unit cell having a square elastic inclusion (material 1) of varying size embedded in a viscoelastic matrix (material 2) the upper bound is approached for the complex bulk modulus. For orthotropic materials with square symmetry two shear moduli exist and as seen from the figure one of these shear moduli violates the isotropic upper bound while the other stays inside the bounds.

For the opposite material configuration, a viscoelastic square embedded in an elastic matrix, it is possible to approach the lower bound for the complex bulk modulus, while the isotropic bounds for the shear modulus are again violated due to the lack of isotropy. Furthermore, it is evident that when the upper bound is approached the left part is well resolved using a coarse unit cell representation, while the right part of the upper bound is difficult to resolve (indicated by the distance between the markers). In order to reach the bound in this region a high resolution is required to resolve fine micro-structural details with very thin layers of the lossy material phase. The same observation is done for the upper bound on the shear modulus.

3.3. Topology optimization

In the previous section the bounds were reached using a simple orthotropic microstructure with square symmetry. However, obtaining isotropic microstructures by pure intuition is more difficult, thus the use of topology optimization is proposed in order to obtain microstructures that approach the bound. Furthermore, an automated process for obtaining microstructures makes it possible to impose multiple constraints such as e.g. volume and/or connectivity constraints.

The discrete problem of (12) is relaxed by introducing a continuous parameter $\rho \in [0; 1]$, named the relative density, which indicates the fraction of phase-1 material (the stiff phase) in every material point while the rest is phase-2 material. As the optimization proceeds, the material points may take any intermediate value, however, towards the end a 0–1 solution is desired such that the composite can be produced and makes physical sense. Typically, a power-law scheme is chosen for the interpolation

$$C_{ijkl}(\rho) = \rho^p C^1_{ijkl} + (1-\rho)^p C^2_{ijkl} \tag{16}$$

in which ρ is the relative density of phase 1 while p is a penalization parameter that makes intermediate design variables values uneconomical in the optimization process.

For topology optimization of multi-material problems in the frequency domain it has previously been reported (Sigmund and Jensen, 2003) that using a penalization factor of $p = 1$ (linear interpolation) works well. However, the problem at hand is different and hence we investigate the consequences of choosing another penalization parameter. In order to investigate the influence from the penalization parameter, the effective complex moduli of the structures used in the previous section are plotted versus the relative density in Fig. 6. It is clearly seen that for both the real part of the bulk and shear modulus a power-law interpolation with an exponent larger than one, resulting in a convex function, would be representative. However, for the complex part it is seen that the largest imaginary part is present when the relative density is approximately 0.8 and that it is lower in both ends of the density range. This is approximated much better by a concave

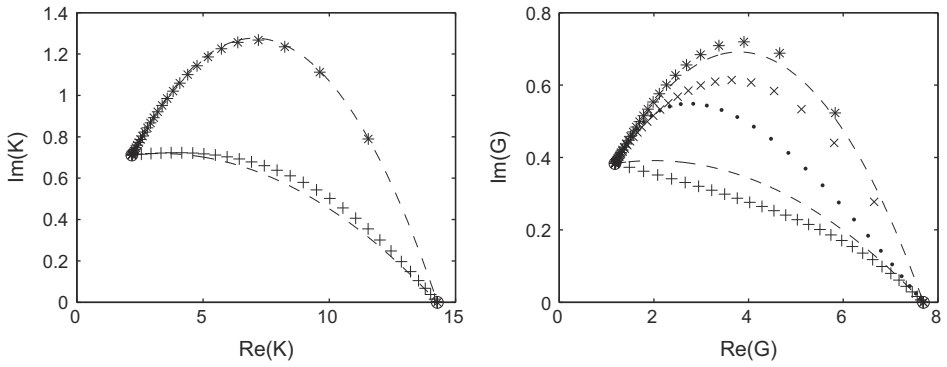

Fig. 5. Upper and lower bounds for an isotropic composite consisting of materials mentioned in Table 1. The asterisk (∗) and cross (x) markers correspond to the composite with a square inclusion of elastic material in a viscoelastic matrix. Plus (+) and dot (·) is vice versa. As the microstructure only exhibits square symmetry two shear moduli exist, hence four datasets are plotted in the right figure. Bounds from Gibiansky and Lakes (1997).

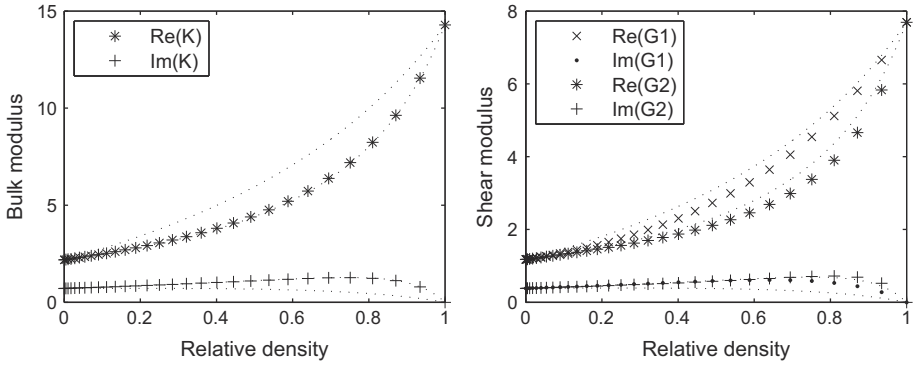

Fig. 6. Effective complex moduli vs. relative density corresponding to the composite with a square inclusion of elastic material in a viscoelastic matrix for $\omega = 0.01$. Two shear moduli exist as the material exhibits square symmetry. Bounds (Gibiansky and Lakes, 1997) are plotted as dotted lines.

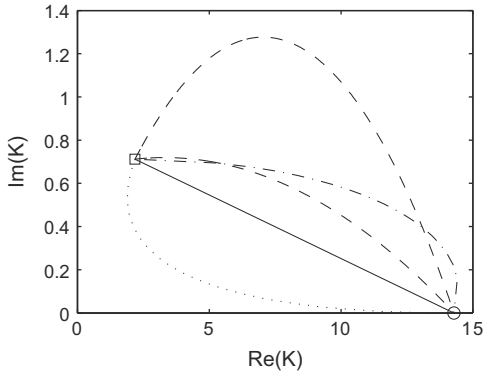

Fig. 7. Interpolation function from (16) and bounds (dashed lines) (Gibiansky and Lakes, 1997). Solid line is the interpolation with $p=1$, Upper dash-dotted line is interpolation with $p=0.5$ and the dotted lower line is interpolation $p=2$.

function i.e. power-law with exponent less than one. As a compromise no penalization is used, i.e. $p=1$ for both real and complex moduli, which yields a linear interpolation function. As can be seen in Fig. 7, the interpolation violates the lower bound for the complex bulk modulus. However, this is not seen as a problem for an objective function where the imaginary part of the modulus is maximized since material points having intermediate densities perform worse than black/white.

In relation to vibration damping it is of great interest to approach the upper bound for the complex modulus as this, for a given real modulus, will result in the highest possible damping cf. (10). The problem of distributing material within a unit cell in order to achieve maximum damping is formulated as a topology optimization problem

$$\begin{array}{lllll} \max\limits_{\boldsymbol{\rho}\in\mathbb{R}^N} & Im(K^H) & & & \text{Loss modulus} \\ \text{subject to} & \mathbf{K}\mathbf{u}^k = \mathbf{b}^k & \text{for } k=1,\ldots,3(d-1) & & \text{State equations (15)} \\ & Re(K^H) < K_{min} & & & \text{Minimum storage} \\ & g < 0 & & & \text{Isotropy constraint} \\ & 0 \le \rho_e \le 1 & \text{for } e=1,\ldots,N & & \text{Box constraints} \end{array} \tag{17}$$

where N denotes the number of design variables and K_{min} denotes the minimum desired real bulk modulus. As the underlying homogenization method computes the homogenized stiffness matrix the bulk and shear moduli can be computed assuming isotropy based on the C^H_{11} and C^H_{12} coefficients. However, in order to increase the robustness in case of anisotropic intermediate designs the bulk modulus is computed as the average of two expressions. In 2D this yield

$$K^H = (C^H_{11} + C^H_{22} + 2C^H_{12})/4 \tag{18}$$

and the shear modulus is computed as

$$G^H = (C^H_{11} + C^H_{22} - 2C^H_{12} + 2C^H_{33})/6 \tag{19}$$

Please cite this article as: Andreasen, C.S., et al., On the realization of the bulk modulus bounds for two-phase viscoelastic composites. J. Mech. Phys. Solids (2013), http://dx.doi.org/10.1016/j.jmps.2013.09.007

The isotropy constraint is formulated as the error between the effective stiffness matrix and the corresponding isotropic stiffness matrix based on the homogenized K^H and G^H i.e.

$$g = \sum_{i=1}^{6}\sum_{j=1}^{6}\frac{(C_{ij}^H - C_{ij}^{iso})^2}{(C_{11}^H)^2} - \varepsilon^2 < 0 \tag{20}$$

where ε is a small number (i.e. 10^{-3}).

3.3.1. Connectivity of the elastic phase

Connectivity of the elastic phase can be ensured in different ways. One option is to impose a stiffness constraint assuming that the viscoelastic phase is softer than the elastic one and thereby force connectivity between regions of elastic material. This, however, is problematic when the frequency goes up as the stiffness of the viscoelastic material will increase and the connectivity of the elastic phase cannot be ensured.

As a better alternative we solve an additional homogenization problem, namely a conductivity problem similar to Sigmund (1999) on top of the existing problem. Using the same design but assigning good conductive properties to the elastic phase and poor to the viscoelastic phase, connectivity can be ensured by enforcing a lower bound on the conductivity i.e. an additional constraint

$$g = 1 - \sigma^H/\sigma_0 \leq 0 \tag{21}$$

where σ_0 is the desired minimum effective conductivity.

Cross property bounds between bulk modulus and electrical/thermal conductivity exist for isotropic materials with real material properties and are described in Gibiansky and Torquato (1996). These bounds are also constructed using the translation method and span an area in the conduction-bulk modulus plane. The cross property bounds for bulk storage and conductivity can be seen in Fig. 8 where three infeasible property combinations are indicated, namely the combinations ($K=3$, $\sigma=0.1$), ($K=3$, $\sigma=0.2$), ($K=4$, $\sigma=0.2$). These points are marked as they belong to the set of investigated material designs and become unrealizable due to the conductivity constraint and cross property bound.

Alternatively, connectivity can be ensured by constraining the lowest eigenfrequency of the metallic phase in the unit cell to be greater than zero (letting the stiffness of the second phase vanish) (Wang et al., 2011). However, there are two issues with such a procedure for the present design problem. The first is that the computational effort is much larger than solving the heat conduction problem. The second, which might be more problematic, is that it is not straightforward to impose boundary conditions for the associated eigenvalue problem as the metallic structure may not be present at the boundary of the domain cf. Fig. 9.

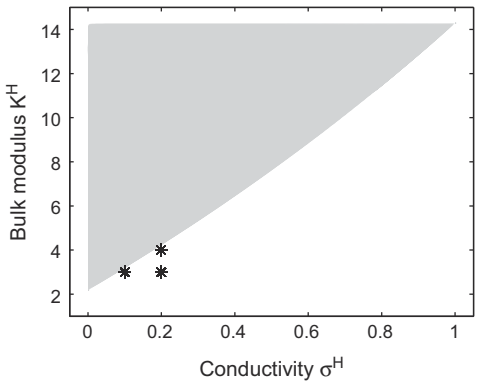

Fig. 8. The shaded area is the feasible set of conductivity and bulk storage properties. The three markers indicate the points ($K=3$, $\sigma=0.1$), ($K=3$, $\sigma=0.2$) and ($K=4$, $\sigma=0.2$) which lie outside the cross property bounds (Gibiansky and Torquato, 1996) and thus cannot be realized.

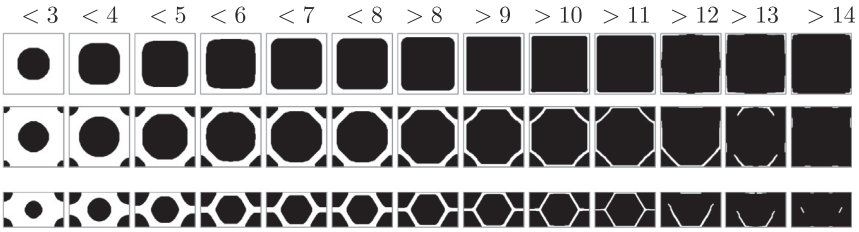

Fig. 9. Optimized microstructures for maximum bulk loss modulus. Top row using square design domain and square symmetry, middle row using a square design domain with isotropic symmetry and bottom row using a rectangular design domain with isotropic symmetry. Each column corresponds to a different constraint on the effective bulk storage modulus.

Please cite this article as: Andreasen, C.S., et al., On the realization of the bulk modulus bounds for two-phase viscoelastic composites. J. Mech. Phys. Solids (2013), http://dx.doi.org/10.1016/j.jmps.2013.09.007

4. Implementation

In order to solve the inverse homogenization problem by topology optimization a numerical homogenization procedure (cf. Guedes and Kikuchi, 1990) is implemented. The practical implementation is twofold, one for the two-dimensional problem implemented in Matlab and another for the three-dimensional problem implemented using a parallel C++ framework DFEM (Aage and Lazarov, 2013), however, they have much in common. They both use linear elements and the periodic boundary conditions are imposed by sharing nodes between elements on each side of the unit cell. A single node is fully constrained in order to avoid rigid body motion.

The equation system differs from that of the corresponding elastic problem as it includes complex variables and the system matrix is non-Hermitian which means that neither a direct solver based on a Cholesky factorization nor a conjugate gradient method can be used. Instead the 2D implementation uses a direct solver with LU-factorization while the 3D implementation uses a block version of a Jacobi-preconditioned stabilized bi-conjugate gradient method (van der Vorst, 1992). For the 2D problems the unit cells have been discretized using square regular bi-linear finite elements which, for the square domains, consist of 100×100 elements while the rectangular domains consist of 140×80 elements. For the 3D problems the cubic unit cells have been discretized using tri-linear elements and the resolution of either $40 \times 40 \times 40$ or $60 \times 60 \times 60$ elements.

The topology optimization procedure is similar to that in Sigmund (1995) used for elastic materials and the optimization problem is solved using the Method of Moving Asymptotes (MMAs) kindly provided by Svanberg (1987). The design is regulated using a Heaviside projection filter (Guest et al., 2004; Sigmund, 2007) in order to get black/white designs. By experience the regularization is only needed when the conductivity constraint is imposed, however, for consistency it is applied to all designs.

Material microstructure design problems are prone to local minima related to small details in the microstructure or reentrant structures. A continuation scheme has been imposed in the discreteness measure of the Heaviside projection filter and the isotropy error (ε) in order to give the optimizer more freedom in the beginning of the optimization process, and avoid getting stuck prematurely in a local minimum.

5. Results and discussion

In this section the composites that realize the upper bound for viscoelastic bulk modulus will be presented both in two and three dimensions. This is followed by manufacturable optimized designs in two and three dimensions which is ensured by the conductivity constraint.

5.1. Extreme bulk modulus structures in 2D

Optimizing for the bulk loss modulus the upper bound is approached and in order to find structures along the upper bound, restrictions are imposed on the effective bulk storage modulus. Vigdergauz (1994) presented optimal single scale microstructures for elastic materials, which also showed up in Sigmund (2000) where extremal two phase elastic composites were investigated. The microstructures that exhibit the highest bulk modulus either have a honeycomb structure (near circular void inclusions in a triangulas) which requires a rectangular unit cell or an octagonal structure with circular inclusions of two different sizes supporting a square unit cell. For this first case both unit cell types have been investigated for the maximization of the bulk loss modulus. The performances of the realized structures are shown in Fig. 10 while the corresponding designs are shown in Fig. 9. From the figure it is clearly seen that Vigdergauz structures are obtained. The upper row exhibits square symmetry while the two lower rows exhibit isotropic symmetry. As the requirements for the bulk storage are increased (moving towards right in the plot) it gets progressively

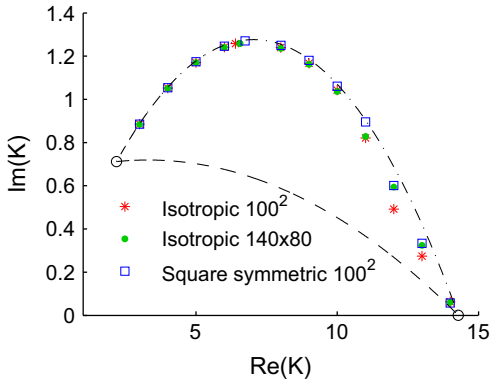

Fig. 10. Performance of the optimized microstructures for maximum imaginary bulk modulus along with the corresponding bounds (Gibiansky and Lakes, 1997) for $\omega = 0.01$. The optimized designs are shown in Fig. 9.

Please cite this article as: Andreasen, C.S., et al., On the realization of the bulk modulus bounds for two-phase viscoelastic composites. J. Mech. Phys. Solids (2013), http://dx.doi.org/10.1016/j.jmps.2013.09.007

more difficult to resolve the details of the microstructures so, due to the finite mesh resolution, the designs lose geometric symmetry and the performances decrease in comparison to the upper bound.

5.2. Extreme bulk modulus structures in 3D

Fig. 11 shows four 3D isotropic microstructures obtained by tracing the upper complex bulk modulus bound. The phase properties used are the same as for the 2D case and the homogenized complex bulk modulus of the obtained designs are compared to the bounds from Gibiansky and Lakes (1993) in Fig. 12, where it can be seen that, as in the 2D case, the right part of the bound is not attained due to the limited discretization. With the coarsest discretization (40^3 elements) the obtained designs deviate more from the bounds, because the loss is maximized by making sure the stiff phase is unconnected. Assuring an unconnected stiff phase requires a larger volume fraction of the soft phase for a coarser discretization, and for the material in Fig. 11(d) there is simply not enough soft material to isolate the stiff phase. From a manufacturing point of view a connected phase is desired in e.g. selective laser sintering. However, the connectivity of the structure should rather be ensured by imposing a constraint than by relying on the coarseness of the discretization.

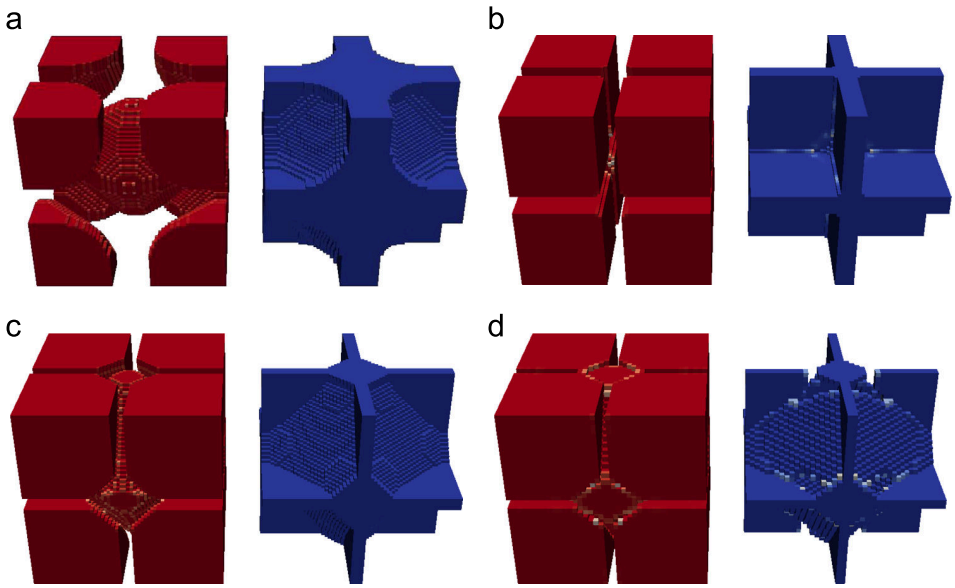

Fig. 11. Optimized microstructures for maximum imaginary part of bulk modulus. Left: stiff phase. Right: soft phase. (a), (c) and (d) are isotropic, while (b) is cubic symmetric.

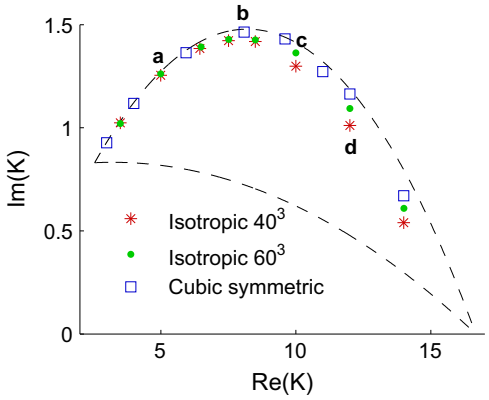

Fig. 12. Performance of the optimized three-dimensional microstructures compared to the theoretical bounds (Gibiansky and Lakes, 1993) for $\omega = 0.01$. The letters refer to the designs in Fig. 11.

Please cite this article as: Andreasen, C.S., et al., On the realization of the bulk modulus bounds for two-phase viscoelastic composites. J. Mech. Phys. Solids (2013), http://dx.doi.org/10.1016/j.jmps.2013.09.007

5.3. Manufacturability in 2D

The structures optimized in the previous section might not be realized easily as an inclusion of the elastic phase is embedded into a viscoelastic matrix. The targeted manufacturing process is a two step procedure in which the first step is to create a metallic matrix by selective laser sintering and the second step is to infiltrate the matrix with a viscoelastic filler. Hence, the elastic phase should be connected in order to function as a matrix. The infiltration process also requires the structures to be open. However, for 2D designs, both conditions cannot be fulfilled. In this case we consider the open cell requirement to relate to the out-of-plane direction and thus to be fulfilled.

Based on the above considerations the optimization formulation is modified by adding a conductivity constraint. The optimized designs with this constraint are shown in Fig. 13. Rows one and two are obtained imposing a conductivity constraint of $\sigma^H > 0.1\sigma_0$ and square and isotropic symmetry, respectively. Rows three and four are obtained imposing a conductivity constraint of $\sigma^H > 0.2\sigma_0$ for square and isotropic symmetry, respectively. Each column corresponds to a specific constraint on the effective bulk storage modulus ranging from $Re(K^H) < 3$ to $Re(K^H) > 14$ in order to assess the entire upper bound. The designs in row one and three are more easily obtained than the other two due to the lower degree of material symmetry. In comparison to the structures in Fig. 9 (upper row) the designs differ by the connection such that the elastic material now forms a matrix instead of being inclusions. For the lowest effective bulk storage the designs deviate more and the joint of the matrix takes a flower shape. This, however, might be a local minima rather than a global one. When tightening the conductivity constraint we generally observe that the *connectors* between the inclusions get wider.

For the isotropic designs in the second and fourth row the structures do show similarities with the ones obtained without conductivity constraint. Except for the connections between the solid inclusions they also, at least until $Re(K^H) > 9$, roughly consist of two different sized inclusions connected by thin pins. For the designs $Re(K^H) > 9$ until $Re(K^H) > 14$ there is a change in topology that performs better than if the previous topology was adapted to the increased storage demands.

The designs ($Re(K^H) > 3$, $\sigma^H/\sigma_0 > 0.1$) and ($Re(K^H) > 4$, $\sigma^H/\sigma_0 > 0.2$) do not fulfill the isotropy constraint completely as the optimizer has a very hard time making the design feasible.

The performances corresponding to the designs are shown in Fig. 14 where the different conditions are indicated by different markers. It is seen that the curves for the square and isotropic symmetry almost overlap. Moving towards right

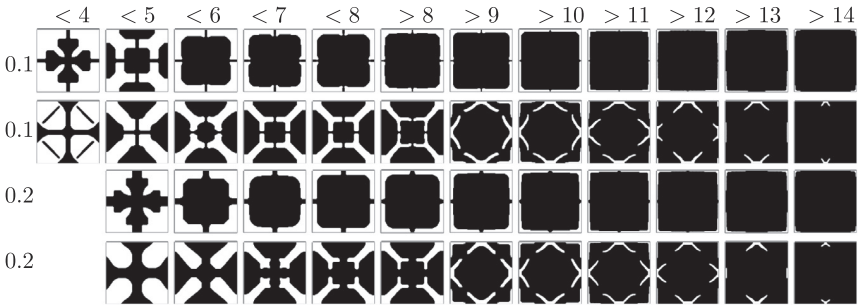

Fig. 13. Optimized microstructures for maximum imaginary bulk modulus subject to constraints on storage modulus (columns) and conductivity (2×2 rows). The microstructures exhibit square symmetry (rows 1 and 3) and isotropic symmetry (rows 2 and 4).

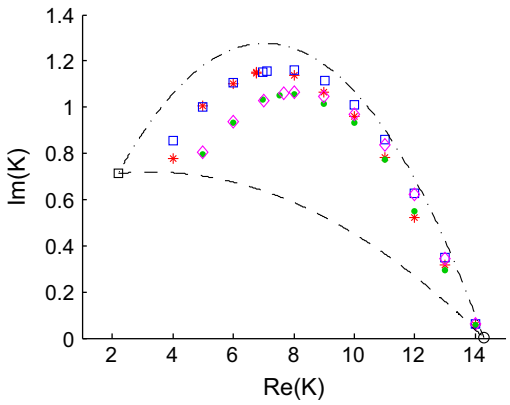

Fig. 14. Performance of the optimized microstructures for maximum bulk loss modulus along with the corresponding bounds (Gibiansky and Lakes, 1997) for $\omega = 0.01$. The blue square (□) and red asterisk (∗) yields $\sigma^H/\sigma_0 > 0.1$ and exhibit square and isotropic symmetry, respectively. The magenta diamond (⋄) and green dot (·) yields $\sigma^H/\sigma_0 > 0.2$ and exhibit square and isotropic symmetry, respectively. (For interpretation of the references to color in this figure caption, the reader is referred to the web version of this paper.)

Please cite this article as: Andreasen, C.S., et al., On the realization of the bulk modulus bounds for two-phase viscoelastic composites. J. Mech. Phys. Solids (2013), http://dx.doi.org/10.1016/j.jmps.2013.09.007

they deviate more as the details within the designs combined with the isotropy constraint make it difficult to obtain feasible designs that are as close to the upper bound as the square symmetric ones. Based on these results a new numerical upper bound can be constructed which bounds the structures with a connected *stiff* elastic phase.

Due to the cross property bounds shown in Fig. 8 it is seen that designs that both restrict the maximum bulk storage and the minimum conductivity might be infeasible. Thus no designs are presented for ($Re(K^H) < 3$, $\sigma^H/\sigma_0 > 0.1$), ($Re(K^H) < 3$, $\sigma^H/\sigma_0 > 0.2$) and ($Re(K^H) < 4$, $\sigma^H/\sigma_0 > 0.2$).

5.4. Manufacturability in 3D

The performance-effect of the conductivity constraint in 3D is the same as in 2D; it limits how closely the bounds can be approached. This is illustrated in Fig. 16 where the upper bound is traced with a conductivity constraint of 10% ($\sigma^H/\sigma_0 > 0.1$).

Opposed to the two-dimensional designs, the designs in three dimensions allow for both phases to be connected. This is clearly seen for the case with cubic-symmetric material design in Fig. 15(a), where the stiff phase is connected with rods compared to Fig. 11(b) where the stiff phase is an inclusion in a lossy matrix.

The constraint ensures some connectivity between the stiff parts, but isolated stiff islands can still appear. This is the case for the isotropic designs in Fig. 15(b) and (c), where the stiff phase is only partially connected and the material is therefore

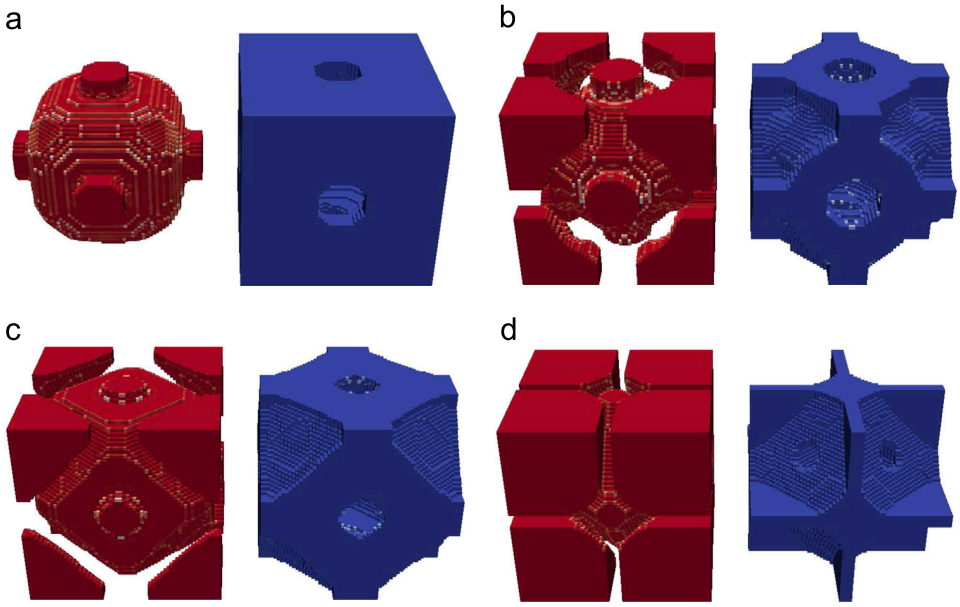

Fig. 15. Optimized microstructures for maximum imaginary part of bulk modulus with a conductivity constraint. In each set of two, left is stiff and right is lossy phase. Design (a) has cubic symmetry and the remaining have isotropic symmetry.

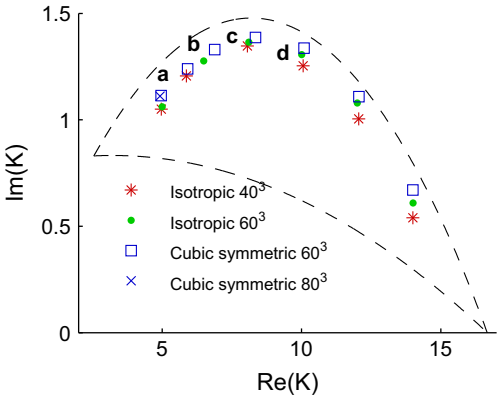

Fig. 16. Performance of the microstructures optimized with a conductivity constraint compared to the theoretical bounds (Gibiansky and Lakes, 1993). The conductivity in the stiff phase is required to be at least ten percent of the phase material's conductivity. $\omega = 0.01$. The letters refer to the designs in Fig. 15.

not readily manufacturable. However, as shown in Fig. 15(d) it is also possible to obtain a manufacturable isotropic material using the constraint. The differences in the designs originate from the two different initial guesses being used. The designs in Fig. 15(b) and (c) were obtained with a stiff cross as an initial guess, while the design in Fig. 15(d) was obtained having stiff spheres in the corners in the initial guess. The performance does not seem to be affected negatively by the full connectivity, since the coarse discretization material next to point (d) in Fig. 16 has the same topology as points (b) and (c). In order to investigate the influence from the discritization the result for a single optimization using a higher resolution (80^3 elements) is presented. The optimized structure is similar to the one in Fig. 15(a) and performs equally good. This indicates that the discretization is not a problem for structures with a moderate storage modulus $Re(K^H)$.

The conductivity constraint can be used to obtain manufacturable designs, but it does not assure manufacturable designs in 3D. It should be mentioned that requiring a larger conductivity is not guaranteed to assure manufacturability, you still risk either isolated stiff or soft islands.

As a larger storage modulus is required the importance of the conductivity constraint diminishes, and the structures at the rightmost part of the upper bound are identical to the ones obtained without the conductivity constraint.

6. Conclusions

This paper presents a method to optimize the damping capabilities of viscoelastic composite materials by designing the material microstructure taking the manufacturability of the microstructure into account. The method is demonstrated for material properties corresponding to a single frequency, however, if the composite material is targeted for a broader frequency range the optimization problem may be changed to a min–max type problem to account for multiple frequencies.

It is demonstrated that the design method is capable of attaining the upper bound for the bulk loss modulus when manufacturability is neglected. If manufacturability is considered the upper bound shrinks such that only lower bulk loss modulus and higher bulk storage modulus are obtainable. This provides new numerical bounds for viscoelastic composites which have stiff elastic matrix constructed for example by additive manufacturing.

The quasi-static approach taken in this paper allows for the design of materials for low frequency application where the wavelength is much larger than the size of the unit cell. For applications at higher frequency/shorter wavelength one can resort to a fully dynamic approach by solving several microscale eigenvalue problems based on a Bloch wave expansion. Additionally a multiscale model could be considered which, in addition, would allow the material microstructure to vary throughout the macrostructure.

Acknowledgments

This research was supported by the Danish Ministry of Science, Technology and Innovation through a Grant to the F.MAT innovation consortium.

Appendix A. Frequency domain stiffness for Standard Linear Solid

If a Maxwell element (spring and dashpot in serial) is mounted parallel to a spring the Standard Linear Solid (SLS) model is constructed. The difference from a Maxwell element is that at infinite time, the material has a stiffness, the relaxation modulus.

Both branches in the SLS model is subjected to the same strain and the total stress is the sum of stresses in each branch. The stress–strain relation for the Maxwell element is given by

$$k\dot{\varepsilon} = \dot{\sigma}_m + \frac{1}{\tau}\sigma_m \tag{22}$$

where $\tau = \mu/k$ is the ratio between the viscosity of the damper and the spring stiffness. The stress–strain relation in the spring follows Hooke's law:

$$\sigma_e = k_e\varepsilon \tag{23}$$

For the case of harmonic excitation the stress and strain can be represented by exponential functions such that

$$\sigma(t) = \sigma_0^* \exp(i\omega t) \quad \text{and} \quad \varepsilon(t) = \varepsilon_0^* \exp(i\omega t) \tag{24}$$

Inserting into (A.(1) and A.2) the total stress is given by

$$\sigma_t^* = \sigma_e^* + \sigma_m^* = \varepsilon_0^*\left(k_e + \frac{i\omega k\tau}{1+i\omega\tau}\right) \tag{25}$$

which is now independent of time but dependent on frequency. The complex relaxation modulus can be obtained from the relation between stress and strain as

$$C^*(\omega) = \frac{\sigma_t^*}{\varepsilon_0^*} = k_e + \frac{i\omega k\tau}{1+i\omega\tau} = k_e + \frac{k\omega^2\tau^2}{1+\omega^2\tau^2} + i\frac{k\omega\tau}{1+\omega^2\tau^2} \tag{26}$$

Please cite this article as: Andreasen, C.S., et al., On the realization of the bulk modulus bounds for two-phase viscoelastic composites. J. Mech. Phys. Solids (2013), http://dx.doi.org/10.1016/j.jmps.2013.09.007

A drawback of the SLS model is that the stiffness drops in two decades of time which compared to *real* materials is too fast (Lakes, 2009). A more sophisticated model can be obtained by adding more Maxwell elements in parallel. For each extra Maxwell element there will be another 2 parameters, stiffness and viscosity, which will add an extra term to the total stress in (25).

References

Aage, N., Lazarov, B., 2013. Parallel framework for topology optimization using the method of moving asymptotes. Struct. Multidiscip. Optimization 47 (4), 493–505.
Bensoussan, A., Lions, J., Papanicolaou, G., 1978. Asymptotic Analysis for Periodic Structures. North-Holland Publishing Co..
Brodt, M., Lakes, R., 1995. Composite materials which exhibit high stiffness and high viscoelastic damping. J. Compos. Mater. 29 (14), 1823–1833.
Cherkaev, A.V., Gibiansky, L.V., 1994. Variational principles for complex conductivity, viscoelasticity, and similar problems in media with complex moduli. J. Math. Phys. 35 (1), 127–145.
Francfort, G.A., Murat, F., 1986. Homogenization and optimal bounds in linear elasticity. Arch. Ration. Mech. Anal. 94, 307–334.
Gibiansky, L., Lakes, R., 1997. Bounds on the complex bulk and shear moduli of a two-dimensional two-phase viscoelastic composite. Mech. Mater. 25 (2), 79–95.
Gibiansky, L., Torquato, S., 1996. Connection between the conductivity and bulk modulus of isotropic composite materials. Proc. R. Soc. London Ser. A Math. Phys. Eng. Sci. 452 (1945), 253–283.
Gibiansky, L.V., Lakes, R., 1993. Bounds on the complex bulk modulus of a 2-phase viscoelastic composite with arbitrary volume fractions of the components. Mech. Mater. 16 (3), 317–331.
Gibiansky, L.V., Milton, G.W., 1993. On the effective viscoelastic moduli of two-phase media. I. Rigorous bounds on the complex bulk modulus. Proc. R. Soc. London Ser. A Math. Phys. Sci. 440 (1908), 163–188.
Guedes, J., Kikuchi, N., 1990. Preprocessing and postprocessing for materials based on the homogenization method with adaptive finite element methods. Comput. Methods Appl. Mech. Eng. 83 (2), 143–198.
Guest, J.K., Prévost, J.H., Belytschko, T., 2004. Achieving minimum length scale in topology optimization using nodal design variables and projection functions. Int. J. Numer. Methods Eng. 61 (2), 238–254.
Hashin, Z., 1965. Viscoelastic behavior of heterogeneous media. J. Appl. Mech. 32 (3), 630–636.
Hashin, Z., 1970. Complex moduli of viscoelastic composites. I. General theory and application to particulate composites. Int. J. Solids Struct. 6 (5), 539–552.
Hashin, Z., Shtrikman, S., 1963. A variational approach to the theory of the elastic behaviour of multiphase materials. J. Mech. Phys. Solids 11 (2), 127–140.
Lakes, R.S., Wineman, A., 2006. On Poisson's ratio in linearly viscoelastic solids. J. Elasticity 85, 45–63.
Lakes, R.S., 2009. Viscoelastic Materials. Cambridge University Press.
Lurie, K.A., Cherkaev, A.V., 1986. Exact estimates of the conductivity of a binary mixture of isotropic materials. Proc. R. Soc. Edinburgh Sect. A Math. 104 (1–2), 21–38.
Meaud, J., Hulbert, G.M., 2012. Dependence of the dynamic properties of Voigt and Reuss composites on the Poisson's ratio and bulk loss factors of the constituent materials. J. Compos. Mater., published online, http://dx.doi.org/10.1177/0021998312463456.
Millet, P., Schaller, R., Benoit, W., 1981. Characteristic internal friction spectrum of grey cast iron. J. Phys. Colloq. 42 (C5). C5-929–C5-934.
Milton, G.W., Berryman, J.G., 1997. On the effective viscoelastic moduli of two-phase media. ii. rigorous bounds on the complex shear modulus in three dimensions. Proc. R. Soc. London Ser. A Math. Phys. Eng. Sci. 453 (1964), 1849–1880.
Otomori, M., Andkjaer, J., Sigmund, O., Izui, K., Nishiwaki, S., 2012. Inverse design of dielectric materials by topology optimization. Prog. Electromagnetics Res. 127, 93–120.
Sanchez-Palencia, E., 1980. Non-homogeneous media and vibration theory. Lecture Notes in Physics, vol. 127. . Springer-Verlag, Berlin, Heidelberg, New York.
Sigmund, O., 1994. Materials with prescribed constitutive parameters: an inverse homogenization problem. Int. J. Solids Struct. 31 (17), 2313–2329.
Sigmund, O., 1995. Tailoring materials with prescribed elastic properties. Mech. Mater. 20 (4), 351–368.
Sigmund, O., 1999. On the optimality of bone microstructure. In: Pedersen, P., Bendse, M. (Eds.), Synthesis in Bio Solid Mechanics. IUTAM, Kluwer, pp. 221–234.
Sigmund, O., 2000. A new class of extremal composites. J. Mech. Phys. Solids 48 (2), 397–428.
Sigmund, O., Jensen, J.S., 2003. Systematic design of phononic bandgap materials and structures by topology optimization. Philos. Trans. R. Soc. London A 361, 1001–1019.
Sigmund, O., 2007. Morphology-based black and white filters for topology optimization. Struct. Multidiscip. Optimization 33 (4–5), 401–424.
Svanberg, K., 1987. The method of moving asymptotes—a new method for structural optimization. Int. J. Numer. Methods Eng. 24 (2), 359–373.
van der Vorst, H., 1992. Bi-cgstab: a fast and smoothly converging variant of bi-cg for the solution of nonsymmetric linear systems. SIAM J. Sci. Stat. Comput. 13 (March (2)), 631–644.
Vigdergauz, S.B., 1994. Two-dimensional grained composites of extreme rigidity. J. Appl. Mech. 61 (2), 390–394.
Wang, F., Jensen, J.S., Sigmund, O., 2011. Robust topology optimization of photonic crystal waveguides with tailored dispersion properties. J. Opt. Soc. Am. B 28 (3), 387–397.
Yi, Y.-M., Park, S.-H., Youn, S.-K., 1998. Asymptotic homogenization of viscoelastic composites with periodic microstructures. Int. J. Solids Struct. 35 (17), 2039–2055.
Yi, Y.-M., Park, S.-H., Youn, S.-K., 2000. Design of microstructures of viscoelastic composites for optimal damping characteristics. Int. J. Solids Struct. 37 (35), 4791–4810.
Zener, C., 1948. Elasticity and Anelasticity of Metals. University of Chicago Press, Chicago.

Please cite this article as: Andreasen, C.S., et al., On the realization of the bulk modulus bounds for two-phase viscoelastic composites. J. Mech. Phys. Solids (2013), http://dx.doi.org/10.1016/j.jmps.2013.09.007

Publication [P5]

Analysis of phononic bandgap structures with dissipation

Analysis of Phononic Bandgap Structures With Dissipation

Erik Andreassen

Jakob S. Jensen
e-mail: jsj@mek.dtu.dk

Department of Mechanical Engineering,
Technical University of Denmark,
Building 404, 2800 Denmark

We study wave propagation in periodic materials with dissipation using two different formulations. An $\omega(\mathbf{k})$-formulation yields complex frequency solutions for nonvanishing dissipation whereas a $\mathbf{k}(\omega)$-formulation leads to complex wave numbers. For small (realistic) levels of material dissipation and longer wavelengths, we show that the two formulations produce nearly identical results in terms of propagation constant and wave decay. We use the $\mathbf{k}(\omega)$-formulation to compute loss factors with dissipative bandgap materials for steady-state wave propagation and create simplified diagrams that unify the spatial loss factor from dissipative and bandgap effects. Additionally, we demonstrate the applicability of the $\mathbf{k}(\omega)$-formulation for the computation of the band diagram for viscoelastic composites and compare the computed loss factors for low frequency wave propagation to existing results based on quasi-static homogenization theory. [DOI: 10.1115/1.4023901]

1 Introduction

Phononic bandgap materials have been studied extensively since the early 1990s. These periodic materials are often characterized by their band diagram, which relates the wave vector for freely propagating waves to the frequency of propagation. This was done, e.g., in Ref. [1], wherein a numerical study of in-plane wave propagation in a two-dimensional periodic material consisting of circular steel inclusions in an epoxy matrix was conducted and the existence of gaps in the band diagram, for which waves cannot propagate regardless of their direction, was demonstrated. This early work was followed by a large number of papers on the subject, e.g., Ref. [2] that considers a three-dimensional periodic material made up of spherical tungsten inclusions in an polyethylene matrix. In this paper, numerical evidence for the existence of large bandgaps was given. A number of experimental studies has been conducted as well, e.g., Ref. [3], and has supported the theoretical findings and demonstrated bandgaps in practice.

The work on phononic bandgap materials was partly motivated by similar work on photonic bandgap materials initiated by pioneering work that demonstrated the spontaneous emission of photons in periodic configurations of dielectric materials [4,5], and the comprehensive work in Ref. [6], which provided band diagrams and demonstrated bandgaps for a large number of periodic configurations of dielectric materials. However, the initial studies on elastic materials also root back to fundamental work on wave propagation in periodic media by Lord Rayleigh [7] and the thorough study on waves in lattices conducted by Brillouin [8], who extensively discusses the existence of pass and stop bands for waves encompassing the bandgap phenomenon.

A key point in the study of time-harmonic waves in a periodic medium is the use of the Bloch wave expansion [9] which consists in an expansion of the wave solution on the following form:

$$\mathbf{u}(\mathbf{x},t) = \tilde{\mathbf{u}}(\mathbf{x})e^{i\mathbf{k}^T\mathbf{x}}e^{i\omega t} \tag{1}$$

in which ω is the wave frequency, $\mathbf{k}$ is the wave vector, and $\tilde{\mathbf{u}}$ is a periodic wave function on the repetitive unit cell of the periodic material. As an important feature, the Bloch wave expansion allows us to construct the entire band diagram from analysis on the unit cell only.

As has been thoroughly demonstrated in the many papers dealing with the bandgap phenomenon, no real solutions in the band diagram $(\omega,\mathbf{k})$ exist in the bandgap frequency range. Instead, solutions with real ω and purely imaginary $\mathbf{k} = i\mathbf{k}''$ exist, which lead to the solution form

$$\mathbf{u}(\mathbf{x},t) = (\tilde{\mathbf{u}}(\mathbf{x})e^{i\omega t})e^{-(\mathbf{k}'')^T\mathbf{x}} \tag{2}$$

that describes standing waves with an exponentially decaying amplitude (evanescent waves). Consequently, waves within the bandgap are rapidly attenuated spatially. This is also reflected in the very low vibration and wave transmission levels encountered in finite structures made up of a periodic material and subjected to time-harmonic loading at these frequencies [10,11]. The role of structural damping for the dynamics of finite bandgap structures has been analyzed in a number of papers as well (see, e.g., Refs. [12,13]).

The basic influence of damping on the wave propagation in periodic materials has been studied less intensively. An analysis method based on a fixed real wave vector and complex frequencies ($\omega(\mathbf{k})$-formulation) was used to describe the temporal decay of freely propagating waves in the presence of structural damping [14] and a viscous fluid phase [15,16]. In Ref. [17], this approach was used to compute band diagrams for one-dimensional periodic structures with a viscoelastic material constituent. The computational procedure is here complicated by frequency dependent material properties that necessitate an iterative solution procedure of the eigenvalue problem for the complex frequencies. In Refs. [18,19], the effect of viscous damping on the bandgap properties was studied and the dispersive behavior of freely propagating waves was characterized in terms of the complex frequencies. An alternative approach is to use a fixed real frequency and complex wave vectors ($\mathbf{k}(\omega)$-formulation) [15,20]. This method has been applied in a number of recent papers in order to characterize the behavior of phononic crystals with dissipative materials by describing the spatial decay of waves for steady-state wave propagation [21–23].

In this work, we compute band diagrams for two-dimensional periodic structures made up of dissipative materials. We set up eigenvalue problems for determining $(\omega,\mathbf{k})$-solutions and solve it using the $\omega(\mathbf{k})$ approach (Sec. 3.1) as well as the $\mathbf{k}(\omega)$-formulation (Sec. 3.2). We compare the two formulations via the computed band diagrams and by relating spatial and temporal decay properties (Sec. 3.3). We also introduce a simplified band diagram encompassing the complex information on loss properties in the material (Sec. 4). Finally, we compute band diagrams for viscoelastic periodic materials with frequency-dependent material properties for which the presented $\mathbf{k}(\omega)$-formulation is directly suitable. In Sec. 5, we compare the results with existing computations on loss factor based on quasi-static homogenization theory.

Contributed by the Design Engineering Division of ASME for publication in the JOURNAL OF VIBRATION AND ACOUSTICS. Manuscript received May 14, 2012; final manuscript received February 12, 2013; published online June 6, 2013. Assoc. Editor: Massimo Ruzzene.

2 In-Plane Wave Propagation

First we develop the basic analysis model. Although similar derivations can be found in literature in various forms, we have chosen to include details for completeness. As a starting point, we consider in-plane wave propagation in a linear elastic medium governed by

$$\rho\frac{\partial^2\mathbf{u}}{\partial t^2}=\boldsymbol{\partial}^{\mathrm{T}}\mathbf{C}\boldsymbol{\partial}\mathbf{u}$$

$$\boldsymbol{\partial}=\begin{bmatrix}\frac{\partial}{\partial x} & 0\\ 0 & \frac{\partial}{\partial y}\\ \frac{\partial}{\partial y} & \frac{\partial}{\partial x}\end{bmatrix},\quad \mathrm{C}=\begin{bmatrix}2\mu+\lambda & \lambda & 0\\ \lambda & 2\mu+\lambda & 0\\ 0 & 0 & \mu\end{bmatrix} \tag{3}$$

where μ and λ are Lame's coefficients, ρ is the material density, and $\mathbf{u}$ is the in-plane displacement vector.

For a periodic medium, we can apply the Bloch wave expansion and insert the solution form from Eq. (1)

$$\begin{aligned}-\omega^2\rho\tilde{\mathbf{u}}e^{i\mathbf{k}^T\mathbf{x}}&=\boldsymbol{\partial}^T\mathbf{C}\boldsymbol{\partial}\left(\tilde{\mathbf{u}}e^{i\mathbf{k}^T\mathbf{x}}\right)\\&=\boldsymbol{\partial}^T\mathbf{C}\left(\boldsymbol{\partial}\tilde{\mathbf{u}}+i\left(\boldsymbol{\alpha}_1k_x+\boldsymbol{\alpha}_2k_y\right)\tilde{\mathbf{u}}\right)e^{i\mathbf{k}^T\mathbf{x}}\end{aligned} \tag{4}$$

in which the time-dependence via the exponential term $e^{i\omega t}$ has been divided out, where $\mathbf{k}^T=(k_x,k_y)$, and

$$\boldsymbol{\alpha}_1=\begin{bmatrix}1 & 0\\ 0 & 0\\ 0 & 1\end{bmatrix},\quad \boldsymbol{\alpha}_2=\begin{bmatrix}0 & 0\\ 0 & 1\\ 1 & 0\end{bmatrix} \tag{5}$$

The differential operator can be written as

$$\boldsymbol{\partial}=\boldsymbol{\alpha}_1\frac{\partial}{\partial x}+\boldsymbol{\alpha}_2\frac{\partial}{\partial y} \tag{6}$$

Introducing the definition

$$\boldsymbol{\kappa}=i\left(\boldsymbol{\alpha}_1k_x+\boldsymbol{\alpha}_2k_y\right) \tag{7}$$

and inserting Eq. (6) into Eq. (4) yields

$$\begin{aligned}-\omega^2\rho\tilde{\mathbf{u}}e^{i\mathbf{k}^T\mathbf{x}}&=\boldsymbol{\alpha}_1^T\frac{\partial}{\partial x}\left(\mathbf{C}(\boldsymbol{\partial}\tilde{\mathbf{u}}+\boldsymbol{\kappa}\tilde{\mathbf{u}})e^{i\mathbf{k}^T\mathbf{x}}\right)+\boldsymbol{\alpha}_2^T\frac{\partial}{\partial y}\left(\mathbf{C}(\boldsymbol{\partial}\tilde{\mathbf{u}}+\boldsymbol{\kappa}\tilde{\mathbf{u}})e^{i\mathbf{k}^T\mathbf{x}}\right)\\&=\left(\boldsymbol{\partial}^T\mathbf{C}\right)(\boldsymbol{\partial}\tilde{\mathbf{u}}+\boldsymbol{\kappa}\tilde{\mathbf{u}})e^{i\mathbf{k}^T\mathbf{x}}+\boldsymbol{\alpha}_1^T\mathbf{C}\frac{\partial}{\partial x}(\boldsymbol{\partial}\tilde{\mathbf{u}}+\boldsymbol{\kappa}\tilde{\mathbf{u}})e^{i\mathbf{k}^T\mathbf{x}}\\&\quad+\boldsymbol{\alpha}_2^T\mathbf{C}\frac{\partial}{\partial y}(\boldsymbol{\partial}\tilde{\mathbf{u}}+\boldsymbol{\kappa}\tilde{\mathbf{u}})e^{i\mathbf{k}^T\mathbf{x}}\end{aligned} \tag{8}$$

where, after expanding the two last terms and dividing through with the exponential term, the right-hand side can be written as

$$\begin{aligned}&\left(\boldsymbol{\partial}^T\mathbf{C}\right)(\boldsymbol{\partial}\tilde{\mathbf{u}}+\boldsymbol{\kappa}\tilde{\mathbf{u}})+\boldsymbol{\alpha}_1^T\mathbf{C}\left(\frac{\partial}{\partial x}\boldsymbol{\partial}\tilde{\mathbf{u}}+\boldsymbol{\kappa}\frac{\partial\tilde{\mathbf{u}}}{\partial x}\right)\\&+ik_x\boldsymbol{\alpha}_1^T\mathbf{C}(\boldsymbol{\partial}\tilde{\mathbf{u}}+\boldsymbol{\kappa}\tilde{\mathbf{u}})+\boldsymbol{\alpha}_2^T\mathbf{C}\left(\frac{\partial}{\partial y}\boldsymbol{\partial}\tilde{\mathbf{u}}+\boldsymbol{\kappa}\frac{\partial\tilde{\mathbf{u}}}{\partial y}\right)\\&+ik_y\boldsymbol{\alpha}_2^T\mathbf{C}(\boldsymbol{\partial}\tilde{\mathbf{u}}+\boldsymbol{\kappa}\tilde{\mathbf{u}})\end{aligned} \tag{9}$$

After gathering terms, the resulting equation is:

$$-\omega^2\rho\tilde{\mathbf{u}}=\boldsymbol{\partial}^T\mathbf{C}\boldsymbol{\partial}\tilde{\mathbf{u}}+\boldsymbol{\partial}^T\mathbf{C}\boldsymbol{\kappa}\tilde{\mathbf{u}}+\boldsymbol{\kappa}^T\mathbf{C}(\boldsymbol{\partial}\tilde{\mathbf{u}}+\boldsymbol{\kappa}\tilde{\mathbf{u}}) \tag{10}$$

which can be written in compact form as

$$-\omega^2\rho\tilde{\mathbf{u}}=\boldsymbol{\partial}_k^T\mathbf{C}\boldsymbol{\partial}_k\tilde{\mathbf{u}} \tag{11}$$

where

$$\boldsymbol{\partial}_k=\boldsymbol{\alpha}_1\left(\frac{\partial}{\partial x}+ik_x\right)+\boldsymbol{\alpha}_2\left(\frac{\partial}{\partial y}+ik_y\right) \tag{12}$$

and subjected to appropriate periodic boundary conditions on the unit cell.

In order to model wave propagation in dissipative materials, we consider a general viscoelastic model with a complex and potentially frequency dependent Young's modulus

$$E(\omega)=E'(\omega)+iE''(\omega) \tag{13}$$

which converts the two Lamé parameters into complex and frequency dependent quantities

$$\lambda(\omega)=\lambda'(\omega)+i\lambda''(\omega) \tag{14}$$

$$\mu(\omega)=\mu'(\omega)+i\mu''(\omega) \tag{15}$$

2.1 Discretization. We will now solve Eq. (11) using the FE method. A standard Galerkin approach yields

$$(\mathbf{K}_0-i\left(k_x\mathbf{K}_1+k_y\mathbf{K}_2\right)+k_x^2\mathbf{K}_3+k_xk_y\mathbf{K}_4+k_y^2\mathbf{K}_5-\omega^2\mathbf{M})\mathbf{d}=\mathbf{0} \tag{16}$$

where

$$\begin{aligned}\mathbf{M}&=\sum\nolimits_e\rho_e\int_{\Omega^e}\mathbf{N}^T\mathbf{N}d\Omega^e\\\mathbf{K}_0&=\sum\nolimits_e\int_{\Omega^e}\mathbf{B}^T\mathbf{C}\mathbf{B}d\Omega^e\\\mathbf{K}_1&=\sum\nolimits_e\int_{\Omega^e}\mathbf{N}^T\boldsymbol{\alpha}_1^T\mathbf{C}\mathbf{B}-\left(\mathbf{N}^T\boldsymbol{\alpha}_1^T\mathbf{C}\mathbf{B}\right)^Td\Omega^e\\\mathbf{K}_2&=\sum\nolimits_e\int_{\Omega^e}\mathbf{N}^T\boldsymbol{\alpha}_2^T\mathbf{C}\mathbf{B}-\left(\mathbf{N}^T\boldsymbol{\alpha}_2^T\mathbf{C}\mathbf{B}\right)^Td\Omega^e\\\mathbf{K}_3&=\sum\nolimits_e\int_{\Omega^e}\mathbf{N}^T\boldsymbol{\alpha}_1^T\mathbf{C}\boldsymbol{\alpha}_1\mathbf{N}d\Omega^e\\\mathbf{K}_4&=\sum\nolimits_e\int_{\Omega^e}\mathbf{N}^T\left(\boldsymbol{\alpha}_1^T\mathbf{C}\boldsymbol{\alpha}_2+\left(\boldsymbol{\alpha}_1^T\mathbf{C}\boldsymbol{\alpha}_2\right)^T\right)\mathbf{N}d\Omega^e\\\mathbf{K}_5&=\sum\nolimits_e\int_{\Omega^e}\mathbf{N}^T\boldsymbol{\alpha}_2^T\mathbf{C}\boldsymbol{\alpha}_2\mathbf{N}d\Omega^e\end{aligned} \tag{17}$$

Here, the subscript e refers to element properties, $\sum_e$ is a sum over all elements, $\mathbf{N}$ is a matrix with the shape functions, $\mathbf{B}=\partial\mathbf{N}$, and Ω^e is the element volume. With the boundary condition, $\mathbf{d}$ is periodic.

From Eq. (16), different eigenvalue problems can be constructed. If the wavevector is specified, i.e., k_x and k_y, then we obtain an eigenvalue problem for the frequency ω. Alternatively, the frequency can be specified and an eigenvalue problem can be constructed for the wave numbers. In the following these two approaches will be outlined and later the results for the two formulations will be compared.

3 Comparing $\omega(\mathbf{k})$ and $\mathbf{k}(\omega)$

In this section, band diagrams obtained with the $\omega(\mathbf{k})$- and $\mathbf{k}(\omega)$-formulation are compared. The periodic material considered in this paper have a unit cell with two different material phases

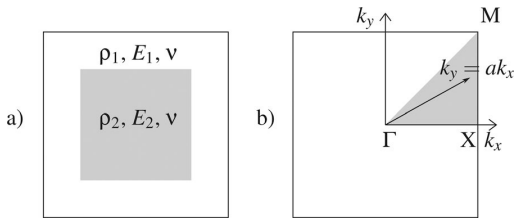

Fig. 1 (*a*) Unit cell of periodic material consisting of two phases with different density and elasticity modulus. The cell side is 1 cm. (*b*) Illustration of the irreducible Brillouin zone and propagation directions specified by the linear relation between the two wave vector components $k_y = ak_x$.

arranged as illustrated in Fig. 1(*a*) and is the same periodic material previously considered in Ref. [24]. The material parameters are initially assumed to be frequency independent and are specified in Table 1. In Sec. 5, we will consider an example with frequency dependent material parameters.

3.1 Frequency Solutions $\omega(\mathbf{k})$. First we convert the general FE Eq. (16) into a linear eigenvalue problem in ω^2

$$\left(\mathbf{K} - \omega^2\mathbf{M}\right)\mathbf{d} = \mathbf{0} \tag{18}$$

where

$$\mathbf{K} = \mathbf{K}_0 - i\left(k_x\mathbf{K}_1 + k_y\mathbf{K}_2\right) + k_x^2\mathbf{K}_3 + k_xk_y\mathbf{K}_4 + k_y^2\mathbf{K}_5 \tag{19}$$

is the effective stiffness matrix for a given wave vector corresponding to k_x and k_y.

The band diagram is computed by specifying k_x and k_y and solving the eigenvalue problem for ω^2. As is the general procedure, this is done by traversing the boundaries of the irreducible Brillouin zone shown as the shaded area in Fig. 1(*b*). In Fig. 2, the band diagram showing the real part of ω for one nondissipative (ND) and three dissipative materials (D1–D3) are shown (Table 1). The effect of the added material dissipation is seen as a shift upwards in the frequency of the bands. A higher loss factor $\eta = E''/E'$ results in a larger shift. However, even a very high loss factor of 0.5 (D3) does not cause a very large shift of the real part of the solution.

For the nondissipative material, the eigensolutions are purely real. However, in the case of dissipative materials, the solutions become complex. In order to interpret the complex frequency solutions for nonvanishing material dissipation, we insert the complex solution form into the Bloch wave expansion

$$\mathbf{u}(\mathbf{x}, t) = (\tilde{\mathbf{u}}(\mathbf{x})e^{i\mathbf{k}^T\mathbf{x}}e^{i\omega' t})e^{-\omega'' t} \tag{20}$$

and note that the imaginary part of the complex wave solution naturally implies a temporally attenuating wave rather than a steady-state wave solution. For steady-state wave propagation at a fixed frequency, we can instead describe the spatial attenuation of

Table 1 Material parameters for example materials

Material	ρ_1 $\left[10^3\,\frac{\text{kg}}{\text{m}^3}\right]$	ρ_2 $\left[10^3\,\frac{\text{kg}}{\text{m}^3}\right]$	E_1' (GPa)	E_1' (GPa)	E_2' (GPa)	E_2'' (GPa)	ν
ND	1	2	4	0	20	0	0.34
D1	1	2	4	0.04	20	0.2	0.34
D2	1	2	4	0.04	20	0	0.34
D3	1	2	4	2	20	10	0.34

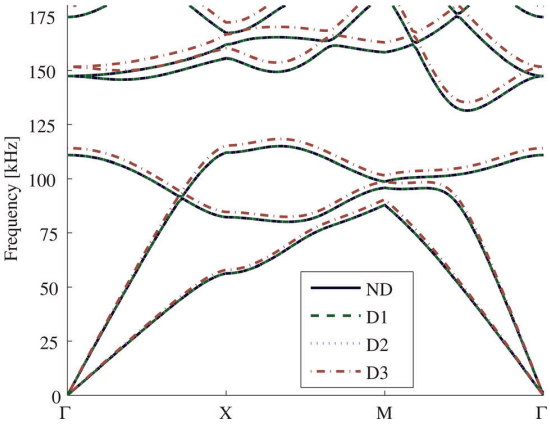

Fig. 2 Band diagram considering the boundary of the irreducible Brillouin zone for the four materials in Table 1. Equation (21) has been solved for 120 points along each edge for the first six eigenvalues.

waves by resorting to an alternative formulation based on complex wave vector solutions to the eigenvalue problem.

3.2 Wave Vector Solutions $\mathbf{k}(\omega)$. We now assume that ω is specified and reconstruct Eq. (16) into an eigenvalue problem for the wave vector, the so-called $\mathbf{k}(\omega)$-formulation. However, since the wave vector consists of the two independent components, k_x and k_y, we will specify a relation between the two in order to be able to construct a standard eigenvalue problem.

We choose to consider the linear relation $k_y = ak_x$, where a is a real constant, which allows us to construct band diagrams along specified lines through the irreducible Brillouin zone (Fig. 1(*b*)). Inserting this relation into Eq. (16) immediately converts the eigenvalue problem into a quadratic eigenvalue problem in k_x, which is easiest solved by putting the problem into first-order form through a reformulation [21]

$$(\mathbf{K}_k - k_x\mathbf{M}_k)\mathbf{d}_k = \mathbf{0} \tag{21}$$

where

$$\begin{aligned}\mathbf{K}_k &= \begin{bmatrix} -i(\mathbf{K}_1 + a\mathbf{K}_2) & (\mathbf{K}_0 - \omega^2\mathbf{M}) \\ \mathbf{I} & \mathbf{0} \end{bmatrix} \\ \mathbf{M}_k &= \begin{bmatrix} -(\mathbf{K}_3 + a\mathbf{K}_4 + a^2\mathbf{K}_5) & \mathbf{0} \\ \mathbf{0} & \mathbf{I} \end{bmatrix}, \quad \mathbf{d}_\mathbf{k} = \begin{bmatrix} k_x\mathbf{d} \\ \mathbf{d} \end{bmatrix}\end{aligned} \tag{22}$$

First, we recompute the band diagram corresponding to material ND, i.e. without dissipation present and compare it to the results for the $\omega(\mathbf{k})$-model. We show the results in Fig. 3 and it can be seen that the results, as they should, agree perfectly. However, it should be noted that the $\mathbf{k}(\omega)$-formulation captures complex (spatially decaying) modes that are not found with the $\omega(\mathbf{k})$ formulation. However, only solutions where $\mathbf{k}'' < \delta\mathbf{k}'$, where δ is a small number (0.01), have been included in the figure. The additional modes not included in the figure comprise the evanescent modes in the bandgap between ≈110−150 kHz as well as other fast-decaying modes.

In the case of dissipative materials, we can construct the band diagram for sections Γ–X and sections M–Γ by setting $a = 0$ and $a = 1$, respectively. However, for section X–M we need to fix $k_x' = \pi$ but do not readily know neither k_x'' nor k_y'', which makes the construction of this part of the diagram problematic. Instead, we construct alternative band diagrams by choosing different values of the constant a in the range from 0 to 1. The resulting

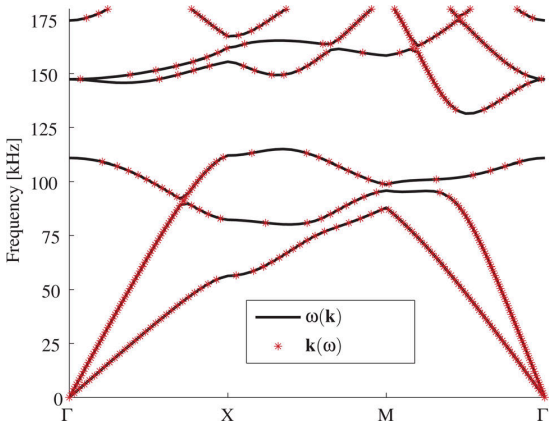

Fig. 3 Band diagram for the nondissipative material ND

diagrams encompass the information from the traditional band diagrams (given sufficiently fine resolution of the a-range) and also provide details from the interior of the Brillouin zone, which is not covered in standard band diagrams and which, for dissipative materials, is not well documented. Even for nondissipative materials, it has recently been demonstrated that it is not always sufficient to traverse only the boundaries of the Brillouin zone when locating band extrema [25].

In Figs. 4–6 we show band diagrams for the three dissipative materials. Shown also in the figure are corresponding results obtained from the $\omega(\mathbf{k})$-formulation (plotting the real part of ω). Again, the $\mathbf{k}(\omega)$-formulation provides a number of additional modes that we discard by using the threshold δ for the imaginary part. It should be emphasized that when considering dissipative materials, the value of δ must be chosen carefully because all modes will be decaying. Here, it is appropriate to separate the previously mentioned fast-decaying modes from slow-decaying modes, which decay due to the dissipation. The justification for this separation is that we assume the material to be relatively lightly damped. From the figures we can see that for small damping (D1, D2) and for long wavelengths (D3) there is a very good correspondence between the results from the two formulations. Only for high damping and shorter wavelengths (D3) do we see a discrepancy between the results from the two formulations.

Our main interest is to evaluate the dissipation or decay of waves (represented by the imaginary part of the solution). A possible application is in the design of periodic materials in order to obtain the largest possible wave decay by combining the effects of material dissipation and bandgaps. This will indeed be the subject of future work. However, the comparison of the wave decay predicted by the two formulations is more difficult since the imaginary parts of the solutions represent a temporal and a spatial decay, respectively.

3.3 Relation Between Spatial and Temporal Decay. As mentioned, the imaginary part of the computed wave vector is a measure of the spatial wave decay. Thus, if we pair this information with knowledge of the velocity of the wave (group velocity), we can then compute an equivalent temporal decay as well. Based on a complex wave solution, we get the temporal decay (TD) as the product between the imaginary part of the wave number k and the group velocity c_g in the direction of propagation

$$(TD)_k = k'' c_g \tag{23}$$

where we can compute the group velocity in the direction of propagation for dissipative materials as [21]

$$\frac{1}{c_g} = \left(\frac{\partial k}{\partial \omega}\right)' \tag{24}$$

For comparison, we get the temporal decay directly from the $\omega(\mathbf{k})$-formulation as

$$(TD)_\omega = \omega'' \tag{25}$$

In Fig. 7, the temporal decay found using Eq. (23) is compared to the temporal decay found using Eq. (25) for the three dissipative materials in Table 1.

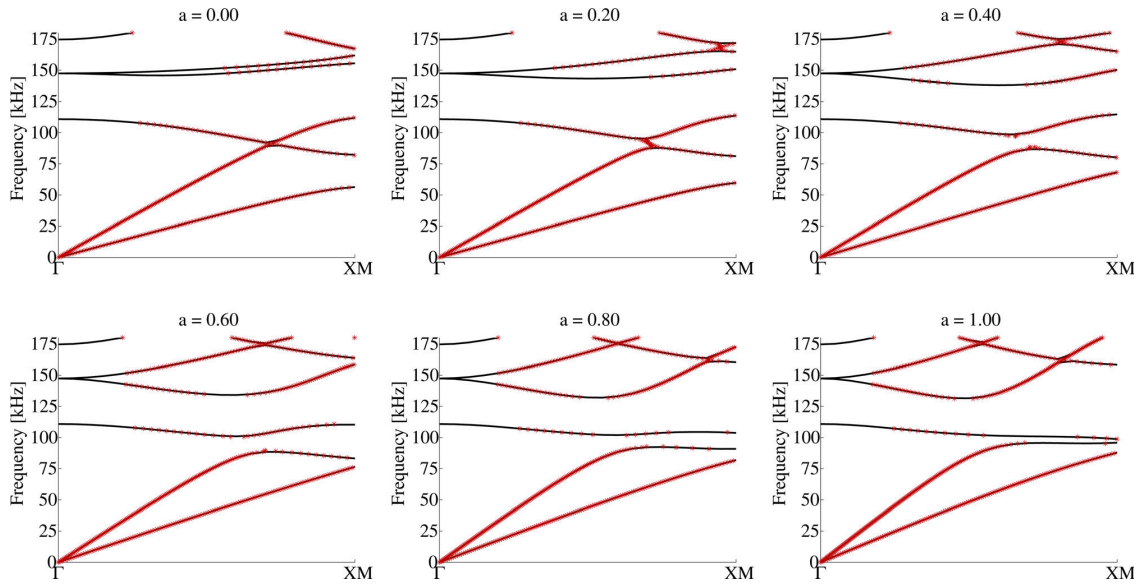

Fig. 4 Each band diagram is created by solving Eq. (21) for a specific value of *a*, which is shown above the corresponding plot. Material D1 with $\delta = 0.1$.

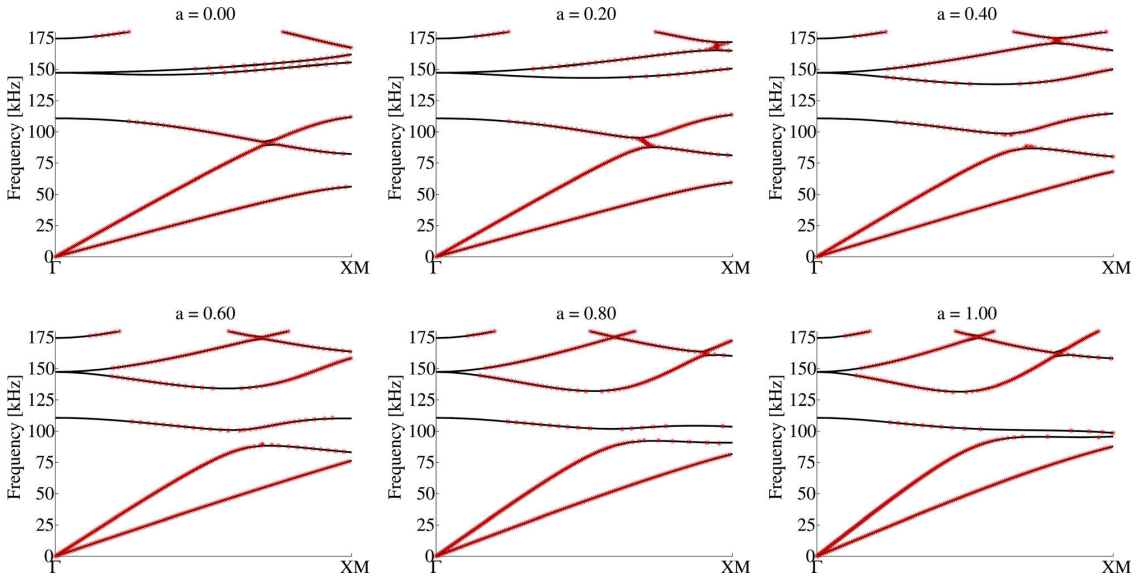

Fig. 5 Each band diagram is created by solving Eq. (21) for a specific value of *a*, which is shown above the corresponding plot. Material D2 with $\delta = 0.1$.

From the figure, we note a good correlation between the predicted temporal decay for the two formulations. This is especially evident for longer wavelengths and small dissipation but even for larger dissipation the correlation is good in the long wavelength limit but then significantly deteriorates as the wavelength decreases and the decay grows. It should be noted that the predicted temporal decay using the $\mathbf{k}(\omega)$-formulation may be inaccurate for certain points in higher mode branches, due to the difficulty in identifying modes when computing the group velocity in Eq. (24). Additionally, it should be emphasized that not all modes are shown due to the choice of the threshold δ.

4 Simple Band Diagrams

Now we will present an alternative way to represent the imaginary part of the wave vector in order to characterize the loss in the material. We will apply the $\mathbf{k}(\omega)$-formulation in order to unify the loss in the periodic material from dissipation and bandgap effects.

With the $\mathbf{k}(\omega)$-formulation, there is no obvious way to separate the eigenvalues into first band, second band, etc. Since we aim at applying the formulation in an optimization framework, this may create problems. We use instead a simplified band diagram plot that illustrates the minimum spatial wave decay for given frequencies. In this way, we encompass information about the loss in the material regardless of its origin from a bandgap phenomenon or

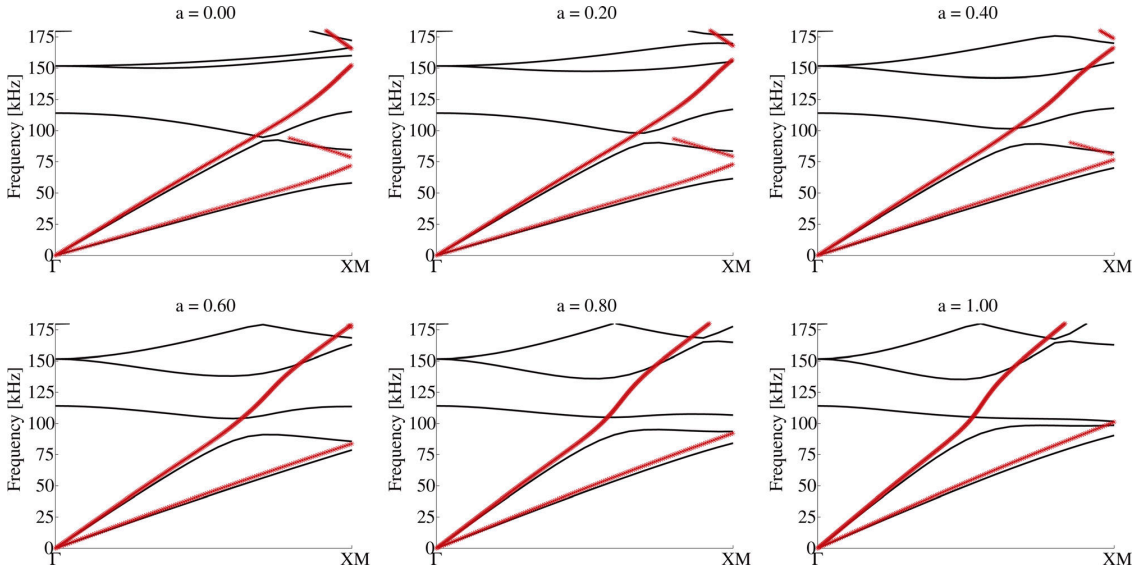

Fig. 6 Each band diagram is created by solving Eq. (21) for a specific value of *a*, which is shown above the corresponding plot. Material D3 with $\delta = 0.5$.

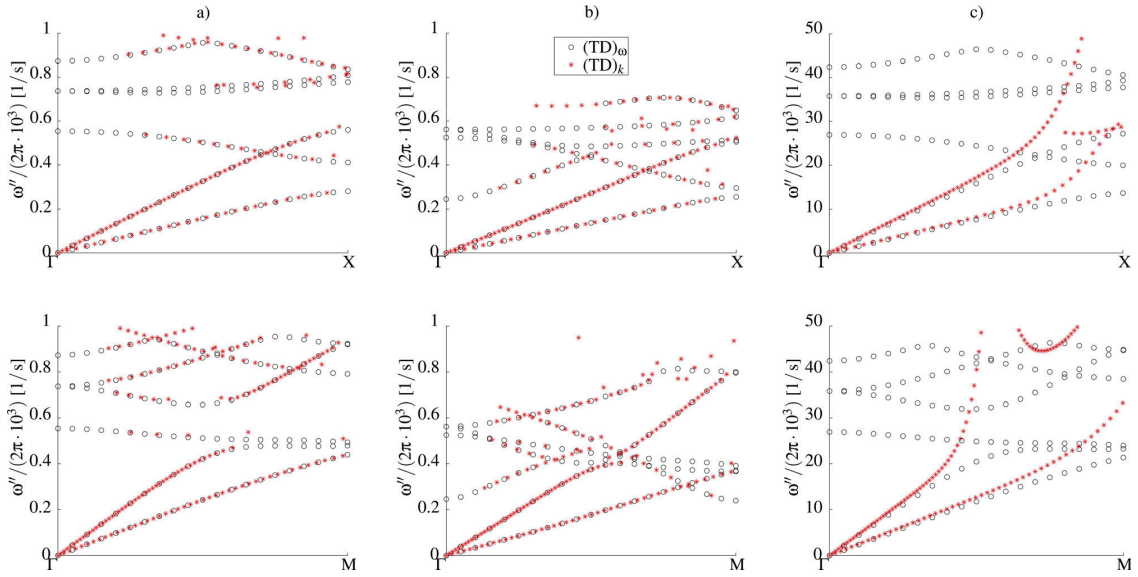

Fig. 7 Illustration of how spatial and temporal decay is related through Eq. (23). Top row shows solutions from Γ to X, while bottom row shows solutions from Γ to M, for (*a*) material D1 with $\delta = 0.1$, (*b*) material D2 with $\delta = 0.1$, and (*c*) material D3 with $\delta = 0.5$.

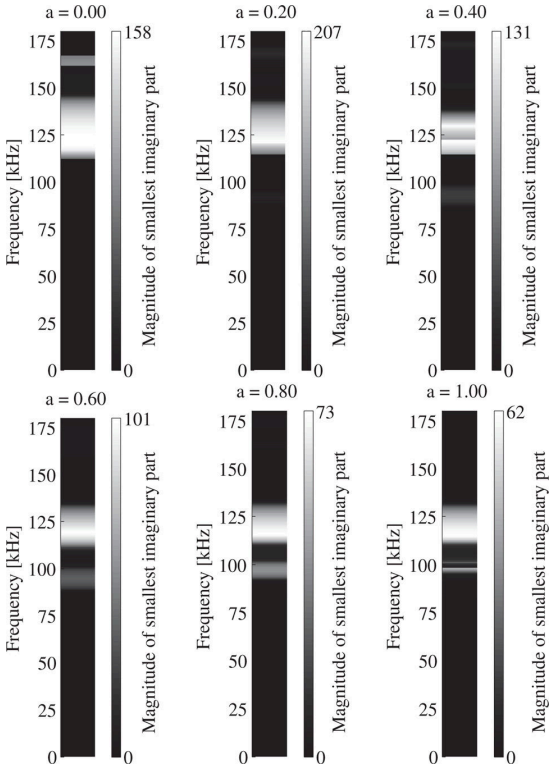

Fig. 8 Each simple band diagram is created by solving Eq. (21) for a specific value of *a*, which is shown above the corresponding plot. The considered material is D2.

merely material dissipation. Figure 8 has been created by solving Eq. (21) for a range of a values, where for each value of a we have recorded the minimum value of the imaginary part of k_x. The dark regions correspond to frequencies with propagating modes that are only slightly damped whereas lighter regions correspond to frequencies for which all modes are strongly attenuated spatially (e.g. in the band gap frequency range). All eigenvalues with a real part within the Brillouin zone are considered when constructing the simple band diagram. The imaginary part of all eigenvalues k_x (remember $k_y = ak_x$—there is a proportionality both between the real and the imaginary part) belonging to a specific frequency ω are compared, and the imaginary part with the smallest magnitude is included in the simplified band diagram. As explained above, the simplified band diagram also implies that it is no longer necessary to specify the semiheuristic parameter δ to separate the slow- from the fast-decaying modes.

For further simplification, all plots can be collected into a single plot that shows, for each frequency, the smallest imaginary part

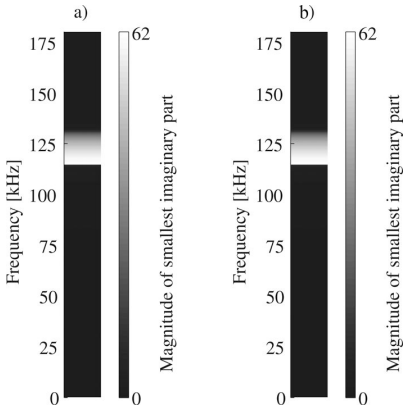

Fig. 9 Simple band diagram for material D2 created by (*a*) solving Eq. (21) for a range of *a* values from 0 to 1, or (*b*) traversing only the border of the irreducible Brillouin zone

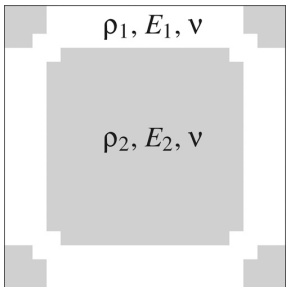

Fig. 10 Unit cell of material optimized for high loss factor, from Ref. [26]. The cell side is 1 cm.

for all propagating modes within the irreducible Brillouin zone (Fig. 9(*a*)). This plot can immediately be used to identify frequency ranges for which all waves will be attenuated and can be used as the basis for an optimization formulation that we will present in future work. The simple band diagram could also be plotted as a k_x'' versus ω as done in Ref. [23]. Here, the colorbar approach is used to save space.

Creating the simplified band diagram when points inside the irreducible Brillouin zone are taken into account is computationally expensive. Therefore, it is valuable to have an indication to whether this is necessary or a simpler approach can be applied. In Fig. 9(*b*), a simple band diagram for material D2 has been created by only traversing the border of the irreducible Brillouin zone, which means between X and M, k_x is still kept constant, so between X and M it is the imaginary part of k_y that has been considered which is not fully correct. However, the two band diagrams in Figs. 9(*a*) and 9(*b*) do look identical which is an indication that the simplified approach is valid, although it is not proven that this is always the case. It should be mentioned here that the simple band diagrams for the border and the whole of the irreducible Brillouin zone do not deviate even when considering larger damping, as in, e.g., material D3.

5 Example—Frequency Dependent Material

If the material properties are frequency dependent, such as, e.g., for viscoelastic materials, a straightforward implementation using the traditional $\omega(\mathbf{k})$-formulation is not possible. Instead an iterative procedure can be applied as demonstrated in Ref. [17].

However, with the $\mathbf{k}(\omega)$-formulation, the treatment of viscoelastic material properties is straightforward. Here, we demonstrate the computation of the band structure for a viscoelastic periodic composite with the unit cell shown in Fig. 10. This unit cell has been created by utilizing a topology optimization procedure to find the material distribution that maximizes the imaginary part of a material's bulk modulus [26]. Quasi-static conditions have been applied so that a standard homogenization approach can be used to determine the constitutive tensor and the corresponding effective loss factor of the composite. In this case, the homogenization predicts a loss factor of 0.2 for longitudinal waves.

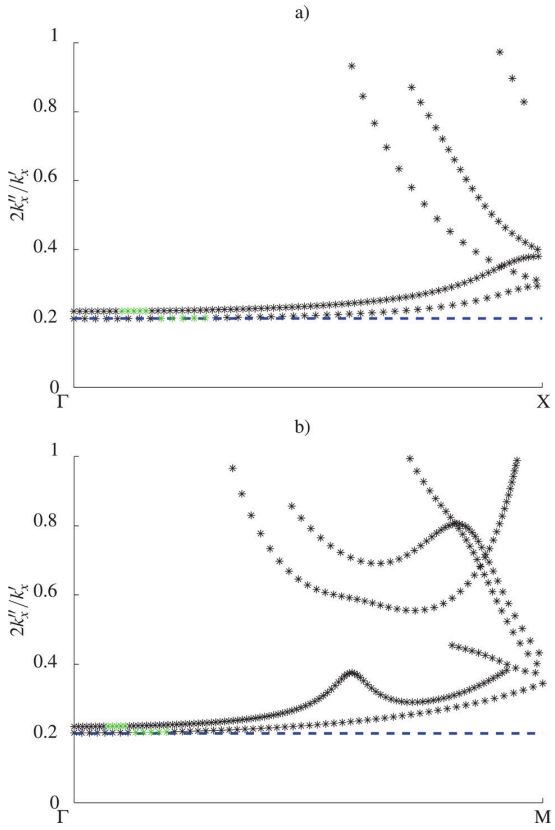

Fig. 11 Ratio according to Eq. (26) for the material in Fig. 10 with constant phase properties. (*a*) Top and (*b*) bottom border of the irreducible Brillouin zone.

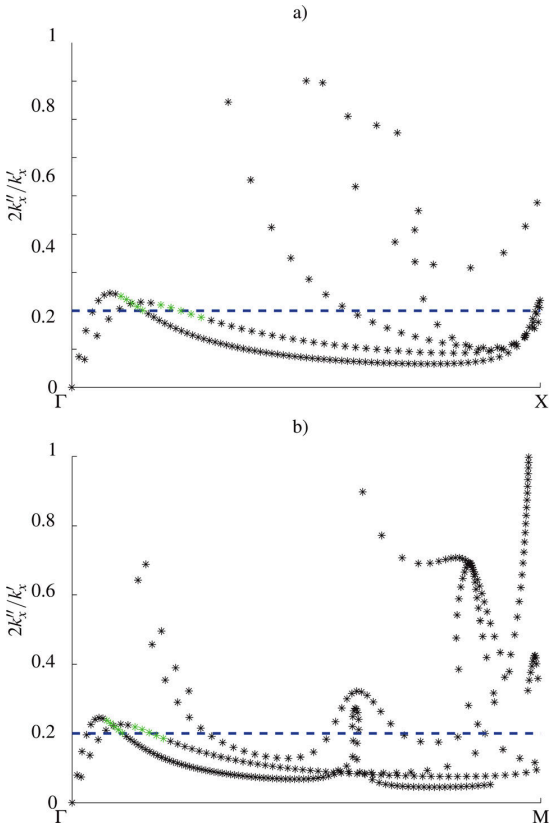

Fig. 12 Ratio according to Eq. (26) for the material in Fig. 10 with frequency dependent phase properties. (*a*) Top and (*b*) bottom border of the irreducible Brillouin zone.

Phase 2 is the stiff phase with a frequency independent elasticity modulus $E_2 = 20$ GPa. The viscoelasticity is introduced by phase 1, which in the optimization, has been assigned a frequency independent complex elasticity modulus $E_1^c = 3.1\ \text{GPa} + i \cdot 1.0\ \text{GPa}$. Both materials have $\nu = 0.3$, and the density is set to $\rho_1 = \rho_2 = 10^3\ \text{kg/m}^3$.

In order to compare the results from the band structure computations, we can approximately relate the predicted loss factor to the ratio between the imaginary and complex part of the wave number as follows [27]:

$$\frac{k_x''}{k_x'} = \frac{\eta}{2} \tag{26}$$

From Fig. 11, where the complex wave number ratio is plotted for wave numbers between Γ–X and Γ–M, it seems that relation holds very well for long waves (small wave numbers). However, when the wavelength increases and approaches the dimensions of the unit cell, the quasi-static approximation used in Ref. [26] ceases to be valid.

However, for a viscoelastic material, the elasticity modulus of the viscous phase will vary with frequency. Assuming a standard linear solid model, the frequency dependency could be modeled as

$$E_1(\omega) = E_1^0 + \frac{\kappa(\tau\omega)^2}{1+(\tau\omega)^2} + i\frac{\kappa\tau\omega}{1+(\tau\omega)^2} \tag{27}$$

where the parameter choices $E_1^0 = 2.0\,\text{GPa}$, $\kappa = 2.0\,\text{GPa}$, and $\tau = 8.5 \cdot 10^{-6}\text{s}$ imply $E_1(20\ \text{kHz}) = E_1^c$.

In Fig. 12, the ratio from Eq. (26) is shown when the frequency dependent stiffness is taken into account. It is clear that the loss factor obtained from the quasi-static homogenization theory for a single frequency does not hold over a broader frequency range. The green asterisks in Figs. 11 and 12 are those with a frequency between 15 and 25 kHz.

6 Conclusion

Wave propagation and loss factors in periodic materials with dissipation have been analyzed using an $\omega(\mathbf{k})$-formulation and a $\mathbf{k}(\omega)$-formulation. We computed band diagrams and temporal wave decay with both methods and demonstrated that the results obtained with the two formulations agree well for small to medium amounts of material dissipation and for long wavelengths. The $\mathbf{k}(\omega)$-formulation is more computational demanding, but well suited for computing spatial loss factors in the case of steady-state propagation at fixed wave frequencies. This formulation can also directly be applied for the computation of band diagrams for viscoelastic materials where the properties are dependent on the frequency. Additionally, we introduced a simplified band diagram in order to quantify the loss in a simple manner and which is directly amenable to an optimization study which will be the subject of future work. Finally, we have demonstrated that for a viscoelastic composite the loss computed from the band diagram agrees well with loss computed from quasi-static homogenization theory in the low frequency range when the material properties are frequency independent.

Acknowledgment

This work was support by the Danish Research Agency through the innovation consortium FMAT. The authors are grateful to Fengwen Wang for valuable discussions, and to Casper S. Andreasen for providing the optimized unit cell shown in Sec. 5.

References

[1] Sigalas, M. M., and Economou, E. N., 1992, "Elastic and Acoustic Wave Band Structure," J. Sound Vib., **158**(2), pp. 377–382.
[2] Suzuki, T., and Yu, P. K. L., 1998, "Complex Elastic Wave Band Structures in Three-Dimensional Periodic Elastic Media," J. Mech. Phys. Solids, **46**(1), pp. 115–138.
[3] Liu, Z., Chan, C. T., Sheng, P., Goertzen, A. L., and Page, J. H., 2000, "Elastic Wave Scattering by Periodic Structures of Spherical Objects: Theory and Experiment," Phys. Rev. B, **62**(4), pp. 2446–2457.
[4] Yablonovitch, E., 1987, "Inhibited Spontaneous Emission in Solid-State Physics and Electronics," Phys. Rev. Lett., **58**(20), pp. 2059–2062.
[5] John, S., 1987, "Strong Localization of Photons in Certain Disordered Dielectric Superlattices," Phys. Rev. Lett., **58**(23), pp. 2486–2489.
[6] Joannopoulos, J. D., Meade, R. D., and Winn, J. N., 1995, *Photonic Crystals*, Princeton University Press, Princeton, NJ.
[7] Rayleigh, L., 1887, "On the Maintenance of Vibrations by Forces of Double Frequency, and on the Propagation of Waves Through a Medium Endoved With a Periodic Structure," Philos. Mag., **24**, pp. 145–159.
[8] Brillouin, L., 1953, *Wave Propagation in Periodic Structures*, 2nd ed., Dover Publications, New York.
[9] Bloch, F., 1929, "Über die Quantenmechanik der Elektronen in Kristallgittern," Zeitsch. Phys., **52**(7–8), pp. 555–600.
[10] Elachi, C., 1976, "Waves in Active and Passive Periodic Structures: A Review," Proc. IEEE, **64**(12), pp. 1666–1698.
[11] Mead, D. J., 1996, "Wave Propagation in Continuous Periodic Structures: Research Contributions From Southampton, 1964–1995," J. Sound Vib., **190**(3), pp. 495–524.
[12] Langley, R., 1994, "On the Forced Response of One-Dimensional Periodic Structures: Vibration Localization by Damping," J. Sound Vib., **178**(3), pp. 411–428.
[13] Jensen, J. S., 2003, "Phononic Band Gaps and Vibrations in One- and Two-Dimensional Mass-Spring Structures," J. Sound Vib., **266**(5), pp. 1053–1078.
[14] Mukherjee, S., and Lee, E., 1975, "Dispersion Relations and Mode Shapes for Waves in Laminated Viscoelastic Composites by Finite Difference Methods," Comput. Struct., **5**(5–6), pp. 279–285.
[15] Sprik, R., and Wegdam, G. H., 1998, "Acoustic Band Gaps in Composites of Solids and Viscous Liquids," Solid State Commun. **106**(2), pp. 77–81.
[16] Zhang, X., Liu, Z., Mei, J., and Liu, Y., 2003, "Acoustic Band Gaps for a Two-Dimensional Periodic Array of Solid Cylinders in Viscous Liquid," J. Phys.: Condens. Matt., **15**(49), pp. 8207–8212.
[17] Zhao, Y. P., and Wei, P. J., 2009, "The Band Gap of 1D Viscoelastic Phononic Crystal," Comput. Mater. Sci., **46**, pp. 603–606.
[18] Hussein, M. I., 2009, "Theory of Damped Bloch Waves in Elastic Media," Phys. Rev. B, **80**, p. 212301.
[19] Hussein, M. I., and Frazier, M. J., 2010, "Band Structure of Phononic Crystals With General Damping," J. Appl. Phys., **108**, p. 093506.
[20] Mead, D., 1973, "A General Theory of Harmonic Wave Propagation in Linear Periodic Systems With Multiple Coupling," J. Sound Vib., **27**(2), pp. 235–260.
[21] Moiseyenko, R. P., and Laude, V., 2011, "Material Loss Influence on the Complex Band Structure and Group Velocity in Phononic Crystals," Phys. Rev. B, **83**, p. 064301.
[22] Farzbod, F., and Leamy, M. J., 2011, "Analysis of Bloch's Method in Structures With Energy Dissipation," ASME J. Vib. Acoust., **133**(5), p. 051010.
[23] Collet, M., Ouisse, M., Ruzzene, M., and Ichchou, M. N., 2011, "Floquet-Bloch Decomposition for the Computation of Dispersion of Two-Dimensional Periodic, Damped Mechanical Systems," Int. J. Solids Struct., **48**(20), pp. 2837–2848.
[24] Sigmund, O., and Jensen, J. S., 2003, "Systematic Design of Phononic Band-Gap Materials and Structures by Topology Optimization," Philos. Trans. R. Soc. Lond. A, **361**(1806), pp. 1001–1019.
[25] Farzbod, F., and Leamy, M. J., 2011, "Analysis of Bloch's Method and the Propagation Technique in Periodic Structures," ASME J. Vib. Acoust., **133**(5), p. 031010.
[26] Andreasen, C. S., Andreassen, E., Jensen, J. S., and Sigmund, O., 2012, "On the Realization of the Bounds for Two Phase Viscoelastic Composites," J. Mech. Phys. Solids (submitted).
[27] Cremer, L., Heckl, M., and Petersson, B. A. T., 2005, *Structure-Borne Sound: Structural Vibrations and Sound Radiation at Audio Frequencies*, Springer, Berlin.

Publication [P6]

Topology optimization of periodic microstructures for enhanced dynamic properties of viscoelastic composite materials

Struct Multidisc Optim (2014) 49:695–705
DOI 10.1007/s00158-013-1018-2

RESEARCH PAPER

Topology optimization of periodic microstructures for enhanced dynamic properties of viscoelastic composite materials

Erik Andreassen · Jakob Søndergaard Jensen

Received: 29 May 2013 / Revised: 29 August 2013 / Accepted: 25 October 2013 / Published online: 28 November 2013

Abstract We present a topology optimization method for the design of periodic composites with dissipative materials for maximizing the loss/attenuation of propagating waves. The computational model is based on a finite element discretization of the periodic unit cell and a complex eigenvalue problem with a prescribed wave frequency. The attenuation in the material is described by its complex wavenumber, and we demonstrate in several examples optimized distributions of a stiff low loss and a soft lossy material in order to maximize the attenuation. In the examples we cover different frequency ranges and relate the results to previous studies on composites with high damping and stiffness based on quasi-static conditions for low frequencies and the bandgap phenomenon for high frequencies. Additionally, we consider the issues of stiffness and connectivity constraints and finally present optimized composites with direction dependent loss properties.

Keywords Topology optimization · Microstructure · Attenuation factor · Bandgap material

1 Introduction

The effective elastic material properties of a periodic composite can be determined using homogenization (Bensoussan et al. 1978; Sanchez-Palencia 1980), and an example of a numerical finite element based homogenization procedure is given by Guedes and Kikuchi (1990). With viscoelastic materials (Christensen 1971; Lakes 2009) the correspondence principle (Hashin 1970) shows that the effective properties, in the quasi-static limit, can be found by using a standard homogenization procedure by utilizing complex stiffness moduli in the computation. In this way a loss factor for the composite can be computed based on the real and imaginary parts of its effective complex elastic properties. Gibiansky and Lakes (1997) derived bounds for the quasi-static complex bulk and shear moduli for two-phase isotropic composites. The bounds on the complex elasticity modulus, for example, can be plotted in a loss versus stiffness map, as is done in Fig. 1 for a stiff, low-loss and a soft, lossy constituent. In Fig. 1 the soft phase is shown as white, while the stiff material is shown as black. This practice will be followed in the rest of the paper.

The bounds in Fig. 1 illustrate that the loss factor in the composite, for quasi-static conditions, is bounded by the loss factors of the material constituents (and so is the stiffness). However, the bounds also indicate that composites with a good compromise between loss and stiffness can be constructed. Naturally, there has been a large interest in creating composites with such a favorable combination, since most pure high damping materials (such as polymers) exhibit a stiffness that is too low for practical application, while high stiffness materials (such as most metals) have low damping capabilities. Brodt and Lakes (1995) investigated metal composites in the form of laminates with a relatively high damping matrix (cast indium tin alloy) and high stiffness inclusions (tungsten), and they demonstrated experimentally a combination of high stiffness and high loss. Kim et al. (2002) studied composites with spherical and cubic inclusions of stiff silicon-carbide in a high damping indium tin eutectic matrix. Here it was found that a

This work was funded by the Danish Research Agency through the innovation consortium F·MAT.

E. Andreassen · J. S. Jensen (✉)
Department of Mechanical Engineering, Technical University of Denmark, Nils Koppels Allé, Building 404, 2800 Lyngby, Denmark
e-mail: jsj@mek.dtu.dk

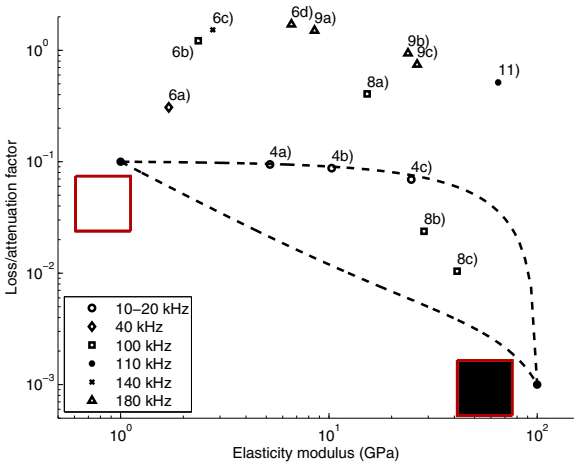

Fig. 1 Quasi-static bounds in a stiffness-loss map for a two-phase composite material. Bounds valid for cubic symmetric materials, where both phases have equal Poisson's ratio. Points refer to optimized material structures presented in Section 3

high volume fraction of the inclusion gave rise to the most favorable combination of stiffness and loss.

Furthermore, the design of *optimal* composites obtaining the upper theoretical bound has also received interest. Yi et al. (2000) used the method of topology optimization (Bendsøe and Sigmund 2003) to design viscoelastic composites with high damping and a constraint on the minimum stiffness of the composite. However, the performance of the composites was not directly compared to the theoretical bounds. In a recent paper by the authors and co-workers (Andreasen et al. 2013) we used topology optimization to design 2D and 3D composites on the upper theoretical bound and found that high loss, high stiffness composites are obtained with thin layers of the soft, lossy constituent combined with large stiff inclusions which is also concluded in Kim et al. (2002). Meaud et al. (2013) also use a material distribution approach to design layered composites (laminates) with a favorable combination of high stiffness and high damping. They additionally investigate the nonlinear effect associated with large strains in the soft polymer material. Sain et al. (2013) study high damping composites with thin wavy layers of a nonlinear viscoelastic material embedded in metal and obtained high damping due to the high shear strain in the lossy material and also high stiffness due the bulk volume of the metal.

Related work on the design of high damping composites can be found in a paper by Prasad and Diaz (2009), who used topology optimization to design viscoelastic composites with inclusions of negative stiffness. High damping in composites with negative stiffness inclusions has also been reported in other works, e.g. by Lakes et al. (2001).

In addition to the quasi-static loss-stiffness bounds, Fig. 1 also contains a range of points indicating the performance of the optimized microstructures presented in Section 3. These results indicate that it is possible to obtain losses that exceed the quasi-static bounds when we go to higher wave frequencies and shorter wavelengths that approach the periodicity of the material. In order to compute and optimize the loss at higher frequencies we must include inertial effects and cannot apply the correspondence principle. For a periodic medium the wave solution to the full dynamic problem can be expanded according to the Bloch theorem that allows a characterization of the dynamic properties of the composite by analysis of the unit cell (Bloch 1929):

$$\mathbf{u}(\mathbf{x}, t) = \tilde{\mathbf{u}}(\mathbf{x}) e^{i\mathbf{k}^T\mathbf{x}} e^{i\omega t} \tag{1}$$

in which ω is the wave frequency, $\mathbf{k} = (k_x, k_y, k_z)^T$ is the wave vector and $\tilde{\mathbf{u}}$ is a periodic mode on the unit cell of the periodic material. Without going into details with the equations, which are saved to Section 2, the Bloch expansion in (1) yields an eigenvalue problem in which either the wave vector $\mathbf{k}$ or the frequency ω must be specified. Since we introduce the material loss in our model as a complex material parameter, where the elasticity modulus of the material is given as:

$$E(\omega) = E'(\omega) + iE''(\omega) = E'(\omega)(1 + i\eta(\omega)) \tag{2}$$

with η as the material loss factor, the eigenvalue problem will yield a complex solution. Depending on whether the wave vector or frequency is specified, the solution will be in the form of either a complex frequency or complex wave vector. This describes wave attenuation that can then be interpreted as either temporal (Hussein and Frazier 2010) or spatial (Moiseyenko and Laude 2011; Farzbod and Leamy 2011; Collet et al. 2011). The two methods have recently been compared in Andreassen and Jensen (2013) and have also been examined in detail in the context of wave propagation in lossy photonic crystals by Huang et al. (2004).

In this paper we choose to specify the frequency and solve for the complex wave vector. Then the complex eigenvalue problem results in a complex wave number that can be used to compute an equivalent loss factor. We emphasize that in this context the loss factor should be interpreted as an attenuation factor that quantifies the spatial decay of the waves. In this way the loss may origin in reflection of the waves as well as in dissipation of waves. The approach where the wave frequency is specified also has the advantage that it allows for treating frequency dependent material parameters in a straightforward manner.

We will use a gradient-based topology optimization strategy to design unit cell microstructures in order to maximize the overall loss (attenuation) factor of the composite

material. The use of topology optimization to design material microstructures of periodic materials with prescribed elastic properties—known as inverse homogenization—was introduced by Sigmund (1994) and has also been used to design materials with other interesting properties, e.g. negative thermal expansion coefficients (Sigmund and Torquato 1997), maximum heat dissipation (Wang and Cheng 2005), and maximum permeability (Guest and Prevost 2007). Gradient-based topology optimization has also been used to design dielectric and elastic materials with maximized bandgaps (Cox and Dobson 1999; Sigmund and Jensen 2003) and metamaterials with negative permeability (Diaz and Sigmund 2010), and a genetic algorithm was used recently by Bilal and Hussein (2011) to design phononic bandgap structures with large bandgaps. The present study is closely related to the mentioned works on optimization of bandgap structures, but here we do not directly consider the gaps in the frequency spectrum in the optimization formulation—instead they appear automatically when we optimize the attenuation for higher frequencies. Related to the present approach is the recent study by Søe-Knudsen (2011), who maximized the wave attenuation in periodic curved pipes by considering the imaginary part of the eigenvalues.

2 Theory

Wave propagation in a linear elastic medium is governed by the dynamic equilibrium equation:

$$\rho \frac{\partial^2 \mathbf{u}}{\partial t^2} = \boldsymbol{\partial}^T \mathbf{C} \boldsymbol{\partial} \mathbf{u},$$

$$\boldsymbol{\partial} = \begin{bmatrix} \frac{\partial}{\partial x} & 0 & 0 \\ 0 & \frac{\partial}{\partial y} & 0 \\ 0 & 0 & \frac{\partial}{\partial z} \\ \frac{\partial}{\partial y} & \frac{\partial}{\partial x} & 0 \\ 0 & \frac{\partial}{\partial z} & \frac{\partial}{\partial y} \\ \frac{\partial}{\partial z} & 0 & \frac{\partial}{\partial x} \end{bmatrix} = \boldsymbol{\alpha}_1 \frac{\partial}{\partial x} + \boldsymbol{\alpha}_2 \frac{\partial}{\partial y} + \boldsymbol{\alpha}_3 \frac{\partial}{\partial z} \tag{3}$$

where ρ is the material density, $\mathbf{u}$ is the displacement vector, and $\mathbf{C}$ is the constitutive matrix.

In the case of a periodic medium the solution can be expressed using the Bloch wave expansion in (1). After inserting the expansion into the wave equation we obtain the following eigenvalue problem:

$$-\omega^2 \rho \tilde{\mathbf{u}} = (\boldsymbol{\partial} + \boldsymbol{\kappa})^T \mathbf{C} (\boldsymbol{\partial} + \boldsymbol{\kappa}) \tilde{\mathbf{u}} \tag{4}$$

which has appearance of a standard eigenvalue problem in linear elasticity but with the additional term

$$\boldsymbol{\kappa} = i \left(\boldsymbol{\alpha}_1 k_x + \boldsymbol{\alpha}_2 k_y + \boldsymbol{\alpha}_3 k_z \right) \tag{5}$$

In the following the analysis will be restricted to consider waves propagating in-plane, that is $k_z = 0$.

By using a standard Galerkin FE approach it is straightforward to obtain a discretized version of the equation. In this work we focus on the spatial attenuation, thus we formulate the eigenvalue problem in terms of the wave number as the eigenvalue and by setting the wave vector components $k_x = k\cos(\theta)$, $k_y = k\sin(\theta)$, and $k_z = 0$, with θ as the angle determining the wave propagation direction as illustrated in Fig. 2, the following discretized eigenvalue problem is obtained:

$$(\mathbf{K} - k\mathbf{M})\mathbf{U} = (\mathbf{K}(\theta, \omega) - k\mathbf{M}(\theta)) \begin{bmatrix} k\mathbf{d} \\ \mathbf{d} \end{bmatrix} = \mathbf{0} \tag{6}$$

where the matrices $\mathbf{K}$ and $\mathbf{M}$ are computed as stated in Appendix A, and $\mathbf{d}$ is the discretized periodic eigenmode.

From the complex wave number $k = k' + ik''$, the attenuation factor can be determined as Cremer et al. (2005):

$$\eta = 2\frac{k''}{k'} \tag{7}$$

In order to estimate the smallest η of the material for a given frequency, (6) is solved for a range of angles θ in order to cover the wavenumber range corresponding to the irreducible Brillouin zone. In this paper the main focus will be on the design of material microstructures with a 45° symmetry, and thus $\theta \in [0°, 45°]$ will cover the irreducible part of the Brillouin zone.

For low frequencies, when the wave length is larger than the unit cell size, the attenuation factor η will correspond to the loss factor obtained by quasi-static homogenization using the correspondence principle (as done in Yi et al. (2000), Andreasen et al. (2013)). For quasi-static conditions η is the ratio been the imaginary and real part of the homogenized stiffness at a given frequency or the range of low frequencies with the same (frequency independent) material properties.

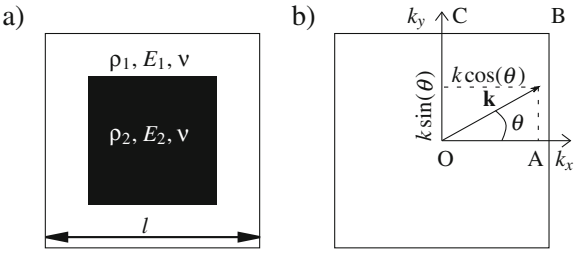

Fig. 2 **a** Unit cell of periodic material consisting of two phases with different density and elasticity modulus. The cell side is quadratic with side length l. **b** Illustration of the Brillouin zone and propagation directions specified by the angle θ. For materials with 45° symmetry the irreducible Brillouin zone is a triangle connecting O-A-B-O

2.1 Optimization problem

We introduce element-wise design variables $\varphi_e \in [0, 1]$ to describe the material distribution in the unit cell. We apply a gradient-based topology optimization scheme and it is thus necessary to introduce a continuous interpolation between the soft and stiff material in each finite element, as in the following

$$\rho_e = (1-\varphi_e)\rho_1 + \varphi_e \rho_2 \tag{8}$$

$$E'_e = (1-\varphi_e)E'_1 + \varphi_e E'_2 \tag{9}$$

$$E''_e = \left(2E''_1 + 2E''_2 - 4E''_{\min}\right)\varphi_e^2 + \left(-3E''_1 - E''_2 + 4E''_{\min}\right)\varphi_e + E''_1 \tag{10}$$

Thus, we apply a linear interpolation of the mass density and the real part of Young's modulus. The quadratic interpolation of the imaginary part is chosen such that it has its minimum at $E''_{\min}$ and becomes linear if we set

$$E''_{\min} = \frac{E''_1 + E''_2}{2} \tag{11}$$

By setting $E''_{\min}$ to a lower value (e.g. $E''_{\min} = 0$, which in our experience works well) elements with intermediate values are discouraged, because they have a lower loss factor. This is illustrated in Fig. 3.

The basic optimization problem can be stated as follows:

$$\begin{aligned} \max_{\varphi}: \ & \min_{\omega} (\eta) \\ & (\mathbf{K}(\theta,\omega) - k\mathbf{M}(\theta))\mathbf{U} = \mathbf{0}, \quad \omega \in [\omega_1, \omega_2] \\ & 0 \le \varphi_e \le 1, \qquad\qquad e = 1, ..., N \end{aligned} \tag{12}$$

where ω_1 to ω_2 is the frequency range.

For the sake of convenience the optimization problem is restated using a bound formulation. That is, the first line of the optimization problem in (12) is substituted with:

$$\begin{aligned} \max_{\varphi}: \ & c \\ \text{s.t.}: \ & \eta \ge c \ \ i = 1, ..., N \end{aligned} \tag{13}$$

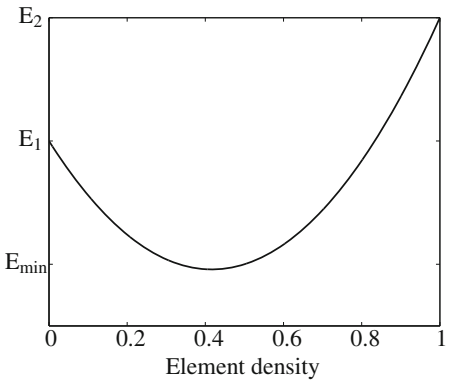

Fig. 3 Illustration of how the imaginary part of the elasticity modulus vary with the element density according to the interpolation in (10)

where c is an artificial optimization variable, N is the total number of loss factors computed for a range of frequencies ω and wave vector angles θ.

Topology optimization is then used iteratively to decide whether one finite element should contain the soft or the stiff material. In each iteration all densities are adjusted using a nonlinear optimization algorithm (we have used the Method of Moving Asymptotes-MMA (Svanberg 1987)), which must be supplied with the gradients (sensitivities) of the objective and constraints.

2.1.1 Regularization scheme

From numerical experiments we have observed that very thin layers of the soft lossy material is often favorable for high loss and high stiffness composites. In order to avoid feature sizes at the order of single element layers we apply a regularization scheme to the optimization problem (see Bendsøe and Sigmund 2003). We find that a good regularization scheme for this problem is to apply a filter on the design variables (Bruns and Tortorelli 2001):

$$\tilde{\varphi}_e = \frac{\sum_{i\in N_e} w(\mathbf{x}_i)\varphi_e}{\sum_{i\in N_e} w(\mathbf{x}_i)} \tag{14}$$

where

$$w(\mathbf{x}_i) = R - \|\mathbf{x}_i - \mathbf{x}_e\| \tag{15}$$

is a linearly decaying weight function, N_e is a list of elements for which the centers lie inside the filter radius R, and $\mathbf{x}_i$ is the spatial location of element center i.

The filtering often implies that even the final design contains some elements with intermediate material properties; neither pure stiff, nor pure soft material. This can be avoided by gradually reducing the filter radius R (or alternatively by using a projection scheme as first suggested by Guest et al. (2004)). Starting with a large filter radius has the advantage that it convexifies the optimization problem, and is particularly useful if you start with a random initial guess. However, for the majority of the results presented in Section 3 a constant filter radius $R = 1.2$ elements has been used.

2.2 Sensitivities

The sensitivities of η w.r.t. a change in an element design variable is computed as (note that primes and double-primes are used to denote real and imaginary parts):

$$\frac{d\eta}{d\varphi_e} = \frac{2\left(k'\left(\frac{dk}{d\varphi_e}\right)'' - k''\left(\frac{dk}{d\varphi_e}\right)'\right)}{(k')^2} \tag{16}$$

where the sensitivities of k with respect to the element variables φ_e is found by differentiating the eigenvalue problem

$$\frac{d((\mathbf{K}-k\mathbf{M})\mathbf{U})}{d\varphi_e} = \frac{d\mathbf{K}}{d\varphi_e}\mathbf{U} + \mathbf{K}\frac{d\mathbf{U}}{d\varphi_e} - \frac{dk}{d\varphi_e}\mathbf{M}\mathbf{U} - k\frac{d\mathbf{M}}{d\varphi_e}\mathbf{U} - k\mathbf{M}\frac{d\mathbf{U}}{d\varphi_e} \tag{17}$$

We define the adjoint problem as the left eigenvalue problem:

$$(\mathbf{K}-k\mathbf{M})^T\mathbf{V} = \mathbf{0} \Leftrightarrow \mathbf{V}^T(\mathbf{K}-k\mathbf{M}) = \mathbf{0} \tag{18}$$

And premultiply (17) with $\mathbf{V}^T$ to get

$$\mathbf{V}^T\frac{d\mathbf{K}}{d\varphi_e}\mathbf{U} + \mathbf{V}^T\mathbf{K}\frac{d\mathbf{U}}{d\varphi_e} - \frac{dk}{d\varphi_e}\mathbf{V}^T\mathbf{M}\mathbf{U} - k\mathbf{V}^T\frac{d\mathbf{M}}{d\varphi_e}\mathbf{U} - k\mathbf{V}^T\mathbf{M}\frac{d\mathbf{U}}{d\varphi_e} = \mathbf{0} \tag{19}$$

which can be simplified to

$$\mathbf{V}^T\frac{d\mathbf{K}}{d\varphi_e}\mathbf{U} - \frac{dk}{d\varphi_e}\mathbf{V}^T\mathbf{M}\mathbf{U} - k\mathbf{V}^T\frac{d\mathbf{M}}{d\varphi_e}\mathbf{U} + \mathbf{V}^T(\mathbf{K}-k\mathbf{M})\frac{d\mathbf{U}}{d\varphi_e} = \mathbf{0} \tag{20}$$

The last term is zero by the definition of the adjoint problem. Thus

$$\frac{dk}{d\varphi_e} = \frac{\mathbf{V}^T\left(\frac{d\mathbf{K}}{d\varphi_e} - k\frac{d\mathbf{M}}{d\varphi_e}\right)\mathbf{U}}{\mathbf{V}^T\mathbf{M}\mathbf{U}} \tag{21}$$

Details on how to compute the derivatives of $\mathbf{K}$ and $\mathbf{M}$ can be found in Appendix A.

2.3 Stiffness constraints

Simply maximizing η in the low frequency range is a trivial optimization problem since (as noted in Fig. 1) the composite with the highest loss factor is pure soft material-this is verified by numerical experiments. In order to obtain high loss combined with a certain stiffness for low frequencies a stiffness constraint is introduced. This is done by requiring that the homogenized elasticity modulus E^* of the composite is larger than a specified threshold. E^* can be computed from the initial slopes of the two first bands in a band diagram, or it can be found by numerical homogenization of the corresponding static problem. In any case the constraint is formulated as:

$$E^* \geq f_E E_2' \tag{22}$$

where f_E is the required fraction of the elastic modulus of the stiffest of the two material phases.

Details of how to compute E^* and the corresponding sensitivities (gradients) can be found in several papers (e.g. Sigmund 1995).

2.4 Connectivity constraint

Andreasen et al. (2013) observe that the stiffness constraint does not lead to a connected stiff phase when optimizing for the loss. A connected stiff phase could be a requirement for a manufacturing process where the stiff phase is created first and afterwards infused by the soft phase. The microstructure of the stiff phase could for example be produced using an additive manufacturing process, which would be most relevant for three-dimensional microstructures, or by perforating a plate, which would be applicable to two-dimensional microstructures. In both cases the connectivity of the stiff phase is crucial.

As in Andreasen et al. (2013) we obtain the connectivity through a lower bound on the conductivity of the microstructure with the soft phase modelled as an insulator. This is essentially equivalent to a stiffness constraint where the soft phase is replaced by void, but the conductivity problem is a scalar problem and thus computationally much cheaper. The constraint is:

$$\kappa^* \geq f_\kappa \kappa_2 \tag{23}$$

where κ^* is the homogenized conductivity, and f_κ is the required fraction. Computing the homogenized connectivity implies introducing another material interpolation:

$$\kappa_e = (1-\varphi_e)^{p_\kappa}\kappa_1 + \varphi_e^{p_\kappa}\kappa_2 \tag{24}$$

where the insulator is simulated by setting $\kappa_1 = 10^{-6}\kappa_2$, assuming κ_2 is the material phase that should be connected. A penalization parameter p_κ is here introduced in order to penalize intermediate design variable values. In order to obtain well defined structures a value of 1 or 2 is used in the examples.

The constraint cannot guarantee connectivity, but the results presented in Section 3 indicate that it works in practice.

3 Results

The results presented are all obtained with a mesh consisting of 50 times 50 bilinear elements of a square unit cell with side lengths $l = 1$ cm. However, the discussed optimization method could be applied to an arbitrarily shaped unit cell and is in no way limited to a square unit cell. The material properties of the two phases (constituents) can be found in Table 1.

The stiff material could be a metal, e.g. aluminum or titanium, and the soft material could be a polypropylene (PP) polymer. Remark, even though the stiff material is modeled as a viscoelastic material (with a very small loss factor) this is not necessary for the optimization, but is done because in practice the stiff material will also have a small loss.

Table 1 Material parameters for the two materials

Material	ρ [kg/m^3]	E' [GPa]	E'' [GPa]	ν [–]
(1) Soft	1000	1	0.1	0.3
(2) Stiff	4500	100	0.1	0.3

Furthermore, we should point out that in reality the soft material would have a somewhat higher Poisson's ratio, but keeping Poisson's ratio constant allows us to interpolate between material in ρ and E only (8–10). However, we have performed optimizations with different Poisson's ratios without observing any qualitative changes in the resulting topologies. However, to model incompressible materials (with Poisson's ratio equal to 0.5) would require a different model, and is an interesting topic for future research.

What can be considered low and high frequencies depend on the material properties. Therefore, in the figures containing band diagrams, we have scaled the frequency as $\tilde{\omega}$:

$$\tilde{\omega} = \frac{\omega l}{2\pi\sqrt{E_2'/\rho_2}} \tag{25}$$

3.1 Structures with 45 degree symmetry

In these first examples we restrict the study to structures that possess 45 degree symmetry. We consider both the cases of low and high frequencies and address the issue of connectivity for manufacturing purposes.

For all optimizations in this section three directions for the wave vector have been included ($\theta \in (0°, 22.5°, 45°)$). Three were chosen as a compromise between solution time and accuracy of the estimate of the lowest attenuation factor. With this choice each iteration takes approximately five seconds per frequency included on a single processor, and each optimization can require several hundred iterations. However, we have afterwards checked the results using more directions in order to make sure that the results are representative.

The attenuation factors obtained for different frequencies and constraint values are compared in Fig. 1, and the corresponding material structures are presented in the following.

3.1.1 Low frequency

With the specified choice of materials and unit cell dimensions, the frequency band 10–20 kHz is in the linear part of the dispersion diagram, which we will denote the low frequency range. Maximizing the loss for this frequency range with three different stiffness constraints result in the material structures in Fig. 4. For all three structures the initial filter radius $R = 0.1l$ was gradually decreased by a factor 1/1.2 and eventually turned off. After each decrease the design was allowed to converge before a new decrease. The exact initial filter radius and the decrease factor are of little importance, as long as the initial radius is large enough and the decrease is slow the optimization will, in our experience, converge to the same microstructure.

That being said, the microstructure in Fig. 4a) is seen to be qualitatively different from the two others, but does obtain the upper quasi-static bound. The main criterion is that the stiff material phase is unconnected, such that large deformations take place in the soft and lossy phase. To achieve a larger elasticity modulus, the size of the stiff inclusion should be increased, which is also the conclusion reached by Andreasen et al. (2013) using a quasi-static model in the optimization.

It should be mentioned that by using an even larger initial filter radius the resulting microstructure resembles the slightly simpler topology seen Fig. 4b and c. Alternatively, one could have started with one stiff inclusion as the initial guess, but we find it convincing that the optimization is actually able to find a nearly optimal solution (it obtains the upper bound) from a random initial guess. A summary of the iteration history for Fig. 4b can be seen in Fig. 5.

In Fig. 1 the point indicating the performance of the microstructure with the tightest stiffness constraint, is seen to be slightly below the upper bound. This is due to the discretization of the unit cell, which does not allow for a thinner gap between the stiff inclusions, so that the stiff inclusions are connected by a small amount of intermediate densities at the corners to fulfill the stiffness constraint (a gray dot can be identified at the corners by zooming in on the figure).

3.1.2 High frequency

We now consider the higher frequency range. We observe that the attenuation now can exceed the quasi-static bounds considerably due to the dynamic effects leading to the opening of bandgaps in the frequency spectrum.

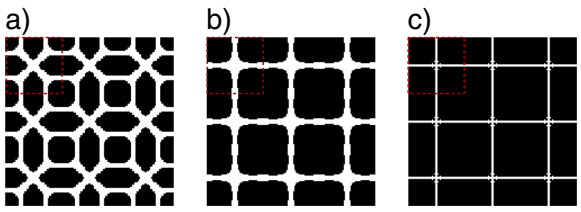

Fig. 4 Resulting microstructures when maximizing the loss for the frequency range 10–20 kHz. One unit cell is indicated by a dashed box. Stiffness constraints: **a** $f_E = 0.05$, **b** $f_E = 0.1$, and **c** $f_E = 0.25$

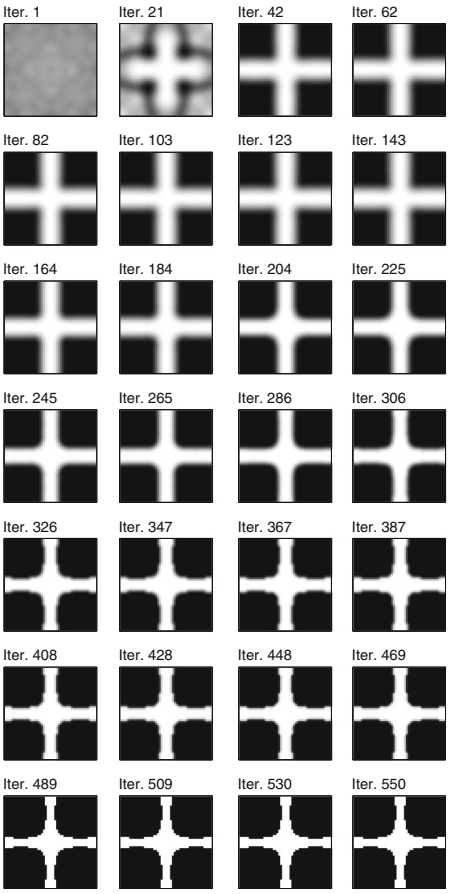

Fig. 5 The iteration history for the microstructure in Fig. 4b

In Fig. 6 the resulting microstructures optimized for the loss at four individual higher frequencies are shown. To facilitate the discussion of these results the corresponding real parts of the band diagrams are displayed in Fig. 7. A band diagram is constructed by traversing the boundary of the irreducible Brillouin zone, which for a 45 degree symmetry structure corresponds to the line O-A-B-O in Fig. 2b. For each point on the boundary (k_x, k_y) the eigenvalue problem in (6) is solved for ω. The corresponding frequencies are plotted as functions of the position on the O-A-B-O line. Gaps in the frequency range are called bandgaps, and for those frequencies waves will not propagate in the material. All four microstructures exhibit large bandgaps, even though the loss is only maximized for one frequency, however, the broad bandgaps ensure that the spatial decay at the optimization frequencies is large.

Interestingly, we note that the 40 kHz microstructure has a relatively high loss-higher than the pure soft phase-without exhibiting a bandgap at this frequency. However, the optimization frequency resides in the near vicinity of a bandgap

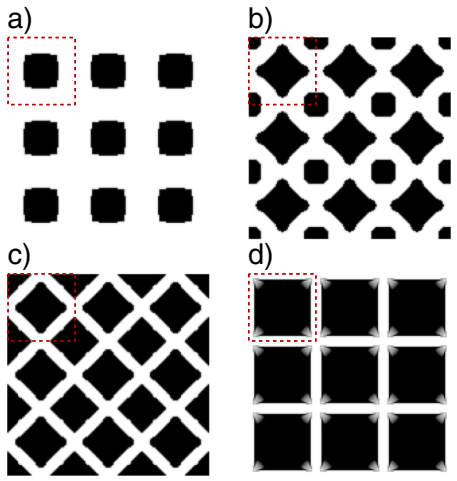

Fig. 6 Resulting microstructures when maximizing the loss, without any constraints, for the frequencies **a** 40 kHz, **b** 100 kHz, **c** 140 kHz, and **d** 180 kHz. One unit cell is indicated by a dashed box

where the propagating bands are flat (low group velocity), which results in an enhanced attenuation in this frequency range.

The structure with a maximized loss at 180 kHz can be seen to contain some intermediate design variables. However, as will be shown in Section 3.1.3, it is possible to obtain high attenuation at this frequency without "gray" material. However, for this specific set of parameters and choice of interpolation they do appear. To give a fair comparison with phononic bandgap structures reported in the literature, all band diagrams are created using a threshold

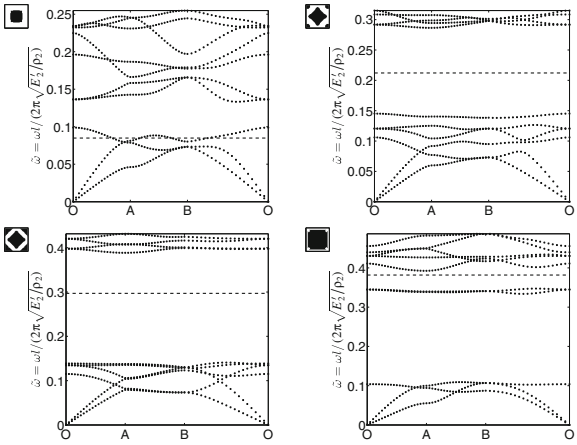

Fig. 7 Band diagrams for the optimized microstructures in Fig. 6. A dotted line shows the frequency for which the loss has been maximized. In the upper left corner the thresholded version of the unit cell is shown

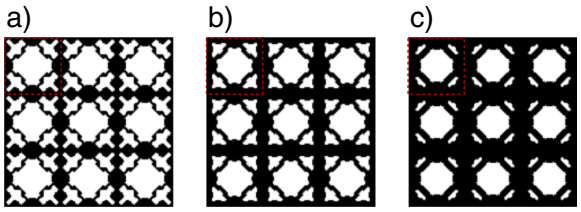

Fig. 8 Resulting microstructures when maximizing the loss at 100 kHz, with a conductivity constraint of **a** $f_\kappa = 0.2$, **b** $f_\kappa = 0.35$, and **c** $f_\kappa = 0.5$. One unit cell is indicated by a dashed box

version of the design (threshold value is $\varphi_e = 0.5$) to ensure the interpolation does not influence the dispersion relations.

3.1.3 Connected stiff phase

Without any constraints, the loss optimized microstructures seem to favor a disconnected stiff phase. However, by applying the previously discussed conductivity constraint, a microstructure with a connected stiff phase can be obtained. This is illustrated in Figs. 8 and 9, where conductivity constraints have been applied when optimizing η at 100 and 180 kHz, respectively. All six microstructures have a connected stiff phase.

The corresponding band diagrams can be seen in Fig. 10. It is noted that even though a decent attenuation factor can be obtained for the 100 kHz microstructure with the lowest conductivity constraint, it is not accompanied by a full bandgap in the band diagram. But compared to the two designs with a stricter conductivity constraint, which have a much lower attenuation factor, the mode just below the 100 kHz line is flat and there is a narrow partial bandgap at 100 kHz. The microstructures optimized for 180 kHz, however, show very large bandgaps. The structure in Fig. 9a has a relative bandgap of more than 1, which is comparable to the largest reported bandgaps in the literature (Bilal and Hussein 2011). Changing the soft material to void and disregarding dissipation, as in Bilal and Hussein (2011), increases the magnitude of the bandgap to a relative size of 1.3.

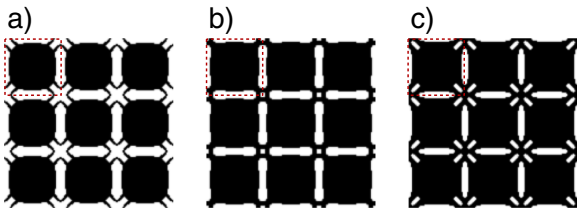

Fig. 9 Resulting microstructures when maximizing the loss at 180 kHz, with a conductivity constraint of **a** $f_\kappa = 0.2$, **b** $f_\kappa = 0.35$, and **c** $f_\kappa = 0.5$. One unit cell is indicated by a dashed box

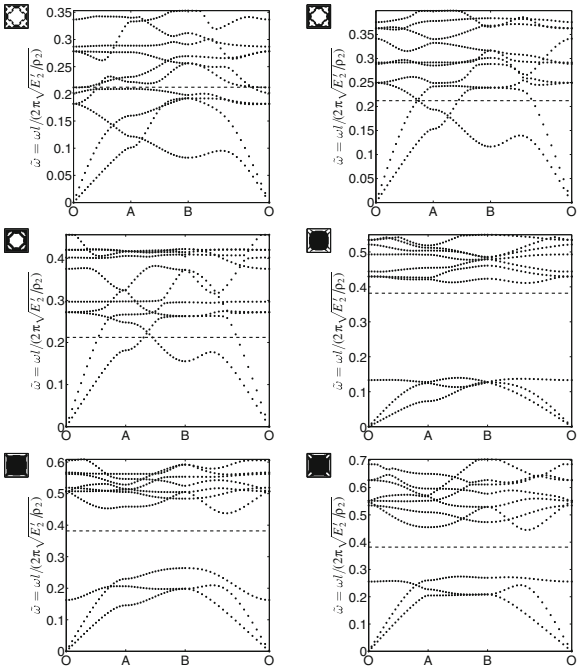

Fig. 10 Band diagrams for the optimized microstructures in Figs. 8 and 9. A dotted line shows the frequency for which the loss has been maximized. In the upper left corner the thresholded version of the unit cell is shown

3.1.4 Localized loss—internal resonator

Figure 11 shows the structure corresponding to the only point in Fig. 1 that is left to discuss. Here we obtain a structure with a resonating inclusion embedded in a soft region that is again enclosed by the connected stiff structure. It has been obtained by maximizing the loss at 110 kHz with a stiffness constraint $f_E = 0.65$, which assures the stiff connected frame. In order to obtain the structure the initial structure was chosen as a stiff frame with the soft material inside.

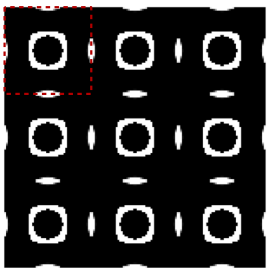

Fig. 11 Microstructure of material with maximized loss factor at 110 kHz and a stiffness constraint $f_E = 0.65$. Again, one unit cell is indicated by a dashed box

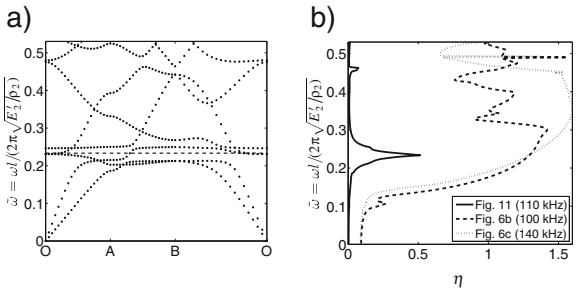

Fig. 12 **a** Band diagram for microstructure in Fig. 11. **b** Comparison of loss factor as function of frequency for the microstructures in Fig. 6b, c and 11

As is seen in Fig. 1 this microstructure exhibits a very favorable combination of attenuation and stiffness residing in the very upper right corner of the map. These kind of structures have also received considerable interest in the literature in the past decade for this very reason (Liu et al. 2000). The corresponding band diagram in Fig. 12a) shows significant band distortion and flat bands (low group velocity) at the optimization frequency. However, the high attenuation factor is much localized in the frequency domain, as opposed to the structures shown previously. This can be seen by plotting the attenuation factor as a function of the frequency as done in Fig. 12b, where, for comparison purposes, the attenuation factors for the microstructures in Fig. 6b and c are included. However, the localized loss can be expected since the high attenuation is caused by a local resonance of the inclusion inside the embedded soft layer.

3.2 Optimizing for directional dependent loss

The optimization problem is now modified such that a material with a directional dependent loss is achieved. For this purpose we consider the case where the material does not

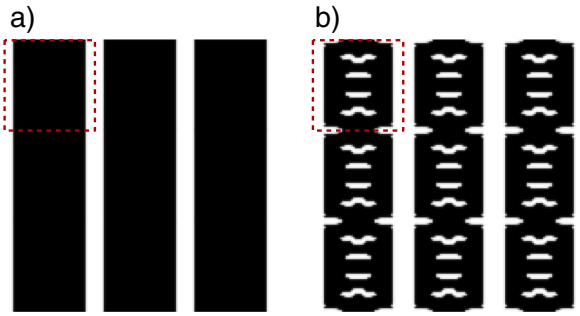

Fig. 13 Resulting microstructures when maximizing the ratio between the loss in the horizontal and vertical direction. **a** Without any constraints. **b** With a minimum loss factor of 0.05 in the vertical direction

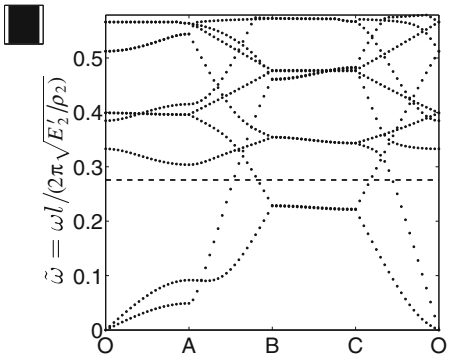

Fig. 14 Band diagram for the microstructure in Fig. 13a. For the considered frequency there are no modes propagating in the horizontal direction

have 45 degree symmetry, but only 90 degree symmetry. The objective is to maximize the ratio between the smallest loss in the $\theta_1 = 0°$ direction and the smallest loss in the

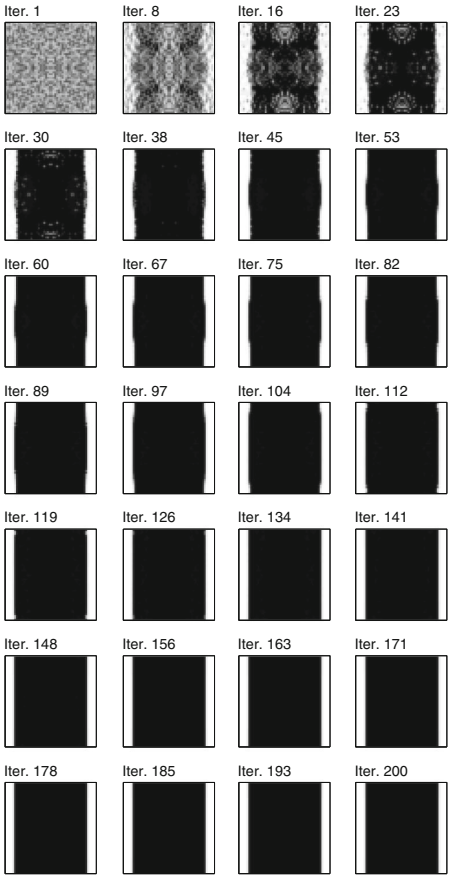

Fig. 15 The iteration history for the microstructure in Fig. 13a

direction corresponding to $\theta_2 = 90°$. For this approach the penalization scheme in Eq. 10 with $E''_{\min} = 0$ will not be a suitable choice, because intermediate values of the design variables can be used to decrease the loss in the θ_2-direction. However, by setting $E''_{\min} = (E''_1 + E''_2)/2$, the penalization becomes linear (in our case constant, because $E''_1 = E''_2$), and the optimization ends up with the grating-like design in Fig. 13a, where the corresponding real part of the band diagram in Fig. 14 shows how there are no modes propagating in the θ_1-direction for $\omega = 130$ kHz, but there are modes propagating in the θ_2-direction. The iteration history for the design can be seen in Fig. 15, from where it can be seen that even with a random initial guess the optimization ends up with the grating like design.

This approach could also be combined with a constraint on the minimum loss in the θ_2-direction. That is, we want a larger loss in the θ_1-direction, but we want to make sure the loss in the $\theta = 90°$ is at least $\eta_{\min} = 0.05$. The resulting material structure, which fulfills this constrain, can be seen in Fig. 13b.

4 Conclusion

The proposed loss optimization method works well for both low and high frequencies and can be used to optimize for a frequency dependent loss. By changing the objective function, and combining it with suitable constraints, it is possible to obtain close to the optimal microstructure for a given application. The approach described can easily be implemented for three-dimensional problems, and even though the computational cost of solving each eigenvalue problem will be relatively high, each problem is independent and the procedure can without much effort be parallelized. Another positive aspect of the described method is the ease with which frequency dependent material parameters can be taken into account in the optimization.

Appendix A: System matrices

The system matrices in (6) are

$$\mathbf{K} = \begin{bmatrix} -i(\cos(\theta)\mathbf{K}_1 + \sin(\theta)\mathbf{K}_2) & \mathbf{K}_0 - \omega^2\mathbf{M}_0 \\ \mathbf{I} & \mathbf{0} \end{bmatrix} \tag{26}$$

$$\mathbf{M} = \begin{bmatrix} -\cos^2(\theta)\mathbf{K}_3 - \cos(\theta)\sin(\theta)\mathbf{K}_4 - \sin^2(\theta)\mathbf{K}_5 & \mathbf{0} \\ \mathbf{0} & \mathbf{I} \end{bmatrix} \tag{27}$$

with

$$\begin{aligned}
\mathbf{M}_0 &= \sum_e \int_{\Omega^e} \rho_e \mathbf{N}^T \mathbf{N}\, \mathrm{d}\,\Omega^e \\
\mathbf{K}_0 &= \sum_e \int_{\Omega^e} \mathbf{B}^T \mathbf{C}\mathbf{B}\, \mathrm{d}\,\Omega^e, \\
\mathbf{K}_1 &= \sum_e \int_{\Omega^e} \mathbf{N}^T \boldsymbol{\alpha}_1^T \mathbf{C}\mathbf{B}\, \mathrm{d}\,\Omega^e, \\
\mathbf{K}_2 &= \sum_e \int_{\Omega^e} \mathbf{N}^T \boldsymbol{\alpha}_2^T \mathbf{C}\mathbf{B}\, \mathrm{d}\,\Omega^e, \\
\mathbf{K}_3 &= \sum_e \int_{\Omega^e} \mathbf{N}^T \boldsymbol{\alpha}_1^T \mathbf{C}\boldsymbol{\alpha}_1 \mathbf{N}\, \mathrm{d}\,\Omega^e, \\
\mathbf{K}_4 &= \sum_e \int_{\Omega^e} \mathbf{N}^T \left(\boldsymbol{\alpha}_1^T \mathbf{C}\boldsymbol{\alpha}_2 + \left(\boldsymbol{\alpha}_1^T \mathbf{C}\boldsymbol{\alpha}_2\right)^T\right) \mathbf{N}\, \mathrm{d}\,\Omega^e, \\
\mathbf{K}_5 &= \sum_e \int_{\Omega^e} \mathbf{N}^T \boldsymbol{\alpha}_2^T \mathbf{C}\boldsymbol{\alpha}_2 \mathbf{N}\, \mathrm{d}\,\Omega^e,
\end{aligned} \tag{28}$$

where $\sum_e$ is a sum over all finite elements, $\mathbf{N}$ is a matrix with the shape functions, $\mathbf{B} = \partial\mathbf{N}$, $\mathbf{C}$ is the constitutive matrix, and Ω^e is the volume of element e.

A.1 Derivatives of system matrices

To keep the notation compact $c = \cos(\theta)$ and $s = \sin(\theta)$ are used below. It is important to remember that $\mathbf{K}_i$ depend on E_e, and $\mathbf{M}_0$ depends on ρ_e. Such that:

$$\frac{d\mathbf{K}}{d\varphi_e} = \frac{dE_e}{d\varphi_e}\begin{bmatrix} -i\left(c\mathbf{K}_1^e + s\mathbf{K}_2^e\right) & \mathbf{K}_0^e \\ \mathbf{0} & \mathbf{0} \end{bmatrix} - \frac{d\rho_e}{d\varphi_e}\begin{bmatrix} \mathbf{0} & \omega^2\mathbf{M}^e \\ \mathbf{0} & \mathbf{0} \end{bmatrix} \tag{29}$$

and

$$\frac{d\mathbf{M}^e}{d\varphi_e} = \frac{dE_e}{d\varphi_e}\begin{bmatrix} -\left(c^2\mathbf{K}_3^e + cs\mathbf{K}_4^e + s^2\mathbf{K}_5^e\right) & \mathbf{0} \\ \mathbf{0} & \mathbf{0} \end{bmatrix} \tag{30}$$

where

$$\frac{dE'_e}{d\varphi_e} = E'_2 - E'_1 \tag{31}$$

$$\begin{aligned}
\frac{dE''_e}{d\varphi_e} &= 2\left(2E''_1 + 2E''_2 - 4E''_{\min}\right)\varphi_e \\
&\quad + \left(-3E''_1 - E''_2 + 4E''_{\min}\right)
\end{aligned} \tag{32}$$

The derivatives of the interpolated density ρ_e and conductivity κ_e are analogous to the (31). If the filtering scheme in (14) is applied, the sensitivities of a function g (an objective

or constraint) must be modified according to the chain rule. The modified sensitivities can be expressed as:

$$\frac{dg}{d\varphi_e} = \sum_{i \in N_e} \frac{dg}{d\tilde{\varphi}_i} \frac{d\tilde{\varphi}_i}{d\varphi_e} \tag{33}$$

Furthermore, if a projection is applied, which has not been the case for any of the results presented in this paper, the element sensitivities should be multiplied with the derivative of the projection.

References

Andreasen CS, Andreassen E, Jensen JS, Sigmund O (2013) On the realization of the bulk modulus bounds for two-phase viscoelastic composites. J Mech Phys Solids. doi:10.1016/j.jmps.2013.09.007

Andreassen E, Jensen JS (2013) Analysis of phononic bandgap structures with dissipation. ASME J Vib Acoust 135:041, 015

Bendsøe M, Sigmund O (2003) Topology optimization. Theory, methods and applications. Springer, Berlin

Bensoussan A, Lions JL, Papanicolaou G (1978) Asymptotic analysis for periodic structures. North-Holland, Amsterdam

Bilal OR, Hussein MI (2011) Ultrawide phononic band gap for combined in-plane and out-of-plane waves. Phys Rev E 84(6–2):065, 701

Bloch F (1929) Über die quantenmechanik der elektronen in kristallgittern. Z Phys 52(7–8):555–600

Brodt M, Lakes R (1995) Composite-materials which exhibit high stiffness and high viscoelastic damping. J Compos Mater 29(14):1823–1833

Bruns TE, Tortorelli DA (2001) Topology optimization of non-linear elastic structures and compliant mechanisms. Comput Method Appl M 190(26–27):3443–3459

Christensen R (1971) Theory of viscoelasticity. An introduction. Academic, New York

Collet M, Ouisse M, Ruzzene M, Ichchou MN (2011) Floquet-Bloch decomposition for the computation of dispersion of two-dimensional periodic, damped mechanical systems. Int J Solids Struct 48(20):2837–2848

Cox S, Dobson D (1999) Maximizing band gaps in two-dimensional photonic crystals. Siam J Appl Math 59(6):2108–2120

Cremer L, Heckl M, Petersson BAT (2005) Structure-borne sound. Structural vibrations and sound radiation at audio frequencies. Springer, Berlin

Diaz AR, Sigmund O (2010) A topology optimization method for design of negative permeability metamaterials. Struct Multidisc Optim 41(2):163–177

Farzbod F, Leamy MJ (2011) Analysis of Bloch's method in structures with energy dissipation. ASME J Vib Acoust 133(5):051, 010

Gibiansky L, Lakes R (1997) Bounds on the complex bulk and shear moduli of a two-dimensional two-phase viscoelastic composite. Mech Mater 25(2):79–95

Guedes JM, Kikuchi N (1990) Preprocessing and postprocessing for materials based on the homogenization method with adaptive finite element methods. Comput Method Appl M 83(2):143–198

Guest J, Prevost J, Belytschko T (2004) Achieving minimum length scale in topology optimization using nodal design variables and projection functions. Int J Numer Meth Eng 61(2):238–254

Guest JK, Prevost JH (2007) Design of maximum permeability material structures. Comput Method Appl M 196(4–6):1006–1017

Hashin Z (1970) Complex moduli of viscoelastic composites – i. general theory and application to particulate composites. Int J Solids Struct 6(5):539–552

Huang K, Lidorikis E, Jiang X, Joannopoulos J, Nelson K, Bienstman P, Fan S (2004) Nature of lossy Bloch states in polaritonic photonic crystals. Phys Rev B 69(19):195111

Hussein MI, Frazier MJ (2010) Band structure of phononic crystals with general damping. J Appl Phys 108:093, 506

Kim HJ, Swan CC, Lakes RS (2002) Computational studies on high-stiffness, high-damping SiC-InSn particulate reinforced composites. Int J Solids Struct 39(23):5799–5812

Lakes R (2009) Viscoelastic materials. Cambridge University Press, Cambridge

Lakes R, Lee T, Bersie A, Wang YC (2001) Extreme damping in composite materials with negative stiffness inclusions. Nature 410:565–567

Liu Z, Zhang X, Mao Y, Zhu YY, Yang Z, Chan CT, Sheng P (2000) Locally resonant sonic materials. Science 289:1734–1736

Meaud J, Sain T, Hulbert G, Waas AM (2013) Analysis and optimal design of layered composites with high stiffness and high damping. Int J Solids Struct 50(9):1342–1353

Moiseyenko RP, Laude V (2011) Material loss influence on the complex band structure and group velocity in phononic crystals. Phys Rev B 83:064, 301

Prasad J, Diaz A (2009) Viscoelastic material design with negative stiffness components using topology optimization. Struct Multidisc Optim 38(6):583–597

Sain T, Meaud J, Hulbert G, Arruda EM, Waas AM (2013) Simultaneously high stiffness and damping in a class of wavy layered composites. Compos Struct 101:104–110

Sanchez-Palencia E (1980) Non-homogeneous media and vibration theory. Lecture notes in physics. Springer-Verlag, p 127

Sigmund O (1994) Materials with prescribed constitutive parameters: an inverse homogenization problem. Int J Solids Struct 31(17):2313–2329

Sigmund O (1995) Tailoring materials with prescribed elastic properties. Mech Mater 20(4):351–368

Sigmund O, Jensen JS (2003) Systematic design of phononic band-gap materials and structures by topology optimization. Phil Trans R Soc Lond A 361(1806):1001–1019

Sigmund O, Torquato S (1997) Design of materials with extreme thermal expansion using a three-phase topology optimization method. J Mech Phys Solids 45(6):1037–1067

Søe-Knudsen A (2011) Design of stop-band filter by use of curved pipe segments and shape optimization. Struct Multidisc Optim 44(6):863–874

Svanberg K (1987) Method of moving asymptotes—a new method for structural optimization. Int J Numer Meth Eng 24(2):359–373

Wang B, Cheng G (2005) Design of cellular structures for optimum efficiency of heat dissipation. Struct Multidisc Optim 30(6):447–458

Yi YM, Park SH, Youn SK (2000) Design of microstructures of viscoelastic composites for optimal damping characteristics. Int J Solids Struct 37(35):4791–4810

Publication [P7]

Directional bending wave propagation in periodically perforated plates

Journal of Sound and Vibration 335 (2015) 187–203

Contents lists available at ScienceDirect

Journal of Sound and Vibration

journal homepage: www.elsevier.com/locate/jsvi

Directional bending wave propagation in periodically perforated plates

Erik Andreassen [a,*], Kevin Manktelow [b], Massimo Ruzzene [b]

[a] Department of Mechanical Engineering, Technical University of Denmark, Nils Koppels Allé, Building 404, Denmark
[b] School of Aerospace Engineering, Georgia Institute of Technology, Atlanta, GA 30332, United States

ARTICLE INFO

Article history:
Received 11 February 2014
Received in revised form
24 September 2014
Accepted 24 September 2014
Handling Editor: G. Degrande
Available online 18 October 2014

ABSTRACT

We report on the investigation of wave propagation in a periodically perforated plate. A unit cell with double-C perforations is selected as a test article suitable to investigate two-dimensional dispersion characteristics, group velocities, and internal resonances. A numerical model, formulated using Mindlin plate elements, is developed to predict relevant wave characteristics such as dispersion, and group velocity variation as a function of frequency and direction of propagation. Experimental tests are conducted through a scanning laser vibrometer, which provides full wave field information. The analysis of time domain wave field images allows the assessment of plate dispersion, and the comparison with numerical predictions. The obtained results show the predictive ability of the considered numerical approach and illustrate how the considered plate configuration could be used as the basis for the design of phononic waveguides with directional and internal resonant characteristics.

1. Introduction

Recently, materials and structures with periodic modulations in their physical properties have attracted significant attention due to their unusual electromagnetic, acoustic and elastic properties. Such properties lead to unique wave propagation characteristics that can be exploited for the design of waveguides, filters, focusing devices, as well as structural assemblies with negative inertial properties and refractive characteristics. Thus, periodic structural configurations often form the basis for the design of metamaterials, and photonic and phononic crystals [1–4].

Several configurations of acoustic metamaterials and phononic crystals have been proposed in recent years. These designs have illustrated the ability to tailor equivalent material properties, and to achieve interesting dynamic phenomena such as negative refraction [5–8], wave beaming [9], and bandgaps [10–13]. Among the configurations proposed, the use of plate structures as propagation media is an attractive solution due to the existence of several theories to support the formulation of numerical models, and the ease of experimentation provided by optical measurement systems such as scanning laser vibrometers and interferometers. For these reasons, a number of recent studies have investigated elastic plates with periodic inclusions and voids, microstructures, and sources of impedance mismatch such as surface mounted stubs [14–16] to generate phononic plates and elasto-acoustic metamaterials [17,18]. In particular, the work of [12,6–8] focuses on flexural (transverse) waves in periodically perforated plates.

* Corresponding author.
E-mail address: erand@mek.dtu.dk (E. Andreassen).

http://dx.doi.org/10.1016/j.jsv.2014.09.035
0022-460X/

The objective of this paper is to conduct the numerical and the experimental investigation of transverse wave motion in a periodically perforated plate. Transversely polarized plate wave modes correspond to those modes characterizing the low frequency/long wavelength Lamb wave spectrum and often specifically to the first asymmetric mode (A_0) [19]. At low enough frequencies this mode can be well approximated by plate theories such as Kirchhoff's and Mindlin's [20]. The configuration of the unit cell of the periodic assembly consists of double-C perforations following Guenneau et al. [5], which are also reminiscent of electromagnetic metamaterial designs [21]. This specific configuration is interesting for a number of reasons. First, the periodic array of perforations is expected to provide the plate with partial and full frequency bandgaps, i.e. frequency ranges within which wave propagation is impeded either omnidirectionally or only for a specific range of directions. Such bandgaps may be the result of Bragg scattering, or may be produced by local resonances within the unit cell [22]. In addition, the non-isotropic unit cell design is also expected to lead to an overall, frequency-dependent anisotropy of the plate behavior, and consequently to the onset of wave directionality [9,23].

A numerical model is developed for the perforated plate using rectangular Mindlin plate elements. The model is validated by comparing with the predictions of a solid model. This also highlights the frequency range of accuracy of the formulation. Next, scanning laser vibrometer wave field measurements are conducted to further validate the numerical model and highlight the occurrence of anomalous wave motion, directional behavior and local resonances occurring within the considered plate. Specifically, wave field data are recorded over the entire plate to compute dispersion relations through the application of multidimensional (2D and 3D) Fourier transforms (FTs) [24], to visualize the shape of propagating wavefronts, and compare them with estimations based on dispersion surfaces and group velocity computations based on unit cell analysis and the application of Bloch theorem [25].

The paper is organized in four sections, including this introduction. Section 2 briefly describes the considered plate configuration, and presents the formulation of the numerical model for the evaluation of the dispersion characteristics of the plate. Section 3 illustrates the experimental setup, the procedures, and the signal processing methodologies used for the evaluation of the wave properties based on experimental data. Finally, Section 4 summarizes the main findings of the work and provides recommendations for future investigations.

2. Numerical analysis of wave motion

2.1. Configuration

The considered periodic plate and unit cell configuration are shown in Fig. 1. This configuration is expected to be characterized by higher equivalent stiffness along the longitudinal direction, and lower stiffness along the vertical direction, and thus appears as inherently anisotropic. Stiffness directionality has previously been described as one essential mechanism for the generation of frequency "caustics" [26,27], which in turn are responsible for the angular concentration of wave vectors at specific frequencies and their directional interference. In addition, the double-C perforations naturally define a resonating unit within the unit cell, which leads to localized modes and the generation of internal resonance frequency bandgaps [22,28,29]. The considered plate arrangement therefore appears as a convenient configuration for the numerical and the experimental investigation of wave directionality and resonant bandgaps, which are two of the predominant features of elastic metamaterials.

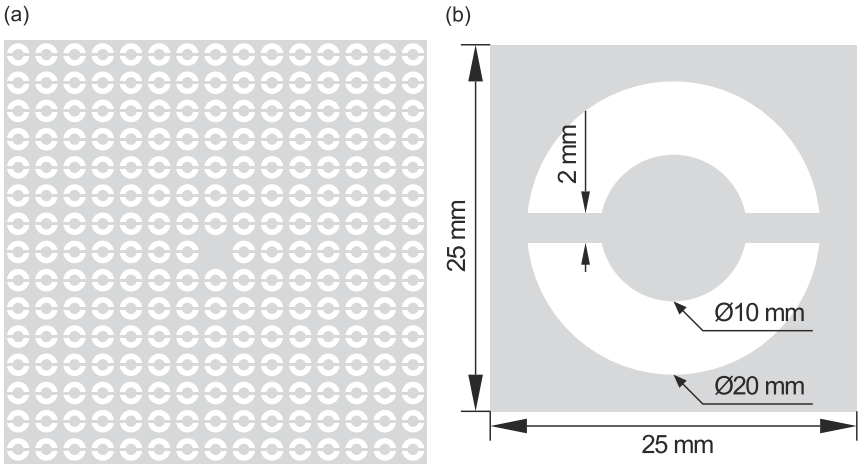

Fig. 1. (a) Perforated plate and (b) unit cell geometry and dimensions. The thickness of the plate is 1 mm.

2.2. Approach

A numerical model of the plate in Fig. 1 is developed to estimate its dynamic behavior, and in particular to predict its dispersion properties and corresponding wave velocities. The model is a finite element (FE) based discretization of the structure by means of four-node Mindlin plate (MP) elements [20]. MP elements are here used as a best compromise between the ability to capture high frequency Lamb wave modes that are typically too coarsely approximated by Kirchoff plate formulations, and the computational cost that is associated with the three-dimensional (3D) discretization of the plate. Remark, for at least the lower part of the frequency range considered in this paper Kirchhoff plate formulation would have been just as good, but the presented Mindlin formulation is directly applicable to higher frequencies and thicker plates. Focus is placed on the out-of-plane motion (bending) of the plate, which can be conveniently measured through the available scanning laser vibrometer system. Results in the upcoming subsections illustrate how the considered model is effective at capturing the low frequency predominantly transversely polarized, or antisymmetric, Lamb modes of the plate, which are of interest to the present study [19].

2.3. Governing equations

The out-of-plane dynamic behavior of the plate considered herein can be described by the following coupled set of governing differential equations [30]:

$$\nabla^T \mathbf{G}(\nabla w - \boldsymbol{\Theta}) = \rho h \frac{\partial^2 w}{\partial t^2} \tag{1}$$

$$\partial^T \mathbf{D} \partial \boldsymbol{\Theta} + \mathbf{G}(\nabla w - \boldsymbol{\Theta}) = \frac{\rho h^3}{12} \frac{\partial^2 \boldsymbol{\Theta}}{\partial t^2} \tag{2}$$

where $w(\mathbf{x}, t)$ denotes the out-of-plane deflection of a point of the mid-surface at location $\mathbf{x} = [x,\ y]^T$, $\boldsymbol{\Theta} = [\theta_x,\ \theta_y]^T$ is a vector containing the two rotations of a material line normal to the mid-surface about the two in-plane axes, ρ is the material density, while h is the plate thickness. Also, $\mathbf{D} = \mathbf{D}(\mathbf{x})$ and $\mathbf{G} = \mathbf{G}(\mathbf{x})$ are the plate constitutive matrices. At a given point in the plate material, which is locally isotropic, these are

$$\mathbf{D} = \frac{Eh^3}{12(1-\nu^2)} \begin{bmatrix} 1 & \nu & 0 \\ \nu & 1 & 0 \\ 0 & 0 & \frac{(1-\nu)}{2} \end{bmatrix} \tag{3}$$

and

$$\mathbf{G} = \frac{E}{2(1+\nu)} \begin{bmatrix} \frac{5}{6}h & 0 \\ 0 & \frac{5}{6}h \end{bmatrix} \tag{4}$$

Finally, the differential operator ∂ in Eq. (1) is defined as

$$\partial = \begin{bmatrix} 1 & 0 \\ 0 & 0 \\ 0 & 1 \end{bmatrix} \frac{\partial}{\partial x} + \begin{bmatrix} 0 & 0 \\ 0 & 1 \\ 1 & 0 \end{bmatrix} \frac{\partial}{\partial y} = \boldsymbol{\alpha}_1 \frac{\partial}{\partial x} + \boldsymbol{\alpha}_2 \frac{\partial}{\partial y} \tag{5}$$

The objective is to investigate the propagation of plane waves associated with the bending motion of the periodic plate. Therefore, solutions are in the form of a Bloch-expansion [25]:

$$\begin{bmatrix} w(\mathbf{x}, t) \\ \boldsymbol{\Theta}(\mathbf{x}, t) \end{bmatrix} = \begin{bmatrix} \tilde{w}(\mathbf{x}) \\ \tilde{\boldsymbol{\Theta}}(\mathbf{x}) \end{bmatrix} e^{i(\mathbf{k}\cdot\mathbf{x} + \omega t)} \tag{6}$$

where $\tilde{w}$ and $\tilde{\boldsymbol{\Theta}}$ are periodic functions whose period coincides with the unit cell, ω is the angular frequency, and $\mathbf{k} = [k_x,\ k_y]^T$ is the wave vector.

Eq. (1) can be rewritten in terms of the periodic fields to give

$$\nabla_k^T \mathbf{G}(\nabla_k \tilde{w} - \tilde{\boldsymbol{\Theta}}) = -\omega^2 \rho h \tilde{w} \tag{7}$$

where a new operator ∇_k is defined as

$$\nabla_k = \nabla + i\mathbf{k} = \boldsymbol{\beta}_1 \left(\frac{\partial}{\partial x} + ik_x \right) + \boldsymbol{\beta}_2 \left(\frac{\partial}{\partial y} + ik_y \right) \tag{8}$$

where $\boldsymbol{\beta}_1 = (1, 0)^T$, and $\boldsymbol{\beta}_2 = (0, 1)^T$.

Similarly, Eq. (2) can be rewritten as

$$\partial_k^T \mathbf{D} \partial_k \tilde{\boldsymbol{\Theta}} + \mathbf{G}(\nabla_k^T \tilde{w} - \tilde{\boldsymbol{\Theta}}) = -\omega^2 \frac{\rho h^3}{12} \tilde{\boldsymbol{\Theta}} \tag{9}$$

where the operator ∂_k is defined as

$$\partial_k = \boldsymbol{\alpha}_1\left(\frac{\partial}{\partial x}+ik_x\right)+\boldsymbol{\alpha}_2\left(\frac{\partial}{\partial y}+ik_y\right) \tag{10}$$

2.4. Finite element discretization

Eqs. (7) and (9) can be discretized using a standard Galerkin approach. The result can be cast in the same form as the in-plane wave propagation problem described in [31]. The mesh consists of 6560 square-shaped Mindlin plate (MP) elements with side lengths of 0.25 mm. The mesh is selected upon a convergence study conducted on the predicted dispersion relations evaluated over the frequency range of interest in this study, as specified below. The smallest wavelength of interest is around half the unit cell width, which means the chosen discretization should be fine enough to resolve it. Also the mesh is refined enough to produce an acceptable description of the internal geometry of the cell perforations, which cannot be perfectly resolved by the considered the mesh, as illustrated in Fig. 2. However, the use of square-shaped elements simplifies the meshing procedure and the model formulation as a whole, and represents a natural choice when considering a possible future extension of this work to design optimization of the unit cell. Furthermore, MP elements provide acceptable approximation of the lower frequency wave modes of the plate with a computational cost that enables the exploration of the full dispersion surfaces and the estimation of wave velocities, which is one of the objectives of this study. In order to avoid numerical inaccuracies due to shear locking, selective reduced integration of shear deformation terms has been used when computing element stiffness matrices.

2.5. Estimation of dispersion properties

The discretized equation for a unit cell can be generally expressed as

$$(\mathbf{K}-\omega^2\mathbf{M})\mathbf{u}=\mathbf{0} \tag{11}$$

where

$$\mathbf{K}=\mathbf{K}_0-i(k_x\mathbf{K}_1+k_y\mathbf{K}_2)+k_x^2\mathbf{K}_3+k_xk_y\mathbf{K}_4+k_y^2\mathbf{K}_5 \tag{12}$$

and $\mathbf{u}$ is the vector of the generalized nodal displacements of the unit cell. Expressions for the matrices above can be found in Appendix A. Solution of Eq. (11) in terms of ω for an assigned wave vector $\mathbf{k}$ leads to the dispersion relation of the periodic plate. As customary, the dispersion relations are evaluated and plotted for a wave vector varying along the boundary of the irreducible Brillouin zone, which leads to the band diagram representation. The boundary of the irreducible Brillouin zone is the line O–A–B–C–O in Fig. 3.

The procedure above is applied to compute the band diagram for the considered periodic domain, which is shown in Fig. 4. The diagram is estimated by considering the mesh presented in Fig. 2, which corresponds to the discretization of the thinnest member of the assembly being discretized by eight elements, an even number that helps preserving the symmetry of the geometry. This mesh provides an accurate estimation of the band diagram within the considered frequency range. This is verified by comparing the corresponding diagrams with those obtained from a mesh with elements of half the size. Such comparison does not show any noticeable difference, thus the coarser mesh is used for follow on investigations because of computational efficiency.

Fig. 4 compares the dispersion branches estimated through the MP elements (red dots), and through a 3D mesh consisting of eight-node solids (open circles) using three elements to discretize the plate thickness. The 3D model also

Fig. 2. The mesh used to discretize the unit cell consists of 6560 square-shaped elements.

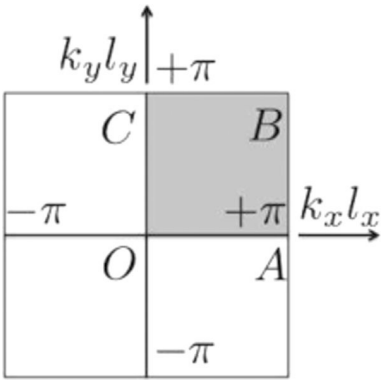

Fig. 3. Illustration of the first Brillouin zone and of the irreducible Brillouin zone (gray area). The parameters l_x and l_y are the unit cell's width and height, respectively.

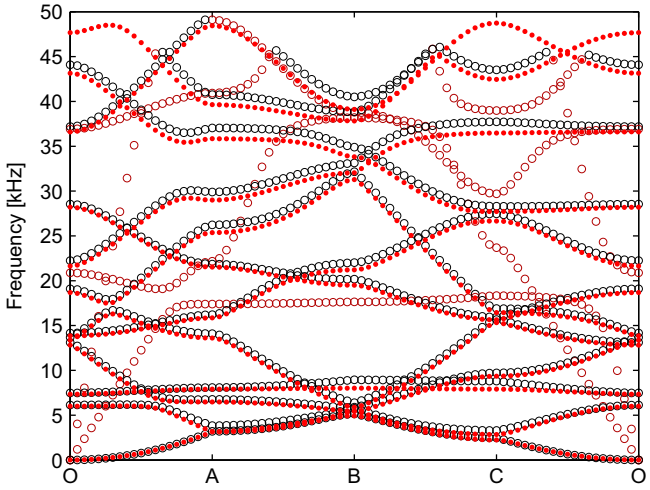

Fig. 4. Band diagram: comparison of MP model (red dots) and 3D model predictions showing the decoupling of in-plane (red circles) and out-of-plane (black circles) polarized modes in the considered range of frequencies. (For interpretation of the references to color in this figure caption, the reader is referred to the web version of this paper.)

provides the in-plane polarized modes (red circles), which mostly appear independent of the predominantly out-of-plane branches (black circles) in a frequency range up to approximately 40 kHz. The comparison confirms that a plate model is suitable for wave propagation characterization in the considered frequency range.

The contour plots of the first four dispersion surfaces corresponding to the first four branches in Fig. 4 are shown in Fig. 5, which illustrates the potential for directionality of the considered plate configuration. Namely, the isofrequency contours for the first dispersion surface appear as approximately circular, which suggests a quasi-isotropic behavior in this frequency range. In contrast, the dispersion surfaces for the third and the fourth mode in particular appear as mostly aligned along the vertical axis, at frequencies around 7 and 9 kHz respectively. This suggests that directionality along the horizontal direction may occur when wave motion at these frequencies and according to these modes takes place within the plate. Directionality will be further illustrated through the analysis of group velocities, based on the developments presented in the next section.

Additional observations can be made upon the detailed analysis of the out-of-plane branches of the dispersion diagram, which are shown in Fig. 6. In this frequency range, the two largest partial bandgaps occur in the O–C range with center frequencies of approximately 6.75 and 20 kHz. These frequencies are highlighted by a dashed and a solid line, respectively. The O–C direction corresponds to the vertical direction in the plate, which suggests that within these bands motion occurs predominantly along the horizontal direction, thus indicating the directional behavior of wave motion. Furthermore, the branches bounding these partial bandgaps end with a zero slope at O, which identifies a null group velocity. In particular, the lower bandgaps appear to be bounded by branches that remain relatively flat through the entire O–C wavenumber range, which characterizes wave motion remaining localized as a result of the occurrence of internal resonant behavior. This is illustrated by plotting the wave modes associated with these branches. The local wave modes are plotted both at O, which corresponds to the classic eigenmodes of the unit cell, and at the point halfway in between O and C. These mode shapes are all shown in Fig. 7, where it can be seen that the mode changes slightly along the branch.

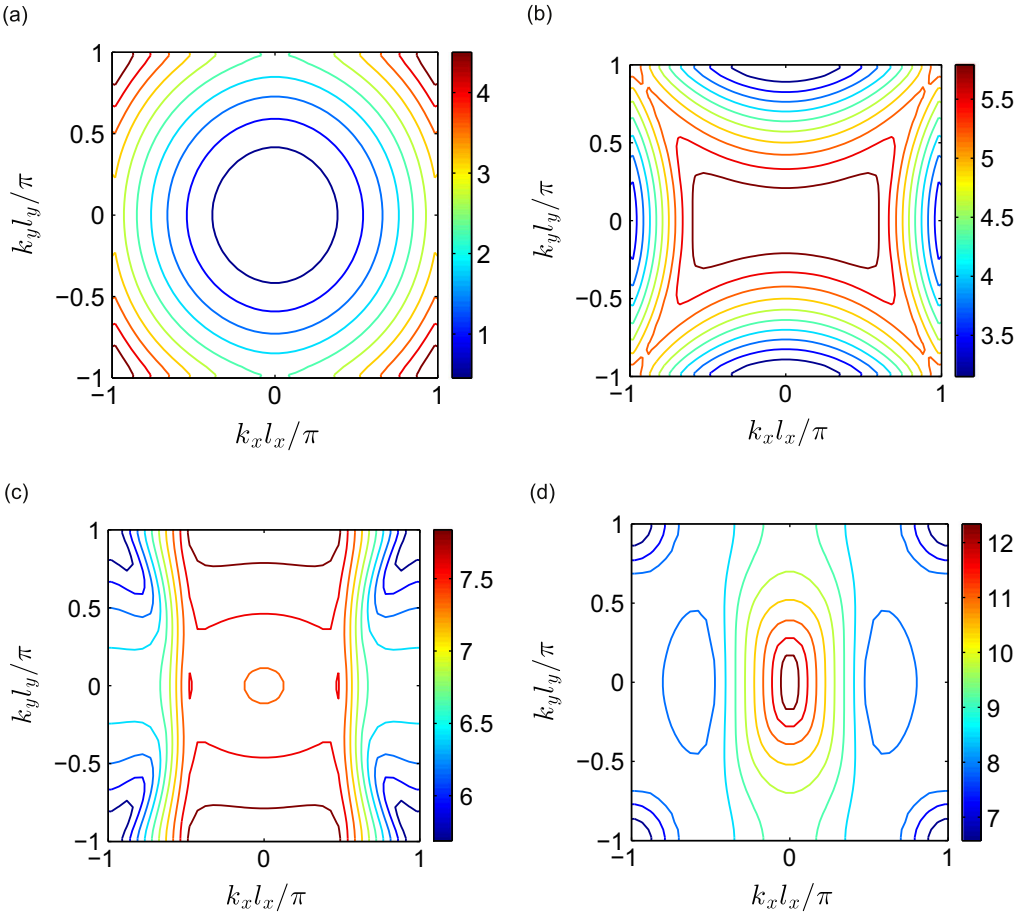

Fig. 5. Contour plots of dispersion surfaces for the first wave modes (contour frequency values are expressed in kHz). (a) Mode 1. (b) Mode 2. (c) Mode 3. (d) Mode 4. (For interpretation of the references to color in this figure caption, the reader is referred to the web version of this paper.)

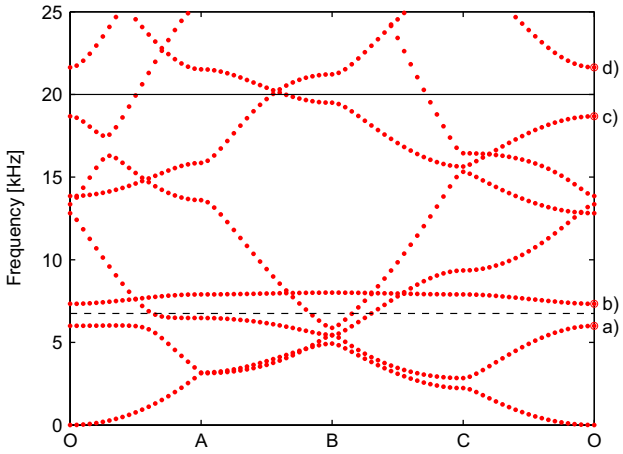

Fig. 6. Illustration of partial bandgaps in the O–C range for out-of-plane polarized branches. Center frequencies of approximately 6.75 and 20 kHz are, respectively, highlighted by the black dashed and solid lines.

The localized nature of the modes associated with the lowest two branches appears evident from Fig. 7(a) and (b), which correspond to the modes belonging to the branches starting at points (a) and (b) in Fig. 6 for frequencies equal to 6.1 and 7.4 kHz. Both modes are characterized by the resonance of the double-C inclusion. One is bending dominated and the other being of a torsion type. The modes associated with the second partial bandgap (Fig. 7(c) and (d)) appear different in nature

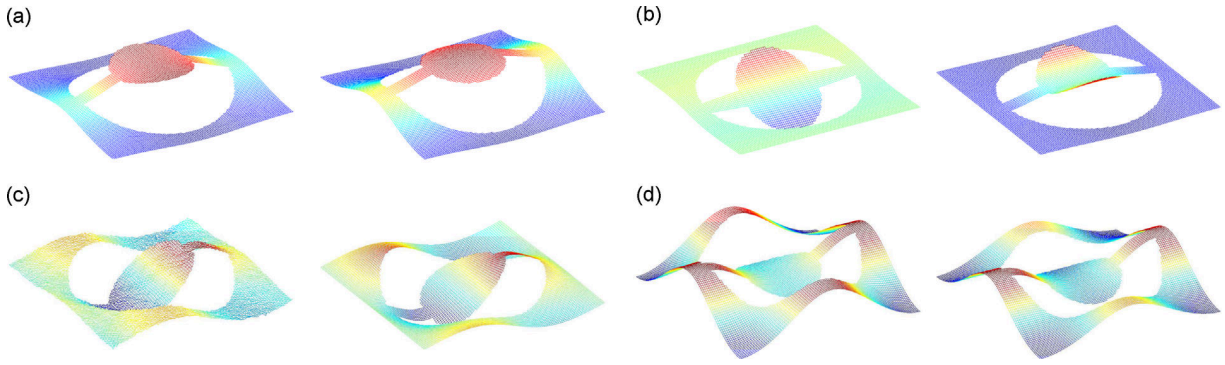

Fig. 7. Wave mode shapes associated with the branches bounding the partial bandgaps. For each branch two modes have been plotted (left is at O, right is halfway between O and C). Modes belonging to branch starting at (a) 6.0 kHz. (b) 7.3 kHz. (c) 18.7 kHz. (d) 21.6 kHz.

as the corresponding dynamic deformations are no longer localized to the inclusion, but occur over the entire unit cell. However, the out-of-phase motion of the internal inclusion with respect to the surrounding medium appears as a common feature of all the modes shown in Fig. 7.

2.6. Group velocity

The group velocity is a vectorial quantity that provides information regarding the speed and direction of wave propagation in the considered medium [25]. The evaluation of group velocities relies on the estimation of the dispersion relations, which can be conducted using the procedure illustrated in the previous section. Subsequently, the estimation of the group velocity follows the approach originally presented in [32] for the case of 1D photonic crystal.

The group velocity $\mathbf{c}_g$ defined as

$$\mathbf{c}_g = \nabla\omega = \left[\frac{\mathrm{d}\omega}{\mathrm{d}k_x}, \frac{\mathrm{d}\omega}{\mathrm{d}k_y}\right]^T \tag{13}$$

is estimated by considering the form of the eigenvalue problem in terms of ω (Eq. (11)), i.e.

$$\mathbf{G}(\mathbf{k}, \omega(\mathbf{k}), \mathbf{u}(\mathbf{k})) = (\mathbf{K} - \omega^2\mathbf{M})\mathbf{u} = \mathbf{0} \tag{14}$$

Differentiating with respect to $\mathbf{k}$ gives

$$\frac{\mathrm{d}\mathbf{G}(\mathbf{k}, \omega(\mathbf{k}), \mathbf{u}(\mathbf{k}))}{\mathrm{d}\mathbf{k}} = \frac{\partial\mathbf{G}}{\partial\mathbf{u}}\frac{\mathrm{d}\mathbf{u}}{\mathrm{d}\mathbf{k}} + \frac{\partial\mathbf{G}}{\partial\omega}\frac{\mathrm{d}\omega}{\mathrm{d}\mathbf{k}} + \frac{\partial\mathbf{G}}{\partial\mathbf{k}} \tag{15}$$

The term $\mathrm{d}\mathbf{u}/\mathrm{d}\mathbf{k}$ can be eliminated by pre-multiplying by a vector $\mathbf{v}^T$:

$$\mathbf{v}^T\frac{\partial\mathbf{G}}{\partial\mathbf{u}}\frac{\mathrm{d}\mathbf{u}}{\mathrm{d}\mathbf{k}} + \mathbf{v}^T\frac{\partial\mathbf{G}}{\partial\omega}\frac{\mathrm{d}\omega}{\mathrm{d}\mathbf{k}} + \mathbf{v}^T\frac{\partial\mathbf{G}}{\partial\mathbf{k}} = 0 \tag{16}$$

and requiring that

$$\mathbf{v}^T\frac{\partial\mathbf{G}}{\partial\mathbf{u}} = \mathbf{0} \tag{17}$$

which corresponds to a left eigenvalue problem. Substituting Eq. (17) into Eq. (15), the group velocity can be obtained as

$$\frac{\mathrm{d}\omega}{\mathrm{d}\mathbf{k}} = -\frac{\mathbf{v}^T\dfrac{\partial\mathbf{G}}{\partial\mathbf{k}}}{\mathbf{v}^T\dfrac{\partial\mathbf{G}}{\partial\omega}} \tag{18}$$

with

$$\frac{\partial\mathbf{G}}{\partial k_x} = (-i\mathbf{K}_1 + 2k_x\mathbf{K}_3 + k_y\mathbf{K}_4)\mathbf{u} \tag{19}$$

$$\frac{\partial\mathbf{G}}{\partial k_y} = (-i\mathbf{K}_2 + k_x\mathbf{K}_4 + 2k_y\mathbf{K}_5)\mathbf{u} \tag{20}$$

$$\frac{\partial\mathbf{G}}{\partial\omega} = -2\omega\mathbf{M}\mathbf{u} \tag{21}$$

In general, it is necessary to solve the eigenvalue problem in Eq. (17) to get the left eigenvector **v**. However, if the presence of any dissipation mechanism is neglected, both **K** and **M** are Hermitian and the left eigenvector **v** is the complex conjugate of the right eigenvector, **u**.

In order to compute the group velocity at a given frequency ω, we need to know the corresponding wave vector(s) **k**. Eq. (11) is a quadratic eigenvalue problem in both k_x and k_y. However, by introducing an angle, θ, specifying the direction of a given wave vector, the wave vector is given as

$$\mathbf{k} = [k_x,\ k_y]^T = [k\ \cos(\theta),\ k\ \sin(\theta)]^T$$

such that Eq. (11) can be expressed as a standard eigenvalue problem in terms of the wave vector magnitude k [33]:

$$(\mathbf{K}_k(\theta,\omega) - k\mathbf{M}_k(\theta))\mathbf{u}_k = \mathbf{0} \tag{22}$$

Eq. (22) can be solved in terms of the wave vector for an assigned frequency ω and direction as defined by the angle θ.

Examples of group velocity plots computed at two selected frequencies are shown in Fig. 8(b) and (d), along with the corresponding isofrequency contours of the dispersion surfaces (Fig. 8(a) and (c)). The isofrequency dispersion contour at 2 kHz appears as almost circular, which is an indication of the quasi-isotropic behavior of the plate at low frequencies. The group velocity directional plot at the same frequency shows that propagation appears as occurring with a slightly higher velocity along the horizontal direction, as shown by the lobar shape of the group velocity curve (Fig. 8(b)). The case of 11 kHz includes two sets of curve, as two wave modes contribute to propagation at this frequency (Fig. 8(c) and (d)). The group velocity variation in Fig. 8(d) shows two curves, one of which appears again elongated along the horizontal direction, to indicate faster propagation along the horizontal direction. The second curve is characterized by similar speeds along the

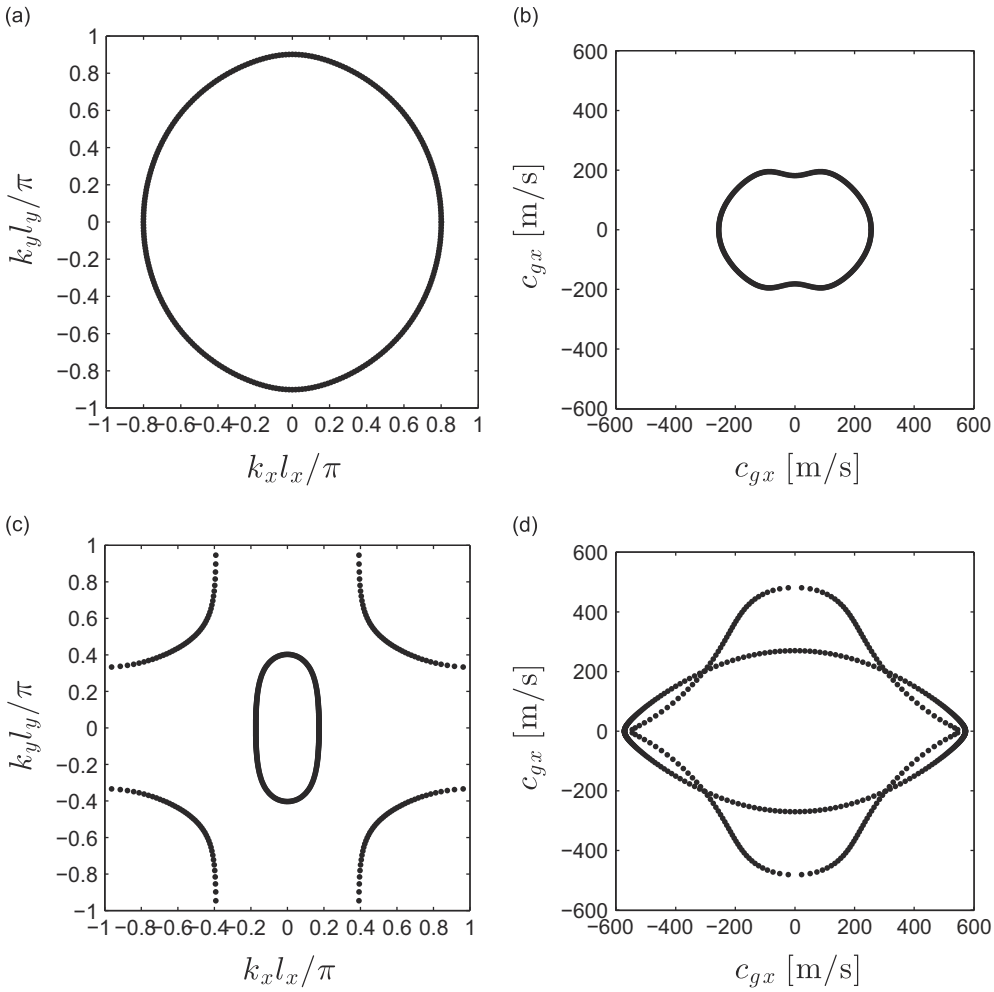

Fig. 8. Isofrequency contour and corresponding group velocity profiles at two selected frequencies. (a) Isofrequency contour 2 kHz. (b) Group velocity 2 kHz. (c) Isofrequency contour 11 kHz. (d) Group velocity 11 kHz.

vertical direction and longitudinal one, however it appears to be characterized by two sharper longitudinal lobes. The group velocity curves in Fig. 8(b) and (d) define the pattern of wave motion within the domain, and essentially predict the shape of the propagating wavefront at the considered frequencies.

3. Experimental investigation of wave motion

3.1. Setup

The wave propagation characteristics of the considered plate are investigated experimentally through measurements conducted using a scanning laser vibrometer (SLV) (Polytec Model PSV 400 M2). The plate specimen was fabricated out of an aluminum (Young's modulus $E=69$ GPa, Poisson's ratio $\nu = 0.33$, and the density $\rho = 2700$ kg/m^3) plate of the dimensions considered for the numerical investigations. A 15×15 array of double-C perforations was obtained through water jet cutting. The resulting plate is shown in Fig. 9, along with the detail of a unit cell. The center cell was not cut in order to maintain a central location where a piezoelectric (PZT) disc is bonded to apply the desired excitation. A PZT disc of 7 mm in diameter from Steminc Corp. was selected as a source capable of introducing the desired excitations at the frequencies/wavelengths of interest to the current study. The choice is based on prior experience on guided wave fields generation and detection in plate structures as described for example in [34]. The piezoelectric disc is excited by a seven cycle Hanning modulated sine burst at the desired center frequency. The plate's out-of-plane response is recorded over a refined grid of points prescribed through the SLV software. At each measurement point, the recorded response is the result of 10 averages taken to minimize distortions due to measurement noise. Complete wave field images are obtained by aggregating single-point measurements at each grid point. Measurements and excitations are synchronized with a trigger signal so that proper phase is maintained among all measurement points. Upon completing the scanning of the measurement grid, the data are post-processed by the SLV software and coherent wave images are obtained. Examples of wave field images obtained for two of the excitation frequencies considered are shown in Figs. 10 and 11.

3.2. Wave modes

A set of verification experiments is conducted to evaluate the modal characteristics of the unit cell at some of the frequencies highlighted by the numerical study. These experiments are conducted by considering a refined local grid over a single unit cell. The plate is excited through harmonic excitation at the frequencies of interest. Frequency domain acquisitions are conducted to measure the dynamic deflection shapes of the unit cell, which are regarded as closely related to the unit cell wave modes of the plate. Results at three selected frequencies displayed in Fig. 11 show significant resemblance to the wave modes presented in Fig. 7. This once again confirms the accuracy of the numerical implementation presented in the first part of this paper, and its ability to predict local resonance characteristics at the unit cell level.

3.3. Evaluation of dispersion

The dispersion relations for the plate are estimated by processing the wave field data recorded during the experiments. Wave field information can be described as an array of matrices $w(x, y, t)$ containing spatial and temporal field information, where w denotes the measured out-of-plane displacement of the plate.

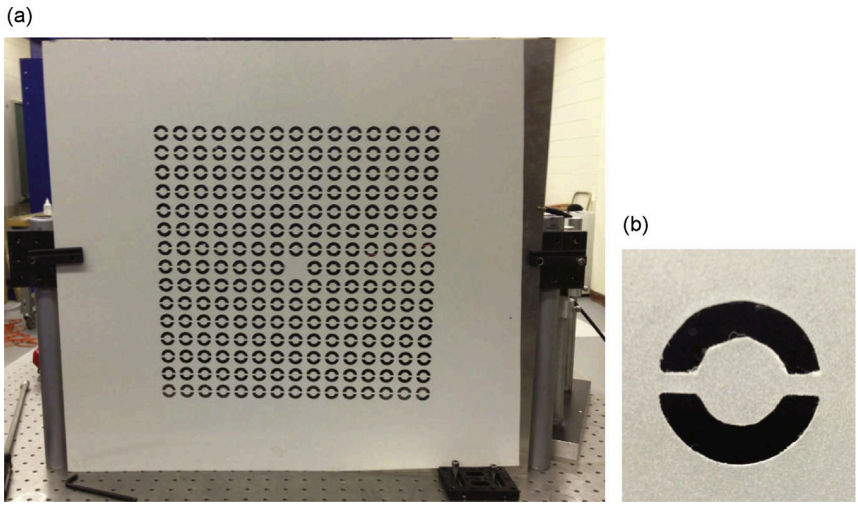

Fig. 9. (a) Experimental plate and (b) close-up containing detail of unit cell.

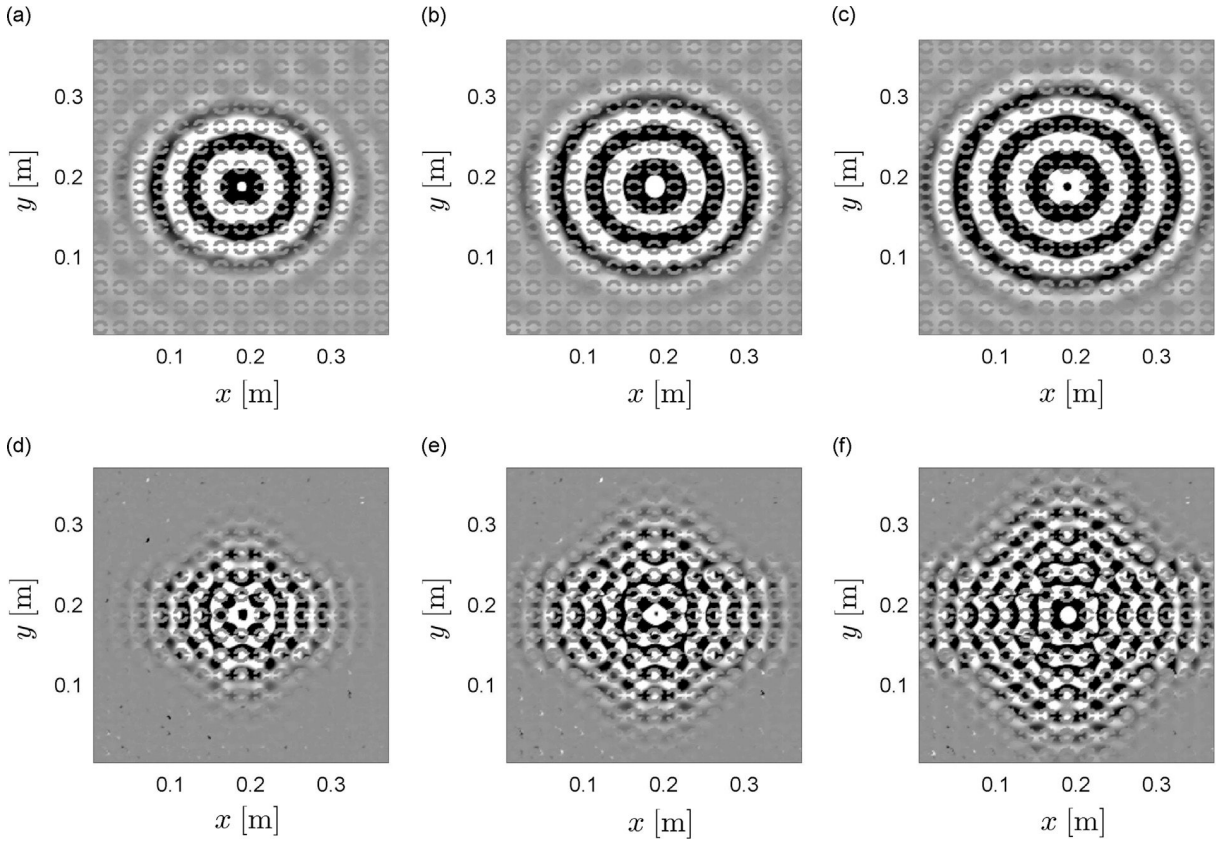

Fig. 10. Snapshots of experimental wave fields for excitation at 3 kHz after (a) $t = 546$ μs, (b) $t = 624$ μs, and (c) $t = 702$ μs, and for excitation at 11 kHz after (d) $t = 312$ μs, (e) $t = 390$ μs, and (f) $t = 468$ μs.

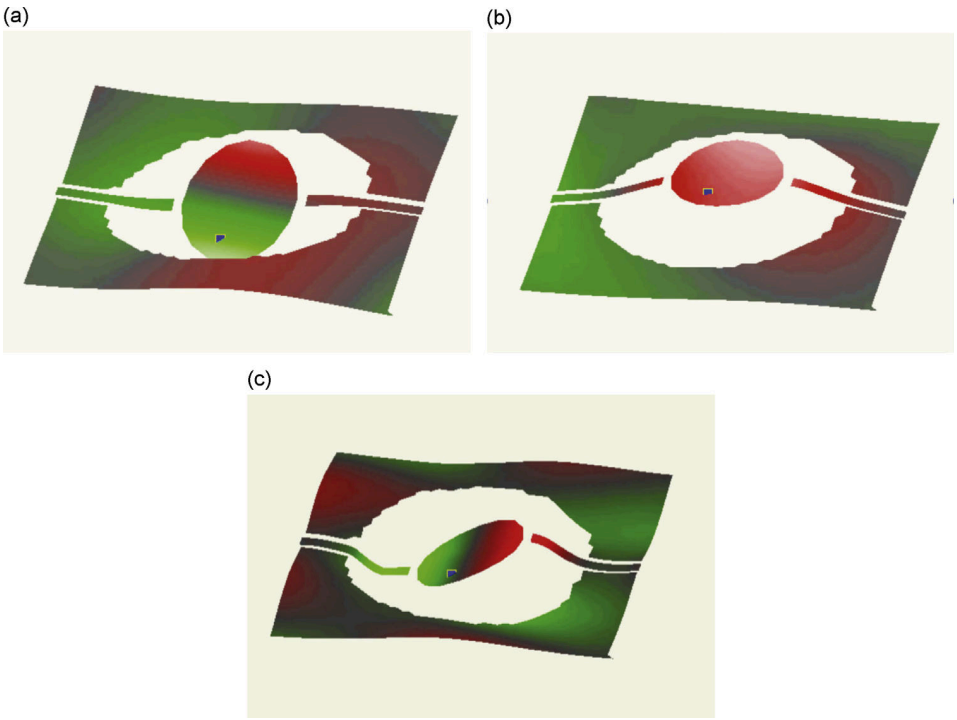

Fig. 11. Dynamic deformed shapes at selected frequencies recorded through local measurements at the unit cell level. (a) 6.0 kHz. (b) 7.3 kHz. (c) 19.3 kHz.

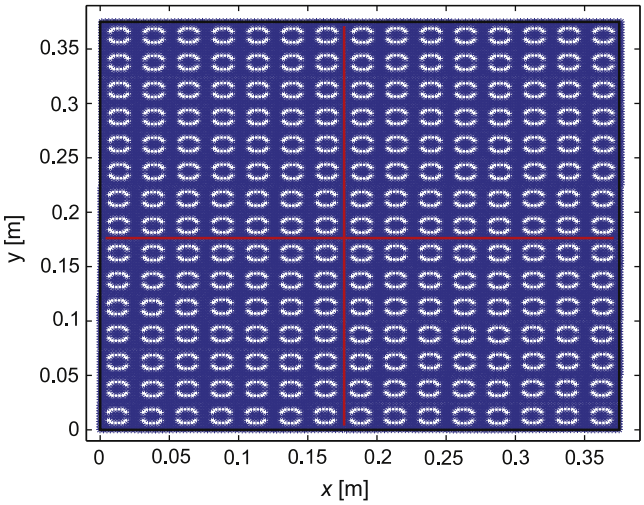

Fig. 12. Experimental grid. Red lines indicate which measurement points are used for evaluation of dispersion relation for O–A (horizontal line) and O–C (vertical line). (For interpretation of the references to color in this figure caption, the reader is referred to the web version of this paper.)

The dispersion properties are first estimated along the O–A and O–C directions – in order to describe the relation between frequency and wavenumber along two of the boundaries of the Brillouin zone – corresponding to the horizontal and vertical directions, respectively. To this end, one of the coordinates is kept fixed in the wave field matrix, and the two-dimensional Fourier transform (2D-FT) in time and space (along the remaining coordinate and time) is evaluated. This operation can be described as follows:

$$\hat{w}(k_x, \omega) = \mathcal{F}_{2D}[w(x, y = y_0, t)] \tag{23}$$

$$\hat{w}(k_y, \omega) = \mathcal{F}_{2D}[w(x = x_0, y, t)] \tag{24}$$

where $\mathcal{F}_{2D}$ denotes the 2D-FT operator, $\hat{w}$ is the representation of the plate response in the frequency/wavenumber (f–k) domain, while x_0, y_0 are the coordinates along which dispersion is estimated.

The process is conducted by extracting data from the measurement grid shown in Fig. 12, specifically along the horizontal and the vertical line shown in the figure, which correspond to the O–A and O–C directions of the band diagram. The procedure is applied to data corresponding to various excitation frequencies, such that a broader band of the spectrum can be covered by superimposing the results of several narrowband experiments. Results for the O–A and O–C directions are presented in Fig. 13, where the experimental contours (from five experiments with excitation frequencies 2 kHz, 3 kHz, 8.5 kHz, 11 kHz, and 15 kHz) are overlaid to the numerically estimated branches for the corresponding directions. As one can easily see, the experimental branches appear in a wavenumber range that exceeds the limits of the first Brillouin zone, as the spatial sampling considered includes several measurement points within each unit cell. In order to enable a comparison with numerical results, the numerical branches are therefore replicated periodically over subsequent intervals in multiples of π in order to observe or resolve potential indetermination associated with branch folding, which is the result of the investigation of Bloch wave modes.

Next, dispersion relations are visualized in the k_x, k_y domain through the application of the 3D FT and the selection of specific frequencies of interest. This operation can be described as follows:

$$\hat{w}(k_x, k_y, \omega) = \mathcal{F}_{3D}[w(x, y, t)] \tag{25}$$

where $\mathcal{F}_{3D}$ denotes the 3D Fourier transform. Representation of $\hat{w}$ at a specified frequency $\omega = \omega_0$ leads to a surface $\hat{w}(k_x, k_y, \omega_0)$ whose magnitude can be represented in the k_x, k_y domain, where direct comparison with the dispersion surfaces at the selected frequency can be conducted.

The dispersion surfaces are evaluated through the Bloch analysis, as presented in the previous sections, conducted over a specified grid of the in-plane wavenumber components. The isofrequency line of interest at $\omega = \omega_0$ is extracted and overlaid to the experimental contour, as shown in Fig. 14. This representation allows the evaluation of the energy content in the wavenumber domain, and the evaluation of potential directionality induced by the anisotropy of the plate at the selected frequencies. In Fig. 14, the numerical contours are black lines (Eq. (11)) and dots (Eq. (22)), while the surfaces $|\hat{w}(k_x, k_y, \omega_0)|$, each normalized to unity for convenience of representation, are shown by the different contours, with red representing the highest values and blue the lower values. For clarity, the boundaries of the first Brillouin zone are also highlighted by the blue square included in the figures. As expected, the numerical solutions found using Eq. (11) coincide with the solutions to Eq. (22). The experimental results confirm the previously observed fact that the measured wavenumbers exceed the boundaries of the Brillouin zone, which requires for the numerical dispersion to be computed beyond this range.

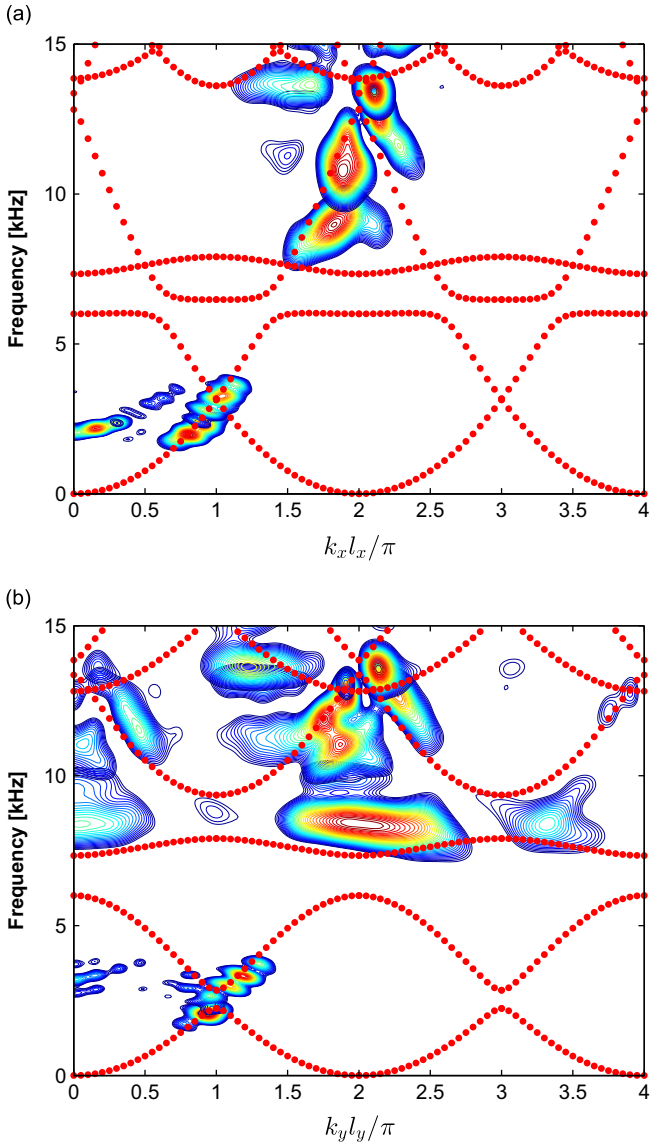

Fig. 13. Dispersion relations k–f representation along the (a) O–A and (b) O–C directions, and comparison with numerical predictions (red dotted lines) (Numerical branches are replicated periodically in intervals of π). (For interpretation of the references to color in this figure caption, the reader is referred to the web version of this paper.)

The numerical results show the expected periodicity in the wavenumber domain, and generally overlay well with the experimental results. At low frequencies, the results indicate that the plate behavior is approximately isotropic, as demonstrated by the quasi-circular isofrequency lines obtained experimentally and numerically (see Fig. 14(a) and (b) for results corresponding to 2 kHz and 3 kHz, respectively). At higher frequencies (see Fig. 14(c) and (d) for results corresponding to 8.5 kHz and 11 kHz, respectively) the distributions show occurrences of preferential directions corresponding to peaks of the surface $|\hat{w}(k_x, k_y, \omega_0)|$ in the wavenumber domain. A good agreement is observed in particular for the low frequency cases. At higher frequencies, the predictions appear less accurate which may be attributed to the reduced fidelity of the model and to the contribution of other wave modes not included in the numerical isofrequency contour displayed.

3.4. Directionality and group velocities

The dispersion plots presented in Fig. 14 reveal the complex plate behavior as the frequency increases, which is characterized by a transition from quasi-isotropic motion, to a more complex pattern with some distinct preferential

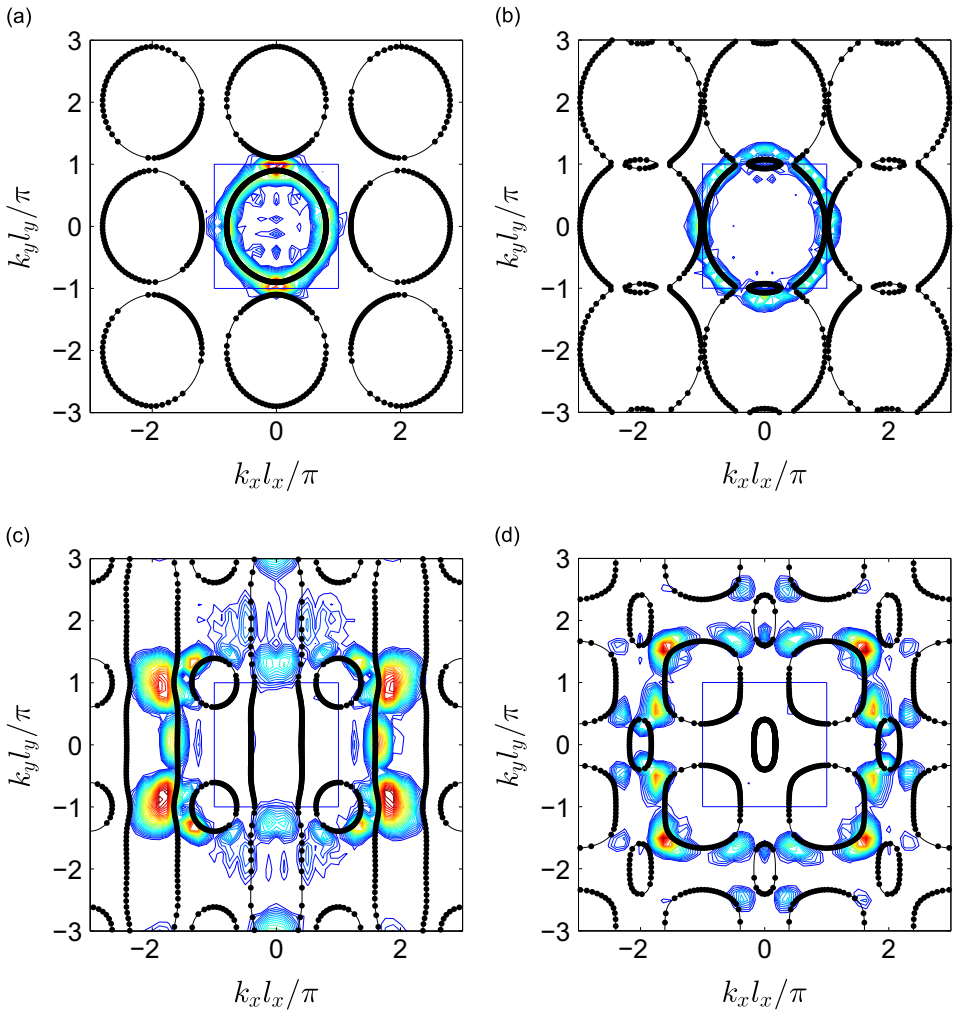

Fig. 14. Experimental 3D FT (contour plots) and isofrequency dispersion surfaces (black dotted line) at selected frequencies for representation of plate dispersion in the k_x–k_y domain. (a) 2 kHz. (b) 3 kHz. (c) 8.5 kHz. (d) 11 kHz. Note that the numerical results are plotted both as contour slices (solid black line), and as solutions to Eq. (22) (black dots) in which the angle and the frequency are specified before solving for k. (For interpretation of the references to color in this figure caption, the reader is referred to the web version of this paper.)

directions. This can be further investigated from the analysis of group velocity at the selected frequencies and their representation in conjunction with time snapshots of the wave field.

In theory, the directional group velocity plots of the kind shown in Fig. 8 describe the pattern of energy flow within the structure, and highlight the concentration of wave vectors in preferential orientations. This is expected to be reflected in the shape of the wavefront observed at specific time instants. This representation is provided in Fig. 15, where the group velocity is overlaid on the wave field generated by excitation at the four selected frequency values. The group velocity and wave field snapshots confirm the quasi-isotropic behaviors at 2 kHz, and show distinct directional characteristics at the higher frequencies where wave motion occurs preferentially along the horizontal direction at 8.5 kHz (see Fig. 15(c)) and both the horizontal and the vertical direction as in the case of the wave field at 11 kHz shown in Fig. 15(d).

In all cases presented, the group velocity predictions provide a good representation of the wavefront and agree with the experimental measurements. Such agreement is somewhat confounded by the fact that the excitation does not consist of a pure tone, but it is defined by a seven cycle burst, which therefore includes a range of frequencies that partially excites other wave modes.

Further, quantitative insight into the directional behavior of the plate can be gained by evaluating the envelope of a propagating waveform. Envelope estimation is conducted through the application of the Hilbert transform (HT) along a selected direction of propagation. The envelope evolution along one of the coordinates, say the horizontal direction x, is estimated as

$$\mathcal{E}(x,t) = |\mathcal{H}[w(x, y = y_0, t)]| \tag{26}$$

where $\mathcal{H}$ denotes the HT of the considered waveform.

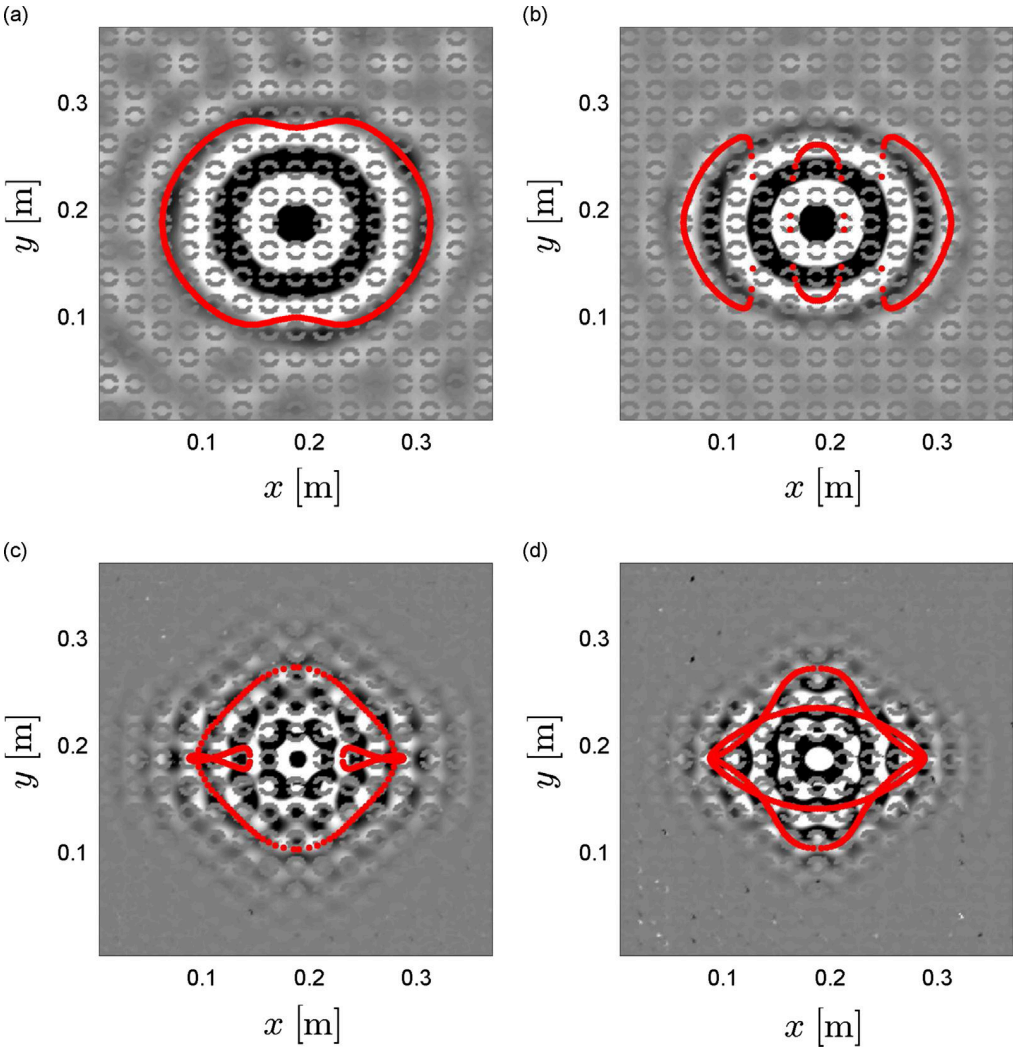

Fig. 15. Experimental wave field and theoretical group velocities at the corresponding excitation frequencies. (a) 2 kHz. (b) 3 kHz. (c) 8.5 kHz. (d) 11 kHz.

The envelopes' evolution at two frequency values along the x- and y-directions is shown in Fig. 16 in the form of space-time amplitude maps on a gray scale (with the black color being associated with the highest amplitude values). The plots also show propagation lines along the considered directions obtained by considering the numerically computed group velocity component along the considered directions. The lines, represented as red dotted lines, are obtained from expressions of the kind of $\pm c_{g_x} t$ and $\pm c_{g_y} t$. These representations again confirm the accurate estimations of group velocities obtained from the considered numerical model, which provides the correct rate of envelope propagation. The plots in Fig. 16 clearly highlight the different wave speeds for the considered mode of propagation along the two principal directions of motion.

4. Conclusion

The work presented the numerical and the experimental investigation of wave motion in a periodic plate with double-C perforations. The considered configuration was chosen because of its expected non-isotropic equivalent behavior, which leads to directional wave motion. Furthermore, the periodic arrangement of perforations produces partial bandgaps due to internal resonances. These wave phenomena are first predicted through a numerical model formulated using MP elements, and are then investigated experimentally through the analysis of wave field images. Numerical and experimental results characterize the 2D dispersion properties of the plate, and its group velocities as a function of direction of propagation and frequency. Furthermore, detailed modeling and measurements at the unit cell level identify modes of resonance associated with partial bandgaps. The results presented in this study illustrate the range of investigations that can be performed on periodic plate waveguides and the wave properties that can be estimated through the presented numerical and experimental

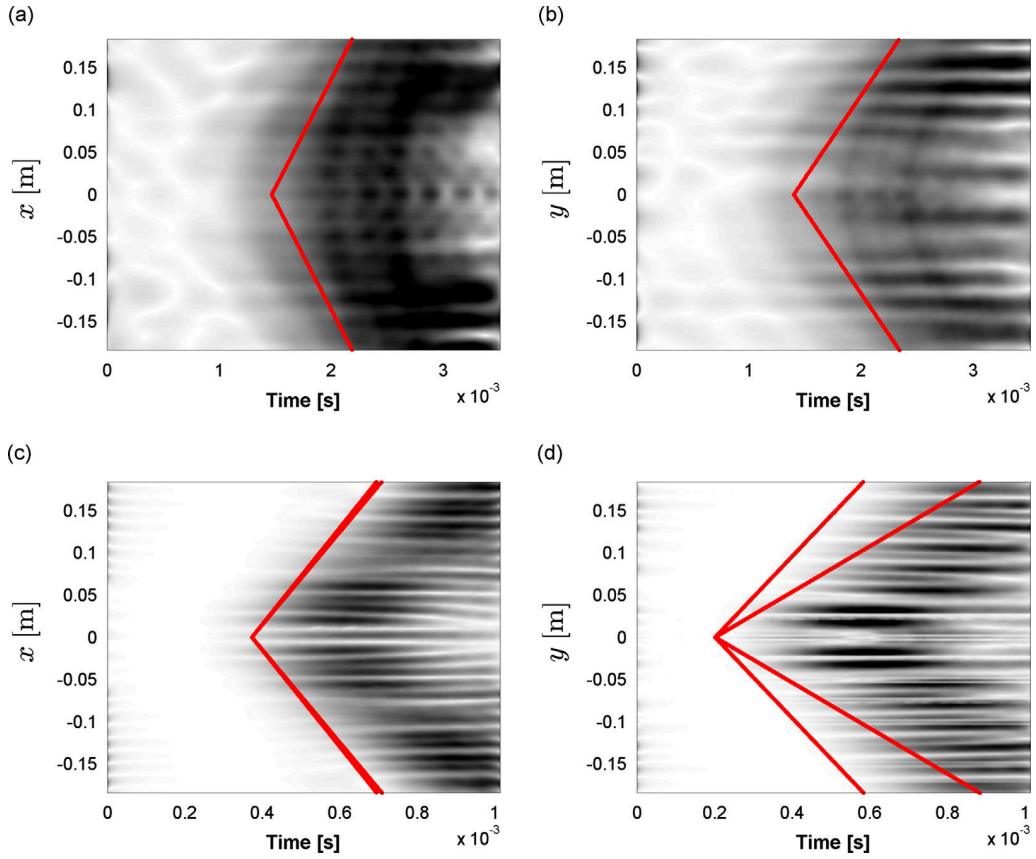

Fig. 16. Space time evolution of wave motion along the vertical and horizontal directions and rate of propagation predicted numerically through the estimation of group velocity (red solid line). (a) 2 kHz, *x*-propagation. (b) 2 kHz, *y*-propagation. (c) 11 kHz, *x*-propagation. (d) 11 kHz, *y*-propagation. (For interpretation of the references to color in this figure caption, the reader is referred to the web version of this paper.)

approaches. In addition, the considered configuration can be used as a baseline for the design of planar waveguides with desired directional and bandgap configurations through unit cell topology optimization.

Acknowledgments

E. Andreassen's support for this work was provided by the Danish Research Agency through the innovation consortium FMAT. M. Ruzzene and K. Manktelow acknowledge the support from the National Science Foundation under Grant nos. 0926776 and 1130368.

Appendix A. System matrices

With the nodal displacements interpolated over the element using the shape function matrices $\mathbf{N}_w$ and $\mathbf{N}_\Theta$ as follows:

$$\mathbf{u}^e = \begin{bmatrix} \mathbf{N}_w(x,y) & \mathbf{0} \\ \mathbf{0} & \mathbf{N}_\Theta(x,y) \end{bmatrix} \begin{bmatrix} \tilde{\mathbf{w}}^e \\ \tilde{\boldsymbol{\Theta}}^e \end{bmatrix} \tag{A.1}$$

the corresponding expressions for the element matrices, in Eq. (11), are

$$\mathbf{k}_0^e = \int_{\Omega^e} \begin{bmatrix} -\nabla \mathbf{N}_w^T \mathbf{G} \nabla \mathbf{N}_w & \left(\mathbf{N}_\Theta^T \mathbf{G} \nabla \mathbf{N}_w\right)^T \\ \mathbf{N}_\Theta^T \mathbf{G} \nabla \mathbf{N}_w & -\partial \mathbf{N}_\Theta^T \mathbf{D} \partial \mathbf{N}_\Theta - \mathbf{N}_\Theta^T \mathbf{G} \mathbf{N}_\Theta \end{bmatrix} \mathrm{d}\Omega^e$$

$$\mathbf{k}_1^e = -\int_{\Omega^e} \begin{bmatrix} \mathbf{N}_w^T \boldsymbol{\beta}_1^T \mathbf{G} \nabla \mathbf{N}_w - \nabla \mathbf{N}_w^T \mathbf{G} \boldsymbol{\beta}_1 \mathbf{N}_w & -\left(\mathbf{N}_\Theta^T \mathbf{G} \boldsymbol{\beta}_1 \mathbf{N}_w\right)^T \\ \mathbf{N}_\Theta^T \mathbf{G} \boldsymbol{\beta}_1 \mathbf{N}_w & \mathbf{N}_\Theta^T \boldsymbol{\alpha}_1^T \mathbf{D} \partial \mathbf{N}_\Theta - \partial \mathbf{N}_\Theta^T \mathbf{D} \boldsymbol{\alpha}_1 \mathbf{N}_\Theta \end{bmatrix} \mathrm{d}\Omega^e$$

$$\mathbf{k}_2^e = -\int_{\Omega^e} \begin{bmatrix} \mathbf{N}_w^T\boldsymbol{\beta}_2^T\mathbf{G}\nabla\mathbf{N}_w - \nabla\mathbf{N}_w^T\mathbf{G}\boldsymbol{\beta}_2\mathbf{N}_w & -\left(\mathbf{N}_\Theta^T\mathbf{G}\boldsymbol{\beta}_2\mathbf{N}_w\right)^T \\ \mathbf{N}_\Theta^T\mathbf{G}\boldsymbol{\beta}_2\mathbf{N}_w & \mathbf{N}_\Theta^T\boldsymbol{\alpha}_2^T\mathbf{D}\partial\mathbf{N}_\Theta - \partial\mathbf{N}_\Theta^T\mathbf{D}\boldsymbol{\alpha}_2\mathbf{N}_\Theta \end{bmatrix} \mathrm{d}\Omega^e$$

$$\mathbf{k}_3^e = -\int_{\Omega^e} \begin{bmatrix} \mathbf{N}_w^T\boldsymbol{\beta}_1^T\mathbf{G}\boldsymbol{\beta}_1\mathbf{N}_w & \mathbf{0} \\ \mathbf{0} & \mathbf{N}_\Theta^T\boldsymbol{\alpha}_1^T\mathbf{D}\boldsymbol{\alpha}_1\mathbf{N}_\Theta \end{bmatrix} \mathrm{d}\Omega^e$$

$$\mathbf{k}_4^e = -\int_{\Omega^e} \begin{bmatrix} \mathbf{N}_w^T(\boldsymbol{\beta}_1+\boldsymbol{\beta}_2)^T\mathbf{G}(\boldsymbol{\beta}_1+\boldsymbol{\beta}_2)\mathbf{N}_w & \mathbf{0} \\ \mathbf{0} & \mathbf{N}_\Theta^T(\boldsymbol{\alpha}_1+\boldsymbol{\alpha}_2)^T\mathbf{D}(\boldsymbol{\alpha}_1+\boldsymbol{\alpha}_2)\mathbf{N}_\Theta \end{bmatrix} \mathrm{d}\Omega^e$$

$$\mathbf{k}_5^e = -\int_{\Omega^e} \begin{bmatrix} \mathbf{N}_w^T\boldsymbol{\beta}_2^T\mathbf{G}\boldsymbol{\beta}_2\mathbf{N}_w & \mathbf{0} \\ \mathbf{0} & \mathbf{N}_\Theta^T\boldsymbol{\alpha}_2^T\mathbf{D}\boldsymbol{\alpha}_2\mathbf{N}_\Theta \end{bmatrix} \mathrm{d}\Omega^e$$

$$\mathbf{m}^e = -\int_{\Omega^e} \begin{bmatrix} \rho h\mathbf{N}_w^T\mathbf{N}_w & \mathbf{0} \\ \mathbf{0} & \frac{\rho h^3}{12}\mathbf{N}_\Theta^T\mathbf{N}_\Theta \end{bmatrix} \mathrm{d}\Omega^e \tag{A.2}$$

where Ω^e is the domain of element e. The matrices in Eq. (11) and (12) are found by summation of the element matrices, that is

$$\mathbf{K}_0 = \sum_{e=1}^{n} \mathbf{k}_0^e, \quad \mathbf{K}_1 = \sum_{e=1}^{n} \mathbf{k}_1^e, \text{ etc} \tag{A.3}$$

where n is the total number of elements, and $\sum$ should be understood as the finite element assembly operator (see e.g. [20]).

References

[1] G.M. Burrow, T.K. Gaylord, Multi-beam interference advances and applications: *nano-electronics, photonic crystals, metamaterials, subwavelength structures, optical trapping, and biomedical structures*, *Micromachines* 2 (2011) 221–257.
[2] M.L. Povinelli, S.G. Johnson, J.D. Joannopoulos, J.B. Pendry, Toward photonic-crystal metamaterials: *creating magnetic emitters in photonic crystals*, *Applied Physics Letters* 82 (2003).
[3] E. Yablonovitch, T. Gmitter, Photonic band structure: *the face-centered-cubic case*, *Physical Review Letters* 63 (1989) 1950–1953.
[4] M. Maldovan, Sound and heat revolutions in phononics, *Nature* 503 (2013) 209–217.
[5] S. Guenneau, A. Movchan, G. Pétursson, S.A. Ramakrishna, Acoustic metamaterials for sound focusing and confinement, *New Journal of Physics* 9 (2007) 399.
[6] M. Farhat, S. Guenneau, S. Enoch, A.B. Movchan, G.G. Petursson, Focussing bending waves via negative refraction in perforated thin plates, *Applied Physics Letters* 96 (2010) 081909.
[7] M. Farhat, S. Guenneau, S. Enoch, High directivity and confinement of flexural waves through ultra-refraction in thin perforated plates, *Europhysics Letters* 91 (2010) 54003.
[8] J. Pierre, O. Boyko, L. Belliard, J.O. Vasseur, B. Bonello, Negative refraction of zero order flexural lamb waves through a two-dimensional phononic crystal, *Applied Physics Letters* 97 (2010) 121919.
[9] M. Ruzzene, F. Scarpa, F. Soranna, Wave beaming effects in two-dimensional cellular structures, *Smart Materials and Structures* 12 (2003) 363.
[10] F.R. Montero de Espinosa, E. Jiménez, M. Torres, Ultrasonic band gap in a periodic two-dimensional composite, *Physical Review Letters* 80 (1998) 1208–1211.
[11] O. Sigmund, J.S. Jensen, Systematic design of phononic band-gap materials and structures by topology optimization, *Philosophical Transactions of Royal Society London A, Mathematical Physical and Engineering Sciences* 361 (2003) 1001–1019.
[12] S. Halkjaer, O. Sigmund, J.S. Jensen, Inverse design of phononic crystals by topology optimization, *Zeitschrift für Kristallographie—Crystalline Materials* 220 (2005) 895–905.
[13] O.R. Bilal, M.I. Hussein, Ultrawide phononic band gap for combined in-plane and out-of-plane waves, *Physical Review E: Statistical, Nonlinear & Soft Matter Physics* 84 (2011).
[14] T.-T. Wu, J.-C. Hsu, J.-H. Sun, Phononic plate waves, *IEEE Transactions on Ultrasonics, Ferroelectrics and Frequency Control* 58 (2011) 2146–2161.
[15] Y. Pennec, B. Djafari-Rouhani, H. Larabi, J.O. Vasseur, A.C. Hladky-Hennion, Low-frequency gaps in a phononic crystal constituted of cylindrical dots deposited on a thin homogeneous plate, *Physical Review B* 78 (2008) 104105.
[16] A. Khelif, B. Djafari-Rouhani, J.O. Vasseur, P.A. Deymier, P. Lambin, L. Dobrzynski, Transmittivity through straight and stublike waveguides in a two-dimensional phononic crystal, *Physical Review B* 65 (2002) 174308.
[17] M. Oudich, M. Senesi, M.B. Assouar, M. Ruzzene, J.H. Sun, B. Vincent, Z.L. Hou, T.T. Wu, Experimental evidence of locally resonant sonic band gap in two-dimensional phononic stubbed plates, *Physical Review B* 84 (2011).
[18] M. Badreddine Assouar, M. Senesi, M. Oudich, M. Ruzzene, Z. Hou, Broadband plate-type acoustic metamaterial for low-frequency sound attenuation, *Applied Physics Letters* 101 (2012) 173505.
[19] K.F. Graff, *Wave Motion in Elastic Solids*, Oxford University Press, London, 1975.
[20] R.D. Cook, D.S. Malkus, M.E. Plesha, R.J. Witt, *Concepts and Applications of Finite Element Analysis*, fourth edition, John Wiley and Sons, Hoboken, New Jersey, 2002.
[21] R. Shelby, D. Smith, S. Nemat-Nasser, S. Schultz, Microwave transmission through a two-dimensional, isotropic, left-handed metamaterial, *Applied Physics Letters* 78 (2001) 489–491.
[22] Z. Liu, X. Zhang, Y. Mao, Y.Y. Zhu, Z. Yang, C.T. Chan, P. Sheng, Locally resonant sonic materials, *Science* 289 (2000) 1734.
[23] S. Gonella, A. Spadoni, M. Ruzzene, F. Scarpa, Wave propagation and band-gap characteristics of chiral lattices, *21st Biennial Conference on Mechanical Vibration and Noise*, Las Vegas, 2007, pp. 505–515.
[24] T.E. Michaels, J.E. Michaels, M. Ruzzene, Frequency–wavenumber domain analysis of guided wavefields, *Ultrasonics* 51 (2011) 452–466.
[25] L. Brillouin, *Wave Propagation in Periodic Structures*, second edition, Dover Publications, New York, 1953.
[26] R.S. Langley, The response of two-dimensional periodic structures to point harmonic forcing, *Journal of Sound and Vibration* 197 (1996) 469.
[27] J. Wolfe, *Imaging phonons: acoustic wave propagation in solids*, Cambridge Univ Press, Cambridge, 1998.
[28] H.H. Huang, C.T. Sun, Wave attenuation mechanism in an acoustic metamaterial with negative effective mass density, *New Journal of Physics* 11 (2009) 013003.
[29] N. Fang, D. Xi, J. Xu, M. Ambati, W. Srituravanich, C. Sun, X. Zhang, Ultrasonic metamaterials with negative modulus, *Nature Materials* 5 (2006) 456.

[30] O.C. Zienkiewicz, R.L. Taylor, *The Finite Element Method, Vol. 2: Solid Mechanics*, fifth edition, Butterworth-Heinemann, 2000, Oxford.
[31] E. Andreassen, J.S. Jensen, Analysis of phononic bandgap structures with dissipation, *Journal of Vibration and Acoustics* 135 (2013). 041015–8.
[32] F. Wang, J.S. Jensen, O. Sigmund, J. Mørk, Systematic design of loss-engineered slow-light waveguides, *Journal of the Optical Society of America A: Optics and Image Science, and Vision* 29 (2012) 2657–2666.
[33] R.P. Moiseyenko, V. Laude, Material loss influence on the complex band structure and group velocity in phononic crystals, *Physical Review B* 83 (2011) 064301.
[34] M. Romanoni, S. Gonella, N. Apetre, M. Ruzzene, Two-dimensional periodic actuators for frequency-based beam steering, *Smart Materials and Structures* 18 (2009) 125023.

Publication [P8]

Optimization of directional elastic energy propagation

Optimization of directional elastic energy propagation

Erik Andreassen[a,*], Hannah R. Chang[b], Massimo Ruzzene[b], Jakob Søndergaard Jensen[a]

[a]*Department of Mechanical Engineering, Technical University of Denmark, Nils Koppels Allé, Building 404, Denmark*
[b]*School of Aerospace Engineering, Georgia Institute of Technology, Atlanta, GA 30332*

Abstract

The aim of this paper is to demonstrate how topology optimization can be used to design a periodically perforated plate, in order to obtain a tailored anisotropic group velocity profile. The main method is demonstrated on both low and high frequency bending wave propagation in an aluminum plate, but is general in the sense that it could be used to design periodic structures with frequency dependent group velocity profiles for any kind of elastic wave propagation. With the proposed method the resulting design is manufacturable.

Keywords: wave propagation, perforated plate, microstructure, topology optimization, phononic crystal, group velocity

1. Introduction

Wave propagation in an elastic medium depends on the stiffness and density distribution. The governing equation for linear elastic wave propagation is:

$$\rho \frac{\partial^2 \mathbf{u}}{\partial t^2} = \boldsymbol{\partial}^T \mathbf{C} \boldsymbol{\partial} \mathbf{u} \tag{1}$$

where ρ is the density, $\mathbf{u}$ is the displacement field, t is time, $\boldsymbol{\partial}$ is the spatial derivative operator, and $\mathbf{C}$ is the constitutive matrix.

By periodic variations in the density or stiffness ($\mathbf{C}$) of the structure, one can achieve unique wave propagation properties, such as bandgaps (Sigalas and Economou, 1992), wave beaming (Ruzzene et al., 2003), and negative refraction (Farhat et al., 2010a,b; Pierre et al., 2010). In photonics, where analogous phenomena can be achieved by periodic variations in optical properties, a phenomenon called slow light (Hau et al., 1999), where the group velocity of a light pulse is lower than the speed of light, has recieved considerable attention. While Cox and Dobson (1999) were some of the first to use topology optimization to design photonic bandgap structures, Stainko and Sigmund (2007) illustrated how topology optimization (Bendsøe and Sigmund, 2003) can be used to design a photonic crystal with tailored group velocity properties.

Returning to elastic wave propagation; for materials where dissipation is negligible, the group velocity corresponds to the energy velocity (Brillouin, 1953), and controlling how the energy propagates have several possible applications. A simple and obvious one is vibration shielding, but it could also be used in more advanced applications, such as energy harvesting (Carrara et al., 2012).

For a periodic structure the wave solution to the full dynamic problem in Eq. 1 can be expanded according to the Bloch theorem (Bloch, 1929):

$$\mathbf{u}(\mathbf{x}, t) = \tilde{\mathbf{u}}(\mathbf{x}) e^{i\mathbf{k}^T \mathbf{x}} e^{i\omega t} \tag{2}$$

where $\tilde{\mathbf{u}}$ is the periodic displacement field, $\mathbf{k} = (k_x, k_y, k_z)^T$ is the wave vector, and ω is the temporal frequency. This allows a characterization of the dynamic properties by analysing the unit cell. Inserting Eq. (2) into Eq. (1) will yield an eigenvalue problem on the unit cell, which, as shown by the authors in an earlier paper (Andreassen et al., 2014), can be used to compute the group velocity $\mathbf{c}_g$ for a given frequency ω.

The aim of this paper is to present a method, based on topology optimization, for tailoring the group velocity profile in a structure by creating a periodic pattern in the structure. The method will be demonstrated with the design of a perforated plate. The goal is to make flexural (transverse) waves propagate faster in one direction.

Focusing on a plate structure, as opposed to a full three-dimensional structure, keeps the computational burden relatively low. And it makes an experimental verification simple, because the flexural wave propagation in a perforated plate can easily be measured using an optical measuring technique, such as a scanning laser vibrometer (SLV). That said, the presented method is also applicable to three-dimensional problems.

As already mentioned, the gradient-based method called topology optimization will be used to tailor the unit cell design. In this paper we present methods to tailor the group velocity profile, while the focus of most of the earlier work in elastic wave propagation in periodic structures has been maximization of bandgaps. The first to apply topology optimization to design periodic structures with elastic wave propagation in mind were Sigmund and Jensen (2003). Halkjær et al. (2005, 2006) used topology optimization to design unit cells for maximum bending wave bandgaps. Similarly, El-Sabbagh et al. (2008) maximized the bandgaps for bending wave propagation, but considered a finite plate with a finite periodic pattern. While Larsen et al. (2009) optimized the wave propagation pattern in a finite plate, without requiring a periodic pattern in the plate.

We start by presenting the optimization problem in Section 2, where the numerical modelling is also discussed. In Section

*E-mail: erand@mek.dtu.dk

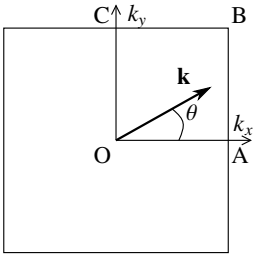

Figure 1: Illustration of the Brillouin zone and wave vector direction specified by the angle θ.

3 several optimized designs are presented and discussed.

2. Theory

It is necessary to start with a brief explanation of how dynamic properties of periodic structures are obtained and presented, before presenting the optimization problem.

The Bloch theorem allows solving the eigenvalue problem for only one unit cell. However, it is not enough to solve one eigenvalue problem - a range of eigenvalue problems must be solved. The wave vector $\mathbf{k}$ must be varied within a domain called the Brillouin zone (Brillouin, 1953), which is illustrated in Fig. 1.

At A in Fig. 1, $k_x = \pi/l_x$ and $k_y = 0$, where l_x is the width of the periodic cell (the unit cell). While at C, $k_x = 0$ and $k_y = \pi/l_y$, where l_y is the height of the unit cell. As illustrated the wave vector could also be given by its length and corresponding angle θ between k_x and k_y. For a unit cell possessing a 90 degree symmetry, it is enough to cover the domain bounded by the line connecting O-A-B-C-O (the irreducible Brillouin zone). And it is common practice for two-dimensional periodic structures to illustrate the dispersion properties in a so-called band diagram, where the temporal frequencies are plotted versus the wave vector position on the line O-A-B-C-O - only covering the boundary of the domain.

2.1. Group velocity of elastic waves

The derivation of the equations necessary to compute the group velocity profile (for flexural waves in a plate with a periodic pattern) is described in detail in (Andreassen et al., 2014). And it will not be repeated here. Numerically, the group velocity profile at a given frequency ω can be computed by first finding the wave vectors by solving the discretized eigenvalue problem

$$(\mathbf{K}_k(\theta,\omega) - k\mathbf{M}_k(\theta))\,\mathbf{u}_k = \mathbf{0} \tag{3}$$

where θ is the angle between the wave vector components k_x and k_y, ω is the temporal frequency, k is the wave vector length, and the finite element matrices $\mathbf{K}_k$ and $\mathbf{M}_k$ for a Mindlin plate problem are given in Appendix A. For a given combination of θ and k the group velocity $\mathbf{c}_g = (c_{gx}, c_{gy})^T$ is given as

$$c_{gx} = \frac{1}{2\omega}\frac{\mathbf{v}^T\,(-i\mathbf{K}_1 + 2k\cos(\theta)\,\mathbf{K}_3 + k\sin(\theta)\,\mathbf{K}_4)\,\mathbf{u}}{\mathbf{v}^T\,\mathbf{M}\mathbf{u}} \tag{4}$$

$$c_{gy} = \frac{1}{2\omega}\frac{\mathbf{v}^T\,(-i\mathbf{K}_2 + 2k\sin(\theta)\,\mathbf{K}_5 + k\cos(\theta)\,\mathbf{K}_4)\,\mathbf{u}}{\mathbf{v}^T\,\mathbf{M}\mathbf{u}} \tag{5}$$

where the computations of the matrices $\mathbf{K}_i$ and $\mathbf{M}$ are detailed in Appendix A. $\mathbf{u}$ can be found from $\mathbf{u}_k$, which is defined as

$$\mathbf{u}_k = \begin{bmatrix} k\mathbf{u} \\ \mathbf{u} \end{bmatrix} \tag{6}$$

while $\mathbf{v}$ is $\mathbf{u}$ conjugated counterpart. If dissipation were to be included, obtaining $\mathbf{v}$ would require the solution of an additional eigenvalue problem.

2.2. Optimization objective

It is important to remark that $\mathbf{c}_g$ does not necessarily point in the same direction as $\mathbf{k}$. However, when $\theta = 0^\circ$ and $\theta = 90^\circ$ the two point in the same direction. Utilizing this makes it simpler to define the objective for the optimization. In order to get a clear directional dependency, we can maximize the ratio between the group speed in those two perpendicular directions. And, thus, define our objective as

$$f_0 = \text{sign}\left(\frac{c_{gx}\big|_{\theta=0}}{c_{gy}\big|_{\theta=\pi/2}}\right)\cdot\frac{c_{gx}\big|_{\theta=0}}{c_{gy}\big|_{\theta=\pi/2}} \tag{7}$$

This ratio will vary with the considered frequency, but for a range of low frequencies (wave lengths larger than the periodic features) this ratio is well-defined and will vary slowly. We will return to the problem of higher frequencies shortly.

2.3. Benchmark design

To have something to benchmark the optimization results against, we introduce an intuitive design. We take outset in a unit cell of 15 times 15 mm and with a thickness of 2 mm. The final plate structure will be manufactured in aluminum (Young's modulus $E = 69$ GPa, Poisson's ratio $\nu = 0.33$, and the density $\rho = 2700$ kg/m^3) using water jetting, with a minimum required width of holes and structural members of 1.2 mm (for the specified thickness). To maximize f_0 for low frequency waves, we assume one can try to block the waves from propagating in the y-direction by making a long thin cut in the x-direction. This is illustrated in Fig. 2, where a unit cell consists of an air gap with the minimum width of 1.2 mm in the vertical direction is illustrated. Thin rods, also with the minimum width of 1.2 mm, hold the design together in the vertical direction. Remark, throughout the paper black regions symbolizes solid material (aluminum), while white regions symbolizes void/air.

The lowest mode in the band diagram for the unit cell in Fig. 2 is plotted in Fig. 3(a). For a given frequency, the group speed for waves propagating in the x-direction, c_{gx}, corresponds to the slope of the O-A part. While the group speed for waves propagating in the y-direction, c_{gy}, is the slope at the given frequency of the O-C part. In Fig. 3(b) the computed group speeds and

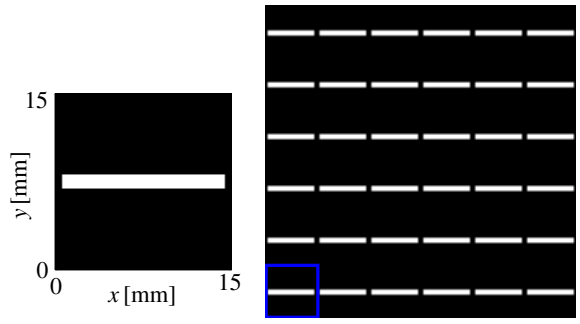

Figure 2: An intuitive design for a unit cell of a plate structure with a high f_0 for low frequencies. Left: One unit cell. Right: An assembly of six times six unit cells.

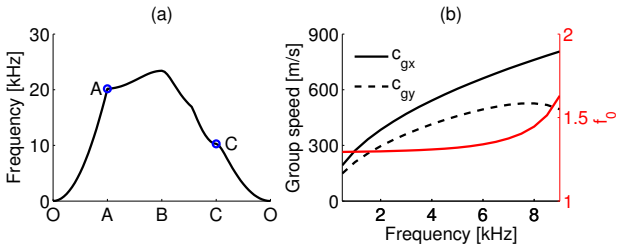

Figure 3: (a) The lowest mode for the unit cell in 2, and (b) the corresponding group speeds and objective function.

their ratio, f_0, are plotted for frequencies up to 9 kHz. The ratio f_0 for the low frequency range has an almost constant value of approximately 1.4 up to 6.0 kHz, before it increases when inertia effects become important. With the given manufacturing constraints a ratio of just below 1.5 for low frequency waves is decent, and will be used to benchmark the optimized designs.

2.4. Topology optimization

In topology optimization the material distribution is iteratively updated based on element gradients. This means that it is necessary to introduce a continuous interpolation between solid and void (corresponding to air) material in each finite element. Here we use a simple linear interpolation, such that the material properties of an element are given as

$$E_e = 10^{-6}E + \varphi_e E(1 - 10^{-6}) \tag{8}$$

$$\rho_e = 10^{-6}\rho + \varphi_e \rho(1 - 10^{-6}) \tag{9}$$

where $\varphi_e \in [0, 1]$ is the element design variable. As can be seen, neither the stiffness nor the density are allowed to vanish completely, since this would make the problem ill-posed.

2.5. Method 1: Only low frequencies

The simple way to maximize f_0 is to maximize the ratio between the frequency at point A and C in Fig. 3(a). This would indirectly affect f_0 for the low frequency range, but does not involve a computation of the group velocity. Thus, instead of solving Eq. (3), one solves the smaller equation system given by

$$\left(\mathbf{K}(\mathbf{k}) - \omega^2\mathbf{M}\right)\mathbf{u} = \mathbf{0} \tag{10}$$

where

$$\mathbf{K}(\mathbf{k}) = \mathbf{K}_0 - i(k_x\mathbf{K}_1 + k_y\mathbf{K}_2) + k_x^2\mathbf{K}_3 + k_xk_y\mathbf{K}_4 + k_y^2\mathbf{K}_5 \tag{11}$$

and, as earlier mentioned, the computations of the matrices $\mathbf{K}_i$ and $\mathbf{M}$ are detailed in Appendix A.

Equation (10) is solved for ω at $\mathbf{k}_A = (\pi/l_x, 0)$ and $\mathbf{k}_C = \left(0, \pi/l_y\right)$, giving us ω_A and ω_C. We choose the objective in the optimization problem to be

$$\min_{\varphi}\left(\frac{\omega_C}{\omega_A}\right) \tag{12}$$

2.5.1. Sensitivities

In topology optimization, the sensitivities (gradients) are found using the adjoint method. The sensitivities of ω_A and ω_C are simply given as the sensitivities of the eigenvalues, which can be found in e.g. (Haftka et al., 1990). Assuming the sensitivities of the eigenvalues have been computed, the sensitivities of the objective can be computed as

$$\frac{d\left(\frac{\omega_C}{\omega_A}\right)}{d\varphi_e} = \frac{\frac{d\omega_C}{d\varphi_e}\omega_A - \frac{d\omega_A}{d\varphi_e}\omega_C}{\omega_A^2} \tag{13}$$

where

$$\frac{d\omega_A^2}{d\varphi_e} = \frac{\mathbf{v}^T\frac{d\mathbf{K}}{d\varphi_e}\mathbf{u} - \omega_A^2\mathbf{v}^T\frac{d\mathbf{M}}{d\varphi_e}\mathbf{u}}{\mathbf{v}^T\mathbf{M}\mathbf{u}} \tag{14}$$

here $\mathbf{v}$ is the complex conjugate of $\mathbf{u}$, and the sensitivity of ω_C can be computed in the same way.

2.6. Method 2: Also for higher frequencies

Method 1 is computationally simple and cheap, but it only indirectly affects f_0. A more general approach can be formulated by computing f_0 from the group velocities at a given frequency ω, and use the adjoint method to directly compute the gradient of f_0. One advantage of this approach is that it can also be used for higher frequencies. Furthermore, with this method a range of specific frequencies can be included in the optimization.

2.6.1. Sensitivities

The computation of the sensitivities of f_0 are slightly more involved and requires the solution of an additional system of equations. Differentiating f_0 with respect to the element design variable, and taking c_{gx} to mean $c_{gx}|_{\theta=0}$ and c_{gy} to mean $c_{gy}|_{\theta=90}$, we get

$$\frac{df_0}{d\varphi_e} = \text{sign}\left(\frac{c_{gx}}{c_{gy}}\right)\left(\frac{\frac{dc_{gx}}{d\varphi_e}c_{gy} - c_{gx}\frac{dc_{gy}}{d\varphi_e}}{c_{gy}^2}\right) \tag{15}$$

where the details of how to compute the sensitivity of the group velocity components are given in Appendix B.

2.6.2. Bandgaps - issue at higher frequencies

At higher frequencies, so-called bandgaps or partial bandgaps, where no waves propagate for a given frequency range, can arise. However, if these occur for the frequencies of interest, f_0 is no longer well-defined. Our formulation is not aimed at obtaining bandgaps, which could be better done with e. g. the formulation in Andreassen and Jensen (2014), but in tailoring the group velocity profile. Therefore, we add the following constraint to avoid the formation of partial bandgaps:

$$c_{gy} \geq c_g^0 \tag{16}$$

where c_g^0 is an apriori defined lower limit on the group speed in the y-direction, e.g. 100 m / s. Defining it as a constant limit instead of a fraction of c_{gx} prevents the optimization from pulling both c_{gy} and c_{gx} down (with the risk of a bandgap forming).

2.7. Manufacturability

Out of consideration for the manufacturing, we choose to work with a unit cell of 15 times 15 mm. After removing material, the remaining aluminum has to be connected, and the minimum width of holes and structural members is 1.2 mm (for a thickness of 2 mm). In order to avoid islands of unconnected material we apply a conductivity constraint. Furthermore, using a regularization technique (filtering of the design variables) is found to be beneficial to get rid of fast oscillations (small features) in the design field.

2.7.1. Conductivity constraint

For a periodic material a homogenized conductivity (a macroscopic conductivity), $\boldsymbol{\kappa}^*$, can be computed. In the low frequency case, the optimizer will try to make the vertical connections as thin as possible. To prevent this we apply a minimum constraint on the conductivity in the y-direction

$$\kappa_y^* \geq f_\kappa \kappa \tag{17}$$

where f_κ is the required fraction of the conductivity, κ, of the base material. Computing the homogenized connectivity implies introducing another material interpolation:

$$\kappa_e = 10^{-6}\kappa + \varphi_e^2 \kappa \left(1 - 10^{-6}\right) \tag{18}$$

The element conductivity, κ_e, is interpolated using a quadratic scheme - in a simple way penalizing intermediate element design variables. The computation of the homogenized conductivity for a periodic material is discussed in detail in (Andreassen and Andreasen, 2014). A stiffness constraint can be used instead of a constraint on the conductivity, but this would have been computationally more costly. A fraction $f_\kappa = 0.15$ has been used for all optimizations, because it gives the unit cell a minimum width of approximately 1.2 mm when only one connecting rod forms.

A conductivity constraint is no guarantee that unconnected islands of material do not appear, but Andreasen et al. (2014) and Andreassen and Jensen (2014) used it with success when optimizing material structures for high loss, and the results presented in Section 3 indicate that it is also enough for the considered problem.

2.7.2. Regularization

Since we want the final design to be manufacturable, we use a regularization scheme in the optimization to avoid too small details in the design (Bendsøe and Sigmund, 2003). A good regularization scheme is to apply a filter on the design variables (see e. g. (Bourdin and Bourdin, 2001)), such as

$$\tilde{\varphi}_e = \frac{\sum_{i \in N_e} w(\mathbf{x}_i)\varphi_e}{\sum_{i \in N_e} w(\mathbf{x}_i)} \tag{19}$$

where

$$w(\mathbf{x}_i) = R - \|\mathbf{x}_i - \mathbf{x}_e\| \tag{20}$$

is a linearly decaying weight function, N_e is a list of elements for which the centers lie inside the filter radius R, and $\mathbf{x}_i$ is the spatial location of element center i. Note, when using a filter, the filtered design variable $\tilde{\varphi}_e$ is then substituted for φ_e in all the previously presented equations.

The problem with the filtering scheme in Eq. (19), is that it enforces areas in the design with intermediate material properties. Since we want to be able to end up with designs that are physically realistic and realizible (where each element represents either no material or material), we apply a so-called threshold projection (Guest et al., 2004) on top of the filtering. We use a projection method similar to (Xu et al., 2010), which is basically a continuous step function thresholding element densities (the filtered design variables) at $\eta = 0.5$. Here given as

$$\bar{\varphi}_e = \frac{\tanh(\eta\beta) + \tanh((\tilde{\varphi}_e - \eta)\beta)}{\tanh(\eta\beta) + \tanh((1-\eta)\beta)} \tag{21}$$

where η is the threshold value, and β is a parameter deciding the steepness of the step function.

The argument for doing this, is that we have observed using a large filter radius of 1.5 mm (5 elements), combined with projection, results in better designs (for the problems considered here) than gradually reducing the filter radius. We use a continuation scheme on the projection parameter, gradually increasing β from 2 to 32, to avoid getting stuck too early in a local minimum.

Remark, in all the previously mentioned formulas the design variable φ_e should be substituted with the projected element density $\bar{\varphi}_e$, and the sensitivity with respect to the design variable is found using the chain rule

$$\frac{d}{d\varphi_e} = \frac{d}{d\bar{\varphi}_e}\frac{d\bar{\varphi}_e}{d\tilde{\varphi}_e}\frac{d\tilde{\varphi}_e}{d\varphi_e} \tag{22}$$

The complete optimization problem for method 1 is

$$\begin{aligned} & \min_{\boldsymbol{\varphi}} \left(\frac{\omega_C}{\omega_A}\right) \\ \text{s.t.:} \quad & \text{Eq. 10} \\ & \kappa_y^* \geq 0.15\kappa \\ & 0 \leq \varphi_e \leq 1 \quad e = 1, ..., N \end{aligned} \tag{23}$$

while for method 2 it is

$$\begin{array}{lll} \max\limits_{\varphi}: & \min\limits_{\omega}\left(f_0\right) & \omega \in [\omega_1, \omega_2] \\ \text{s.t.:} & \text{Eq. 3} & \\ & \text{Eq. B.15} & \\ & \kappa_y^* \geq 0.15\kappa & \\ & \kappa_x^* \geq 0.15\kappa & \\ & c_{gy}\left(\omega\right) \geq c_g^0 & \omega \in [\omega_1, \omega_2] \\ & 0 \leq \varphi_e \leq 1 & e = 1, ..., N \end{array} \tag{24}$$

where the constraints on κ_x and c_{gy} only are necessary for higher frequencies. Something that will be discussed further in Section 3.

Topology optimization is used iteratively to decide if an element should contain material (aluminum) or not. In each iteration the nonlinear optimization algorithm MMA (Svanberg, 1987) is used to update the design variables in order to improve the objective while satisfying the constraints. All results presented in Section 3 are obtained within 300 iterations.

As a final note, it should be mentioned that since we are using projection the filtering does not guarantee a minimum length scale. Furthermore, the optimization can still end up with a certain amount of intermediate material (neither solid nor void) when it is beneficial for the performance. This is not a problem for the low frequency designs. However for the high frequency designs it is a problem. One way to amend this will be shown in Section 3.3.

3. Results

The result section is divided into three subsections. First, designs obtained using method 1 are presented and discussed. Thereafter, these will be compared to the results obtained using method 2. Before finishing off with designs obtained with method 2 for higher frequencies.

Remark, when computing the performance of the optimized designs we model all elements where $\varphi < 0.5$ as void and all elements with $\varphi \geq 0.5$ as solid.

3.1. Method 1

3.1.1. Comparison to benchmark design

Applying method 1 to maximize the directionality of the low frequency waves results in the design shown in Fig. 4. It is slightly different from the intuitive benchmark design, with two long slits instead of one, and with a small bend at both ends of the slit.

Remark, in the design coming out of the topology optimization there is a slight amount of intermediate densities (shown as gray pixels in the unit cell plot). However, when evaluating the performance all elements with a density above 0.5 are considered to be aluminum and those below are modeled as void. When the amount of gray is small, as in this design, it does not affect the performance. The performance of the design is shown in Fig. 5.

The performance is clearly better than the intuitive slit design, with an f_0 of approximately 1.6 up to around 6 kHz. Around

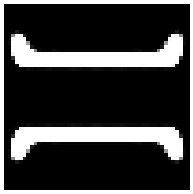

Figure 4: The unit cell resulting from optimizing with method 1.

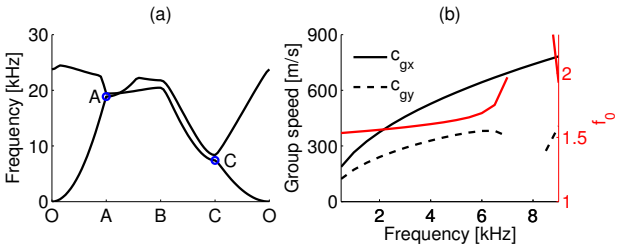

Figure 5: (a) The two lowest modes in the band diagram for the unit cell design in Fig.4, and (b) the corresponding performance (f_0) and group speeds.

7 kHz the performance curve has a discontinuity, which can be best understood by considering Fig. 5(a), where the two first modes in the band diagram are plotted. Point C has a tiny partial bandgap starting just before $\omega = 7.5$ kHz, and the performance curve is based on an evaluation of group velocities at 0.5 kHz intervals. At 7.5 and 8.0 kHz the group velocity in the y-direction is undefined, and it is first defined again at 8.5 kHz (where c_{gx} is computed based on the second band).

3.1.2. Rectangular unit cell

The design in Fig. 4 contains two slits, as opposed to one for the intuitive guess. Thus, it is natural to ask if a non-quadratic unit cell would be beneficial. Therefore, we try to see if an even better performance can be obtained with a rectangular unit cell. Figure 6 shows an optimized rectangular unit cell with a height to width ratio of approximately 3/4 (the height is decreased to 11.4 mm).

The resulting performance plot can be seen in Fig. 7. When looking at the corresponding band diagram, one should not make the mistake of thinking f_0 is just slightly over one because A and B are almost at the same level. Since the unit cell is rectangular the distance O-C is shorter than O-A.

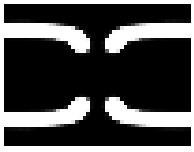

Figure 6: The unit cell resulting from optimizing with method 1 using a rectangular domain.

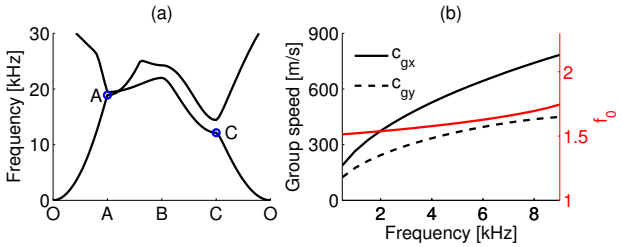

Figure 7: (a) The two lowest modes in the band diagram for the unit cell design in Fig. 6, and (b) the corresponding performance (f_0) and group speeds.

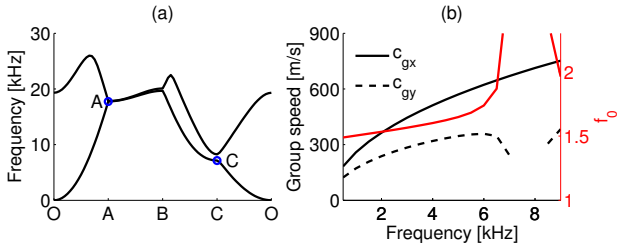

Figure 9: (a) The two lowest modes in the band diagram for the unsymmetric unit cell design in Fig. 6, and (b) the corresponding performance (f_0) and group speeds.

The performance of the rectangular unit cell is approximately the same as the quadratic cell, and so is the topology. Based on this result, there is no immediate reason to believe that the rectangular unit cell will provide an improved performance. Again, note that the frequency at point C in Fig. 7(a) is higher than in Fig. 5(a), because the unit cell height is smaller.

3.1.3. Non-symmetric design

The symmetry in the previously presented designs have been imposed by a vertical and horizontal symmetry line in the optimization. Therefore, it is worthwhile to see if a better performance can be achieved by removing these. For non-symmetric design, one needs to be aware that plotting the first mode by traversing the line O-A-B-C-O leaves a lot of information out. However, we stick with the same performance measure, because if the added freedom is of importance then it should improve. The resulting design is shown in Fig. 8, with the corresponding performance plot in Fig. 9.

The topology of the non-symmetric design is very similar to the symmetric, but with one "bone" displaced slightly. The performance is about the same, but f_0 starts to increase slightly earlier, because point C is pushed a bit lower. We believe this effect can be explained by the increased curvature of the slits.

3.2. Method 2 - low frequencies

3.2.1. Comparison to method 1

With method 2 one can choose to maximize f_0 for one or several frequencies. Since the results from method 1 revealed that f_0 is almost constant (or slightly increasing) up to approximately 6 kHz, we gather that for the low frequency range it does not matter whether we optimize for one or several frequencies.

Figure 8: The unit cell resulting from optimizing with method 1 without symmetry constraints.

And since it is computationally more expensive to optimize for more frequencies, we stick to one frequency.

The unit cell in Fig. 10(a) has been achieved by maximizing f_0 at 3.0 kHz. The topology is very similar to the symmetric design obtained with method 1, but with bi-directional bends at the end of the slits. The corresponding performance, shown in Fig. 11, is almost identical. However, it can be seen that the performance curve flatter (almost constant) for a larger range of frequencies.

3.2.2. Increasing frequency

The result in Fig. 10(a) has been achieved by maximizing f_0 at 3.0 kHz. If we choose a lower or higher frequency, not much happens - we end up with more or less same design - until we reach 5 kHz. As can be seen in Fig. 10(b), where the optimized design for $\omega = 5.0$ kHz is shown, the design now contains the same kind of bends as the one obtained with method 1. The performance, shown in Fig. 12, is slightly improved at 5.0 kHz versus the design in Fig. 10(a).

Now, if the frequency is increased further, a circular inclusion clearly forms. Already at 5.5 kHz the resulting topology

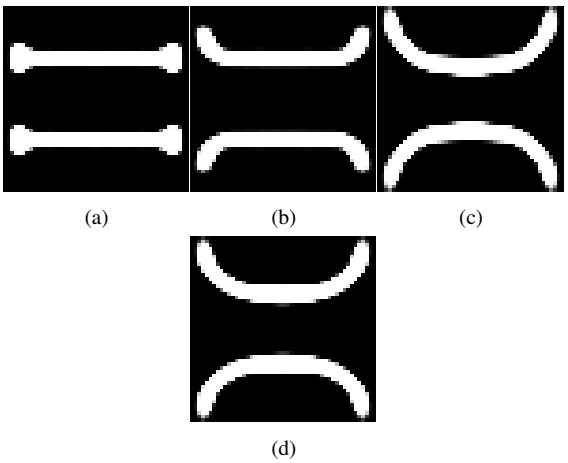

Figure 10: Unit cells from optimization of f_0 at (a) 3.0 kHz, (b) 5.0 kHz, (c) 5.5 kHz, and (d) 5.5 kHz with additional conductivity constraint in x-direction

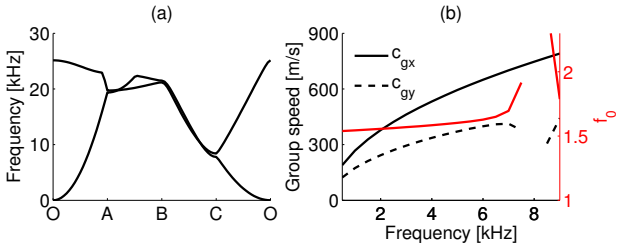

Figure 11: (a) The two lowest modes in the band diagram for the unit cell design in Fig.10(a) optimized at 3.0 kHz, and (b) the corresponding performance (f_0) and group speeds.

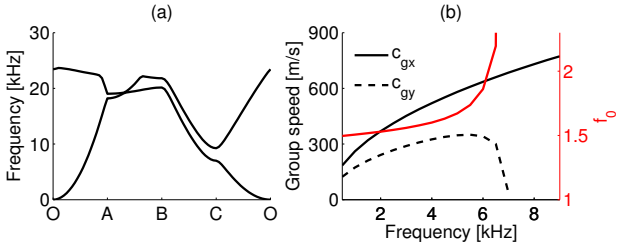

Figure 12: (a) The two lowest modes in the band diagram for the unit cell design in Fig. 10(b) optimized at 5.0 kHz, and (b) the corresponding performance (f_0) and group speeds.

is quite different (see Fig. 10 (c)). It looks like the optimization tries to form a resonant inclusion very similar to the one used in (Andreassen et al., 2014). Actually, the rods connecting the inclusion in the x-direction are low density elements (soft material), and disappear after thresholding (making the structure unphysical). In order to amend this, the optimization at 5.5 kHz is rerun with an additional conductivity constraint in the x-direction (same as in the y-direction). And, even though this is not a guaranteed solution it prevents the closing of the circle, because the isolated island of material would be so large that the design would not fulfill the conductivity constraint. The optimized design is shown in Fig. 10(d), and the performance is plotted in Fig. 13.

The performance of the design in Fig. 10(d) at the lowest frequencies is not as good as the lower frequency designs. However, it has a very good performance at the higher frequencies, until it reaches the first partial bandgap (where c_{gy} is undefined).

3.3. Method 2 - high frequencies

Low frequency wave propagation is to a high degree determined by the stiffness, but as seen in the previous section interesting designs start to appear when the frequency is increased and inertia effects start to play a part. In this section we want to show how method 2 can be applied to create optimized designs for frequencies above the first mode.

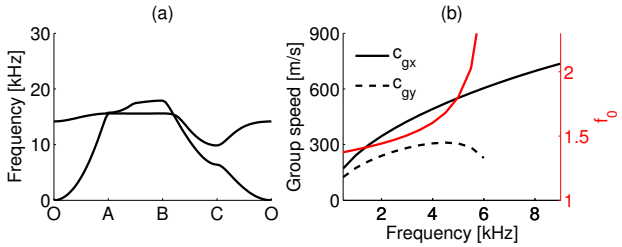

Figure 13: (a) The two lowest modes in the band diagram for the unit cell design in Fig. 10(d) optimized at 5.5 kHz with additional conductivity constraint, and (b) the corresponding performance (f_0) and group speeds.

3.3.1. One frequency

For higher frequencies two additional constraints are active in the optimization, both which are included in Eq. (24). Firstly, for higher frequencies we chose to apply a conductivity constraint in both directions. Unless this is done, designs with a lot of intermediate density or unconnected islands of material form. Secondly, a constraint on the minimum group speed c_{gx} is applied to prevent the optimizer from creating a design with a partial bandgap. For the frequencies considered in the following, we found $c_g^0 = 500$ [m/s] to work well.

Even with these constraints, which are helpful, the optimized designs are somewhat lacking. Figures 14(a) and (b) show designs where f_0 has been optimized for a single frequency - 25 and 30 kHz, respectively. Both designs show some amount of intermediate density, and both have, from a manufacturing point of view, too thin features.

The problem with the intermediate densities is that the optimizer use the interpolation between aluminum and void to create a better performing design by including intermediate densities, which cannot be manufactured. When we threshold the

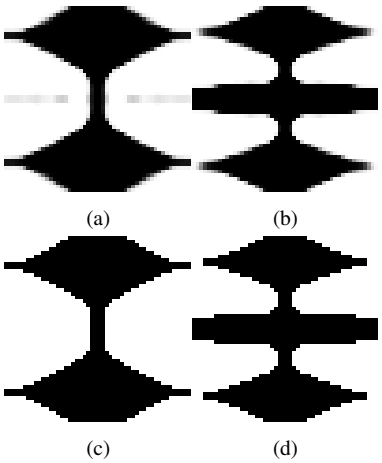

Figure 14: Unit cells from optimization of f_0 at (a) 25 kHz, (b) 30 kHz. (c) and (d) show the corresponding thresholded versions.

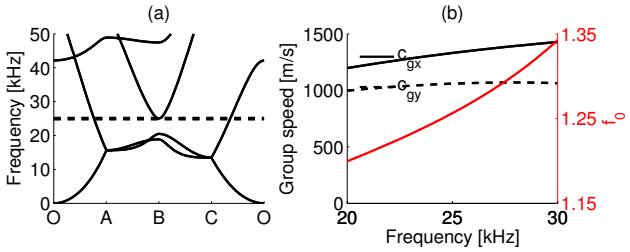

Figure 15: (a) The band diagram up to 50 kHz for the unit cell in Fig.10(c) optimized at 25.0 kHz (dashed line), and (b) the corresponding performance (f_0) and group speeds.

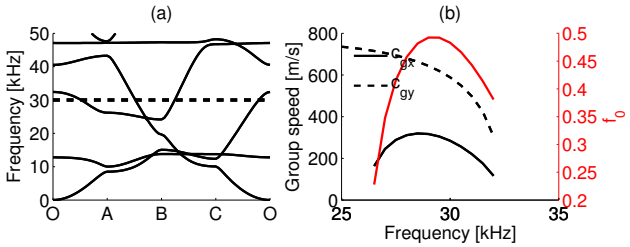

Figure 16: (a) The band diagram up to 50 kHz for the unit cell in Fig.10(d) optimized at 30.0 kHz (dashed line), and (b) the corresponding performance (f_0) and group speeds.

designs to evaluate the performance the result is unpredictable. In most cases the performance will deteriorate drastically. For example the performance, f_0, of the 25 kHz design, shown together with a portion of the band diagram in Fig.15, deteriorates to below 1.3 (as opposed to an $f_0 = 2.3$ for the non-thresholded design). And, the performance of the 30 kHz design is totally ruined (see Fig. 16), because the behavior of the thresholded design is very different from the non-thresholded design (the thin bars at the top and bottom are not connected across unit cells). In Fig. 16(b) c_{gx} is not plotted below 27 kHz, because, as can be seen from Fig. 16(a), there is a partial bandgap in the x-direction. And, for the same reason, neither c_{gx} nor c_{gy} are defined above 32 kHz.

3.3.2. *Frequency range*

The discussed issues do not, unfortunately, disappear when more frequencies are included. Figure 17 shows a design where f_0 is optimized at the frequencies 27.5, 30.0, and 32.5 kHz, simultaneously. The issues are still there, and the performance of the thresholded design is again unsatisfactory. The performance is plotted in Fig. 18 together with a band diagram, where dashed lines indicate the three frequencies included in the optimization. When including the interpolation in the evaluation of f_0, the ratio is above 1.8, which is quite good. But the performance of the thresholded design plotted in 18 is awful for the whole frequency range of interest (27.5-32.5 kHz), for the same reason that the 30.0 kHz design in the previous section performed poorly - it behaves radically different than the non-thresholded design.

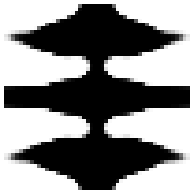

Figure 17: The unit cell resulting from optimizing for a range the frequencies 27.5, 30.0, and 32.5 kHz.

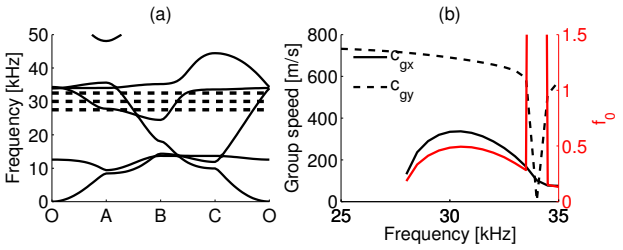

Figure 18: (a) The band diagram up to 50 kHz for the unit cell in Fig.17 (the thresholded version of it) optimized at 27.5-32.5 kHz (dashed lines indicate frequencies included in the optimization), and (b) the corresponding performance (f_0) and group speeds. Remark f_0 is not plotted for frequencies where c_{gx} or c_{gy} are undefined.

3.3.3. *Manufacturable design*

The robust optimization approach proposed by Wang et al. (2011) should be ideally suited to amend the problems discussed above. Instead of optimizing the performance of a single design, we optimize the performance for three versions of the design. In addition to the blueprint design ($\eta = 0.5$ in Eq. (21)), we optimize one eroded (corresponding to a threshold value $\eta_e > 0.5$ in Eq. (21)), and one dilated (corresponding to a threshold value $\eta_d < 0.5$ in Eq. 21) design.

Running such an optimization for the frequency range (27.5-32.5 kHz with $\eta_e = 0.65$ and $\eta_d = 0.35$, we obtain the blueprint design in Fig. 19. There is only a small amount of intermediate densities in the design, and, due to the robustness to dilation and erosion, the performance of the thresholded design (shown in Fig. 20) is good. Furthermore, the design now fulfills the manufacturing constraints.

From Fig. 20 it can be seen that within the considered frequency range f_0 is lowest at 27.5 kHz, but even there f_0 is still

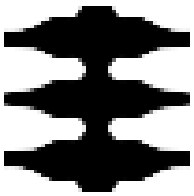

Figure 19: Unit cell of blueprint design resulting from a robust optimization for the frequencies 27.5, 30.0, and 32.5 kHz.

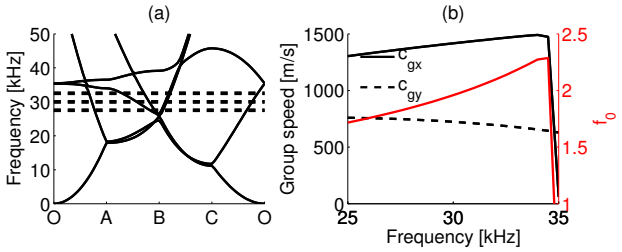

Figure 20: (a) The band diagram up to 50 kHz for the unit cell in Fig.19 (as always the thresholded version) optimized at 27.5-32.5 kHz (dashed lines indicate frequencies included in the optimization), and (b) the corresponding performance (f_0) and group speeds.

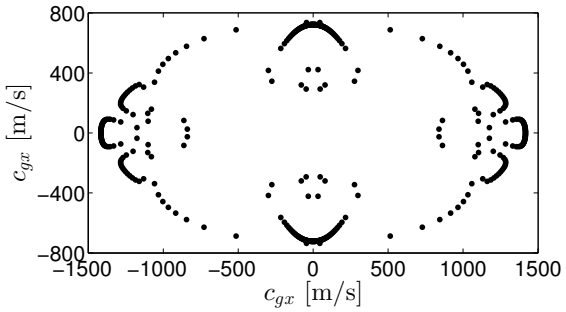

Figure 21: The group velocity profile at 30.0 kHz for the unit cell in Fig. 19. Each point corresponds to the group velocity (or velocities) at a discrete angle.

above 1.8 and the ratio increases slightly towards 32.5 kHz. The group velocity profile at 30.0 kHz for the optimized robust design is plotted in Fig. 21 - illustrating how the energy would propagate about twice as fast in the horizontal direction.

4. Conclusion

Two methods to design materials with specific group velocity profiles for elastic waves have been presented. The simplest method only works for low frequencies, while the more advanced method is shown to work well in both the low and high frequency regime, as long as additional constraints are applied.

Acknowledgement

This work was funded by the Danish Research Agency through the innovation consortium F•MAT.

Appendix A. System matrices

To find the system matrices for the eigenvalue problem

$$(\mathbf{K}_k(\theta,\omega) - k\mathbf{M}_k(\theta))\,\mathbf{u}_k = \mathbf{0} \tag{A.1}$$

we consider the governing plate equations, as given in Zienkiewicz and Taylor (2000):

$$\boldsymbol{\nabla}^T\mathbf{G}\,(\boldsymbol{\nabla}w - \boldsymbol{\Theta}) = \rho h\frac{\partial^2 w}{\partial t^2} \tag{A.2}$$

$$\boldsymbol{\partial}^T\mathbf{D}\boldsymbol{\partial}\boldsymbol{\Theta} + \mathbf{G}\,(\boldsymbol{\nabla}w - \boldsymbol{\Theta}) = \frac{\rho h^3}{12}\frac{\partial^2\boldsymbol{\Theta}}{\partial t^2} \tag{A.3}$$

where $w(\mathbf{x},t)$ denotes the out-of-plane deflection of a point of the mid-surface at location $\mathbf{x} = [x,\ y]^T$, $\boldsymbol{\Theta} = [\theta_x,\ \theta_y]^T$ is a vector containing the the two rotations of a material line normal to the mid-surface about the two in-plane axes, ρ is the material density, while h is the plate thickness. Also, $\mathbf{D} = \mathbf{D}(\mathbf{x})$ and $\mathbf{G} = \mathbf{G}(\mathbf{x})$ are the plate constitutive matrices. At a given point in the plate material, which is locally isotropic, these are:

$$\mathbf{D} = \frac{Eh^3}{12\,(1-\nu^2)}\begin{bmatrix}1 & \nu & 0\\ \nu & 1 & 0\\ 0 & 0 & \dfrac{(1-\nu)}{2}\end{bmatrix} \tag{A.4}$$

and

$$\mathbf{G} = \frac{E}{2\,(1+\nu)}\begin{bmatrix}\dfrac{5}{6}h & 0\\ 0 & \dfrac{5}{6}h\end{bmatrix} \tag{A.5}$$

where E is the elasticity module of the material, ν is Poisson's ratio, and h is the thickness of the plate.

Finally, the differential operator $\boldsymbol{\partial}$ is defined as:

$$\boldsymbol{\partial} = \begin{bmatrix}1 & 0\\ 0 & 0\\ 0 & 1\end{bmatrix}\frac{\partial}{\partial x} + \begin{bmatrix}0 & 0\\ 0 & 1\\ 1 & 0\end{bmatrix}\frac{\partial}{\partial y} = \boldsymbol{\alpha}_1\frac{\partial}{\partial x} + \boldsymbol{\alpha}_2\frac{\partial}{\partial y} \tag{A.6}$$

After applying the Bloch theorem and discretizing we end up with the system matrices

$$\mathbf{K}_k(\theta,\omega) = \begin{bmatrix}-i\mathbf{A}_1 & \mathbf{A}_0 - \omega^2\mathbf{M}_0\\ \mathbf{I} & \mathbf{0}\end{bmatrix} \tag{A.7}$$

$$\mathbf{M}_k(\theta) = \begin{bmatrix}-\mathbf{A}_2 & \mathbf{0}\\ \mathbf{0} & \mathbf{I}\end{bmatrix} \tag{A.8}$$

where the three submatrices are given as sums over element matrices

$$\mathbf{A}_0 = \sum_e \mathbf{k}_0^e \tag{A.9}$$

$$\mathbf{A}_1 = \sum_e \left(\cos(\theta)\,\mathbf{k}_1^e + \sin(\theta)\,\mathbf{k}_2^e\right) \tag{A.10}$$

$$\mathbf{A}_2 = \sum_e \left(\cos^2(\theta)\,\mathbf{k}_3^e + \cos(\theta)\sin(\theta)\,\mathbf{k}_4^e + \sin^2(\theta)\,\mathbf{k}_5^e\right) \tag{A.11}$$

With the nodal displacements interpolated over the element using the shape function matrices $\mathbf{N}_w$ and $\mathbf{N}_\Theta$, as follows

$$\mathbf{u}^e = \begin{bmatrix}\mathbf{N}_w(x,y) & \mathbf{0}\\ \mathbf{0} & \mathbf{N}_\Theta(x,y)\end{bmatrix}\begin{bmatrix}\tilde{\mathbf{w}}^e\\ \tilde{\boldsymbol{\Theta}}^e\end{bmatrix} \tag{A.12}$$

the corresponding expressions for the element matrices are

$$\mathbf{k}_0^e = \int_{\Omega^e} \begin{bmatrix} -\boldsymbol{\nabla}\mathbf{N}_w^T\mathbf{G}\boldsymbol{\nabla}\mathbf{N}_w & \left(\mathbf{N}_\Theta^T\mathbf{G}\boldsymbol{\nabla}\mathbf{N}_w\right)^T \\ \mathbf{N}_\Theta^T\mathbf{G}\boldsymbol{\nabla}\mathbf{N}_w & -\boldsymbol{\partial}\mathbf{N}_\Theta^T\mathbf{D}\boldsymbol{\partial}\mathbf{N}_{\boldsymbol{\Theta}} - \mathbf{N}_\Theta^T\mathbf{G}\mathbf{N}_{\boldsymbol{\Theta}} \end{bmatrix} d\Omega^e \tag{A.13}$$

$$\mathbf{k}_1^e = -\int_{\Omega^e} \begin{bmatrix} \mathbf{N}_w^T\boldsymbol{\beta}_1^T\mathbf{G}\boldsymbol{\nabla}\mathbf{N}_w - \boldsymbol{\nabla}\mathbf{N}_w^T\mathbf{G}\boldsymbol{\beta}_1\mathbf{N}_w & -\left(\mathbf{N}_\Theta^T\mathbf{G}\boldsymbol{\beta}_1\mathbf{N}_w\right)^T \\ \mathbf{N}_\Theta^T\mathbf{G}\boldsymbol{\beta}_1\mathbf{N}_w & \mathbf{N}_\Theta^T\alpha_1^T\mathbf{D}\boldsymbol{\partial}\mathbf{N}_{\boldsymbol{\Theta}} - \boldsymbol{\partial}\mathbf{N}_\Theta^T\mathbf{D}\alpha_1\mathbf{N}_{\boldsymbol{\Theta}} \end{bmatrix} d\Omega^e \tag{A.14}$$

$$\mathbf{k}_2^e = -\int_{\Omega^e} \begin{bmatrix} \mathbf{N}_w^T\boldsymbol{\beta}_2^T\mathbf{G}\boldsymbol{\nabla}\mathbf{N}_w - \boldsymbol{\nabla}\mathbf{N}_w^T\mathbf{G}\boldsymbol{\beta}_2\mathbf{N}_w & -\left(\mathbf{N}_\Theta^T\mathbf{G}\boldsymbol{\beta}_2\mathbf{N}_w\right)^T \\ \mathbf{N}_\Theta^T\mathbf{G}\boldsymbol{\beta}_2\mathbf{N}_w & \mathbf{N}_\Theta^T\alpha_2^T\mathbf{D}\boldsymbol{\partial}\mathbf{N}_{\boldsymbol{\Theta}} - \boldsymbol{\partial}\mathbf{N}_\Theta^T\mathbf{D}\alpha_2\mathbf{N}_{\boldsymbol{\Theta}} \end{bmatrix} d\Omega^e$$

$$\mathbf{k}_3^e = -\int_{\Omega^e} \begin{bmatrix} \mathbf{N}_w^T\boldsymbol{\beta}_1^T\mathbf{G}\boldsymbol{\beta}_1\mathbf{N}_w & \mathbf{0} \\ \mathbf{0} & \mathbf{N}_\Theta^T\alpha_1^T\mathbf{D}\alpha_1\mathbf{N}_{\boldsymbol{\Theta}} \end{bmatrix} d\Omega^e \tag{A.15}$$

$$\mathbf{k}_4^e = -\int_{\Omega^e} \begin{bmatrix} \mathbf{N}_w^T\left(\boldsymbol{\beta}_1+\boldsymbol{\beta}_2\right)^T\mathbf{G}\left(\boldsymbol{\beta}_1+\boldsymbol{\beta}_2\right)\mathbf{N}_w & \mathbf{0} \\ \mathbf{0} & \mathbf{N}_\Theta^T\left(\alpha_1+\alpha_2\right)^T\mathbf{D}\left(\alpha_1+\alpha_2\right)\mathbf{N}_{\boldsymbol{\Theta}} \end{bmatrix} d\Omega^e \tag{A.16}$$

$$\mathbf{k}_5^e = -\int_{\Omega^e} \begin{bmatrix} \mathbf{N}_w^T\boldsymbol{\beta}_2^T\mathbf{G}\boldsymbol{\beta}_2\mathbf{N}_w & \mathbf{0} \\ \mathbf{0} & \mathbf{N}_\Theta^T\alpha_2^T\mathbf{D}\alpha_2\mathbf{N}_{\boldsymbol{\Theta}} \end{bmatrix} d\Omega^e \tag{A.17}$$

$$\mathbf{m}^e = -\int_{\Omega^e} \begin{bmatrix} \rho h\mathbf{N}_w^T\mathbf{N}_w & \mathbf{0} \\ \mathbf{0} & \dfrac{\rho h^3}{12}\mathbf{N}_{\boldsymbol{\Theta}}^T\mathbf{N}_{\boldsymbol{\Theta}} \end{bmatrix} d\Omega^e \tag{A.18}$$

where Ω^e is the domain of element e. And the two vectors $\beta_1 = (1,0)^T$ and $\beta_2 = (0,1)^T$.

The matrices in Eq. 4 are found by summation of the element matrices, e.g.

$$\mathbf{K}_1 = \sum_e \mathbf{k}_1^e \tag{A.19}$$

Appendix B. Group velocity sensitivities

The derivation is explained in detail below for the x-component of the group velocity. Since we specify the frequency, ω, and the angle, α, these are considered constant with respect to the density, φ^e, such that

$$c_{gx} = F_0(\varphi^e, k(\varphi^e), \mathbf{u}(\varphi^e), \mathbf{v}(\varphi^e)) \tag{B.1}$$

To make the derivations simplier, we introduce the following normalized eigenvectors

$$\mathbf{h}_1 = \frac{\mathbf{u}}{\sqrt{\mathbf{v}^T\,\mathbf{M}\mathbf{u}}} \tag{B.2}$$

$$\mathbf{h}_2 = \frac{\mathbf{v}}{\sqrt{\mathbf{v}^T\,\mathbf{M}\mathbf{u}}} \tag{B.3}$$

implying

$$F_0(\varphi^e, \omega(\varphi^e), \mathbf{h}_1(\varphi^e), \mathbf{h}_2(\varphi^e)) = \frac{1}{2\omega}\mathbf{h}_2^T\left(-i\mathbf{K}_1 + 2k_x\mathbf{K}_3 + k_y\mathbf{K}_4\right)\mathbf{h}_1 \tag{B.4}$$

The derivative with respect to φ^e is:

$$\begin{aligned} \frac{dF_0}{d\varphi^e} &= \frac{\partial F_0}{\partial\varphi^e} + \frac{\partial F_0}{\partial k}\frac{dk}{d\varphi^e} + \frac{\partial F_0}{\partial\mathbf{h}_1}\frac{d\mathbf{h}_1}{d\varphi^e} + \frac{\partial F_0^T}{\partial\mathbf{h}_2}\frac{d\mathbf{h}_2}{d\varphi^e} \\ &= \frac{1}{2\omega}(\mathbf{h}_2^T\,\frac{\partial\left(-i\mathbf{K}_1 + 2k_x\mathbf{K}_3 + k_y\mathbf{K}_4\right)}{\partial\varphi^e}\mathbf{h}_1 \\ &+ \mathbf{h}_2^T\,\frac{\partial\left(-i\mathbf{K}_1 + 2k_x\mathbf{K}_3 + k_y\mathbf{K}_4\right)}{\partial k}\mathbf{h}_1\frac{dk}{d\varphi^e} \\ &+ \mathbf{h}_2^T\left(-i\mathbf{K}_1 + 2k_x\mathbf{K}_3 + k_y\mathbf{K}_4\right)\frac{d\mathbf{h}_1}{d\varphi^e} \\ &+ \mathbf{h}_1^T\left(-i\mathbf{K}_1 + 2k_x\mathbf{K}_3 + k_y\mathbf{K}_4\right)^T\frac{d\mathbf{h}_2}{d\varphi^e}) \end{aligned} \tag{B.5}$$

To get rid of the implicit derivatives, we need to add three adjoint problems to the original eigenvalue problem

$$F_1 = \mathbf{x}_1^T\left(\mathbf{K} - \omega^2\mathbf{M}\right)\mathbf{h}_1 = 0 \tag{B.6}$$

$$F_2 = \mathbf{x}_2^T\left(\mathbf{K} - \omega^2\mathbf{M}\right)^T\mathbf{h}_2 = 0 \tag{B.7}$$

$$F_3 = x\left(\mathbf{v}^T\mathbf{K}\mathbf{u} - \omega^2\mathbf{v}^T\mathbf{M}\mathbf{u}\right) = 0 \tag{B.8}$$

where $\mathbf{x}_1$, $\mathbf{x}_2$, and x are arbitrary. That is, they are considered constant in the differentiation. Dividing both sides of F_3 with $\mathbf{v}^T\mathbf{M}\mathbf{u}$ yields

$$F_3 = x(\mathbf{h}_2^T\mathbf{K}\mathbf{h}_1 - \omega^2) = 0 \tag{B.9}$$

Adding the adjoint problems to F_0, differentiating, and gathering terms result in:

$$\begin{aligned} \frac{dc_{gx}}{d\varphi^e} = \frac{d(F_0+F_1+F_2+F_3)}{d\varphi^e} &= \frac{\partial F_0}{\partial\varphi^e} + \frac{\partial F_1}{\partial\varphi^e} + \frac{\partial F_2}{\partial\varphi^e} + \frac{\partial F_3}{\partial\varphi^e} + \\ &\left(\frac{\partial F_0}{\partial k} + \frac{\partial F_1}{\partial k} + \frac{\partial F_2}{\partial k} + \frac{\partial F_3}{\partial k}\right)\frac{dk}{d\varphi^e} + \\ &\left(\frac{\partial F_0}{\partial\mathbf{h}_1} + \frac{\partial F_1}{\partial\mathbf{h}_1} + \frac{\partial F_3}{\partial\mathbf{h}_1}\right)\frac{d\mathbf{h}_1}{d\varphi^e} + \\ &\left(\frac{\partial F_0^T}{\partial\mathbf{h}_2} + \frac{\partial F_2}{\partial\mathbf{h}_2} + \frac{\partial F_3^T}{\partial\mathbf{h}_2}\right)\frac{d\mathbf{h}_2}{d\varphi^e} \end{aligned} \tag{B.10}$$

Now, the adjoint variables are chosen such that the terms with implicit derivatives become zero. Resulting in the sensitivities

$$\begin{aligned} \frac{dc_{gx}}{d\varphi^e} &= \frac{\partial F_0}{\partial\varphi^e} + \frac{\partial F_1}{\partial\varphi^e} + \frac{\partial F_2}{\partial\varphi^e} + \frac{\partial F_3}{\partial\varphi^e} \\ &= \frac{1}{2\omega}\mathbf{h}_2^T\,\frac{\partial\left(\left(-i\mathbf{K}_1 + 2k_x\mathbf{K}_3 + k_y\mathbf{K}_4\right)\right)}{\partial\varphi^e}\mathbf{h}_1 + \mathbf{x}_1^T\frac{\partial\left(\mathbf{K} - \omega^2\mathbf{M}\right)}{\partial\varphi^e}\mathbf{h}_1 \\ &+ \mathbf{x}_2^T\frac{\partial\left(\mathbf{K} - \omega^2\mathbf{M}\right)^T}{\partial\varphi^e}\mathbf{h}_2 + x\mathbf{h}_2^T\frac{\partial\mathbf{K}}{\partial\varphi^e}\mathbf{h}_1 \end{aligned} \tag{B.11}$$

when the three adjoint equations are set equal to zero. First adjoint equation:

$$\begin{aligned} &\left(\frac{\partial F_0}{\partial k} + \frac{\partial F_1}{\partial k} + \frac{\partial F_2}{\partial k} + \frac{\partial F_3}{\partial k}\right) = \\ &\frac{1}{2\omega}\mathbf{h}_2^T\left(2\cos(\theta)\,\mathbf{K}_3 + \sin(\theta)\,\mathbf{K}_4\right)\mathbf{h}_1 + \mathbf{x}_1^T\left(\frac{\partial\mathbf{K}}{\partial k}\right)\mathbf{h}_1 \\ &+ \mathbf{x}_2^T\left(\frac{\partial\mathbf{K}}{\partial k}\right)^T\mathbf{h}_2 + x\mathbf{h}_2^T\frac{\partial\mathbf{K}}{\partial k}\mathbf{h}_1 = 0 \end{aligned} \tag{B.12}$$

Second adjoint equation:

$$\begin{aligned} &\left(\frac{\partial F_0}{\partial\mathbf{h}_1} + \frac{\partial F_1}{\partial\mathbf{h}_1} + \frac{\partial F_3}{\partial\mathbf{h}_1}\right) = \\ &\frac{1}{2\omega}\mathbf{h}_2^T\left(-i\mathbf{K}_1 + 2k_x\mathbf{K}_3 + k_y\mathbf{K}_4\right) + \mathbf{x}_1^T\left(\mathbf{K} - \omega^2\mathbf{M}\right) + x\mathbf{h}_2^T\mathbf{K} = \mathbf{0} \end{aligned} \tag{B.13}$$

Third adjoint equation:

$$\begin{aligned} &\left(\frac{\partial F_0^T}{\partial\mathbf{h}_2} + \frac{\partial F_2}{\partial\mathbf{h}_2} + \frac{\partial F_3^T}{\partial\mathbf{h}_2}\right) = \\ &\frac{1}{2\omega}\mathbf{h}_1^T\left(-i\mathbf{K}_1^T + 2k_x\mathbf{K}_3^T + k_y\mathbf{K}_4^T\right) + \mathbf{x}_2^T\left(\mathbf{K} - \omega^2\mathbf{M}\right)^T + x\mathbf{h}_1^T\mathbf{K}^T = \mathbf{0} \end{aligned} \tag{B.14}$$

Or in matrix form

$$\begin{bmatrix} \left(\frac{\partial \mathbf{K}}{\partial k}\right)\mathbf{h}_1 & \left(\mathbf{K}-\omega^2\mathbf{M}\right) & \mathbf{0} \\ \left(\frac{\partial \mathbf{K}}{\partial k}\right)^T\mathbf{h}_2 & \mathbf{0} & \left(\mathbf{K}-\omega^2\mathbf{M}\right)^T \\ \mathbf{h}_2^T\frac{\partial \mathbf{K}}{\partial k}\mathbf{h}_1 & \mathbf{h}_2^T\mathbf{K} & \mathbf{h}_1^T\mathbf{K}^T \end{bmatrix}^T \begin{bmatrix} \mathbf{x}_1 \\ \mathbf{x}_2 \\ x \end{bmatrix} = -\begin{bmatrix} \frac{1}{2\omega}\mathbf{h}_2^T\left(2\cos(\alpha)\mathbf{K}_3+\sin(\alpha)\mathbf{K}_4\right)\mathbf{h}_1 \\ \frac{1}{2\omega}\mathbf{h}_2^T\left(-i\mathbf{K}_1+2k_x\mathbf{K}_3+k_y\mathbf{K}_4\right) \\ \frac{1}{2\omega}\mathbf{h}_1^T\left(-i\mathbf{K}_1+2k_x\mathbf{K}_3+k_y\mathbf{K}_4\right)^T \end{bmatrix} \tag{B.15}$$

References

M. M. Sigalas, E. N. Economou, Elastic and acoustic wave band structure, Journal of Sound and Vibration 158 (1992) 377–382.

M. Ruzzene, F. Scarpa, F. Soranna, Wave beaming effects in two-dimensional cellular structures, Smart Materials and Structures 12 (2003) 363.

M. Farhat, S. Guenneau, S. Enoch, A. B. Movchan, G. G. Petursson, Focussing bending waves via negative refraction in perforated thin plates, Applied Physics Letters 96 (2010a) 081909.

M. Farhat, S. Guenneau, S. Enoch, High directivity and confinement of flexural waves through ultra-refraction in thin perforated plates, EPL (Europhysics Letters) 91 (2010b) 54003.

J. Pierre, O. Boyko, L. Belliard, J. O. Vasseur, B. Bonello, Negative refraction of zero order flexural lamb waves through a two-dimensional phononic crystal, Applied Physics Letters 97 (2010) 121919.

L. Hau, S. Harris, Z. Dutton, C. Behroozi, Light speed reduction to 17 metres per second in an ultracold atomic gas, Nature 397 (1999) 594–598.

S. Cox, D. Dobson, Maximizing band gaps in two-dimensional photonic crystals, Siam J Appl Math 59 (1999) 2108–2120.

R. Stainko, O. Sigmund, Tailoring dispersion properties of photonic crystal waveguides by topology optimization, Waves in Random and Complex Media 17 (2007) 477–489.

M. Bendsøe, O. Sigmund, Topology Optimization. Theory, Methods and Applications, Springer, 2003.

L. Brillouin, Wave propagation in periodic structures, 2 ed., Dover Publications, 1953.

M. Carrara, M. R. Cacan, M. J. Leamy, M. Ruzzene, A. Erturk, Dramatic enhancement of structure-borne wave energy harvesting using an elliptical acoustic mirror, Applied Physics Letters 100 (2012) 204105.

F. Bloch, Über die quantenmechanik der elektronen in kristallgittern, Zeitschrift für Physik 52 (1929) 555–600.

E. Andreassen, K. Manktelow, M. Ruzzene, Directional bending wave propagation in periodically perforated plates, Journal of Sound and Vibration Submitted (2014).

O. Sigmund, J. S. Jensen, Systematic design of phononic band-gap materials and structures by topology optimization, Philos. Trans. R. Soc. Lond. A, Math. Phys. Eng. Sci. (UK) Philosophical transactions - Royal Society. Mathematical, Physical and engineering sciences 361 (2003) 1001–1019.

S. Halkjær, O. Sigmund, J. S. Jensen, Inverse design of phononic crystals by topology optimization, Zeitschrift für Kristallographie - Crystalline Materials 220 (2005) 895–905.

S. Halkjær, O. Sigmund, J. S. Jensen, Maximizing band gaps in plate structures, Structural and Multidisciplinary Optimization 32 (2006) 263–275.

A. El-Sabbagh, W. Akl, A. Baz, Topology optimization of periodic mindlin plates, Finite Elements in Analysis and Design 44 (2008) 439–449.

A. A. Larsen, J. S. Jensen, O. Sigmund, Topological material layout in plates for vibration suppression and wave propagation control, Structural and Multidisciplinary Optimization 37 (2009) 585–594.

R. Haftka, Z. Gürdal, M. Kamat, Elements of Structural Optimization, Kluwer Academic Publishers, 1990.

E. Andreassen, J. S. Jensen, Topology optimization of periodic microstructures for enhanced dynamic properties of viscoelastic composite materials, Structural and Multidisciplinary Optimization 49 (2014) 695–705.

E. Andreassen, C. S. Andreasen, How to determine composite material properties using numerical homogenization, Computational Materials Science 83 (2014) 488–495.

C. S. Andreasen, E. Andreassen, J. S. Jensen, O. Sigmund, On the realization of the bulk modulus bounds for two-phase viscoelastic composites, Journal of the Mechanics and Physics of Solids 63 (2014) 228–241.

B. Bourdin, B. Bourdin, Filters in topology optimization, International Journal for Numerical Methods in Engineering 50 (2001) 2143–2158.

J. Guest, J. Prevost, T. Belytschko, Achieving minimum length scale in topology optimization using nodal design variables and projection functions, International Journal for Numerical Methods in Engineering 61 (2004) 238–254.

S. Xu, Y. Cai, G. Cheng, Volume preserving nonlinear density filter based on heaviside functions, Structural and Multidisciplinary Optimization 41 (2010) 495–505.

K. Svanberg, Method of moving asymptotes - a new method for structural optimization., International Journal for Numerical Methods in Engineering 24 (1987) 359–373.

F. Wang, B. S. Lazarov, O. Sigmund, On projection methods, convergence and robust formulations in topology optimization, Structural and Multidisciplinary Optimization 43 (2011) 767–784.

O. C. Zienkiewicz, R. L. Taylor, The Finite Element Method. Fifth Edition. Volume 2: Solid Mechanics, Butterworth-Heinemann, 2000.

Publication [P9]

A practical multiscale approach for optimization of structural damping

Noname manuscript No.
(will be inserted by the editor)

A practical multiscale approach for optimization of structural damping

Erik Andreassen · **Jakob Søndergaard Jensen**

Received: date / Accepted: date

Abstract A simple and practical multiscale approach suitable for topology optimization of structural damping in a component ready for additive manufacturing is presented. The approach consists of two steps: First, the homogenized loss factor is maximized. This is done in order to obtain several connected and isotropic microstructures. Second, the structural damping of the component is maximized using material interpolations based on the homogenized properties of the microstructures. In order to achieve convergence towards a discrete set of material phases in the macroscopic problem, a material interpolation that favors values close to the predefined material densities is introduced.

Keywords damping · microstructure · topology optimization · homogenization · multiscale · additive manufacturing

1 Introduction

The aim of this paper is to propose a practical multiscale formulation for the maximization of a component's structural damping, which yields a component that can be manufactured by printing the stiff phase (typically a metal), e. g. using the additive manufacturing method selective laser sintering, and then be used as a mold for the soft phase.

The basic idea of much of the multiscale work in the field of topology optimization is that it is possible to map intermediate densities to microstructures with properties found by solving a set of local microstructure optimization problems. Rodrigues et al (2002) were among the first to suggest such an iterative approach, based on earlier works by among others Bendsøe et al (1994), and Theocaris and Stavroulakis (1999). Coelho et al (2008) extended the approach to three-dimensional problems, and even applied it to bone replacement designs (see e.g. Coelho et al 2011). The approach is relatively straightforward to implement for minimization of compliance, and it has been shown to work well. It should also be mentioned that Barbarosie and Toader (2012) have worked on extending the approach to include shape optimization on the unit cell level.

One drawback with the method is that it is not guaranteed to converge towards a manufacturable design. The fact that the microstructures are not necessarily connected can, at least for minimum compliance problems, be amended by post-processing (shifting the base unit cells until they match). However, this would be rather time-consuming. Furthermore, it is uncertain whether the approach would work equally well for more complex problems.

An alternative approach is to predefine regions which should have the same material, and then optimize the material structure in each of these regions for a macroscopic response (as done by Andreasen and Sigmund (2012), and with a full solution of the macroscopic problem by Alexandersen and Lazarov (2014)). Thus, simplifying the matter and making it easier to generalize to problems involving multiphysics, but also restricting the design space.

This work was funded by the Danish Research Agency through the innovation consortium F·MAT.

E. Andreassen · J. S. Jensen
Department of Mechanical Engineering, Technical University of Denmark, Nils Koppels Allé, Building 404, 2800 Lyngby, Denmark
E-mail: json@elektro.dtu.dk

A third approach, suggested by among others Theocaris and Stavroulakis (1999), is to base the material interpolation on an a priori defined material library. A manufacturable two-dimensional (2D) bone replacement prototype was achieved by Khanoki and Pasini (2012) using a precomputed interpolation for a simple orthotropic microstructure in the optimization.

In the following we will show how this third approach can be applied in a multiscale optimization of the structural damping of a component. First, the homogenized loss factor is maximized by using an approach similar to the one described in (Andreasen et al 2014). This is done in order to obtain several connected and isotropic microstructures, which can be used as material phases in a multi-material optimization problem. In order to achieve convergence towards a discrete set of material phases in the macroscopic problem, a material interpolation that favors values close to the predefined material densities is introduced.

An alternative way to achieve a design with discrete microstructures, would be to use an approach similar to what is done in optimization of fiber reinforced composites with a discrete set of fiber angles (see description of discrete material optimization (DMO) by Stegmann and Lund 2005). The implementation would require multiple design fields, and this is not necessary with the formulation presented here. However, a DMO approach would probably be useful if the presented method should be extended to anisotropic material structures.

The structure of the paper is such that most of the theory is presented in Section 2, where first the macroscopic problem is presented in Section 2.1 , which also includes a justification for the multiscale approach, and then the microscopic problem is presented in Section 2.2 . Thereafter, Section 3 follows with an example illustrating how a realistic material interpolation for the macroscopic problem can be obtained and how this influences the macroscopic design. The manufacturability of the design is not considered in Section 3.

Results for manufacturable microstructures are presented in Section 4. Then, with basis in the obtained results, Section 5 presents the material interpolation that makes the macroscopic problem converge to a discrete set of densities. The results for the macroscopic problem are presented in Section 6, before the conclusion in Section 7.

2 Theory

2.1 Macroscopic optimization problem

The basic formulation of the macroscopic problem is similar to the one presented by Kim et al (2013), who use topology optimization to find the best layout of damping treatments on a cylindrical shell structure. Other similar formulations have been suggested by Ling et al (2011); El-Sabbagh and Baz (2014) for damping treatments of plane plate structures, but the presented results in these are less convincing than those of Kim et al (2013).

The problem considered here is that of maximizing a component's structural damping for a range of eigenfrequencies by optimizing the distribution of the material. The macroscopic optimization problem is:

$$\begin{array}{lll} \min\limits_{\boldsymbol{\rho}}: & \max\left(-\log\zeta_i\right), & i=1,...,n \\ \text{s. t.:} & (\mathbf{K}-\omega^2\mathbf{M})\mathbf{U}=\mathbf{0}, & \text{Eigenvalue problem} \\ & \mathrm{Re}(\omega_1)\geq\omega_0, & \text{Constraint on first eigenvalue} \\ & 0\leq\varphi_e\leq 1, \quad e=1,...,m & \text{Macroscopic design variables} \end{array} \tag{1}$$

where the objective is to maximize the smallest of the structural damping ratios ζ_i for the n first eigenfrequencies. ζ_i can be computed from the complex eigenvalue ω_i as

$$\zeta_i=\sqrt{\frac{1}{1+(\mathrm{Re}(\omega_i)/\mathrm{Im}(\omega_i))^2}}. \tag{2}$$

The eigenvalue problem is a standard finite element eigenvalue problem, where the component's stiffness and mass matrix, $\mathbf{K}$ and $\mathbf{M}$, are assembled in the standard manner by summing over the elements. Remark, though, $\mathbf{K}$ will be complex since the component's damping is modelled as structural damping, where the elasticity tensor has both a real and imaginary part.

The constraint on the lowest eigenvalue is present to assure a minimum stiffness of the component, which would be required in most applications. Without this constraint, the optimal design would be to use only the

Table 1: Material properties for the stiff material phase and two different soft material phases. The material phases are isotropic, and, thus, the material properties are uniquely given by Young's modulus $E = E'(1+i\eta)$ and Poisson's ratio ν, but for the sake of clarity K' and G' are also stated.

Material	ρ [kg/m^3]	E' [GPa]	ν [-]	G' [GPa]	K' [GPa]	η [-]
Titanium	4500	100	0.3	38.46	83.33	0.001
S1	1000	2	0.4	0.71	3.33	0.05
S2	1000	0.05	0.495	0.017	1.67	0.5

Fig. 1: Result obtained using the optimization formulation in Eq. (1) with a linear interpolation between the material properties of S1 (white) and titanium (black). The design mesh consists of 40×10 elements, and the finite element mesh of 80×20 elements.

softest material. Note, this macroscopic optimization problem requires no filtering of the design variables to be well posed.

The key point of the multiscale approach is to base the material interpolation in the macroscopic problem on the homogenized material properties of corresponding microstructures. That is, the design variable value for an element, corresponding to a normalized density, can be mapped to a microstructure with material properties found from homogenization - also when the design variable is in-between 0 and 1.

There are two main reasons to use a multiscale approach. First, and most important to us, to assure the stiff phase can be manufactured in one piece using additive manufacturing and infused with the soft material. Second, because resolving the macroscopic problem down to the manufacturing precision can be extremely computationally expensive, especially since it involves solving an eigenvalue problem.

2.1.1 Simply supported beam

The macroscopic design problem considered in this paper is that of a 2D simply supported beam with dimensions 200 mm $\times$ 50 mm. The dimensions are chosen based on the fact that few additive manufacturing machines have a build chamber where the largest dimension is larger than 200 mm. Furthermore, assume the minimum feature size (wall thickness) is $1/4$ mm. To resolve the manufacturing precision of this simple 2D problem, 800×200 elements would be necessary. However, if each element was mapped to a microstructure with a unit cell size of 5×5 mm, a mere 40×10 design elements are necessary.

Solving the optimization problem in Eq. (1) on this coarse design variable mesh with a linear interpolation between the material properties of a stiff phase (titanium, see Tab. 1) and a soft phase (S1 in Tab. 1), with $\omega_0 = 80\%\,\mathrm{Re}(\omega_1^t)$, where ω_1^t is the first eigenfrequency of pure titanium, results in the design in Fig. 1. Even though we use a design mesh of 40×10 elements, the finite element mesh consists of 80×20 elements. Partly, because we want to make sure the physics is captured properly, and partly, because it makes the comparison with one of the examples in Section 5, where a finer design mesh is used, more fair.

The design consists mostly of intermediate densities (gray). However, this is not only due to the coarse mesh, but also because the material properties are interpolated linearly, which is not realistic. In order to obtain a more realistic interpolation, it is necessary to consider the design of the microstructure.

2.2 Microscopic optimization problem

As mentioned, a practical approach to multiscale optimization is to optimize the properties of the microstructure first, and then use these optimized microstructures as material phases to interpolate between with a multi-material interpolation scheme. With this approach the connectivity of the graded microstructure can be assured a priori, which is an important consideration and not trivial to achieve. Furthermore, the computational burden is very low compared to a coupled multiscale optimization problem. The drawback is that the solution space is more limited. For the problem presented here, where the focus is on isotropic microstructures, this is not a big issue. If arbitrarily anisotropic microstructures should be allowed, the approach might not be suitable. However, this would most likely lead to a structure which would be difficult to manufacture.

In Section Andreasen et al (2014), a formulation to obtain microstructures with a maximized bulk loss modulus is presented. This results in microstructures that can have very different loss factors in bulk and shear. Therefore, a slightly modified approach is used here, where the goal is to maximize the smallest of the bulk and shear loss factor. Furthermore, the stiffness constraint is on the shear modulus instead of the bulk modulus. For a 2D unit cell, this can be formulated as:

$$
\begin{array}{lll}
\min\limits_{\boldsymbol{\rho}}: & \max\left(\eta_G^*, \eta_K^*\right) & \text{Loss factors (also dilated and eroded design)} \\
\text{s. t.:} & \mathbf{KU} = \mathbf{F}, & \text{Homogenization equations} \\
& \mathrm{Re}(G^*) \geq a\,\mathrm{Re}(G_{\text{stiff}}), & \text{Shear storage modulus constraint} \\
& \dfrac{\sum_{i,j}\left(\mathrm{Re}(C_{ij}^{\text{iso}} - C_{ij}^*)\right)^2}{\left(\mathrm{Re}(C_{11}^{\text{iso}})\right)^2} \leq \varepsilon, \quad i,j = 1,...,3 & \text{Isotropy constraint (real part)} \\
& \dfrac{\sum_{i,j}\left(\mathrm{Im}(C_{ij}^{\text{iso}} - C_{ij}^*)\right)^2}{\left(\mathrm{Im}(C_{11}^{\text{iso}})\right)^2} \leq \varepsilon, \quad i,j = 1,...,3 & \text{Isotropy constraint (imaginary part)} \\
& \mathbf{K}_\sigma \mathbf{U}_\sigma = \mathbf{F}_\sigma, & \text{Conductivity homogenization equations} \\
& \sigma^* \geq b\sigma_{\text{stiff}}, & \text{Conductivity constraint on stiff phase} \\
& 0 \leq \varphi_e^{\text{micro}} \leq 1, \quad e = 1,...,N & \text{Local design variables}
\end{array}
\tag{3}
$$

where η_G^* and η_K^* are the homogenized shear and bulk modulus loss factors, respectively. G^* is the homogenized shear modulus, and G_{stiff} is the shear modulus of the stiffest material phase. Isotropy is enforced on both the real and imaginary part of the homogenized constitutive matrix with entries C_{ij}^* ($\varepsilon = 10^{-5}$ and C_{ij}^{iso} is computed based on the average of C_{11}^* and C_{22}^*, and C_{12}^*). The conductivity constraint is there to assure a connected stiff phase, therefore the homogenized conductivity is computed by setting the conductivity of the soft phase $\sigma_{\text{soft}} = 10^{-6}\sigma_{\text{stiff}}$.

Note, both the shear modulus constraint and the conductivity constraint are on the eroded design. With this formulation, the resulting microstructure has a connected stiff phase, and has a minimum length scale on both the soft and stiff phase (the robust formulation of Wang et al (2011) is used). Furthermore, if the obtained shear and bulk loss factor are equal, the material phase can be fully described using only three parameters: G', K', and η, which can be interpolated using the same design variable. The material interpolation in the microscopic elasticity problem is linear, and for the conductivity problem, a penalization factor of 3 is used.

3 Realistic material interpolations

A simple way to obtain a material interpolation between titanium and S1, is to use the formulation in Eq. (3) to find a microstructure with an intermediate density, and use the microstructures homogenized properties to create a power law interpolation between the material properties of S1 and titanium. In this section we want to obtain a material interpolation with the highest possible loss factor for the intermediate microstructure, and, therefore, the requirements necessary for manufacturing (robustness and conductivity of stiff phase) are disregarded.

For $a = 0.1$ the resulting microstructure is shown in Fig. 2(a) and denoted microstructure 2 (microstructure 1 is pure S1, and microstructure 2 is pure titanium). White is used to indicate the soft material phase, while black is used for the stiff material phase (titanium). The material properties of the obtained microstructure are plotted together with the material properties of S1 and titanium in Fig. 2(b-c), together with power law fitted functions, which can be used as material interpolation functions in the macroscopic problem.

Rerunning the macroscopic problem with the power law interpolations depicted in Fig. 2(b-c), results in the designs in Fig. 3, where also two designs obtained with finer design meshes are depicted.

With this more realistic interpolation, the design contains a much lower fraction of intermediate densities. However, there are still intermediate densities present - also when the resolution is increased. There is no guarantee that all points in the interpolation can be mapped to microstructures, and this could possibly to some degree explain the intermediate densities in the designs, but the results still indicate that even with a realistic interpolation a very fine discretization can be necessary to obtain a design without intermediate densities.

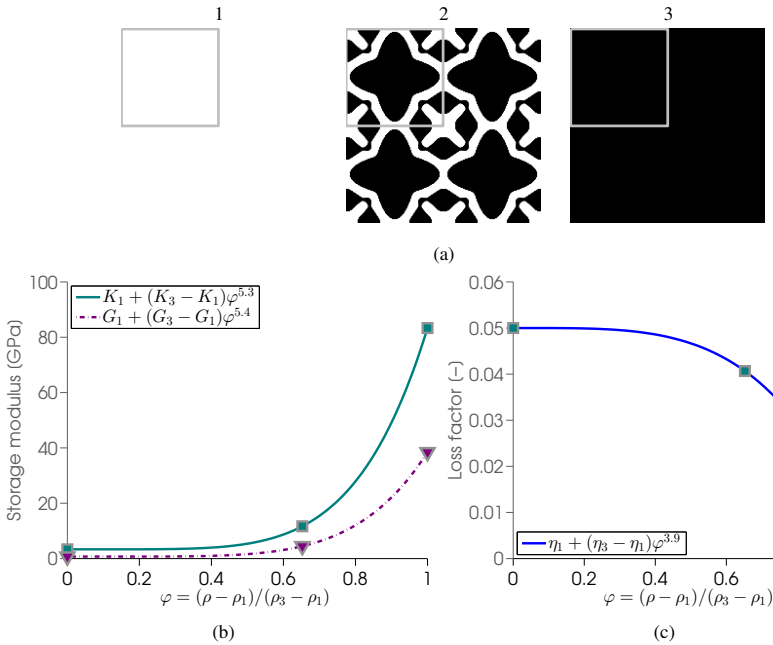

Fig. 2: (a) Microstructure 2 is obtained with the optimization formulation in Eq. (3) with S1 as the soft phase (microstructure 1) and no robustness requirement or conductivity constraint. (b-c) Power law interpolation between pure soft/stiff phase and the microstructure in (a). The shear and bulk loss factor are the same.

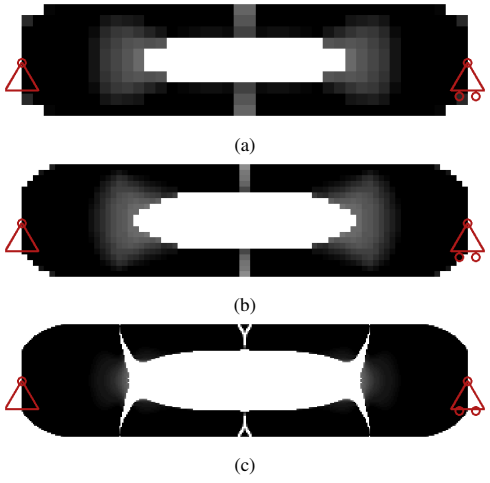

Fig. 3: Result obtained using the optimization formulation in Eq. (1) with the power law interpolations stated in Fig. 2 between the material properties of S1 (white) and titanium (stiff). In (a) the design mesh consists of 40×10 elements, while in (b) it consists of 80×20 elements. In both (a) and (b) the finite element mesh consists of 80×20 elements. In (c) both the design and finite element mesh consist of 320×80 elements.

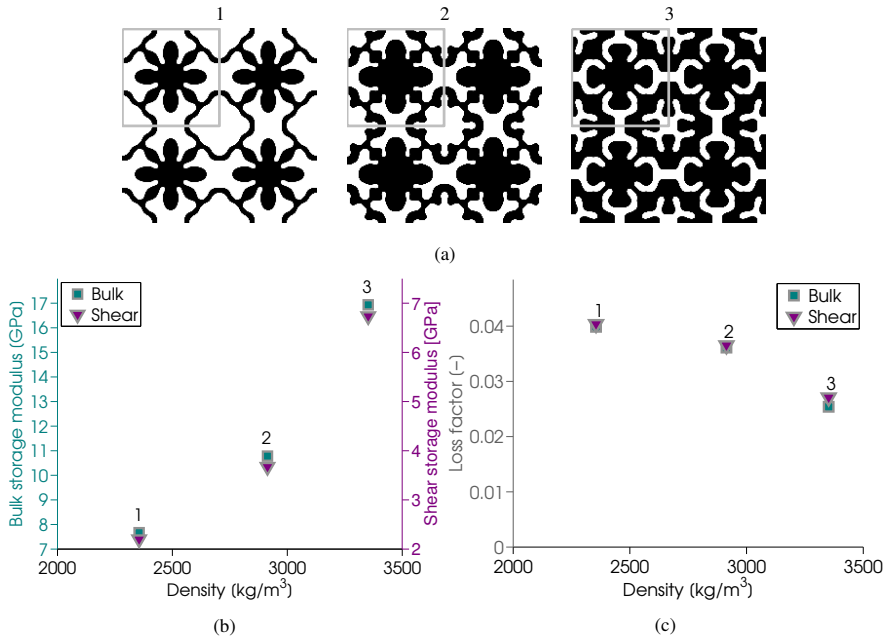

Fig. 4: Results obtained using the optimization formulation in Eq. (3) with S1 as the soft phase. (a) The three microstructures, and (b-c) their corresponding properties.

4 Microstructure results

In this section results for manufacturable microstructures with a stiff phase are presented. The microscopic formulation in Eq. (3) is used to maximize the loss factor of three connected microstructures consisting of titanium and S1, and titanium and S2.

A plane strain formulation is used, such that material phase S2, which has a Poisson's ratio close to 0.5, will be nearly incompressible. In order to prevent volumetric locking, the B-Bar method (Hughes 1980), which for rectilinear elements is equivalent to selective reduced integration, is used. However, for the microscopic homogenization problem, where S2 is used, locking does not seem to be an issue. The reason for this might be that the constitutive tensor is also reflected in the load. Therefore, almost identical results can be obtained without using selective reduced integration.

First, the microscopic formulation in Eq. (3) is used to maximize the loss factor of three connected microstructures consisting of titanium and S1, and titanium and S2.

For both cases, the loss factor is maximized with three different values a for the stiffness constraint. The conductivity constraint value is set to $b = 0.05$, and the robust formulation with $\eta_{\text{eroded}} = 0.4$ and $\eta_{\text{eroded}} = 0.6$ and a filter radius of 0.07 times the unit cell width, have been used for all designs. A higher conductivity constraint would typically give larger stiff material phase feature sizes, and a larger filter radius (or wider η-values) will increase the minimum feature size. A 45 degree symmetry has been enforced in all designs - this makes it easier to fulfill the isotropy constraints and do not, based on numerical experiments, affect the performance.

The resulting microstructures when using S1 are shown in Fig. 4(a). The corresponding homogenized material properties (evaluated from the thresholded designs) are plotted in Fig. 4(b-c). The stiffness of the microstructures follow a power law with a low exponent, and the loss factors seem to follow a similar power law, just with the opposite sign. Furthermore, note that the bulk storage modulus is always larger than the shear, even though the constraint is on the shear storage modulus.

The resulting microstructures when using S2 are shown in Fig. 5(a), and the corresponding homogenized material properties are plotted in Fig. 5(b-c). Due to the high bulk modulus of S2, it is possible to obtain four connected microstructures with a high loss factor. Even though the shear loss factor is lower than the bulk loss factor for all the microstructures, the S2 microstructures seem to have a good compromise between

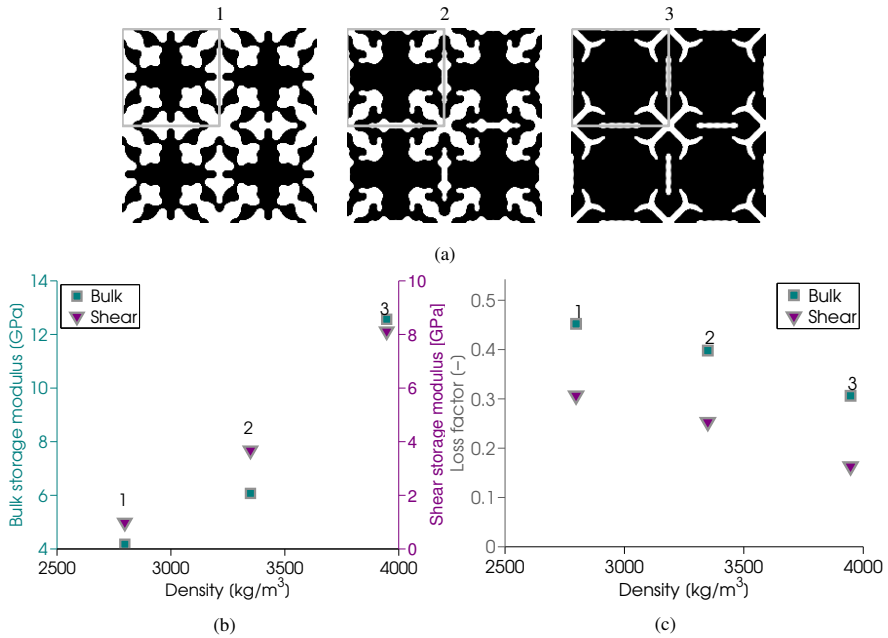

Fig. 5: Results obtained using the optimization formulation in Eq. (3) with S2 as the soft phase. (a) The three microstructures, and (b-c) their corresponding properties.

Table 2: Material properties for the titanium-S1 and the titanium-S2 microstructures in Fig. 4 and 5.

Material	ρ [kg/m^3]	G' [GPa]	K' [GPa]	η_G [-]	η_K [-]
S1-T (1)	2355	2.2	7.7	0.040	0.040
S1-T (2)	2914	3.7	10.8	0.037	0.036
S1-T (3)	3352	6.7	16.9	0.027	0.025
S2-T (1)	2798	1.0	4.2	0.31	0.45
S2-T (2)	3349	3.7	6.1	0.25	0.40
S2-T (3)	3947	8.1	12.6	0.16	0.31

damping and stiffness, but are denser and all the microstructures have a slightly lower bulk modulus than the corresponding S1 microstructures.

The homogenized material properties of both the titanium-S1 and the titanium-S2 microstructures are summarized in Tab. 2.

5 Material interpolation ensuring discrete design

In order to obtain a macroscopic structure consisting of only the discrete set of a priori obtained microstructures, we present a material interpolation for ”guiding” multiscale optimizations to this discrete set.

First, power law interpolations between the material properties of the microstructures are created. These are plotted in Fig. 6, where the x-axis shows the normalized density φ.

The storage moduli follow power law functions, while the loss factors are described by similar power law functions (with opposite signs). This opposite relation between storage and loss moduli, where the two intermediate density microstructures have proportionally higher loss, but lower stiffness, is what makes it possible to introduce an interpolation on the loss factors that guides the macroscopic problem to a discrete set of densities and corresponding microstructures.

First, the macroscopic optimization problem is solved using one of the power law interpolations stated in Fig. 6. The resulting design is used as the initial design for a new optimization where the power law interpolation on the loss factors are exchanged with multi-step Heaviside functions (continuous step functions),

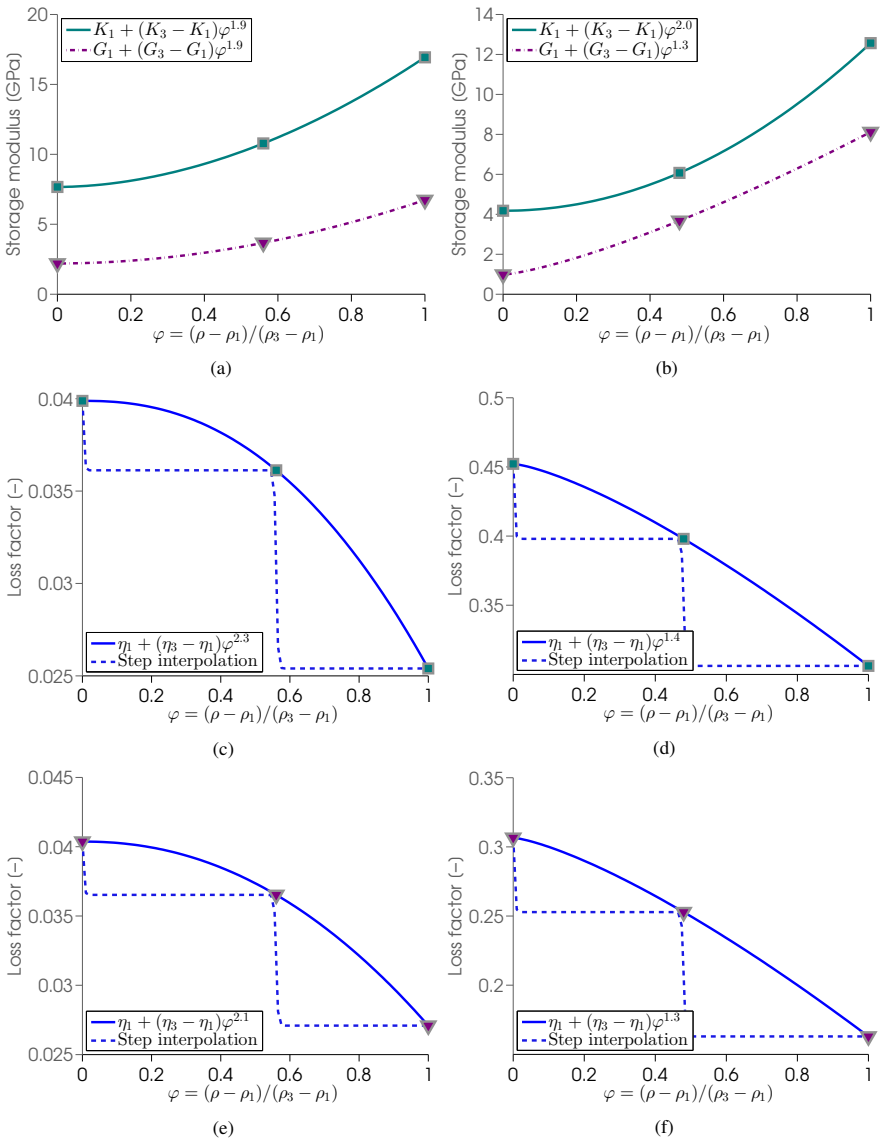

Fig. 6: (a), (c), and (e) show material interpolations between microstructures 1-3 in Fig. 4(a). (b), (d), and (f) show material interpolations between microstructures 1-3 in Fig. 5(a). (a-b) show the storage moduli interpolations, and (c-f) show the loss factor interpolation.

which are also illustrated in Fig. 6(c-f). These functions are constructed to favor the densities corresponding to the microstructures Fig. 6(a-b), because the densities in-between microstructures become sufficiently uneconomical when the goal is to maximize the structural damping with a constraint on the stiffness (the first eigenvalue constraint).

The interpolation builds on ideas first presented by (Guest et al 2004) and extended by (Xu et al 2010) (projection of filtered densities), but the multistep version introduced here is only meant as a material interpolation for the loss factors and not in conjunction with any filtering. As mentioned, no filtering is used in the macroscopic problem.

Remark, a modified Heaviside side function shifted to have the step at φ_i can be expressed as:

$$f_i(\varphi) = \tanh(\beta\varphi_i - \beta\varphi) + 1. \tag{4}$$

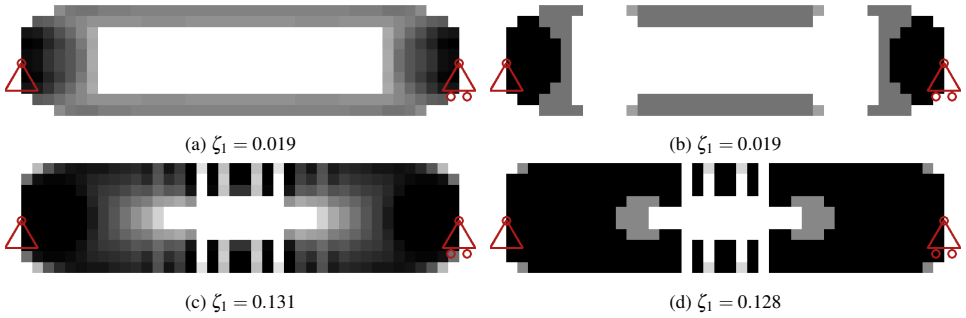

(a) $\zeta_1 = 0.019$ (b) $\zeta_1 = 0.019$

(c) $\zeta_1 = 0.131$ (d) $\zeta_1 = 0.128$

Fig. 7: Optimized beams, where white indicates microstructure 1 and black indicates microstructure 3. Gray corresponds to intermediate microstructures. (a) shows the design obtained using the power law interpolation for S1 microstructures, and (b) shows the final design after continuing optimization with Heaviside interpolation. (c) shows the design obtained using the power law interpolation for S2 microstructures, and (d) shows the final design after continuing the optimization with Heaviside interpolation.

At $\varphi = 1$ the function value is

$$f_i(1) = \tanh(\beta\varphi_i - \beta) + 1, \tag{5}$$

and we subtract this value from f_i, because we want the function to take the value 0 at $\varphi = 1$, and redefine f_i:

$$f_i(\varphi) = \tanh(\beta\varphi_i - \beta\varphi) - \tanh(\beta\varphi_i - \beta), \tag{6}$$

which will take the value

$$f_i(0) = \tanh(\beta\varphi_i) - \tanh(\beta\varphi_i - \beta), \tag{7}$$

at $\varphi = 0$. We want the function to take the value 1 at $\varphi = 0$, and therefore we again redefine f_i:

$$f_i(\varphi) = \frac{\tanh(\beta\varphi_i - \beta\varphi) - \tanh(\beta\varphi_i - \beta)}{\tanh(\beta\varphi_i) - \tanh(\beta\varphi_i - \beta)}. \tag{8}$$

By creating a weighted sum of these functions with step values φ_i corresponding to the material densities of the microstructures, a multiple step function between the loss factors of the microstructures can be obtained. This can be expressed as:

$$\eta = \eta_n + \sum_{i=1}^{n-1} (\eta_i - \eta_{i+1}) f_i, \tag{9}$$

where η_i is loss factor for microstructure i, and n is the number of microstructures.

The step function interpolation is first introduced after a good design has been obtained, and, therefore, the parameter controlling the steepness of the steps is set to a constant high value $\beta = 200$.

6 Macroscopic results

Consider the earlier described simply supported beam. If there is no constraint on the lowest eigenvalue, the optimized structure would be one purely consisting of microstructure 1. With S1 as the soft phase, the stiffest microstructure has $\zeta_1 = 0.013$ and $\mathrm{Re}(\omega_1) = 1219$ Hz. Thus, for the optimized beam we allow a slightly lower first eigenfrequency of $0.8 \cdot 1219$ Hz $= 975$ Hz, with the aim of achieving a higher structural damping.

The result of the first part of the optimization, using only the power law interpolations for the S1 microstructures from Fig. 6, is shown in Fig. 7(a). The optimized beam has $\zeta_1 = 0.019$. Continuing with the step function interpolation results in the design in Fig. 7(b) . A design with three discrete density values is nearly obtained. This beam also has a damping ratio that is only one percent lower than the beam in Fig. 7(a).

Now we run the same optimization, that is with the same eigenvalue constraint, but with the material interpolations for S2 from Fig. 6. The beam designs with the power law and the step function interpolation can be seen in Fig. 7(c) and (d), respectively. The damping ratios for the two designs are 0.131 and 0.128.

The large difference in damping ratios between the beam with S1 and S2, is to be expected since the base material properties are very different. However, it is also clear that the beam with S2 will contain much more

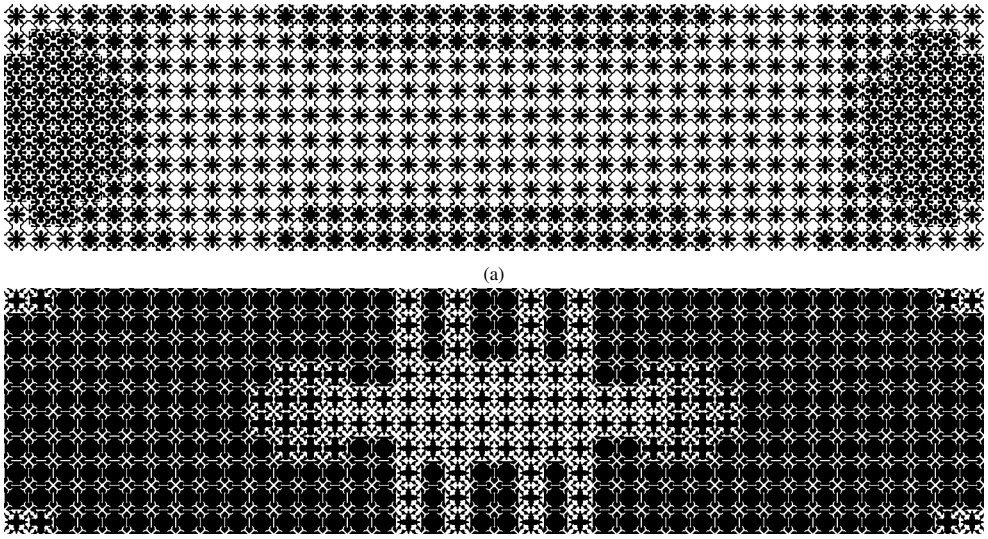

(a)

(b)

Fig. 8: Optimized beams from Fig. 7(b) and (d) with microstructure. (a) S1 microstructure, (b) S2 microstructure. Black indicates stiff material phase and white indicates soft material phase.

titanium in order to achieve the eigenvalue constraint. This is very clearly seen in Fig. 8, where the beams from Fig. 7(b,d) are shown with the full microstructural pattern.

Finally, it should be remarked that only the first eigenfrequency has been included in the optimizations here, even though the min-max formulation in Eq. (1) allows for a range of eigenfrequency. And the approach does work equally well with a range of eigenfrequencies, but in most cases the structural damping of the first one or two eigenfrequencies will drive the optimization.

7 Conclusion

The presented simple multiscale formulation makes it computationally feasible to maximize the structural damping ratio of a component with fine details. Furthermore, it assures the component is manufacturable, because the microstructural design guarantees the connectivity of the stiff phase, and the suggested material interpolation guides the design to a discrete set of microstructures.

References

Alexandersen J, Lazarov BS (2014) Robust topology optimisation of microstructural details without length scale separation - using a spectral coarse basis preconditioner. In review Preprint available, arXiv:14113923

Andreasen CS, Sigmund O (2012) Multiscale modeling and topology optimization of poroelastic actuators. Smart Materials and Structures 21(6), DOI 10.1088/0964-1726/21/6/065005

Andreasen CS, Andreassen E, Jensen JS, Sigmund O (2014) On the realization of the bulk modulus bounds for two-phase viscoelastic composites. Journal of the Mechanics and Physics of Solids 63(1):228–241, DOI 10.1016/j.jmps.2013.09.007

Barbarosie C, Toader AM (2012) Optimization of bodies with locally periodic microstructure. Mechanics of Advanced Materials and Structures 19(4):290–301, DOI 10.1080/15376494.2011.642939

Bendsøe M, Guedes J, Haber R, Pedersen P, Taylor J (1994) An analytical model to predict optimal material properties in the context of optimal structural design. Journal of Applied Mechanics - Transactions of the ASME 61(4):930–937

Coelho PG, Fernandes PR, Guedes JM, Rodrigues HC (2008) A hierarchical model for concurrent material and topology optimisation of three-dimensional structures. Structural and Multidisciplinary Optimization 35(2):107–115, DOI 10.1007/s00158-007-0141-3

Coelho PG, Cardoso JB, Fernandes PR, Rodrigues HC (2011) Parallel computing techniques applied to the simultaneous design of structure and material. Advances in Engineering Software 42(5):219–227

El-Sabbagh A, Baz A (2014) Topology optimization of unconstrained damping treatments for plates. Engineering Optimization 46(9):1153–1168, DOI 10.1080/0305215X.2013.832235

Guest J, Prevost J, Belytschko T (2004) Achieving minimum length scale in topology optimization using nodal design variables and projection functions. International Journal for Numerical Methods in Engineering 61(2):238–254

Hughes TJR (1980) Generalization of selective integration procedures to anisotropic and nonlinear media. International Journal for Numerical Methods in Engineering 15(9):1413–1418

Khanoki SA, Pasini D (2012) Multiscale design and multiobjective optimization of orthopedic hip implants with functionally graded cellular material. Journal of Biomechanical Engineering - Transactions of the ASME 134(3):–, DOI 10.1115/1.4006115

Kim SY, Mechefske CK, Kim IY (2013) Optimal damping layout in a shell structure using topology optimization. Journal of Sound and Vibration 332(12):2873–2883, DOI 10.1016/j.jsv.2013.01.029

Ling Z, Ronglu X, Yi W, El-Sabbagh A (2011) Topology optimization of constrained layer damping on plates using method of moving asymptote (mma) approach. Shock and Vibration 18(1-2):221–244, DOI 10.3233/sav-2010-0583

Rodrigues H, Guedes JM, Bendsoe MP (2002) Hierarchical optimization of material and structure. Structural and Multidisciplinary Optimization 24(1):1–10, DOI 10.1007/s00158-002-0209-z

Stegmann J, Lund E (2005) Discrete material optimization of general composite shell structures. International Journal for Numerical Methods in Engineering 62(14):2009–2027, DOI 10.1002/nme.1259

Theocaris PS, Stavroulakis GE (1999) Optimal material design in composites: An iterative approach based on homogenized cells. Computer Methods in Applied Mechanics and Engineering 169(1-2):31–42

Wang F, Lazarov BS, Sigmund O (2011) On projection methods, convergence and robust formulations in topology optimization. Structural and Multidisciplinary Optimization 43(6):767–784

Xu S, Cai Y, Cheng G (2010) Volume preserving nonlinear density filter based on heaviside functions. Structural and Multidisciplinary Optimization 41(4):495–505

DTU Mechanical Engineering
Section of Solid Mechanics
Technical University of Denmark

Nils Koppels Allé, Bld. 404
DK- 2800 Kgs. Lyngby
Denmark
Phone (+45) 4525 4250
Fax (+45) 4593 1475
www.mek.dtu.dk
ISBN: 978-87-7475-394-0

DCAMM
Danish Center for Applied Mathematics and Mechanics

Nils Koppels Allé, Bld. 404
DK-2800 Kgs. Lyngby
Denmark
Phone (+45) 4525 4250
Fax (+45) 4593 1475
www.dcamm.dk
ISSN: 0903-1685